Elektrische Energietechnik an der TU Berlin Band 14

Julian Long

Detection and characterization of lithium plating

Universitätsverlag der TU Berlin

Technische Universität Berlin

Julian Long

Detection and Characterization of Lithium Plating

The scientific series *Elektrische Energietechnik an der TU Berlin* is edited by:

Prof. Dr. Sibylle Dieckerhoff

Prof. Dr. Julia Kowal

Prof. Dr. Ronald Plath

Prof. Dr. Uwe Schäfer

Elektrische Energietechnik an der TU Berlin | 14

Julian Long

Detection and Characterization of Lithium Plating

Universitätsverlag der TU Berlin

Bibliographic information published by the Deutsche Nationalbibliothek
The Deutsche Nationalbibliothek lists this publication in the
Deutsche Nationalbibliografie; detailed bibliographic data are
available on the internet at http://dnb.dnb.de.

Universitätsverlag der TU Berlin, 2023
https://verlag.tu-berlin.de

Fasanenstr. 88, 10623 Berlin
Tel.: +49 (0)30 314 76131
Email: publikationen@ub.tu-berlin.de

Zugl.: Berlin, Techn. Univ., Diss., 2022
Gutachterin: Prof. Dr.-Ing. Julia Kowal
Gutachterin: Prof. Dr.-Ing. Ulrike Krewer (Karlsruher Institut für Technologie)
Gutachter: Prof. Dr. rer. nat. Dirk Uwe Sauer (RWTH Aachen)
Die Arbeit wurde am 13. Juli 2022 an der Fakultät IV unter
dem Vorsitz von Prof. Dr.-Ing. Ronald Plath erfolgreich verteidigt.

Print: docupoint GmbH
Layout/Typesetting: Julian Long

ISBN 978-3-7983-3278-2 (print)
ISBN 978-3-7983-3279-9 (online)

ISSN 2367-3761 (print)
ISSN 2367-377X (online)

Published online on the institutional repository of the
Technische Universität Berlin:
DOI 10.14279/depositonce-16978
https://dx.doi.org/10.14279/depositonce-16978

“Knowledge is knowing a tomato is a fruit; wisdom is not putting it in a fruit salad.”
(Miles Kington)

Acknowledgement

First of all I want thank Prof. Dr. Julia Kowal for her support and trust. She was always helpful and supportive without putting pressure on me or trying to imprint her style on the thesis. I am very grateful for her supervision. Furthermore I want express my thanks to the Fraunhofer IZM for letting me perform battery material measurements using their XPS device and especially to Steffen Rauschenbach whose patient help and explanations enabled me to do these experiments in the first place. I want to thank all my colleagues that have accompanied me for all these years at the TU for their comradeship, smart inputs and valuable criticisms. Because of all of you I was always looking forward to come to work. I'm also very grateful for my examiners Prof. Dr. Ulrike Krewe and Prof Dr. Dirk Uwe Sauer who came the long way to Berlin to attend my defense. I also want to thank the students mentioned in this thesis whose contributions in their master thesis' made this work possible. Last but not least I want to thank my family for always believing in me and never pushing me to anything I didn't want and my amazing wife for surviving the lock-down year with me without any mayor complaints.

Abstract

Lithium plating is not only the most severe ageing mechanism in lithium-ion batteries (LIBs) but also becoming more and more important due the increasing presence of electric vehicles (EVs). In EVs the extreme conditions causing lithium plating, like very high charging currents and low environment temperatures, are much more prevalent than in consumer electronics. Due to the high number of factors that influence the plating process, ranging from the cell geometry to the chemical composition of the electrolyte, a deeper understanding of the plating process is still lacking. Without this knowledge it is hard to design cells in a plating resistant way, or to operate cells under the ideal conditions to minimize plating. This thesis aims at showing different methods to investigate the plating process on three different levels.

The first method is on the cell level, investigating the behaviour of the whole cell during plating. It contains the analysis of the voltage and current profiles that show an atypical behaviour during plating. The focus of the analysis is on the current profile of the constant voltage (CV) phase during charging under low temperature conditions leading to plating. This current profile can be fitted with the Johnson-Mehl-Avrami-Kolmogorov (JMAK) function that describes the electrochemical deposition process of a metallic species on a surface. The resulting fitting parameters can be utilized to characterize the plating behaviour of the cell as well as better estimate the amount of plated lithium than commonly used methods. It can also potentially predict the future safety risk due to dendrite formation.

In the second part the chemical composition of the surface electrolyte interface (SEI) is investigated using X-ray photoelectron spectroscopy (XPS). The composition as well as the mechanical properties of the SEI are strongly

influencing the plating process and preliminary work has shown that plating is also changing the morphology of the SEI and increasing its thickness drastically. Cells under different conditions (plated, charged and discharged) as well as cells of different manufacturers have been probed using XPS. During the measurements an unwanted side effect of the experimental setup was discovered that lead to a migration of lithium to the surface of the sample and was distorting the measurement results. Regardless of the effect, it was possible to see that the SEI can have a very different composition in cells of different manufacturers and that plating not only changes the morphology but also the composition of the SEI. The unwanted side effect could furthermore be utilized to identify samples that were plated recently and could be used in further more controlled experiments to localize lithium depositions on plated samples.

In the last part the particle structure of the anode surface of cells of different manufacturers was investigated using a watershed particle detection algorithm on laser scanning microscopy (LSM) images of the anode surfaces. The distributions of the particle sizes have then been compared to the capacity loss in plated cells. It was shown that the capacity loss correlates with parameters extracted from the particle size distributions. It is however necessary to create more data to verify this correlation.

In summary this thesis utilized new methods to detect or characterize plating on different levels of magnification, from the cell level to the chemical composition. New approaches were found to predict a cells future plating behaviour, spatially localize plated areas on the anode and design cells in a plating resistant way.

Kurzzusammenfassung

Lithium Plating ist nicht nur der Alterungsmechanismus in Lithium-Ionen Batterien mit dem größten Kapazitätsverlust, sondern wird auch im Zuge der voranschreitenden Elektrifizierung des Personenverkehrs immer wichtiger. In Elektrofahrzeugen finden sich die extremen Zustände, wie niedrige Ladetemperaturen und hohe Ladeströme, unter denen Plating auftritt, deutlich häufiger als in Unterhaltungstechnik. Durch die Vielzahl von Parametern, von der Zellgeometrie bis hin zur Elektrolyzusammensetzung, die Plating beeinflussen, fehlt immer noch ein tieferes Verständnis des Plating-Prozesses. Ohne dieses Wissen ist es schwer, Zellen zu designen, die resistent gegen Plating sind oder Zellen unter optimalen Bedingungen zu betreiben um Plating zu minimieren. Das Ziel dieser Arbeit ist es, verschiedene Methoden aufzuzeigen, die die Untersuchung von Plating auf drei verschiedenen Ebenen ermöglichen.

Die erste Methode untersucht das Gesamtverhalten der Zelle auf Zellebene. Hier-bei wird das atypische Verhalten der Strom- und Spannunsprofile während des Plating-Vorgangs analysiert. Der Fokus liegt dabei auf der Untersuchung der Konstantstrom-Phase bei niedrigen Temperaturen während der Ladung. Das Strom-profil dieser Phase kann mit der JMAK Funktion gefittet werden, welche die elektrochemische Abscheidung eines Metalls auf einer Oberfläche beschreibt. Die resultierenden Fitting-Parameter können genutzt werden, um das Plating-Verhalten vorherzusagen und sind gleichzeitig eine bessere Abschätzung für die Menge an geplatetem Lithium im Vergleich zu gängigen Methoden. Die Ergebnisse könnten außerdem helfen das Sicherheitsrisiko der Zelle bei Dendritenbildung vorherzusagen.

Im zweiten Teil wird die chemische Zusammensetzung der SEI mittels XPS untersucht. Die Zusammensetzung, wie auch die mechanischen Eigenschaften der SEI, beeinflussen den Plating-Prozess stark und es wurde in vorhergehenden Arbeiten gezeigt, dass Plating auch die Morphologie und Dicke der SEI drastisch verändern kann. Zellen in verschiedenen Zuständen (geplatet, geladen, entladen), sowie Zellen verschiedener Hersteller wurden mit XPS untersucht. Während der Messungen wurde ein ungewollter Nebeneffekt des Messaufbaus entdeckt, der zu einer Migration von Lithium an die Oberfläche der Proben geführt und die Messergebnisse verfälscht hat. Unabhängig von diesem Effekt war es dennoch möglich, zu zeigen, dass die SEI in Zellen verschiedener Hersteller stark unterschiedliche Zusammensetzungen haben kann und dass Plating nicht nur die Morphologie der SEI beeinflusst, sondern auch die chemische Zusammensetzung. Weiterhin konnte der ungewollte Nebeneffekt verwendet werden, um Proben zu identifizieren, die vor kurzem geplatet wurden und könnte in zukünftigen Arbeiten verwendet werden, um lokalisiert Lithium-Ablagerungen auf geplateten Proben zu identifizieren.

Im letzten Teil wurde die Partikelstruktur der Anoden von Zellen verschiedener Zellhersteller mit Hilfe einer watershed-Partikeldetektion an LSM Bildern untersucht. Die Verteilung der Partikelgrößen wurde mit dem Kapazitätsverlust gleicher Zelle durch Plating verglichen. Es wurde gezeigt, dass der Kapazitätsverlust mit Parametern, die aus den Partikelverteilungen extrahiert wurden, korreliert. Ein größerer Datensatz ist jedoch notwendig, um diese Ergebnisse zu validieren.

Zusammenfassend hat diese Arbeit verschiedene neue Methoden aufgezeigt, um Plating auf verschiedenen Vergrößerungsebenen zu detektieren und zu charakterisieren. Neue Ansätze wurden gefunden, um das Platingverhalten von Zellen vorher-zusagen, lokalisiertes Lithium auf der Oberfläche zu detektieren und Zellen plating-resistenter designen zu können.

Contents

List of Figures

List of Tables

Chapter 1

Introduction and Motivation

In the last decade LIBs have consolidated their prime position as the go to battery for all consumer electronics [1]. With the climate protection targets and the demand for a rising amount of electric vehicles for private and public transport, the LIB is also the only technology that has the needed energy density, as well as the development level necessary, to support the transition from fossil fuels to CO_2 free transportation. While there are new technologies in development with even higher theoretical energy densities, none of the candidates has reached a technology readiness level yet that could challenge the usability of the LIB [2]. One big concern with batteries in general however is the ongoing degradation through battery ageing during operation that not only increases the running of costs of all EVs but also reduces the customer acceptance of the vehicles, which is vital for a widespread change to electric transportation [3]. With increasing ageing, not only the capacity of a cell fades but also the available power. Presently the main efforts in battery research are targeted towards increasing the energy density to enable higher range on full electric vehicles and to reduce the ageing on the cell to increase the overall lifetime [4, 5]. One of the strongest ageing effects possible in LIBs is the so called lithium plating, which describes the unwanted deposition of metallic lithium on the anode surface during charging. This deposition takes place when the device is charged at very low temperatures, or when very high charging currents are applied. The capacity losses of plating can lead to the end of life of a cell within 10s of cycles, when the nominal cell life can last for hundreds or even thousands of cycles [6]. The plating process can also cause the growth of lithium dendrites, small lithium metal structures that can pierce the separator and cause shortcuts within the cell. These can

lead to cell failure or in the worst case to a thermal runaway of the cell, a process where the cell reaction is self-energizing and causing a cell fire [7].

The conditions for lithium plating are rarely met for cells within consumer electronics, since they are normally charged at moderate rates within living areas. This is different for EVs however. Electric cars are supposed to work under all normal outside conditions and thus charging at low temperatures is something that cannot be prevented. Today the vast majority of customers with electric cars also own a house or have access to a garage to charge their cars at higher temperatures under better conditions [8] which is partly because of the still higher price of the cars and the on average better economical situation of house owners, and partly because of the lack of infrastructure in the area of public charging stations. With the target of a much higher percentage of EVs in the future however, this cannot be guaranteed for each owner of an electric car and some of the vehicles will have to be charged at public charging stations outside. To compensate for this effect, it is possible to equip EVs with a heating system that heats up the battery to the optimal charging temperature prior to the charging process. The drawback of this method is for one the energy losses induced by the necessary heating process that increase the running costs of the car and the increased charging time due to the added heating time. In some cases there may not even be enough energy left in the cell to heat up properly to prevent plating during charging. The batteries are heating up due to the ohmic losses during the charging process, but this does not fully prevent the ageing caused by plating. Another aspect that is of vital importance for EVs is the charging speed [9]. To compete with combustion engine cars the charging speed of EVs would have to be in the range of minutes to increase the acceptance of the EVs as a fully capable replacement. This would however require charging rates that greatly exceed the recommended nominal charging speeds for standard commercials LIBs. To fully charge a battery within ten minutes a charging speed of 6 times higher than average recommended data sheet speeds of higher energy cells of 1C is required. It is possible to manufacture cells that can handle higher charging speeds, but this is always at the cost of energy density, which is vital for the range of the EV.

For these very high charging speeds, plating effects are to be expected even at moderate temperatures, leading to very fast cell degradation [7].

Grid stabilization using EVs could be the solution for the strongly fluctuating energy output of renewable energy sources. All EVs that are not currently in use and that are connected to the power grid could be used to stabilize the grid and store excess energy in times of overproduction, while at the same time providing energy in times of high demand [10, 11, 12, 13]. If the vehicles are used in this way, low environment temperatures could be very damaging for the battery cells. In this case, the energy influx is unpredictable and uncontrollable and thus no prior heating is possible. Always keeping the batteries at a safe temperature however would produce very high energy losses.

The amount of available spent batteries is going to increase significantly within the next few years when the first generations of car batteries will reach the end of life. The plating effect is also attributed to sudden cell death at very low state of health [7, 14] when the surface electrolyte interface (SEI) layer is getting very thick. Predicting this mode of cell failure could be very beneficial for second life usage of spent EV batteries.

Understanding and preventing plating could not only increase the general lifetime for LIBs, but also enable the usage of EVs as a grid support for renewable energies, greatly increasing the usability of fully renewable energy sources to reduce CO_2 emissions. It can also help making second life applications more reliable and thus extend the commercial value of the batteries. At the same time it increases the safety of LIBs by preventing dendrites that can cause cell failure or dangerous thermal runaways. A deeper understanding of the plating process can also help to increase the usability of metallic lithium in future battery technologies. The usage of metallic lithium as the anode in a lithium battery drastically increases the energy density. The redeposition of the lithium on the anode during the charging process in the battery however is hard to control and leads to very low cycle numbers of those cells [15, 16, 17]. Even for completely new technologies, the usage of lithium is highly likely [2]. Lithium is not only the lightest solid material in existence but it also has the highest negative standard electrode potential.

This enables very lightweight batteries with a high voltage and thus high energy density.

To achieve a better understanding about plating and find new methods to prevent plating or reduce the damaging impact of plating, in this thesis in-situ measurements as well as ex-situ post mortem analysis have been applied to cells that were cycled under plating conditions. Electrical measurements for voltage and current as well as electrochemical impedance spectroscopy (EIS) measurements are conducted on cells with prolonged constant-voltage phases to study the lithium metal crystallization process on the anode surface based on the anomaly of the current shape visible under plating conditions in chapter 3.2. EIS measurements are also conducted during the diffusion of the lithium metal into the anode after the charging is completed to see the effect of metallic lithium metal presence on the impedance of the cell. Combining the results of these measurements leads to a comprehensive understanding of plating from the onset during the charge to the consequences of plating afterwards that can be used to help detect plating in operation, but at the same time also help to optimize cell design to reduce the impact of plating. Reducing the lasting effects plating can also help prevent cell degradation caused by the undetectable plating linked to sudden cell deaths.

These in-situ measurements are supported by different post-mortem analysis methods. An LSM has been used for quick surface analysis to check for visible impact of plating on the surface of the anode and also allows for spatially resolved analysis to detect areas of the cell that are affected stronger by plating, visible in chapter 3.1. In chapter 3.4 a study of cells by different manufacturers was also conducted using the LSM to analyze whether certain surface parameters based on the particle size distribution can be linked to a higher plating susceptibility. FIB cross sections in the samples were used in chapter 3.1 to get an understanding of the surface layer changes induced by plating. To analyze the chemical composition of this surface film XPS combined with depth profiling is applied in chapter 3.3.1.

In summary the main questions this thesis aims to answer are the following:

- How can plating be detected during the charging process?
- What are the effects of plating on the morphology as well as the chemical composition of the anode surface layer?
- How can a cell be characterized regarding its plating behaviour without extensive experiments?
- Which design parameters of the cell can help to prevent or reduce plating?

Chapter 2

State of the Art – LIBs

LIBs are using lithium ions to store energy. Contrary to the lithium-metal battery (LMB), where lithium exists in its elemental state inside the battery, the lithium in the LIB only exists in ion form, intercalated, as a free ion in the electrolyte or in a chemical compound. Although the LIB has a lower possible energy density compared to the LMB, the LIB became the standard of lithium batteries. The first lithium batteries on the market in the late 1980s used lithium metal as the anode, but following a series of accidents caused by the re-deposition of the lithium during charging and the resulting risk of lithium dendrites growing on the surface, these cells had to be recalled [18]. The subsequent failure to solve the safety problems of the LMB quickly lead to the discovery of alternate anode materials that where able to store the lithium ions in a safer and more reliable way. The LIB is not only safer than the LMB, it also possesses a much higher cyclability due to the more controlled lithium deposition process on the anode. The LIB quickly took over the market for consumer electronics, completely replacing the leading technology at that time, the nickel-based batteries, due to its superior energy density and cycle life. The introduction of this technology enabled a lot of the mobile devices that are a natural part of our lives today: smartphones, tablets, cameras, smartwatches and so on. As of now the LIB is also the only commercially ready technology that can enable full electric transport for private use and is thus an integral part of the worldwide efforts to become free of fossil fuels and reduce the overall CO_2 emissions. And even though the demand for high energy density in the sector of stationary energy storage is naturally not as high as for mobile applications, LIBs are starting to see usage in large scale stationary storage for grid stabilization as well [19].

2.1 Components and Functionality

The LIB is, like all electrochemical storage systems, made up primarily of an anode and a cathode, that drive the redox-reaction. Figure 2.1 shows the general schematic of a LIB and all its components. In most commercially available LIBs today, the **anode** is mainly composed of Graphite (C_6). This graphite and added binders are pressed onto a copper foil that functions as the current collector, while the **cathode** is a lithium-metal-oxide (LiMeOx) pressed on aluminum foil.

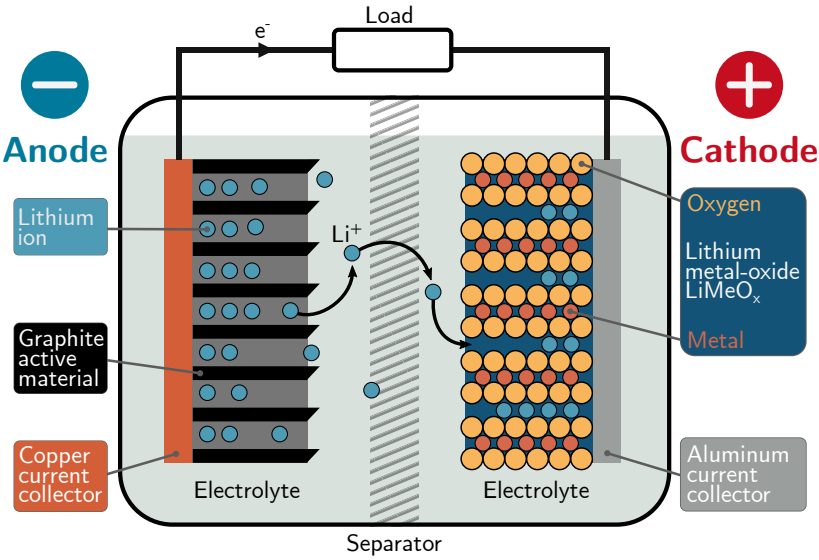

Figure 2.1: Schematic of a general LIB

In the LIB the lithium ions are responsible for the storage of energy. During charging and discharging the ions are moved from the anode to the cathode and vice versa. It is not necessarily always the case in all electrochemical systems that the main ion is moved during the reaction. Even though there always has to be an ion moving inside the cell to close the electrical circuit, e.g. in lead-acid batteries the moving ion is a hydrogen ion, not a lead ion.

The **electrolyte** in LIBs is not taking part in the cell reaction as it was the case in its technological predecessors, the nickel-hydroxide and lead-acid batteries, but is solely in the cell for the ion transport. For this reason the amount of electrolyte in the cell can be reduced to a minimum necessary to properly connect all the cell elements. Normally the electrolyte of commercial LIBs is composed of an organic solvent with a lithium salt as the lithium-ion source. The usage of an aqueous electrolyte in cell cells containing lithium is not possible since lithium reacts with water. Typically the electrolyte is composed of a mixture of organic solvents to get the best performance. The most common solvents used are a combination of ethylene carbonate (EC) and dimethyl carbonate (DMC) with lithium hexafluorophosphate ($LiPF_6$) as the lithium containing salt. This solution has a good combination of temperature stability, good ion conductivity, good wetting ability and no co-intercalation. In the first LIBs propylene carbonate (PC) was used as an electrolyte, a remainder of the short-lived LMB period, having an even better lithium-ion conductivity. This however was causing quick anode degradation when the solvent molecules undesirably intercalated into the graphite together with the lithium ions [18]. The electrolyte also plays a major role in the formation of the SEI layer, that impacts the cell performance as well as the cell degradation and will be explained in detail in chapter 2.2.1.

The **separator** is an element in any electrochemical cell that is physically separating the the two electrodes whilst electrically isolating them against each other. At the same time the separator must be permeable for the ion current inside the cell, which in most cases means a porous separator that is permeable for the electrolyte. In LIBs the most common separator is a polymer membrane, e.g. made of polypropylene (PP) or polyethylene (PE). The desired properties of the separator are a low weight, high thermal and mechanical stability and low material costs [20].

2.1.1 Charging and Discharging

In a fully charged LIB all lithium ions are intercalated inside the anode. Intercalation means that the ions are positioned in between the graphite

layers, but no conversion reaction has taken place. It is described by a reversible process that is keeping the structural integrity of the intercalation host material [21]. The fact that there are no chemical reactions that directly transform materials is one factor of the high lifetime of LIBs. Since there is no new compound forming, the stress due to rearrangement of the material during the charging and discharging process is very low. The graphite is increasing in size by less than 10% during the lithium-ion intercalation [22]. When the battery is discharged the lithium ions de-intercalate from the anode by releasing one electron, becoming Li^+, and move through the electrolyte to the cathode where they intercalate into the metal-oxide to form a lithium-metal oxide. The LIB has "lithium ion" in its name for the fact that there are only intercalations of lithium ions involved on both sides of the cell reaction, regardless of charge or discharge [23]. The total cell reaction in the discharge direction can then be described as:

$$Li_xC_6 + Li_{1-x}MeO_y \rightleftharpoons C_6 + LiMeO_2$$

Where the x describes the ratio of lithium remaining within the anode, this number is equivalent to the state of charge (SOC). The graphite can have different lithiation states that can be seen in plateaus in the open circuit voltage (OCV) [24]. The Me is representative for a group of metals that can be used in the cathode.

During the charging process, this reaction is simply inverted and the lithium ions are moving from the cathode to the anode, where they intercalate into the graphite and take in one electron.

Since LIBs are very sensitive to over- and undercharging it is very important to stay within the voltage limits for the given material combination. For this reason the most common choice of charging method for LIBs is the constant current constant voltage (CCCV) charging method. Using this method the cell is charged with a constant current until the end-of-charge voltage is reached (typically 4.2 V) and then that voltage is held during a constant voltage phase while the current drops. When the current reaches a minimum current threshold the charging process is finished. The minimum

current is necessary due to self discharge and parasitic currents because of which the charging current can never reach zero in a real application. Figure 2.2 shows the voltage, current and SOC curves for CCCV charging, where I_{ch} is the charging current and I_{thres} the threshold current at which the charging process is terminated. V_{max} and V_{min} denote the end-of-charge and end-of-discharge voltage window of the battery, respectively.

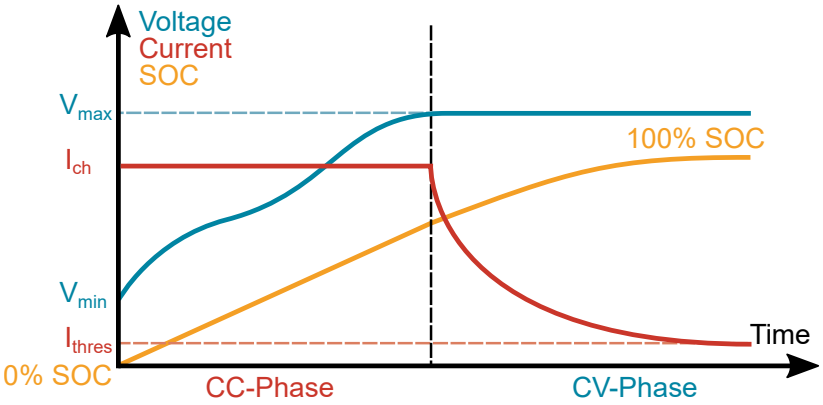

Figure 2.2: Voltage, Current and SOC curves of a typical CCCV charging process

During the CC-phase the majority of charge is put into the battery and the SOC rises linearly. In most cases the battery is charged to around 80% SOC in the CC-phase. The CV-phase then charges the remaining amount to 100% SOC. The CC-phase makes up around half of the total charging time. For this reason a lot of fast-charging methods only use the CC-phase for charging and don‘t use the full battery capacity.

2.2 Anode

Graphite is currently the most used anode material for lithium-ion batteries due to its high practical capacity and low potential vs Li, enabling it to store a high amount of energy, and a rather flat discharge curve, giving a constant power output over a big range of the capacity [21]. The anode of

a commercial LIB as of today is in most cases made of a slurry of graphite (C_6) with added binder and carbon black that is pressed on a copper foil. The binder used is typically polyvinylidenfluorid (PVDF) [25]. The carbon black is added to increase the electric conductivity of the active material. The carbon has the shape of particles with varying sizes depending on the producer. Differently sized particles can have different effects on the cycle-lifetime and other parameters of the battery performance, like the available power density.

The anode is typically oversized by around 10% compared to the cathode to prevent lithium plating at the edges [3, 26]. If the electrodes had the same size local overcharging (or overcharging in general, explained in more detail later in chapter 2.5) caused by inhomogeneous capacity losses of the anode could lead to lithium plating in these regions. The increasing field strength at the edges of the anode could also lead to localized lithium plating [27]. This area is sometimes called the anode overhang [28].

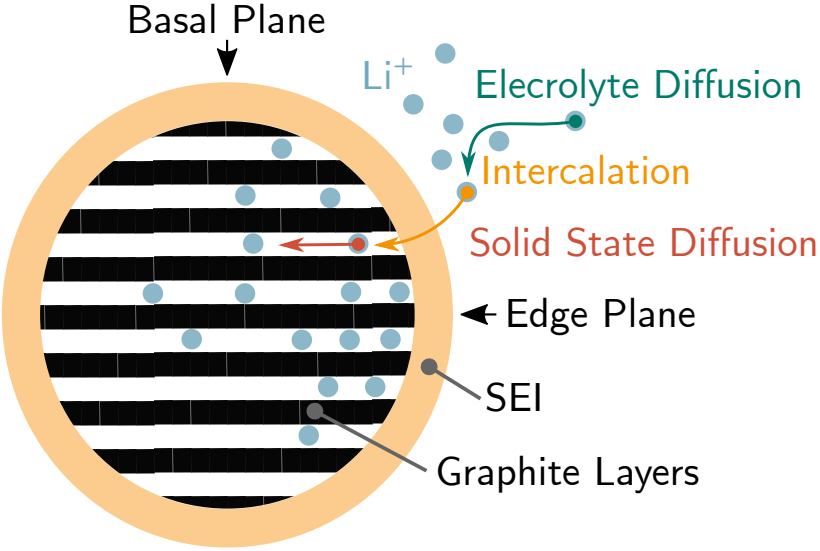

Figure 2.3: Schematic view of one graphite particle inside the anode active material

A graphite particle consist of basal and edge planes. The edge planes are perpendicular to the layer direction of the graphite crystals. They provide an easy entry point for the lithium ions to intercalate into the graphite. This is why most of the lithium-ion insertion and diffusion into the active material starts from the edge planes. The basal planes are along the layer direction of the graphite crystal and lithium ions cannot intercalate across a basal plane into the graphite, which is why they are the less reactive areas of the graphite particles. The ratio of edge planes to basal planes has a high impact on the electrochemical performance of a given graphite material [29]. The same way the orientation of the particles has a similar influence, with less oriented graphite generally having a worse performace due to a more difficult diffusion for the lithium ions [3].

In the charged state the lithium ions are intercalated into the graphite, located between the graphite planes. Lithium can naturally diffuse into graphite and is evenly distributing in the anode active material over time after the charging is finished. The resulting material of graphite with intercalated lithium ions is called a graphite intercalation compound (GIC) that is characterized by a mixed ionic and electric conduction [21].

The volume expansion of graphite (C_6) compared to fully lithiated graphite (LiC_6) is approximately at about 10% to 13% when the lithium ions inhabit the free lattice spots within the graphite [21, 30, 31]. This effect is quite low compared to other materials, but still leads to mechanical stress inside the cell during cycling.

2.2.1 The SEI Layer

The SEI layer does not only have a huge impact on the cell performance, it also is the main reason for cell ageing in LIBs [4]. The SEI is a thin layer on the anode surface that forms due to electrolyte decomposition. There is no electrochemically stable electrolyte for the operating voltage range of a LIB, so a decomposition is unavoidable. Due to the high reactability of water with lithium an aqueous electrolyte is no option in the current state LIBs, only organic electrolytes can be used. The working voltage window in the battery will either cause electrolyte decomposition at the anode or

cathode at the respective voltage values of a fully charged of fully discharged cell [30, 32]. The stability window for most of the commonly used electrolyte parts (e.g. EC,DMC) is from around 0.8 V to 4.7 V vs Li/Li^+ [33, 34]. This window is further decreased by the cell temperature leading to electrolyte degradation at the cathode as well for elevated temperatures [35, 36]. As most commercially available LIBs operate from around 0.2 V vs Li/Li^+ when fully charged to 1.7 V vs Li/Li^+ when fully discharged, the decomposition takes place on the anode side at high SOC. In the decomposition process not only the components of the electrolyte are consumed but also the lithium ions present in the electrolyte. This reduces the total number of available lithium in the cell and in consequence the capacity of the cell. This addition of lithium ions into the SEI enables lithium ions from the electrolyte to pass through it to reach the anode surface. Without the lithium ions in the SEI the cell could not function since the lithium ions from the electrolyte could not reach the anode surface to intercalate. The decomposition reaction can also take place at voltages inside the stable window, but in this case it was shown that the reaction is reversible since the electrolyte molecules stay intact [37].

Since the SEI is electrically insulating [38, 39], the growth of the layer should in theory stop after its initial formation. A freshly formed SEI has a thickness in range of nano meters [29]. In a real cell however there is always a small current due to electron hopping leading to a slow but constant SEI growth over time. This growth is accelerated with higher temperatures. A thicker SEI is going to have a higher ion flow resistance and will thus increase the total internal cell resistance. The thickness and resistance of the SEI is reported to vary over three orders of magnitude, depending on the system and the test conditions of the experiment [40]. During cell cycling the SEI can also be damaged due to the swelling and contraction of the anode during the lithium intercalation and de-intercalation, facilitating a reformation of the SEI at newly exposed anode surface. There can also be co-intercalation of other electrolyte components and gas evolution during the decomposition process causing extra stress on the SEI, with the highly flammable gas additionally posing a safety risk [37, 41] and causing other ageing effects to occur by facilitating inhomogeneous current distributions and increased pressure

in the cell [42, 43]. Due to the fact that the decomposition on the surface of existing SEI is different from the reaction on the anode surface, the mechanisms change with a higher coverage of the electrode surface [32]. The growth of the SEI not only gradually reduces the capacity of the cell but also has a major impact on the self-discharge characteristics, achievable power density and safety of the cell [29].

These effects lead to a number of desired parameters that can create a stable SEI that can lead to a long cell life. The SEI should be as thin as possible while at the same time being highly electrically insulating to prevent further decomposition. Even if the material composition of the layer is technically electrically insulating, it needs to be thick enough to block electron tunneling [30]. But it should also be permeable selectively for lithium ions for a low cell internal resistance [42]. The layer should also be chemically inert towards all other cell components at a wide range of potentials and temperatures to prevent dissolving of parts of the SEI back into the electrolyte. To compensate for the change in anode volume during cycling it should also have a good mechanical stability to prevent breaking and subsequent reformation [29, 32]. The fracturing of the SEI is even reported to have a bigger effect on the capacity fade than the cracking of the underlying graphite particles due to the fact that it has a higher tendency to fracture [44].

To achieve these desired SEI attributes, the cells are normally charged under special conditions by the manufacturer during their first charging cycles. This process is called cell formation. Before the formation process a full coverage of the anode with the electrolyte has to be assured. This is done by the wetting process, which is typically a prolonged period of resting time (sometimes at elevated temperatures) following the electrolyte filling. During the first cycle of the formation 10%–20% of the whole cell capacity are typically consumed for the SEI generation [26, 30, 45]. The factors that the manufacturer can directly control during the formation process are the applied current, the different cut-off voltage levels and the temperature. These all can have a strong influence on the parameters and stability of the formed SEI, creating different microstructural and chemical properties that can lead to a different long-term chemical and mechanical performance [29]. The current during the formation is typically kept at very low C-rates, rang-

ing from C/5 to C/20 [46]. Most of the SEI is theorized to be formed at 0.2 V to 1 V vs Li/Li^+ [29]. It was e.g. shown by [47] that the SEI forms in two steps at 0.25V and 0.4V vs. Li/Li^+. Other parameters that can be adjusted in cell design that also influence the SEI formation are the graphite type, graphite morphology, electrolyte composition and electrolyte additives, but also factors like particle size of the graphite, basal-to-edge-plane ratio, pore size, degree of crystallinity, Li^+ diffusion rate and chemical composition of the surface (e.g. impurities) can affect the SEI composition [29, 37, 48]. A commonly used additive is vinylene carbonate (VC), preventing exfoliation during lithium intercalation in the beginning of the SEI formation [49, 50, 51]. Using bigger particles can lead to a smaller capacity loss during SEI formation since the surface to volume ratio is lower in this case, but these particles are also more prone to exfoliation [29]. The whole wetting and formation process can take up to 0.5 to 2 weeks [46] and needs dedicated cycling capacities for each single cell, making it one the most important bottlenecks of cell production.

The resulting layer has a thickness in the range of nanometers, with reported values going from 3 to 120 nm [29, 37, 39, 48, 52, 53], other publications however also report widely varying thicknesses in the micrometer range [41, 48], Jalkanen et al. [54] even observed an increase in thickness in the range of 10 µm for cells cycled at room temperature and 45 °C, while the highest temperature of 65 °C in their experiment increased the thickness of the anode by 18 µm. Since the intercalation reaction happens on the edge planes of the graphite particles, the potential on these planes is higher than on the basal planes. This leads to a thicker and differently composed SEI on the edge planes [37]. The thickness of the SEI also varies with the position of the electrode, with the SEI generally being thinner towards the center, and dependent on the type of aging, being thicker when it is caused by calendar ageing [55]. All these factors lead to a differing lithium diffusion constant throughout the SEI in different locations [48]. The pressure on the layer also influences the electron tunneling ability, with more tunneling when the layer is under tension and less tunneling if the layer is under pressure [30].

The chemical composition of the SEI layer is also highly dependent on the conditions under which the layer is formed. A loose organic SEI with

rather low conductivity for the lithium ions is formed at higher charging anode potentials and more compact inorganic structures with higher ion conductivity at lower potentials [48, 56]. The charging rate on the first formation cycles on the other hand affects the porosity of the layer, with a more porous layer and higher resistance at higher charging rates. Water residue in the graphite can cause HF creation in electrolytes with $LiPF_6$, which is the most commonly used salt in modern lithium ion batteries. The HF can then attack the SEI and cause a drop in performance of the LIB [29].

The overall structure of the SEI can roughly be described as a multi-structure bilayer [29, 30, 32, 48]. The separator sites mainly contain a loose layer filled with electrolyte of inorganic lithium carbonates, organic lithium alkali carbonates and polymeric compounds on the side facing the electrolyte, while the graphite site is a more dense layer of LiF, Li_2O and Li_2CO_3 [57, 58]. Figure 2.4 shows the schematic structure of the SEI. Between these two phases a mixed layer can be found. In general it can be said that the SEI compounds closer to electrode are reduced stronger than the compounds in contact with the electrolyte [37]. On average more than half of the SEI is composed of LiF and Li_2CO_3, the other half is composed of other lithium decomposition products and organic components like ROLi or $ROCO_2Li$. In these compounds the R stands for an organic rest created by the electrolyte decomposition. Compared to the edge sites, on the basal site a higher concentration of lithium carbonates can be found on the electrolyte site, and a lower content of LiF [57, 58]. For the SEI on a lithium metal anode Fang et al. [59] showed that the biggest part of the SEI was composed of Li_2CO_3 and Li_2O using XPS and high resolution transmission electron spectroscopy (HRTEM). The whole composition on the basal sites is also less organic [37]. To prevent the loss of the SEI due to re-dissolution into the electrolyte [32], it is desired to create a layer mainly composed of inorganic components like Li_2CO_3 rather than ROLi or $ROCO_2Li$. The $ROCO_2Li$ can react with traces of CO_2 or H_2O present to form lithium carbonate [60]. Hao et al. [61] also notes, that the lithium ion concentration in the SEI highly fluctuates due to an heterogeneous SEI structure. The micro structure is also reported to contain nano-crystalline domains of 5-20 nm in size manly consisting of Li_2CO_3 and Li_2CO_2 [48].

In some cases elements from the cathode can cross over to the anode and cause SEI growth, as shown for $Mn_2{}^+$ ions [62].

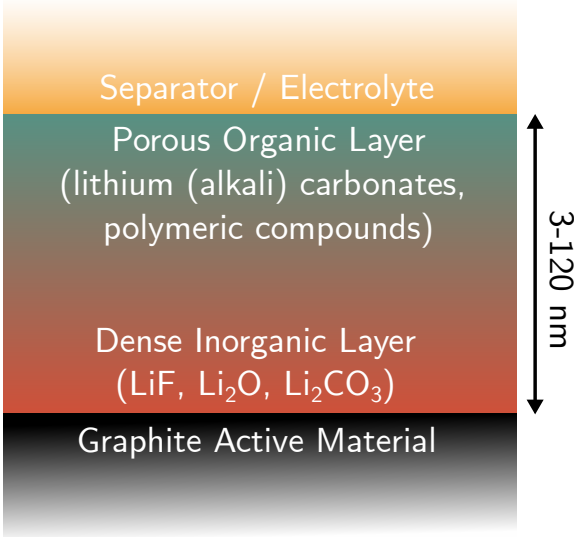

Figure 2.4: Schematic of the theorized SEI structure

The analysis of the SEI is very hard due to its very small layer thickness and sensitivity to oxygen and moisture [29]. To get a deeper understanding of the SEI a number of different measurement and modeling approaches have been used, including initio molecular dynamics (AIMD) simulations [63] to get insight into the reaction dynamics, Shinagawa et al. [52] using a monte carlo simulation to determine the relationship between the layer thickness and its lithium ion conductivity, a mathematical model proposed to describe the mechanical stress on the SEI and subsequent fracturing during cycling [44], while atomic force microscopy (AFM) was used in [48] to measure the thickness and coverage of the SEI.

The continuous growth of the SEI layer over the lifetime of the cell depends on a lot of factors. Firstly a higher cell temperature increases the growth

rate since it increases the reaction rate of all chemical reactions within the cell. High temperature can also lead to a change in the composition and morphology of existing SEI [34]. Secondly mechanical stress can lead to the breaking and subsequent reformation. This is dependent on the charging speeds and flexibility of the SEI. And lastly the aforementioned crossing over of cathode metals that can influence the chemical reactions within the SEI.

Stiaszny et al. [64] and Fu et al. [65] formed the theory that there is a second layer on top of the SEI that is permeable for all components of the electrolyte but leads to an increased ohmic resistance. It is assumed to have a similar chemical composition to the SEI but only has the ionic resistance of pure electrolyte [65]. This layer can grow into the separator pores and also increase the electrolyte resistance within the separator, further increase the total cell resistance. This would also explain why the separator often sticks to the anode surface when disassembling aged cells.

The SEI layer also has a profound impact of the plating behavior of cells. The thickness and ion conductivity of the layer directly influences the potential drop at the anode surface, which is the main driving force of the plating process. The mechanical properties of the layer can influence the morphology and shape of plating, i.e. whether the plated lithium metal forms as a homogeneous layer or in the form of located dendrites, that can cause potential risk to the cell safety [66].

2.2.2 Lithium Diffusion

The lithium diffusion inside the graphite is one of the key drivers of lithium plating. Within the cell there are two different diffusion processes for the lithium ions. One is the diffusion through the electrolyte, which is in a magnitude of 0.4 to $1.4 \times 10^{-5}\,\mathrm{cm^2\,s^{-1}}$ [67]. The second part of the diffusion is the solid state diffusion in the graphite particles occurring when the concentration of lithium ions is non-homogeneous within the anode. This happens whenever ions are removed from, or added to the anode, i.e. during charging and discharging, since the transfer of the ions from the electrolyte to the anode is faster than the distribution of the ions inside the active material. The ions are capable of moving along the vertical direction between the graphite

lattice layer since the bonding between the layers is comparably weak, leaving a gap of 3.35 Å in which the ions can move and intercalate [21]. Since the magnitude of the solid state diffusion is much lower than the value for the electrolyte [68] the diffusion inside the graphite is one of the limiting factors to reach high charging speeds and also the key factor for the occurrence of lithium plating. The value of the diffusion for the solid state phase varies strongly from publication to publication, spanning everything from 1×10^{-15} to $1 \times 10^{-5}\,\mathrm{cm^2\,s^{-1}}$ [68, 69]. The main cause of this big difference stems from the fact that the diffusion rate is dependent on multiple different parameters.

Firstly, the diffusion is dependent on the temperature, with lower diffusion rate at lower temperatures, that can be described by the Arrhenius equation [68, 70]. The diffusion of lithium ions starts at temperatures well below 0 °C, with different literature values of 230 K in [71] while [72] could observe diffusion of a lithium layer into highly oriented graphite at temperatures as low as 100 K. Secondly, it is also dependent on the SOC of the anode, i.e. the amount of lithium that is already intercalated into the [69, 73], although this effect is described to be of lower influence than the effect of the temperature [74, 75]. This make sense as with a higher intercalation depth, the mobility of the lithium ions is hindered by lithium-lithium interactions [69] with the diffusion coefficient having multiple minima over the intercalation levels that can have a difference of up to 2 orders in magnitude [6]. Furthermore the distribution of the lithium ions inside the graphite is not smooth but rather in fixed intercalation levels, called stages. These stages change abruptly when the lithium concentration reaches a certain threshold and are visible in the charge and discharge curves in form of flat plateaus. The intercalation levels are the following [76]:

$$\mathrm{LiC_{72}} \longleftrightarrow \mathrm{LiC_{36}} \longleftrightarrow \mathrm{LiC_{27}} \longleftrightarrow \mathrm{LiC_{18}} \longleftrightarrow \mathrm{LiC_{12}} \longleftrightarrow \mathrm{LiC_6} \tag{2.1}$$

The evolution of these stage structures also influences the diffusion coefficient [21]. Another point is that the diffusion along the edge planes is much higher than along the basal planes [7, 69], with the energy barrier for edge plane diffusion being at 0.3 to 0.7 eV while the basal plane is one order of

magnitude higher with 10 eV [7]. The barrier on the basal plane can be lower however in the presence of defects [77]. Thus the edge to basal rate, particle size and particle orientation of the graphite have a big impact on the diffusion rate as well. This is also true for defects and along the grain boundaries. Here the diffusion is also severely hindered [69]. Lastly, these parameters are also interconnected, with Umegaki et. al [71] showing that the temperature dependency is different for different intercalation stages.

All these influencing factors show that the diffusion coefficient can be vastly different even within the same cell, when particle orientation, size, local temperature or local defects can differ. Thus the lithium plating process, directly affected by the diffusion coefficient, is highly localized on the anode surface and requires a spatially resolved analysis for deeper understanding.

Lithium metal on the surface of the anode, as it is caused by lithium plating, also diffuses into the anode over time. This makes it hard to analyze the plating effect since the depositions are not stable over time. While the diffusion at $-20\,^{\circ}\mathrm{C}$ can take 13 hours or longer, the diffusion at room temperature can be six times as fast [78].

2.3 Cathode

The most commonly used metals used in the cathode are nickel, manganese and cobalt. Since all of these metals have different beneficial effects on the cell performance, a mixture of them can create a good compromise that can achieve the best aspects of all the possible metals. Thus most cells today use a $\mathrm{Li}(\mathrm{Co}_x\mathrm{Ni}_y\mathrm{Mn}_z)\mathrm{O}_2$ mixture, where the fractions of the used materials can vary. These cells are called NMC-cells. Research is aiming at reducing the amount of cobalt in the cells since it is not only the most expensive of the used materials in the cell, it is also mined under questionable conditions for the workers as well as the environment [1]. Apart from these metals there are also lithium-iron-phosphate cells that are cheaper, have a long lifetime and comparably low environmental impact [20] but the downside of a lower energy density, making them less suitable for mobile applications.

Because of the fact that the anode is oversized compared to the cathode, the cathode is never fully charged again after the initial cycle [34].

The influence of the cathode on lithium plating is very small. The only effect that the cathode can have on lithium plating is if the capacity of the cathode is bigger than the anode capacity, e.g. caused by strongly differing ageing rates, and due to manganese cross-over that can influence the parameters of the SEI. This crossing over effect is explained in more detail in the next section.

2.4 Ageing

In general ageing of all cell components can be divided into calendar ageing and cyclic ageing. Calendar ageing describes the chemical degradation over time due to unwanted mostly unavoidable side reactions. Cyclic ageing on the other hand describes the stress on the cell components during cycling, i.e. in case of a LIB when the lithium ions are shifted from anode to cathode and vice versa. For calendar ageing the main influencing factors are the temperature and the SOC of the cell. The result of battery ageing is typically loss of usable capacity and an increase of the internal resistance, leading to a lower available power density [5]. Depending on the occurring ageing mechanisms, there can be primarily capacity loss, primarily an increase in internal resistance or both. The capacity fade caused by cyclic ageing under normal conditions has shown a linear trend in most cases but in some cases a square root dependency on the charge throughput was observed as well [79, 80, 81, 82].

For the anode the main ageing mechanism is the formation, growth and reformation of the SEI layer that forms on the surface of the graphite particles. This layer consumes lithium ions, reducing the available lithium inventory and at the same time increasing the cell impedance. Lithium loss in the cell is normally mainly attributed to the SEI layer growth [14]. A more detailed description of the ageing mechanism can be found in chapter 2.2.1, since this layer also has a big impact on the lithium plating effect [5].

Another ageing effect is the mechanical stress the anode receives during charging and discharging due to the change in volume of the cell. While the volume change of around 10 to 13% is rather small prolonged cycling can lead to contact loss between the graphite particles, the active material

and the current collector and to a change in porosity of the anode material [4]. Other sources of mechanical stress can be the co-intercalation of solvent ions that can cause graphite exfoliation and gas evolution during electrolyte decomposition [5]. These mechanical ageing effects can affect the capacity, due to loss of active material or contact loss with the active material, or internal resistance due to longer diffusion paths [4]. Over time the pores of the anode material can also be clogged with solvent decomposition products, leading to a higher charge transfer resistance [3].

The strongest effect on the capacity loss has the lithium plating, explained in more detail in chapter 2.5. Here an unwanted deposition of metallic lithium on the anode surface can happen under specific conditions, including charging at low temperatures and high charge currents [4].

Overall the capacity fade even under the same conditions is not necessarily linear with time and the shape of the capacity loss function can change depending on the ageing conditions [82]. While the cathode of a LIB also plays a major role for the performance of the cell, the effect of the cathode on cell ageing and especially lithium plating is low compared to the anode. Lithium plating does not happen on the cathode side since the potential of the cathode is very far away from the potential of metallic lithium. One noteworthy ageing mechanism that also affects the SEI growth on the anode side of cell and thus can have an impact on lithium plating is the transition metal dissolution and migration [3, 4, 5, 34]. Here the metal ions of the cathode can be dissolved into the electrolyte and then move over to the anode surface, where they can take part in the chemical processes at the SEI and change the structure, morphology and growth rate of the SEI, often leading to a higher capacity loss and self discharge. This effect is most pronounced with cathodes containing manganese and has a considerably lower impact with cobalt-nickel mixed oxides [83, 84]. This metal dissolution process is intensified by high operation temperatures and HF traces in the cell caused by remaining moisture from the cell productions reacting with the lithium salt [4, 43, 85, 86]. On the cathode surface an SEI similar to the anode SEI can form at the end of charge [34].

The impact on the cell performance of the cathode layer however is much lower on the cell performance. This layers can be isolating and thus lead to an in-homogeneous current distribution in the cathode [3] though.

The cathode is also similarly to the anode subject to mechanical stress during the insertion of lithium ions, which can cause crystal distortion [5].

The overall ageing process in NMC - graphite cells is reported by [87] to take part in two stages. The first stage is loss on lithium due to film growth, mainly SEI on the anode surface. The second state starts at very low SOH of 50% or less, containing active material loss and cathode metal crossing over.

2.5 The Lithium Plating Process

Lithium plating is a special ageing process exclusively occuring at the anode of graphite anode LIBs [88] that can lead to strong capacity loss [7],increase of the cell impedance and a loss of coulombic efficiency [89], while posing a potential safety risk at the same time [7, 40, 88]. It describes the deposition of metallic lithium on the anode surface instead of the desired intercalation. This can happen since the anode potential of a fully charged cell is very close to the potential of metallic lithium [4], with a fully lithiated cell only having a potential of 85 to 100 mV vs. Li/Li^+ [23] with the last phase transition from LiC_{12} to LiC_6 observed to be at an even lower potential of 65 mV vs. Li/Li^+ [70]. Thus if the potential at the anode surface drops further even by small amount, it is thermodynamically favoured for the lithium to deposit on the surface instead of intercalating into the anode material [7, 38, 90, 91]. Downie at al. [92] also found a drop at 28 mV in the dQ/dV curve, signalling the complete filling of all energetically favourable next-nearest neighbor sites between the graphene sheets, marking a point where the lithium ions have to find sites between turbostratically misaligned layers, which is causing a sudden potential drop, bringing the potential closer to the plating onset potential. Although in literature the reasons why this potential drop occurs are various, mainly mentioned are high charge currents [6, 23, 70, 88, 91] and low temperatures [6, 7, 70, 88, 91] resulting in slow solid state diffusion speeds, but the list is also containing mismatched electrodes [93], cell pressure

[14, 94, 95], local defects [14, 49, 91, 94, 95, 96], a thick SEI layer [66], high charge voltages [23, 91] and overcharging [40] – showing that plating is dependent on the operation conditions and cell design parameters at the same time [23]. All the reasons are however interconnected and lead to the same outcome of a lower anode potential which is the actual reason for the plating process taking place. Whenever the potential anywhere on the anode drops below 0 V vs. Li/Li^+ plating can occur. Figure 2.5 shows the interconnection of the parameters that facilitate plating conditions.

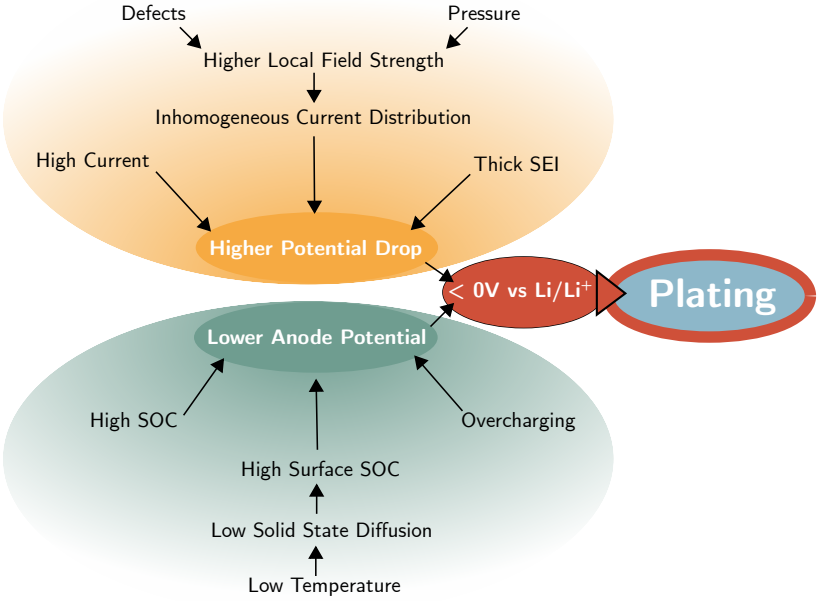

Figure 2.5: Conditions that can lead to lithium plating

The polarization of the anode causing this low potential is caused by an ohmic drop due to the charge tranfer resistance of the SEI, the charge transfer overpotential of the electrochemical double layer on the anode surface and the diffusion overpotential [97]. The creation of the overpotential oc-

curs instantaneously under plating conditions, only slightly delayed by the double layer capacitance time constant of a few milliseconds [70]. Baker and Verbrugge [98] however assume that small amounts of metallic lithium always coexist with the intercalated species, even at potentials well below the plating onset of 0 V vs. Li/Li^+, caused by the so called under potential deposition. At the same time Verbrugge [99] showed that negative potentials for short periods of time do not necessarily have to lead to plating. It has to be kept in mind that plating can occur even when the SOC of the cell is not very high, since the the potential drop just has to be high enough to cause the potential to go lower than 0 V vs. Li/Li^+. This can be caused by a very high current or by the fact that the diffusion speed is so low that the surface of the graphite particle behaves like a fully charged cell, while the active mass bulk is not lithiated to the same level. This was shown by Birkenmaier et al. [91] where plating was detected using changes in the cell thickness in a cycling range of 40–60%. In most cases cells are charged using the CCCV charging method. During the charge most of the plating happens in the CV phase since the cell has reached a very high potential and the anode potential is closest to 0 V vs Li/Li^+ in this phase [100].

The most reliable way to produce plating in LIBs is charging at low temperatures. Discharging a LIB at low temperatures can slightly reduce the available capacity with no further negative effects on the cell while charging under the same conditions will likely cause lithium plating [6]. Being a distinctiveness of lithium plating compared to regular ageing mechanisms like the SEI growth, plating becomes more severe the lower the cell temperature. For the other ageing mechanisms normally an Arrhenius behaviour regarding the temperature can be seen, with higher temperatures increasing the reaction speed of unwanted chemical side reactions inside the cell and thus accelerating ageing [7]. The reason why a lower cell temperature promotes plating is the lower solid state diffusion speed within the anode graphite at these temperatures compared to normal operating temperatures [6, 7, 101]. If the influx of lithium ions intercalated into the anode is higher than the ability of the ions to distribute within the graphite via diffusion, the surface of the anode reaches high lithiation and thus a potential close to 0 V vs Li/Li^+ very fast. A high current has the same effect of increasing

the influx of lithium ions, but at the same time the high current also increases the overpotential, pushing the potential into the plating region even faster. There are observations in literature that plating can occur as high as 10 °C, but the interconnections between the temperature of the cell and the charging current can make it very hard to identify any strict rule at which temperature plating starts. It is also very hard to reliably identify the occurrence of plating during operation at normal operation temperatures, since the diffusion of the deposited lithium into the anode can occur very fast in this temperature range. The charging current is increasing the overpotential at the anode due to the potential drop at the SEI layer, thus also favouring plating, but at the same time higher currents lead to higher ohmic heat losses in the cell increasing the overall cell temperature and thus hindering plating. For this reason the onset point of plating for current and temperature is heavily dependent on the thermal properties and subsequently on the cell geometry and size. Smaller cells have more surface area compared to their volume and because of this have more favourable thermal properties to expel any heat losses to the surroundings while bigger cells heat up more easily under the same conditions (similar cooling and C-rates). The dependency of plating on the charging current can severely limit the ability of the cells to fast charge and recuperate braking energy [7], which is becoming more and more important with an increasing amount of electrical cars on the streets.

In the same way the external thermal management of the cell influences the effect. A very effective external cooling mechanism can reduce the impact of the heat losses and also increase the likelihood of plating caused by higher currents. To investigate lithium plating it is very important to have a good cooling system for the tested cells during the experiments, because otherwise the measured cell surface temperature can be vastly different from the temperature inside the cell. This can also help to prevent strong temperature gradients inside the cell that can lead to different plating behavior at different locations on the anode. This is especially important when investigation methods based on external electrical measurements are used, since these can always only depict an averaged information about the cell state.

Increased pressure inside the cell can locally increase the electrochemical activity, leading to a higher local current. Fuchs et. al [95] applied pressure

to a pouch cell using a steel ball and observed lithium plating especially at the borders of the pressure point. This effect is caused by an increased current at the edges of the defect that was already proved by Oldham in 1981 [102]. Since these kinds of localized effects often only have a marginal influence on the temperature, higher local currents can easily lead to plating without the usual hindering effect of higher temperatures. The same effect can happen when local defects due to manufacturing errors or mechanical stress are present within the cell. Inactive surface regions can still have reachable active material underneath, which causes a higher current at the borders of these inactive regions. These regions can be part of the anode surface, but the same behavior can be observed for defects in the separator, locally blocking ion flow between the electrodes, also causing increased current densities at the borders of the defect [96].

It has been observed early that plating often occurs at the edges of the anode possibly even under conditions that normally do not favour plating [23, 93]. This is due to the fact that the electrical field is stronger at the corners, again also leading to a higher current in these areas. For this reason, and to prevent anode overcharge, the anode in commercial cells is always oversized to disperse the excess ion influx to the overhang anode. This behavior however can still be found if the anode and cathode are not well aligned and the anode edge is within the cathode area, possibly due to a manufacturing error in laboratory cells where the alignment is often done manually. This edge behaviour can also be seen in defects in the cell that normally create inactive areas that are also having an edge around them locally increasing the electrical field. These defects could be a loss of contact between separator and electrode [103], local electrolyte drying, delamination of the current collector [4], clogged separator pores [96], copper plating caused by deep discharge [43], high local tortuosity variation [104] or simple defects caused in production [105] or due to mechanical stress [106, 107]. It was e.g. also shown by Matadi et al. [108] where gas generation was creating electrochemical inactive areas in the cell during high temperature calendar ageing tests, causing lithium plating at the edges of these areas in subsequent checkup tests. Cannarella and Arnold [96] created artificial defects in coin cells observing the same effect and also found that the impact of the effect is

decreasing after a defect size of less than 300 µm and completely disappears for defects smaller than 100 µm. The locations of these spots in commercial cells in applications are however hard to predict since they can be dependent on the design parameters of the cell as well as the cell orientation while testing [7].

While not common in commercial cells, overcharging can also be the cause of lithium plating. When the anode is fully saturated with lithium the remaining lithium has to deposit on the surface instead. This can happen when parts of the anode become electrochemically inactive due to ageing while the lithium ions are located in the cathode material or when the cathode is oversized compared to the anode [40]. Under these circumstances there is an overabundance of lithium ions that can not completely intercalate into the anode. This can be expressed in the ratio of anode capacity to cathode capacity [23]. For this reason the electrode balancing is an important factor in increasing the cell life, the anode capacity must under all circumstances be higher than the cathode capacity [40, 109, 110]. It was already shown by Arora et al. in 1999 [40] that plating starts earlier when there is no excess negative electrode.

This size and shape of the cell also influences the plating locations and onset since longer diffusion ranges have a higher probability of showing inhomogeneities along the way leading to an unbalanced current distribution [89]. But even when the cell is not fully charged, a high SOC is promoting plating since the potential is closer to the critical 0 V vs Li/Li^+ and a lower overpotential can still be causing plating compared a to lower SOC.

Another influence can be found in the material properties of the anode material. Waldmann et al. [111] found that the temperature dependency of the anode potential is different for graphite compared to amorphous carbon. The deposition is also influenced by the anode kinetics, which depend e.g. on the tortuosity and porosity of the anode material [7]. The values for tortuosity and porosity are found to be linked to each other [112] and can have a dependency on the material orientation as well [113].

Bach et al. [14] also found that in cells containing manganese in the cathode (typically NMC) the areas covered by plating contained a much higher amount of manganese crossed over from the cathode than the non plated ar-

eas. They found concentrations of up to twelve times the base line manganese content in areas with mossy lithium structures. This shows that manganese has an influence on the SEI composition as shown in chapter 2.2.1 and thus also indirectly influences the plating behaviour. Arora et al. [40] showed that bigger graphite particles are more susceptible to lithium plating since the diffusion length in those particles is longer and thus can more easily become the limiting factor. Smaller particles exhibit a larger surface area however and lead to more capacity loss during the formation. The same is true for a thicker electrode where the limitations of the solid state diffusion can lead to plating more easily than in thinner electrodes [40]. This means that high energy cells are more prone to plating than high power cells.

During plating often a loss in coulombic efficiency can be observed that is linked to the loss of active lithium and electrolyte due to SEI formation on the new exposed lithium metal surfaces that can break through the existing SEI [114]. For lithium metal batteries some researches suggest that it could also be caused by an increased tutuosity between the electrode and the electrolyte [115, 116].

To initiate the plating process an additional overpotential needs to be overcome at the anode surface which is based on the nucleation barrier of the lithium ions [97]. The effect is theorized to start underneath the SEI layer since the lithium ions need an electron to deposit as metallic lithium and the SEI has very low to no conductivity [38, 39, 117], as discussed in chapter 2.2.1. An additional reason why it is unlikely for the plating to deposit on top of the SEI is the fact that the potential on the SEI surface is higher than on the anode surface, since the SEI itself poses a resistance to ion movement in the cell. This means that the potential is less likely to be at the plating condition of 0 V vs Li/Li^+ on the SEI surface compared to the anode material surface. For this reason the SEI plays an important role in the way the lithium is deposited and how severe the capacity losses caused by the plating are. Hein and Latz [88] showed in simulations that the plating process starts at the particles on the surface of the anode and only spreads into the bulk of the material over time. Even when plating is taking place and metallic lithium is deposited on the anode surface, intercalation of a portion of the ions is still occurring at the same time. These two processes

are always overlapping [7, 23] as seen in figure 2.6 on the left side. When the deposition begins however the deposition part quickly starts to dominate the reaction and the intercalation current is strongly decreased [40].

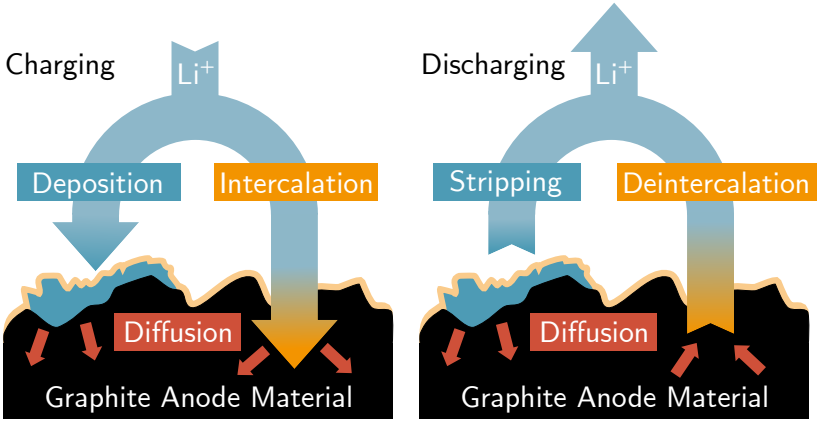

Figure 2.6: The plating process during charging (left) and the subsequent discharge after plating (right)

The ratio of the intercalation current and the plating current can be described using [70]

$$I_{total}(\eta) = I_{intercalation}(\eta) + I_{plating}(\eta)$$

Where both of the currents are defined by a Butler Volmer equation

$$I(\eta) = i_0 A \left(\mathrm{e}^{\frac{\alpha n F}{RT}\eta} - \mathrm{e}^{-\frac{(1-\alpha) n F}{RT}\eta} \right)$$

With the electrode surface area A, the transfer coefficient α, gas and faraday constants R and F, the temperature T, the overpotential η and the exchange current density j_0.

For the intercalation current the exchange current density is dependent on the graphite Li concentration c_s and the electrolyte Li^+ concentration c_l as well as the maximum concentration of lithium in the graphite c_{max} [118].

$$j_0 = k(c_l)^{\alpha}(c_{max} - c_s)^{\alpha}(c_s)^{(1-\alpha)}$$

Where k is a rate constant and $(c_{max} - c_s)$ describes the number of available intecalation spots.

The current density of the plating process on existing lithium is strongly dependent on the surface structure of the already plated lithium, with freshly deposited lithium facilitating the highest current density. This density can vary by two orders of magnitude [119].

The deposited metallic lithium has several effects on the cell. First of all, since the volume of the metallic lithium is bigger than the volume of the intercalated specimen, the cell swells, increasing the pressure on all cell components. Secondly, since the deposition is underneath the SEI, it becomes deformed or stretched. Depending on how flexible the SEI layer is and how much and how fast the lithium is deposited, it can break or rip open, exposing the surface of the plated lithium to the electrolyte. The potential of the metallic lithium is even lower than that of LiC_6, thus the electrolyte decomposition forming the SEI is also occurring on the surface of the metallic lithium when exposed to the electrolyte [120]. This leads to additional SEI formation on the lithium surface causing loss of electrolyte and additional loss of lithium ions [70]. This newly formed SEI layer also has a different chemical composition since it was formed on metallic lithium rather than the anode graphite [66] and can isolate lithium metal grains that become inactive lithium as a consequence [70]. Because of the importance of the SEI the electrolyte can have a strong influence on the plating effect [6, 23], first visible in the change of the coulombic efficiency during the SEI formation [66]. The main potential drop in the cell is attributed to the SEI layer at the anode-electrolyte interface, with the electrolyte itself having a much lower ohmic resistance [66]. But since the composition of the electrolyte has direct influence on the structure of the SEI, the electrolyte has an indirect influence

on the SEI resitance as well [23]. This additional consumption of electrolyte can cause a cell to dry out much faster compared to a cell operated under non-plating conditions and the extended SEI growth can clog the pores thereby decreasing accessible surface area or cause contact loss [54]. The electrical conductivity of a pure lithium film lies at around $10 \times 10^5\,\mathrm{S\,cm^{-1}}$ while the regular SEI composed mostly of Li_2CO_3 shows a conductivity of $10 \times 10^{-8}\,\mathrm{S\,cm^{-1}}$ [40].

The lithium on the surface of the anode is not stable over time. If the cell is left to recover after plating, the lithium will diffuse into the graphite and eventually reach an intercalated state [88]. The time needed for the lithium to diffuse into the anode strongly depends on the temperature and can range from a few seconds at elevated temperatures to hours in a sub-zero environment. It depends on the solid state diffusion speed discussed in more detail in chapter 2.2.2. The second way the lithium on the surface can be removed is during subsequent discharges. When the cell is discharged after plating took place it behaves similar to a metallic lithium cell in the first discharge phase since consuming the metallic lithium is energetically favourable compared to de-intercalation. This effect is called lithium stripping and can be used to estimate the amount of plated lithium [88], it will be discussed further in chapter 2.6.1 taking a closer look at the influence of plating on voltage and current profiles during charge and discharge. During stripping however there is also a de-intercalation current, just like there is an intercalaton current during the lithium deposition, this can be seen on the right side of figure 2.6. Because of this superimposed de-intercalation current and the lithium diffusion that also still occurs at the same time, the amount of plated lithium on the surface will always be underestimated using the aforementioned method of using the stripping voltage profile. Gireaud et al. [94] observed, that the stripping preferably starts at the grain boundaries of a lithium metal surface, since these locations contain the highest interfacial energies and that there are different stripping mechanisms dependent on the current applied. It was shown for cells with metallic lithium that the stripping reaction can be stabilized by using different additives and increasing the cell pressure [17]. Fang et al. [59] also showed that in these cells the stripping rate can change the morphology of the plated lithium, but has

almost no effect on the chemical composition of the SEI. They also noted a different effect of stripping depending on the present electrolyte. Experiments with metallic lithium deposition on copper also have shown that the corrosion of the lithium on the surface can not be fully stopped by the newly formed SEI on the lithium metal surface [66]. This means that on graphite parallel to the diffusion into the anode the lithium is also partly permanently lost due to corrosion. Since the deposition of lithium stretches the SEI layer, after either diffusion into the anode or stripping voids can remain between SEI and anode surface as visible in figure 2.7, further increasing the internal resistance of the whole cell and creating more current inhomogeneities than can lead to further plating.

Depending on the treatment of the cell after plating occurred, parts of the lithium can lose contact and become so called dead lithium that can not take place in the cell reaction anymore, but new SEI can still form on the surface of the dead lithium, possibly causing further electrolyte loss [7]. An example for dead lithium can be seen in figure 2.7. This reduces the available cell capacity. Dead lithium can be created when parts of the lithium loses contact with the lithium metal bulk and are then covered with newly formed SEI effectively electrically isolating that part of the lithium. There are cases however where lithium temporarily loses contact and can be recovered at the end of discharge due to the structural change within the cell during discharge [6]. The likeliness of this effect also depends on the morphology of the lithium deposition and other factors, like the discharge current. Petzl et al. [38] observed a dependency of the reversibility of deposited lithium on the SOC, showing high levels of reversibility for moderate SOC and low levels for high and low SOC, with the lower SOC also showing a higher temperature dependency. This dead lithium is also theorized to increase the cells vulnerability to a thermal runaway, increasing the safety risks of the cell [23]. Other macroscopic effects caused by the plating are a decrease in energy efficiency and an increasing cell resistance [7].

The morphology of the plated lithium is dependent on the applied current [121, 122, 123] and temperature [124]. The most important observed forms of deposition are shown in figure 2.8: dendritic growth, homogeneous plating and moss-like growth.

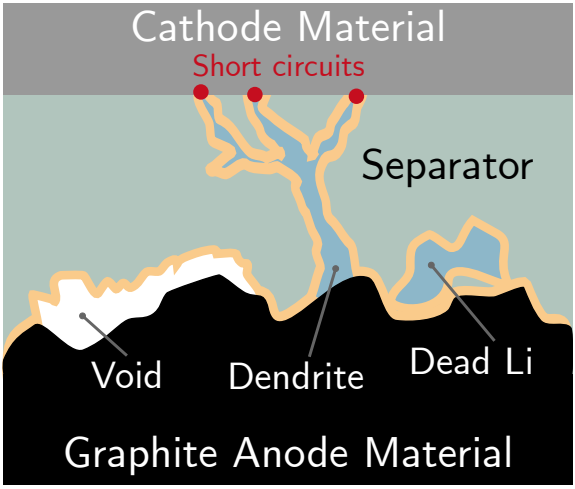

Figure 2.7: Effects caused by lithium plating

In case of the dendritic growth, the lithium forms very sharp tips that quickly pierce the SEI and can also bridge the separator causing short circuits [66] that can lead to safety hazards like thermal runaways [17] or degenerate cell performance [88] by increasing the self discharge rate and consuming big amounts of electrolyte due to SEI formation of their big surface area [95]. Orsini et al. [122, 123] showed that dendritic growth can be linked to a high current density. Since the tip of such a metallic needle-like structure produces a very high electrical field the further growth and lithium deposition is intensified there, creating a process of self-energizing growth [125]. These dendrites are most likely to grow in areas with defects and surface imperfections since the current distribution inhomogeneities are most focused in these areas [126]

The most common form is the mossy deposition [94] facilitated by low current densities [122, 123], also having a high surface are and thus high electrolyte consumption. Due to this high surface area the plated cell can have lower surface resistance than a newly fabricated cell [66].

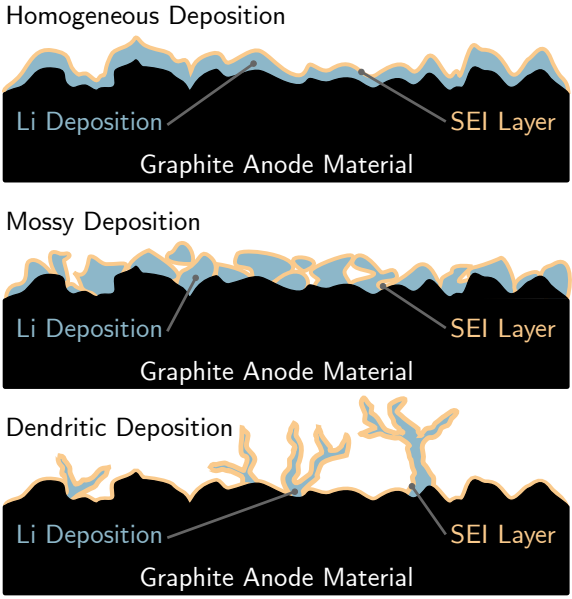

Figure 2.8: The most common types of lithium plating morphology

Deposition around the edge area of the anode is called marginal deposition [7] and can be seen in pouch cells [127]. Another form of deposition is local lithium deposition, prominent for cell cycling at higher temperatures and high charging currents [54, 108, 124, 128]. Homogeneous lithium plating on the other hand is mostly found when cycling at low temperatures [38, 111, 124, 129, 130, 131, 132]. To distinguish between the part of the lithium that diffuses into the anode or can be stripped again during discharge and the permanently lost lithium, the part that can be reused is called reversible plating while the losses are irreversible plating. Ideally all of the deposited lithium could be reused, so that the goal can either be to completely suppress the plating effect in the first place or try to solely facilitate reversible plating.

The dead lithium and SEI formation induced electrolyte consumption are the two main reasons of the drastic capacity loss seen in most cases of lithium plating. Both processes reduce the lithium inventory in the cell, thus reduc-

ing the available capacity. However, the layer of dead lithium and newly formed SEI also influences the cell impedance [6], as will be seen in chapter 2.6.1 looking at the usage of EIS measurements to identify plating in cells.

The main safety risks involved in plating are the piercing of the separator due to dendrite growth, visible in figure 2.7, possibly causing a short circuit facilitating cell heating that can cause a thermal runaway of the cell and exothermic reactions caused by the dead lithium in cell [7]. Since the deposition of metallic lithium also causes increased pressure in the cell caused by the bigger volume of plated lithium compared to intercalated lithium, this increased pressure can also pose a safety risk to the cell, as the cell is not designed for these conditions. Another important safety aspect is the effect of lithium plating on the thermal runaway behavior of the cells. Fleischhammer et al. [133] found that cells cycled at $-10\,^{\circ}\mathrm{C}$ showed a lower temperature onset for a thermal runaway and self heating rate than cells aged under normal conditions, or at high C-rates. This means that lithium plating has a long term effect on the cell safety additionally to the immediate risk of dendrite short circuits inside the cell. They also found a temperature drop at $180.5\,^{\circ}\mathrm{C}$ corresponding to the melting temperature of lithium, further pointing at lithium plating as the cause of the different onset behaviour.

Since the process of lithium plating is dependent on so many variables the capacity loss caused can be very unpredictable [6]. In some cases the capacity of the cell somewhat recovered when the cell was characterized at room temperature after plating cycles [7]. During the cycling process the lithium deposition process can be changing since the surface morphology of the anode is changing with each new plating cycle [66]. The capacity loss caused by plating can take different shapes. In some cases a linear capacity loss was observed [111, 133, 134] hinting at constant loss of available lithium in the cell, while Petzl et al. [130] saw a decelerated capacity loss, where less and less irreversible plating was caused each cycle. Koleti et al. [100] showed that cells with prior ageing conditions and thus a ticker SEI are less pron to plating, which is some what contradictory, since the potential drop at the thicker SEI should be higher. Some publications even link lithium plating with accelerated capacity loss and a sub-sequential sudden cell death after a certain density of lithium in the SEI is reached. These cells show a linear

capacity loss behavior before suddenly ageing much faster after a certain capacity threshold is reached, normally in the range of 70 to 80% SOH [14, 79, 86, 135, 136, 137, 138, 139]. This effect was not seen in cells aged at elevated temperatures although plating was confirmed [54], leading to the assumption that this phenomenon is limited to certain kinds of deposition morphology. Anseán et al. [120] also showed that the plating in their experiment was not induced by a single event but by gradual cell degradation at normal conditions. They showed that the plating inducing condition was caused by a slow gradual loss of delithiated anode material, eventually leading to cell imbalance that facilitated plating. It is also suggested that the sudden increase in capacity loss is caused by local drying of the electrolyte that is consumed forming new SEI on the plated lithium [140] which then causes a defect area prone to even more plating. Bach et al. [14] supported these results by showing that the sudden increase in capacity loss is linked to heterogeneous ageing within the cell, in their experiments caused by varying pressure inside the cell. Broussely et al. [139] were able to link the sudden degradation to inactive lithium in the cell. While this effect is not really of importance for applications in their first life due to most cells considered at their end of life in this capacity range anyway, it makes re-use and second life behavior of the cells much harder to predict and also poses a challenge in accurate lifetime prediction. Bach et al. [14] saw almost not change in the charge and discharge profiles prior to the onset of the increased capacity fade, making the effect very hard to detect, especially when no information about the cell history is available.

2.6 Lithium Plating Detection

In this chapter the different methods than can be used to detect lithium plating in situ as well as post mortem are discussed. The methods used in this thesis and discussed in more detail are electrical measurements, including EIS measurements and partly with reference electrodes as in situ methods, LSM and FIB imaging for optical post mortem analysis and XPS for post mortem material analysis.

The rest of the methods are shortly explained and discussed regarding their potential and disadvantages to give broad overview but they have not been utilized in this thesis.

2.6.1 Relevant in Situ Measurements

In situ measurements allow the characterization of the cell without destroying it and can potentially also been applied while the cell is in operation, being called operando, able to show time dependent porcesses within the cell. In situ methods have the potential to be applied in a real world application if the measurement effort is not too high and no specialized equipment is required for the measurement.

Electrochemical Impedance Measurements

EIS is a technique used very frequently in battery research to characterize battery cells and get a non destructive insight into the processes of the electrochemical reactions. EIS is either applying an alternating voltage or current signal and measuring the response of the system. If the system is time-invariant and linear, this response can be used to create an impedance spectrum over different frequencies. The resulting spectrum can be interpreted to describe different chemical processes in the cell. A battery cell however is an inherently not time-invariant nor linear system so the amplitude of the imprinted signal must be chosen in a way that the system stays in the same state during the measurement and no change in SOC or temperature occurs in that time period. The lowest frequency measured must be chosen accordingly to prevent the cell from changing its SOC too much and thus become not time-invariant anymore [141]. This is necessary since the resulting EIS spectrum is dependent on the SOC and the temperature of the cell. The shape of the spectrum is also dependent on the ageing state of the cell. Figure 2.9 shows an exemplary spectrum with three different frequency areas. The high frequency (HF) area on the left side contains the information about the ohmic resistance in the cell. The point where the spectrum intersects with the real axis describes the true ohmic resistance in the cell caused by the resistance of the active materials, current collectors and the

ion flow resistance of the electrolyte combined. The higher frequencies create an inductive part in the cell that is not of further interest in this work. In the middle frequency (MF) area the impedance describes the charge transfer resistance at the surfaces of the anode and the cathode and the resistance of the SEI. This area is of special interest in the context of lithium plating since the plating effect is influenced by and influences the SEI. The low frequency (LF) area contains a linear slope showing the solid state diffusion within the anode and cathode active materials. The actual frequencies for these areas strongly depend on the cells used in the experiment. For smaller cells the overall impedance is bigger and the intersection point with the real axis is shifted drastically to higher frequencies, often by one or more magnitudes. This requires very different test design when using laboratory vs commercial cells since the cells often have very different capacities.

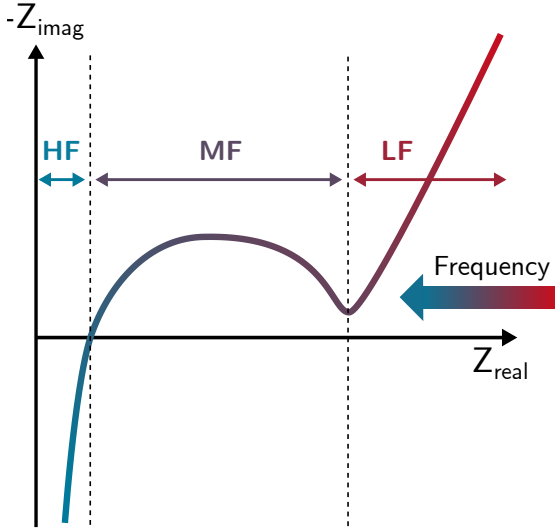

Figure 2.9: Idealized EIS spectrum showing the three different frequency ranges: HF – high frequency, MF – middle frequency and LF – low frequency

The most common elements in EIS spectra of batteries are semi-circles with a negative imaginary part. These semi circles generally describe reactions taking place in different places of the cell. For most LIBs two partly overlapping semi circles can be seen, with each describing the reaction kinetics at one electrode. This can be used to distinguish between effects that happen at either electrode to e.g. find electrode specific ageing effects [54, 64]. It was shown for $LiFePO_4$ cells for example that the cathodic influence on the SEI dominated semi circle can be neglected in the frequency range that is interesting for plating [142].

To better describe the spectra and be able to create a model based on them, they are often fitted with equivalent electrical circuits. To test whether a measured spectrum is valid, a relation called the Kramers-Kronig (KK)-Relation can be used. It connects all imaginary parts of the spectrum to the real parts and vice versa and can be used to verify that linearity and time-independence have not been violated during the measurement [86]. To identify and analyze plating using EIS first the other influences of SOC, temperature and SOH and the spectrum must be clear. Stiazny et al. [86] for example showed that the resistance of the semicircle that corresponds to the SEI becomes less resistive with increasing ageing while the total cell impedance is rising. Zhang et al. [143] observed that the charge transfer resistance is higher for low SOC and that it becomes the dominating part of the full impedance for low temperatures. It was also observed by Dolle et al. [144] that in their experiment to semicircles of the two electrodes became more distinct with increasing ageing. Jansen et al. [145] found that negative and positive electrode are equally increasing the impedance at low temperatures. Dees et al. [146] used a reference electrode to separately measure the resistances of both electrodes and observed that the positive electrode has higher impedance compared to the negative. At low temperatures often used for plating experiments the internal resistance increases drastically, with most of the impedance rise happening in the MF area [145], which shows that the most limiting factor for low temperature charging lies not in the lower conductivity of the electrolyte but rather in the charge transfer at the anode electrolyte interface. This effect is relatively independent of the exact active material in use. Because of that the effect also seems to be independent of the

SEI since every material has its own type of SEI [145]. Wang et al. [147] on the other hand postulate the main effect for bad low temperature resistance stems from the SEI that, according to their measurements, has an increase of resistance by a factor of 30 from 25 °C to −30 °C while the electrolyte resistance only increases by a factor of 10 in the same temperature range. Barsoukov et al. [148] also showed that the spectra can change depending on the thickness of the active material, while Hsien et al. [149, 150] made the same observation to electrode alignment, making comparisons between different cells using EIS very difficult.

Using this general information about the different influencing factors on the spectra, Liu et al. [151], using information obtained from the spectra of the negative electrode, calculated an estimation of the lithium plating onset current for their cells. They used the resistance of the negative electrode to calculate the overpotential at the electrode electrolyte interface and postulated the onset of plating at the potential of 0.08 V vs Li/Li^+ and could determine the onset current this way. This result also shows that cells with a lower negative electrode resistance are less prone to plating. They however did not include the diffusion overpotentials in their equation. Koleti et al. [152] found a difference in the impedance especially pronounced at the turning point in the spectrum between the last semi circle and the diffusion part for cells during the plating process. They specifically measured only this frequency (0.05 Hz) during the charging process and the cells that where subject to plating showed a decrease in the impedance while the non plated cells shows an increase instead. They where able to identify the point of plating onset as a function of the SOC using this measurement.

In summary, EIS measurements can be used to analyze plating but since the EIS signal that is imprinted onto the cell is charging and discharging the cell, it can cause plating or stripping itself during the measurement and must thus be controlled very carefully when measuring cells at low temperatures or cells with deposited lithium on the anode surface. It is also hard to measure the full spectrum of a cell a low temperatures since the required minimum frequencies get very low due to the low cell diffusion and very low EIS frequencies can cause the cell SOC to shift during the measurement violation that stationary condition of the cell.

Electrical Measurements

The easiest way for the in-situ or operando detection of lithium plating is via voltage and current measurements. These measurements are always available in some form in every real world application since every LIB battery pack needs a battery management system (BMS) and thus are a very good basis for plating analysis. The two main ways to identify plating are using the discharge voltage curve [6, 23, 38, 120, 141] or the voltage relaxation curve [141, 153] after a plating event. If the cell is discharged directly after a plating event the discharge curve will show a plateau in the voltage at the beginning of the discharge as visible in the upper plot of figure 2.10. This plateau appears since the stripping reaction that removes the metallic lithium deposition from the surface is energetically more favourable than deintercalation and thus is dominating the total reaction as long as there is sufficient metallic lithium present on the anode surface. The width of this plateau together with the applied discharge current can be used as an estimate for the amount of plated lithium. But it has to be kept in mind that during the stripping here will still be some diffusion into the graphite (as discussed in chapter 2.5) and even though the stripping reaction is dominating there will be a small part of deintercalation at locations where the lithium depositions are not present or are consumed earlier due to a thinner layer. This means that the amount of plated lithium will always be underestimated using this method [88, 153]. Hein et al. [88] also showed in simulations for different micro-structures that the width of the stripping plateau is also dependent on the spatial distribution and micro-structure of the anode, which is likely based on the effects of the micro-structure on the solid-state diffusion within the anode. The diffusion into the graphite is also dependent on the temperature, becoming much faster at higher temperatures, leading to an even higher error in the quantification and making it harder to use this method as a plating validation at room temperature [153]. It should also be kept in mind that the cell is also heating up due to ohmic losses during the discharge, pronouncing that effect even more. This method can also only show the reversible part of the plated lithium since the dead lithium that lost contact to the anode cannot be stripped. To better make the changes

in voltage curve visible often the differential voltage curve dV/dQ is used for analysis, visible in figure 2.11 [141, 153]. Fan at al. [6] detected two peaks during discharge, with one of the peaks disappearing when the cell is heated prior to the discharge. They assume that the second peak is dead lithium that is isolated by the SEI but becomes reactivated at the end of the discharge due to expansion of the SEI. The second peak is also not visible during subsequent discharges following plating in the same cell and only appears at charge rates higher than 0.2C. Uhlmann et al. [97] detected a bend in the voltage curve of lithium half cells, indicating the start of lithium plating. It was observed that the stripping plateau becomes shorter which increasing cycle numbers under plating conditions [100], which means that the amount of reversible plating is reduced. That however not necessarily means that the amount of irreversible plating is reduced at the same time.

A similar effect can be seen when the cell is not discharged by observing the relaxation behaviour after a plating event. As visible in the lower plot of figure 2.10 there is also a plateau in the relaxation voltage. Under normal conditions during the relaxation the overpotentials of the ionic concentration gradients in the electrolyte and the concentration gradients of the intercalated lithium ions within the anode dissipate according to the time constants of those processes and the voltage approaches the open circuit voltage meaning an equal distribution of the intercalated lithium and the lithium ions in the electrolyte. With lithium metal present the voltage reaches a constant plateau when the intercalation current of the lithium deposition equals to the diffusion speeds within the anode material, keeping the potential constant as long as there is sufficient lithium present on the surface [97]. This method has the advantage that no extra heat is transferred into the system. But the relaxation voltage cannot as easily be used for the quantification of the plated lithium amount compared to the discharge voltage method since the diffusion speed and thus the time of the plating plateau is strongly depending on the cell temperature. At higher temperatures the diffusion speed may even be too fast to detect in the relaxation [7]. That temperature however is normally still changing due to heat losses of the preceding charging event dissipating [141]. The plateau can also only be detected above a certain lithium threshold, since the superimposed potential of the the deintercala-

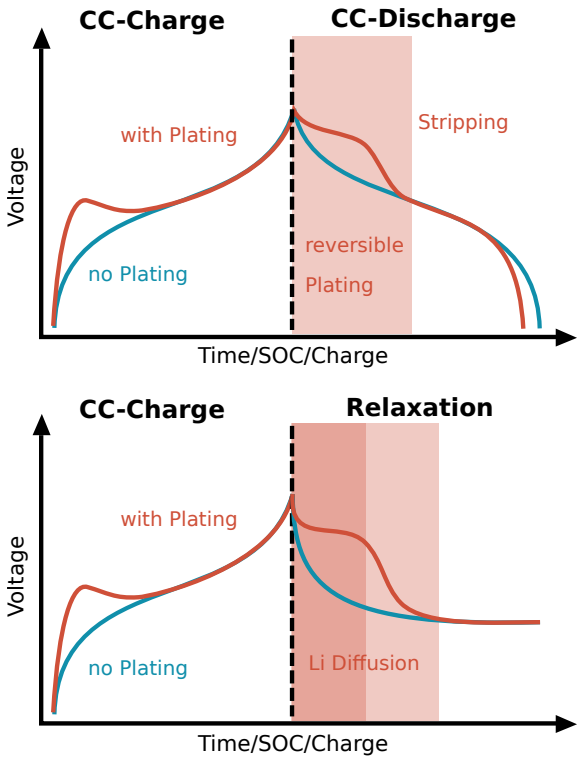

Figure 2.10: Changes in the the discharge curve (top) and relaxation curve (bottom) after a plating event

tion is otherwise dominating [153]. Koleti et al. [100] found that the length of the CV phase during charging has a big influence on the detect-ability of the plating effect in the voltage since a very prolonged CV phase can lead to intercalation of the plated lithium while the charging is still going on. This can happen when the charging current becomes lower than the intercalation current of the deposited lithium.

Another way to detect the effects of plating in the cell is a simple capacity loss estimation. A cell with a plating history will show a much higher capacity loss compared to a cell aged under normal conditions for the same number

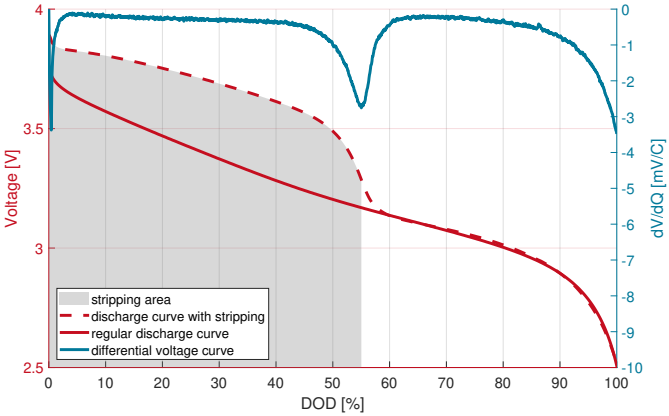

Figure 2.11: Measured stripping voltage with corresponding dV/dQ curve

of cycles. Figure 2.12 shows an exemplary capacity curve for plating and normal cycling. This capacity loss however can only be used to detect the occurrence of plating and estimate the amount of irreversible lithium losses in cell. Paired with the voltage curve analysis, this can be used to determine the relation of reversible versus irreversible capacity loss.

One big disadvantage of all these methods is that they can only detect and/or quantify plating after it has occurred. This means that they can be used as tools to get a better understanding of when and how plating can occur, but they can not be used during the charge to detect and possibly prevent plating. There are however also effects on the voltage and current during the plating event since the internal resistance of the cell is changing during the lithium deposition. The effects can be seen in the CC-phase on the left side of figure 2.10 as well as in the CV-phase on the right side of figure 2.13 [100, 141]. Both effects stem from the same origin, the change of internal resistance, but the effect is more visible in the current curve, where a pulse overlaying the normal exponential decrease of the current is observed. In the voltage curve the effect is overlayed by the more complex shape of the OCV and thus harder to analyze. A closer analysis of this effect can be found in chapter 3.2. All of the electrical methods can however only show

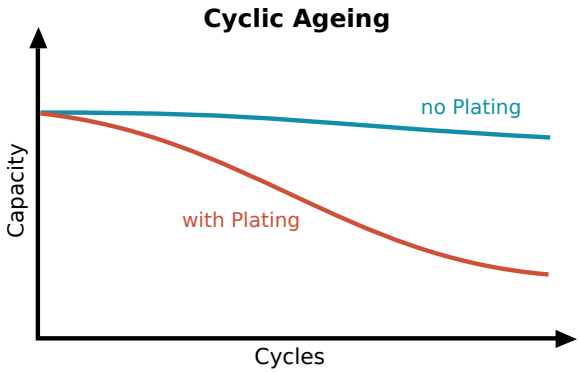

Figure 2.12: Comparison of the capacity loss under plating conditions and under normal conditions

the average state of the cell and have no spatial resolution. Combined with a reference electrode however they can give some degree of spacial resolution, depending on the size and location of the reference electrode. Another effect that is contributing to the change in voltage and current is the nucleation of the lithium crystals at the start of the plating [154], which was made visible in operando using electron paramagnetic resonance spectroscopy (EPR) by Wandt et al. [155]. This effect can be seen in the electrochemical deposition of different metals and describes the extra energy needed to create a crystal seed as a starting point. It should also be kept in mind that while in all real life applications voltage and current data hast to be measured for the BMS, the resolution of this data might not always be sufficient for the plating related analysis [141].

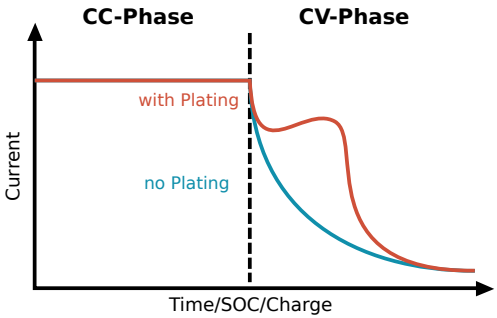

Figure 2.13: Anomaly in the current of the CV-Phase during a plating event

2.6.2 Relevant Post Mortem Analysis

Post mortem analysis requires disassembly or destruction of the cell. It allows for a more thorough analysis of the cell, being able to show spatially resolved results ranging from highly detailed imagery to chemical component analysis. It can be used to gather a deeper understanding of the mechanisms and reaction within the cell, but can not be utilized operando without destroying the cell.

Optical Methods

Optical methods include scanning electron microscopy (SEM), FIB microscopy, LSM and light microscopy, but also just visual inspection. All these methods can create pictures of very small structures with varying degrees of resolution. SEM can produce the pictures with the most resolution but requires a vacuum and cannot show any color information. FIB pictures are in the same category but the FIB is often used for surface modification and instead the picture is created with an additional SEM. The FIB beam can cut into the material and thus allows observation of cross sections in the material while the other methods normally only allow observation of the surface. LSM does not have the resolution of SEM but can be operated under normal atmosphere and has a very good resolution in the z axis, allowing for surface roughness analysis but also can not really show any color information. Only

light microscopy and a simple visual inspections can show color, but light microscopy has the lowest resolution of the microscopy methods. All methods can only create a visual representation but do not show any information about the materials present. They can be used to perform particle analysis, characterize material dimensions and the material morphology. Optical methods are often used in conjunction with other methods that can identify material composition or to explain changes in electrochemical measurements. Almost all optical methods require opening of the cell. Some methods like X-ray microtomography can be used in-situ, but they require a specialized test cell with a casing that is transparent for the used radiation and normally have a lower resolution than ex-situ methods.

When graphite becomes intercalated by lithium the color of the graphite changes from a dark grey/black over a dark red to a golden color tone. This can be used to identify regions of the cell that e.g. did not fully charge or discharge. In the context of plating optical methods are often used to show changes in the surface structure of the anode caused by the plating process. It is however not possible to prove the existence of metallic lithium on the surface using optical methods, only to show that an irregular change on the surface was occurring during plating. To determine whether this layer is mostly electrolyte decomposition or metallic lithium requires different methods that can distinguish chemical composition like XPS or gas chromatography.

Other applications of optical analysis are e.g. in the work of Fang et al. [59], who used cryogenic FIB-SEM and cryogenic transmission electron microscopy (TEM) to show the influence of the plating-morphology on stripping. It was shown that a low turtuosity bulky deposition leads to less dead lithium since such a structure can easier keep contact to the anode during discharge. Uhlmann et al. [97] used in-situ light microscopy to observe the lithium plating process live. They saw a grey coating appear after the anode reached the maximum intercalation level, visible in a golden coloring of the graphite. They also found net like structures using SEM that only existed in cells that exhibited plating behaviour in the electrical measurements and postulated that these structures are metallic lithium depositions.

In summary optical methods are powerful tools to quickly identify or quantify surface changes cause by plating but they can not gather any information about the chemical composition and can thus not be used to prove the existence of metallic. They can and should be used in conjunction with other methods that can identify chemical compounds.

XPS

XPS utilizes the photoelectric effect to distinguish between different materials, composites and even the oxidation states of the materials in the sample [156]. For XPS a high energy X-ray with a specific energy is applied to the sample in an area of at least 10 µm diameter [157]. This energy will cause the electrons of different orbitals of the material to become a free photo-electron with an energy level corresponding to the binding energy of that electron. The kinetic energy of these photo-electrons can then be measured and using the excitation energy of the X-ray source transferred into a binding energy. After the excitation is finished the electron will fall back to its original orbital and in the process release the energy difference from the excited to the original state in form of another photon-electron called an Auger-electron, whose energy is roughly described by the difference between the binding states [158]. Figure 2.14 shows the emission process of a photo-electron and 2.17 the auger electron generation.

By using an electric field to filter the photo-electrons by energy a spectrum can be measured with different intensities for the different energy levels corresponding to the binding states of the originally exited electrons. Some of the emitted electrons will have inelastic scatter interaction within the material of the sample and lose energy because of that. These electrons will cause the so called background in the spectrum causing an underlying increase of all following signals after each material peak [158]. XPS is capable of detecting all elements except for hydrogen and helium and is thus suitable for lithium detection and SEI analysis. The method was frequently used for LIB and LMB surface analysis [26, 55, 86, 156, 159, 160, 161, 162, 163, 164, 165, 166] and e.g. for additive optimizations [167] or coatings [168] for both anodes and cathodes. XPS only has a penetration depth of a few atomic

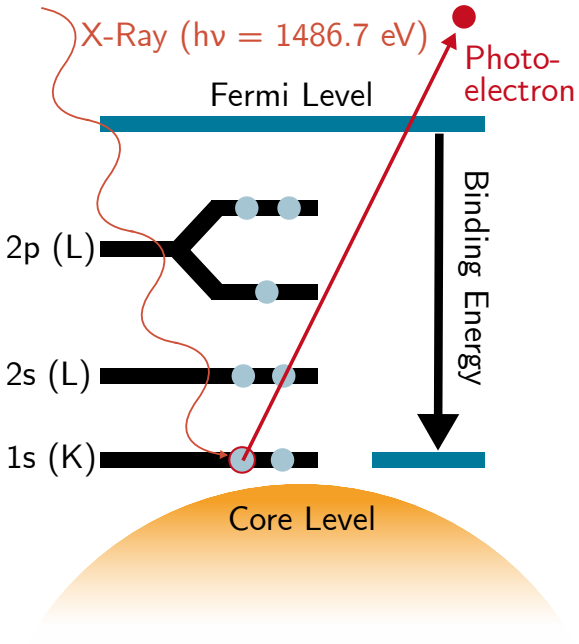

Figure 2.14: Depiction of the photo-electron emission process in XPS

layers (around 5 nm) and is thus only applicable for surface analysis [169]. The penetration depth can be calculated using the following formula [170]:

$$d = 3\lambda sin(\alpha)$$

Here α is the emission angle and λ is the attenuation length of electrons in a solid. λ depends on the element that is exited and the energy of the X-ray beam used for the excitement. The penetration depth of the measurement thus also depends on the element the electron is released from [158] and the intensity of the photoelectron peak will approximately decrease exponentially with penetration depth into the sample. Combined with an etching process and repeated XPS measurements however a depth profile of the material composition for a sample can be achieved [161, 171]. This etching is

normally done by argon sputtering. Oswald et al. [172] however noticed an enrichment of lithium in the sputtering area of fully lithiated graphite which can cause an overestimation of the actual lithium content. The sputtering process is also highly destructive to the surface and can lead to the decomposition of certain components or remove some materials faster and thus cause an uneven surface structure [157, 173]. Andersson et al. [173] report that Li_2CO_3 can be decomposed to LiO_2 due to the Ar sputtering process. Shiraishi et al. [166] and Bhattacharya et al. [48] noticed that the high energy of an XPS beam spot could also alter the chemical composition of the SEI. Shiraishi et al. [166] specifically tested the effect of the X-ray beam and Ar sputtering on the surface and also observed this decomposition, but since they only saw a small decomposition effect of $LiOCO_3$ to LiO_2 they deemed its effect insignificant for the analysis. Aurbach et al. [156] noticed a change in the surface appearance for a lithium electrode for an emission current of 5 mA that was not occurring at 3 mA and concluded that lithium can be altered by higher energy beams. Oswald et al. [174] however stated that they could never observe a change of spectra caused by the X-rays. They also mentioned in another publication that after the sputtering a rest time is necessary to allow for charge equalisation. They used a rest time of 2 minutes in their experiments [175]. They however also mention that the sputtering can damage the bonds especially for oxides and thus a lower ion energy or bigger ion mass is preferred. It was also shown by Wood et al. [176] that even under ultra high vacuum (UHV) conditions a monolayer of contamination could be found on metallic lithium after only 15 minutes so that the detection of lithium metal is only possible when using sputtering right before the measurement.

Monitoring lithium on a graphite surface is made difficult by the fact that the photoionization cross section of lithium is only 6% of that of C1s [72] and thus the signal strength of lithium is by more than a magnitude lower than that of the carbon. Additionally the amount of carbon in the sample is also much higher worsening the effect even more. Lithium also has the lowest sensitivity factor of the list of elements than can be detected using XPS, so in order to get a signal for Li that is strong enough the integration time must be big enough to achieve a good signal-to-noise ratio (SNR) [176].

Another aspect of XPS is the unintended charging of the surface due to the X-ray beam if the conductivity of the sample material is not high enough. This leads to a shift in the whole spectrum since the energy of all photoelectrons emitted is altered by the electrical field caused by the surface charges [176]. To compensate this effect an electron gun can be used to disperse the surface charge for non or low conductivity materials. The problem with battery materials, and in particular for the SEI, is the fact that the conductivity can vary widely, especially when etching is performed on the surface. In this case in some locations the SEI may already be removed, exposing graphite with a good conductivity, while in other locations the isolating SEI is still present. In this case using charge compensation can easily overcompensate and create a shift in the opposite direction by overcharging the surface. Using no charge compensation on the other hand may cause a shift of the spectra over time and cause the measurement to drift between two peaks [158]. Another complication can come from dipole layer formation in materials with different phases of non- or semiconducting materials, as it also can be the case for the SEI layer [157]. The charging effect can also not be uniformly distributed on the surface, especially when different materials with varying conductivities are present or charges can be trapped at interface films or multiphase structures or when the surface roughness is very high in some areas of the sample and thus parts of the surface are shadowed from the X-ray [157, 177]. In these cases not only a shift in the spectrum can occur but also a broadening of peaks. In the worst case the charge buildup can lead to changes of materials in the sample [157]. To compensate for shifts of the whole spectra it is useful to utilize the position of an element that is present in the material analyzed in high quantities as a reference to shift all spectra to the right position. In the case of XPS on anode LIB battery materials often the C1s peak of an adventitious carbon (AC) contamination that can be found on all materials within the battery is used as a reference, but the exact energy level used varies throughout the related publications from 285 eV to 284.3 eV [162, 169, 170, 171, 172]. Some authors also use materials common to LIBs, like LiF or Li_2CO_3 as a reference [174]. Baer et al. [157] criticize the usage of AC as a reliable reference element for several

reasons, including the undefined chemical state, possible differential charging or a lower then necessary intensity of the signal.

Depending on the energy the X-ray can also potentially cause damage to the sample and change the chemical composition. Dedryvère et al. [178] for example did their experiments at $-140\,^{\circ}\mathrm{C}$ to avoid this degradation.

The recorded spectrum of an XPS measurement shows peaks for all binding states of the present elements. The intensity of these peaks is given by the number of electrons collected at the energy level of this particular binding state. The sensitivity of detection of specific elements can be as low as 0.1%, but can differ by a factor of 100 by elements [157]. The result is also influenced by the location of the material in the surface region [158]. If the material is not present in the top atomic layer, the intensity of the peak can be reduced. The width of the peak is also a measure for the exact bond present. If a peak is broader than expected that normally means that more chemical bonds are contributing to this peak, but it can also be caused by unwanted side effects like an X-ray induced change of the sample or local surface charging [158].

Figure 2.15 shows an example spectrum of a new LIB anode after discharging. The spectrum covers the whole binding energy (BE) range that the device can measure. The count value corresponds to the number of photo electrons created at this specific energy level. The peaks are showing compounds that are present in high concentration in the sample. All higher energy levels create scattered photo electrons that are visible in the lower energy levels which creates this stair like effect in the spectrum that is called the background, as described above. The wide spectrum is generally only used to get a overview of the elements and compounds present in the sample. In the further measurement steps spectra with a higher resolution focused on areas of interest are recorded. Figure 2.16 shows such a detail spectrum of the same sample in the energy range of 275 to 300 eV, where carbon peaks are located. To interpret a spectrum the first step is to identify the peaks visible in the spectrum. The example spectrum clearly shows the carbon peak (AC) and two peaks corresponding to the binder in the anode material PVDF. The PVDF contains carbon as well as fluorine, which means that it creates a peak in the carbon spectrum visible here as well as in the fluorine

spectrum in the range of 680 to 700 eV. One of the two binder peaks is overlapping with the carbon peak, which makes it harder to clearly distinguish the two peaks. In the lower part of the plot the fitted background is also visible that has to be removed before further analysis is performed on the spectrum.

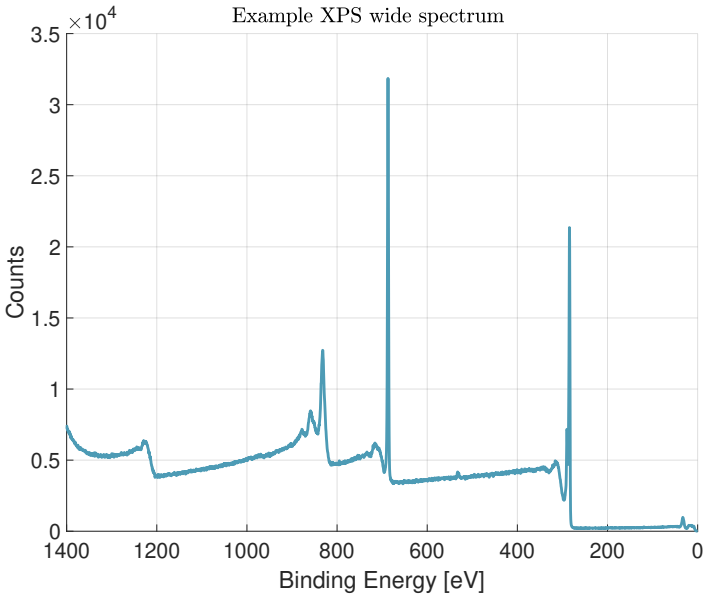

Figure 2.15: Example wide spectrum of a discharged LIB anode

From the raw measurement these peaks only allow identification of the present compound but no quantification. To get information about the element distribution within the sample it is necessary to calculate the atomic percentages from the measurement. To do this a factor for each element is needed that describes the average amount of electrons that can leave the sample. These factors are called Scofield's relative sensitivity factors (RSFs) [179, 180]. They are necessary since the penetration depth depends on the element and thus the intensities, or counts of electrons received at the detector, will not be comparable without that correction factor. The factor also

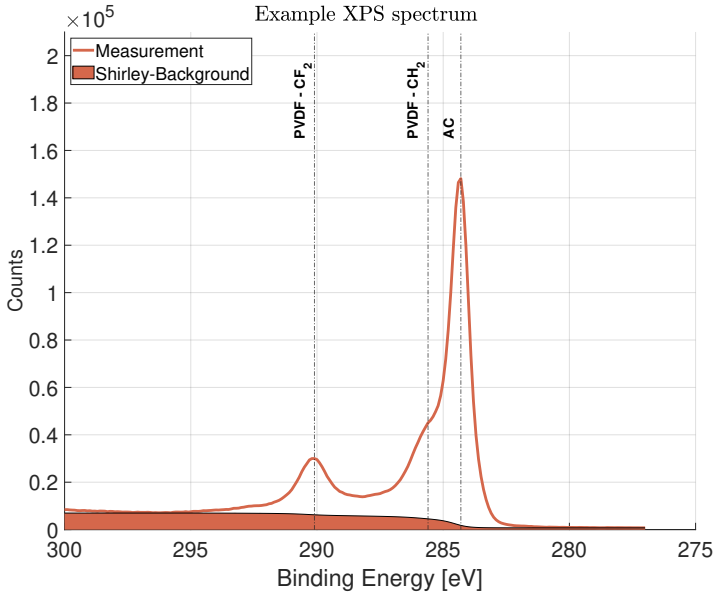

Figure 2.16: Example detail spectrum of the C1s area of a discharged LIB anode

depends on the angle of the X-ray source hitting the sample and the RSF factor tables are always calculated for a certain impact angle [158].

XPS peaks can have the shape of a Gauss or Lorentz function, or a combination of both. The peaks can also show a certain asymmetry. Asymmetry in peaks can be caused by an overlap of close binding state signals, in which case there are actually multiple signals present, but also by vibrational excitation and in the case of metallic samples by multi electron excitation [181]. The free holes in metallic samples can interact with the electrons freed by the photo-electron reaction and create so called shake up events that can create a tail attached the main peak for that material [182]. Over a wider spectrum all elements can create extra peaks in the higher BE regions caused by inelastic scattering of the photoelectrons. This effect is called plasmon excitation [181]. For lithium metal for example the main peak is at about

55 eV with plasmon losses located between 66 and 60 eV [176]. The knowledge of the connected plasmon peak can greatly help in the identification of present species, especially if the main peaks are overlapping with other materials.

For LIB battery materials Oswald et al. observed [172] that all elements containing in the SEI are shifted by about 3 eV to higher binding energy when measured on lithiated graphite. These shifts are especially strong for insulating species in the SEI [175]. They also noticed that Argon was shifted as well, while gold and copper did not shift in the presence of lithium metal. Because of this implanted Argon from the sputtering process can be used to detect these shifts [176]. For a lithium free sample the implanted Argon can be found at 242 eV and it shifts towards 245 eV for higher lithium concentrations. They assume that this shift is caused by electrostatic polarization of the elements close to the lithium. This behaviour can possibly also be caused by metallic lithium depositions due to plating [174]. This was also confirmed by Maibach et al. [183] and according to them is caused by an electrostatic double layer forming between lithium and the SEI components. Tallmann et al. [184] could see a strong contribution of the PVDF F1s signal on a normal anode, but the signal was dampened by the metallic film on the surface in the case of lithium deposition. Helpful for the identification of lithium in the sample in particular can be the fact that the peak shapes of conductive samples are usually less wide (by 0.5 eV) compared to insulators and the majority of the SEI compounds are non-conductive [185]. Metallic samples also show more asymmetry due to interaction of the photo-electrons with the conduction electrons [185]. Additionally the auger electrons (or plasmon losses) can also be used to help identify complex compounds like the SEI. Figure 2.17 shows the auger effect, where the vacancy left by the photoelectric effect is filled up by an electron from a higher orbital. This effect releases the auger electron that also creates peaks in spectrum. It is important to notice that these auger peak positions do not represent a binding energy since they are interactions with electrons of different binding energies and also that this effect is, contrary to the photoelectric peaks, not dependent on the X-ray excitation energy.

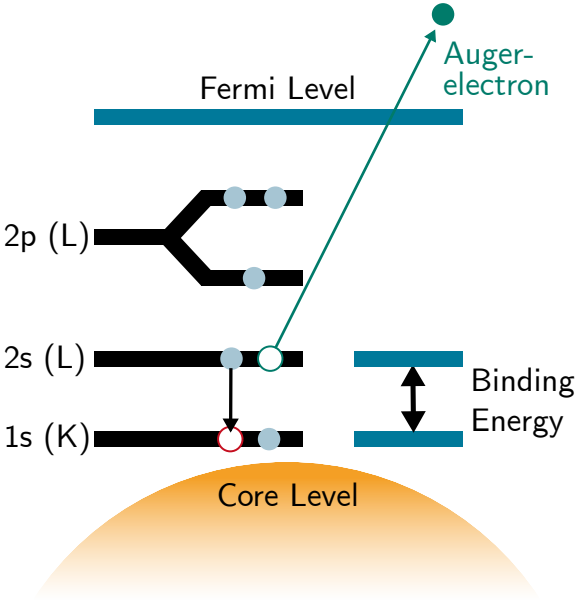

Figure 2.17: Depiction of the auger electron emission process in XPS

When trying to analyze the peaks and elemental ratios it is important to keep in mind that homogeneous distribution of elements in the detection volume can lead to under- or overestimation of element percentages in different layers and lead to wrong results [176, 177]. Due to the shifts caused by surface charging the absolute BE values can be hard to interpret, this is why in some cases the ΔBE values can be used for material identification [176]. Additionally the so called valence-band spectra can help to identify certain composites [176], a slope close to 0 eV can be used to identify metallic species in the sample. The valence band spectra can show all species present on the sample. If the number of species is low the interpretation can be simple [163]. Naille et al. [163] e.g. found an indication of $ROCO_2Li$ species at 17 eV. Using samples from different areas of the battery electrode XPS can also give a somewhat spatially resolved distribution of the elemental composition of the surface. Moertti et al. [161] e.g. found that more electrolyte decomposition

occurred at the edges of the electrodes compared to the center as well as at the outer layers of the cell stack under all ageing conditions. In the case of lithium plating only a small number of papers used XPS. Mussa et al. [55] tried to find lithium depositions in samples cycled at high C rates, but could only find LiF and Li_2CO_3 on the surface of the sample. They however used the amplitude of the 283 eV C1s peak to estimate the thickness of the SEI, with a higher peak contribution hinting at a thinner SEI. Tallmann et al. [184] modified the surface of the anode with nanoscale layers of Cu and Ni to make them more resistant to plating and observed the effect using XPS, but they only looked at the composition of the SEI and didn't do any depth profiling in combination with XPS.

In this thesis it was planned to used XPS to try to identify the location of the dead lithium within the SEI by performing a depth profile. During the measurement however another effect was discovered, most likely caused by the charged compensation of the XPS device that facilitated a lithium migration to the surface of the anode, falsifying the results of the depth profile but opening a different approach of surface analysis.

2.6.3 Other Methods for Lithium Plating Detection

In this chapter the other most common methods used in literature for plating detection and characterization are briefly described to show an overview of the available tools. This list is not exhaustive as there are more methods and new ways of lithium plating detection and analysis are still developed. This list can also be divided into in-situ and post mortem methods. The coulombic efficiency measurements can be used operando when the measurement equipment is precise enough. The measurement of the cell thickness as well as the calorimetry also can be used operando, but they require a special setup around the cell. Neutron Diffraction, Nuclear Magnetic Resonance, Electron Paramagnetic Resonance Spectroscopy and reference electrodes work operando as well but additionally require a specialized cell design. Gas Chromatography and glow-discharge optical emission spectroscopy (GDOES) can only be used post mortem.

Coulombic Efficiency

Lithium plating compared to the normal intercalation mechanism in the cell has a lower coulombic efficiency (CE) since the metallic lithium on the anode surface in creating a fresh SEI on its surface. This is an electrochemical reaction consuming electrons that are lost during the charging process. It is also theorized however that unreacted dead lithium on the SEI might cause in increase in tortuosity at the electrode/electrolyte interface and thus cause a decrease in CE [115, 116]. Using very precise cycling devices, this change in CE can be used to find the onset of lithium plating under a given condition. The typical CE of a LIB lies at 99.5% at room temperature [6]. Fang et al. [59] observed that for a CE of less than 95% deposition of unreacted lithium is dominating the side reactions, while for efficiencies of more than 95% the Li reaction with the SEI is higher and that the amount of unreacted lithium has a linear relationship with the CE . The CE should be getting very close to 1 when charging with very high rates since there is only very little time for parasitic side reactions to take place within one cycle but at a certain threshold this trend is changing due to the onset of lithium plating [129]. Burns et al. where able to identify the plating onset current using the CE data at different temperatures.

The high requirement on the measurement equipment and the fact a fully cycle is necessary to calculate the CE means that this method can not really be used for lithium plating prevention and not suitable for a real world even though it is technically an operando method.

Cell Thickness

The fact that a lithium deposition takes more space than the intercalation of the lithium into the graphite lattice can be used to detect lithium plating in pouch cells. In theory 1 A h of charge plated on the anode surface should increase the cell volume by $0.37\,\mathrm{cm}^3$, which can be calculated from the molar volume of litihum metal compared to the volume of the graphite-lithium intercalation material [91, 131]. In reality this value will be higher, since the deposition is not homogeneous but most of the time in mossy or dendritic form. It also has to be kept in mind that this volume change is superimposed

by the expansion of the anode during simultaneous intercalation, the subsequent shrinkage of the cathode material due to de-intercalation and possible SEI growth and gassing [7]. The volume change of the anode however is at around 10% when fully lithiated, while the cathode shows even lower variation, with no more than 0.1 to 1% change on volume, depending on the cathode material [145, 186], so that the influences of the electrode volume changes can be neglected when the plating amount is significant. Bitzer et al. [131] also showed that in their experiment gassing was not present due to the lower testing temperatures, but did detect gassing when plating was present. The two main methods used for the thickness measurements are mechanical gauges [24, 131, 187] or laser scanning methods [91, 127]. The laser scanning method has a lower influence on the cell, since no mechanical contact is necessary, but requires more measurement effort. Both methods also allow for a spatially resolved measurement on the cell surface, with the laser scanning method offering a much higher resolution, since the laser can easily periodically scan the whole cell surface. Rieger et al. [127] measured their cell from both sides at the same time to make the measurement more robust and showed that even at 17 °C, compared to cells at 25 °C and 40 °C, an increase in thickness was visible, that could be linked to lithium plating by subsequent post mortem analysis of the cells. They found a film on the anode surface of the 17 °C cell with a thickness between 15 and 30 µm. This method is only usable on pouch cell to detect lithium plating though, since the casing of round and prismatic cells is to rigid to measure any change in cell thickness.

Calorimetry

Plating can also be detected using very precise heat measurements of the cell. Using a calorimeter an isothermic heat flow measurement can be done to very precisely measure the heat generation or absorption of the cell. The heat generated in the cell is created by electrical lossses, ionic mixing and chemical reaction. These sources can be divided into irreversible heat losses, caused by ohmic resistance and ion flow resistances in the cell, and reversible heat losses, caused mainly by the reaction entropy of the intercalation and de-

intercalation during charge and discharge inside the anode active material. The irreversible heat losses always create a heat flow from the cell to the environment and they scale with the current applied to cell following the formula for heat losses in electrical systems:

$$W = I^2 \cdot R$$

Since the relevant part for the cell reactions and processes is the reversible heat, the measurements have to be performed at very low C-rates to reduce the superposition of the irreversible heat losses. At for example 1C the reversible heat only makes up 1.6% of the total heat generation, while it is at 24.5% at C/4 [188]. The irreversible heat losses should be constant up to 80% SOC since the internal resistance is not changing much in this area, but it increases at the end of the charging process because of Li-ion repulsion at high intercalation levels [189]. Calorimetry was successfully used to observe the different intercalation levels and order-disorder transformations in graphite [188]. Downie et al. [92] observed a change on the expected heat flow when a cell approaches plating conditions at 0 V vs Li/Li^+. They tested this behaviour on full- and half cells to prove that the thermal response of the anode is much higher than effects on the cathode. They found that the heat flow became significantly lower when plating started since there is a lower entropy connected to metallic deposition compared to intercalation.

This method can be used to detect the plating onset in a specific cell type for very low C-rate which is rarely applicable to a real application, especially applications that favor conditions leading to plating like electric vehicles.

Neutron Diffraction

Neutron diffraction uses a neutron beam to create a diffraction pattern that changes depending on the material under observation. One big advantage of neutron diffraction is the high penetration depth that allows in-situ measurements in a non-destructive way, and the fact that it is very sensitive to lighter elements like lithium [78, 109]. But while it can not detect metallic metallic lithium directly, it can show the different intercalation states of the

graphite and thus be used to indirectly detect the effects of lithium plating and the subsequent diffusion of the lithium depositions into the graphite. Lüders et al. [190] have analyzed the amount of plated lithium by performing neutron diffraction during the relaxation after plating and have obtained the amount of lithium metal that diffused into the anode by measuring the change in intercalation level within the graphite. They performed tests with different charging currents and found a dramatic increase of lithium plating after the current passed C/2 in their experiments, while the diffusion rate of the reversible lithium plated stayed constant.

The biggest disadvantage of neutron diffraction is the need for neutron source which creates the necessity for the nuclear reactor.

Nuclear Magnetic Resonance

The nuclear magnetic resonance spectroscopy (NMR) is a technique frequently used in chemical analysis. Isotopes that contain an odd number of protons and/or neutrons react to a strong magnetic field by creating an electromagnetic signal that can be used to distinguish between the present elements and molecules. NMR is very precise in identifying monomolecular organic compounds. Since lithium metal contains 3 protons, NMR ^{7}Li NMR can be used to detect metallic lithium in LIBs caused by lithium plating [7]. The magnetic field however can not penetrate deeply into bulk the material, but Bhattacharyya et al. [191] using the finite penetration depth of the method, showed that is possible to distinguish whether the lithium deposition has a mossy morphology or forms dendrites on a lithium metal anode and also showed a way to quantify the amount of mossy/dendritic lithium deposited. A similar experiment was repeated by Chang et at. [192]. At the same time NMR is capable of detecting the lithium intercalated into the graphite [160] and can show the different intercalation levels. The measurement method for lithium is fast enough to obtain operando snapshots at a reasonable time frame [191]. According to Wandt et al. a disadvantage of NMR is the low spectral resolution.

The usage of NMR is limited by the very small size sample area and the fact that a specific cell enclosure is necessary for the magnetic field to be able to enter the cell.

Electron Paramagnetic Resonance Spectroscopy

In EPR the same technique as in NMR is used, but instead of exciting the atomic nuclei, in EPR the unpaired free electron spins are excited. This allows EPR the detection of free radicals. EPR just like NMR is also capable of detection metallic lithium [155, 193]. Wandt et al. [194] postulate that EPR should show a higher sensitivity per unit to detect lithium metal compared to NMR. They were able to detect the amount of plated lithium as a function of time and thus could calculate the current that flows into the plating reaction as a function of time by the derivative of the charge amount. Besides that they could also distinguish the portions of the coulombic efficiency that went into the SEI reformation on the surface of the plated lithium and finally calculate the amount of dead lithium remaining after stripping. They did however find a great variance between cells under the same conditions that they attribute to inhomogeneities in cell compression in their test cell. Furthermore the EPR signal was able to show whether the lithium metal was located directly on the anode or was grown into the separator by forming dendrites. They however needed a specialised concentric test cell where the cathode active material was directly coated onto the separator since an aluminum substrate would have shielded the microwave. For EPR as well as NMR the penetration depth, called skin depth, into the material the microwaves are calibrated for, is very small. For lithium metal for example at 9.5 GHz the skin depth is only 1.1 µm, which means that for bulk materials like lithium metal anodes, only the surface of the sample can be probed [194].

Reference Electrodes

A reference electrode is an electrode that is introduced into the cell additionally to the anode and cathode to allow the measurement of the potential or the impedance of the anode and cathode independently. This can be done in-situ, and using the right reference electrode, only has a very small effect

on the cell performance. This is especially interesting for plating in the case of the anode potential, since a drop of the anode potential to a value lower than 0 V vs Li/Li^+ indicates a plating event [111, 134, 195, 196]. It is important to notice however that while a drop to an anode potential lower than 0 V should always indicate plating, it doesn't mean that there could be no plating event in the cell before this potential is reached. This is due to the fact that the potential measured by the reference electrode is only the average potential in the region of the reference electrode. Lithium plating can be a highly localized process, especially if cell defects or regions of different pressure or temperature are involved, which is why the averaged potential might not be an accurate indicator where the conditions for plating are met, since the potential differences on the anode are not taken into account.

For the result of a reference electrode measurement it should also be kept in mind that the measurement includes an ohmic drop within the reference electrode [197].

Nonetheless the reference electrode is a powerful tool for cell analysis. The impedance of the anode measured using EIS can also help to more precisely identify the effects of plating on the SEI since the SEI is represented with a distinguished semi circle in the impedance spectra of the cell, even more pronounced if only the anode impedance is measured.

Such a reference electrode is typically implemented into a test cell produced in a laboratory [134, 195], very often coin cells or small pouch cells, since they can be produced with a small amount of effort and equipment. Another possibility is to implement the reference into a commercial cell [160, 198]. It it can be very challenging however to implement it into a commercial cell and the tampering with the cell can lead to unreliable measurement results. The reference electrode has to meet certain requirements for the measurements to be sound:

1. Very small size to not mechanically influence the cell performance or cause a strong distortion of the electrical field within the cell

2. Chemically inert to most cell components

3. High conductivity to prevent measurement artifacts [149]

4. High reproducibility [199]

In general there are two ways to implement a reference electrode in a cell: interior or exterior implementation [146] visible in figure 2.18. The more common way is to sandwich the reference in between the anode and cathode, surrounded by separator, which is called interior implementation. This way the distance to the anode and cathode are minimized and equidistant, leading to comparable measurement results for both electrodes and there is no extra space needed for the reference in the cell compartment. It is however influencing the electrical field between the electrodes and thus causing a variation in the ion flow, slightly distorting the potentials in the cell [145, 146, 200].

The second method is to keep the reference in a separate compartment connected by excess electrolyte outside of the original cell compartment. This is normally easier to implement and minimizes the influence of the reference on the cell performance but is very susceptible to even a very small misalignment of the electrodes strongly distorting the electrical field in the reference electrode compartment [146]. Because of this, this method is harder to reproduce and can only be used in specialized test cells, like the El-Cell (https://el-cell.com/).

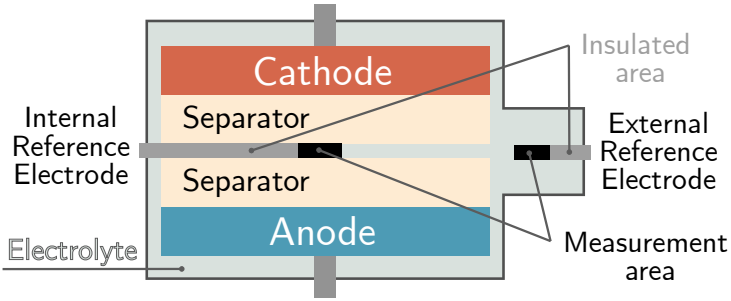

Figure 2.18: Schematic of a cell with internal and external reference electrode

If the electrode is placed in an area with a high variance in current density this can also lead to measurement errors [197].

Another important aspect is the material of the reference electrode. In LIBs a lithium-metal reference electrode is useful since it is immediately measuring the desired potential [160, 201, 202, 203]. But the handling of metallic lithium is very difficult and requires a protective atmosphere [204]. The reactivity of lithium also means that an SEI will be forming on the reference electrode, consuming some of the electrolyte and thus influencing the cell performance. Lithium reference electrodes also have the risk of dendrites forming on the reference, causing a short circuit inside the cell [145]. Other materials might not have the correct potential to begin with, but are more stable and don't disturb the cell as much as a lithium metal electrode. This for example includes lithium-titanate, platinum [205] or lithium-tin-compound LiySn reference electrodes, but it can be hard to determine the true potential of these electrodes. The lithium-tin version for example has multiple voltage plateaus, making determining the potential especially hard [145]. Another method to circumvent the difficult handling of pure lithium metal is using a copper, gold or tin reference electrode that is plated then inside the cell with lithium metal to function as a lithium metal electrode [145]. This however consumes not only electrolyte but also active lithium inside the cell. Abraham et al. [204] noticed, that the potential of their Li_ySn reference electrode was drifting when the cell was stored at higher temperatures but reaching stable voltage plateaus after a while, indicating different lithiation states of the tin alloy. Blyr et al. [199] cold not activate their Li_4Ti_5O reference electrodes. Their explanation was that due to the initial potential of the electrode of 3 V the impurities in the electrolyte reduce first on the reference electrode, poisoning the electrode and making it unusable. Using energy-dispersive X-ray spectroscopy (EDX) they found large amounts of manganese on the surface of the reference, caused by manganese dissolution from the cathode. They solved this problem by already having the cell cycled between the positive and negative electrode previously, which removed the impurities in the electrolyte. Dolle et al. [144] showed that silver is not a suitable material for a reference electrode in a lithium based cell system since even a small current necessary during the measurement using the reference electrode causes a shift in potential, hinting an unidentified electrochemical reaction on the surface of the electrode.

The dimension and shape of the reference electrode compared to the cell size is the last aspect to consider. A bigger reference electrode can significantly distort the measured potential, especially at high currents [146]. The smaller the electrode, the smaller the influence of the electrode, but the smaller the area inside the cell that can be probed. A very small reference electrode can lead to a very localized measurement, that might not reflect the current cell state. Parts of the reference electrode, that connect to the desired measurement point should also be insulated to prevent mixed potentials [204]. A characteristic length lower than the thickness of the separator is suggested by Dees et al. [146] to have an acceptably low influence.

The reference electrode also has a capacity itself. Not all of the ion flow is flowing around the reference electrode, some of the charge is also passing through it by performing opposite redox-reactions on each side of the electrode. If the current in the cell is high enough, this passing through reaction can polarize the electrode, since its internal capacity is reached [146].

The main challenge for reference electrodes is the Creation of reproducible laboratory cells so that the construction errors in the cell manufacturing do not overshadow the actual effects in the cell that are supposed to be measured during the experiment.

GDOES

A plasma and argon ion sputtering are used in GDOES to gradually remove material from the surface of the sample. This removed material is added to the plasma and then emits characteristic wavelengths that allow for element identification and quantification. The argon beam ablates the sample layer by layer and this way allows gathering of depth profiling information. The method was used by Ghanbari et al. [124] to identify localized lithium depositions in the anode. The argon beam can sputter through the whole depth of the anode material, from the surface to the substrate and thus give a whole picture of the material composition. They assumed that all measured oxygen percentage is bound in the form of Li_2O and thus assume that the rest of the lithium percentage must be in the form of metallic lithium. In this way they categorized 88% of the lithium content in the upper SEI layer as metal-

lic lithium caused by lithium plating beforehand in comparison to a sample with no plating, where no lithium was identified in metallic form. Their measurements also showed that an increased lithium concentration goes to a depth of 3 to 4 µm into the sample. This can either mean that the plating can go deeper into the bulk of the anode material, or that plating creates a thicker surface layer compared to the regular SEI. The second theory is in line with what FIB cross-section pictures revealed in this thesis in chapter 3.1.

While for all other measurement methods so far the cell material stays intact and in some cases the cell is even still operable, GDOES consumes the material so that no further experiments or analysis can be performed on the sample.

Gas Chromatography

Fang et al. [59] used the fact that metallic lithium reacts with water forming H_2-gas to identify the amount of metallic lithium in their samples. They used a titration method by adding pure H_2O to their samples and than analyzed the created gas regarding its H_2 content to find the amount of metallic lithium that was present in the sample. They call this combination of tritation and gas chromatography titration gas chromatography (TGC). The only other species that could be possibly found in the SEI that also forms hydrogen gas in contact with water is LiH that can be created by impurities during the cell manufacturing. The authors ruled out the existence of LiH in their samples however by testing plating-free samples that have been cycled 10 times to form a substantial SEI using the same technique. In these samples no H_2 gas could be found, so no LiH was present in the SEI. The method also allows the quantification of the metallic lithium up to 10×10^{-7} gram. It does not allow any spacial resolution into the sample depth however and has the same disadvantage as GDOES of consuming the whole sample in the process.

Chapter 3

Experimental and Analysis

In this chapter first the preceding works are presented and put into context with the present thesis. The preceding works are student theses supervised by the author that laid the foundation for the research done in this thesis. In all tests done in this work cells of the same type or cells that have been utilized before in the student theses are used. This way the results are comparable. In the following chapters the 3 experimental approaches used in this work are introduced and their experimental setup is described. Since the 3 topics require very different analytical methods the evaluation and analysis of the results is directly following each of the experimental setups. The three topics are:

1. Voltage and current anomalies during lithium plating in the CV as well as the constant current (CC) phase in section 3.2
2. XPS measurements on anode materials of plated and fresh cells in section 3.3.
3. Particle analysis of anode LSM images on cells of different manufacturers in section 3.4

All chapters presented here look at a different approach of detecting or analyzing lithium plating either in operando, as is the case for the voltage and current anomalies, or post-mortem for the XPS measurements and the particle analysis.

3.1 Preceding Works

Various theses under the supervision of this author have been creating the foundation of this thesis and in this part the most important findings of these theses will be presented. There have been more theses than are presented in this chapter investigating different theories and methods in the field of plating whose results did not yield usable data or that showed a certain method to not work. In this chapter only the theses are presented whose data or results directly influenced the present thesis.

Stief [206] cycled cells at different temperatures and C-Rates to find the conditions that cause plating and observed the change of the anodes for the different conditions using an LSM. In the thesis by Wink [207] the effects of lithium plating have been analyzed with optical methods utilizing an LSM and a FIB. Jonack [208] analyzed 6 different cells from different manufacturers to identify the cell parameters that can favor plating. She used electrical measurements as well as LSM observations in her analysis.

Optical analysis

Stief cycled ICR18650 HB2 1500mAh LG Chem cells under different conditions. Figure 3.1 shows the conditions under which the cells have been cycled. He used currents from 1C to 3C and a temperature range of 0 °C to −20 °C. Only for the cell with the lowest current and highest temperature (at 1C and 0 °C) no plating could be detected, all other conditions produced plating of differing strength within the cells. The occurrence of plating was detected by evaluating the discharge curve for the characteristic stripping plateau as discussed in Chapter 2.6.1. Figure 3.2 also shows the capacity loss of the cells over the 10 cycles. All cells except for the condition under which not plating was detectable show accelerated degradation caused by plating. All cells at −20 °C show almost the same capacity loss which is because all three cells did not have any CC phase and thus the applied current did not affect the measurement. They are all technically charged under the same conditions. The cell charged at −10 °C at 3C also shows the same ageing behaviour. This cell also did not have a CC phase which indicates that omitting the CC phase seems to have stronger effect on the occurrence

of plating than the temperature. It could be that for all cells showing the highest ageing rate a saturation of metallic lithium deposition was reached and they thus all show similar capacity loss.

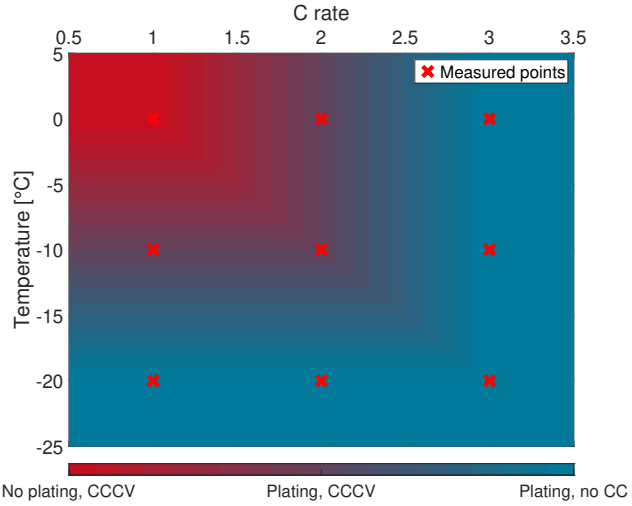

Figure 3.1: Plating conditions under which the cells in Stiefs work have been cycled denoted by the red crosses.

For all currents at $-20\,^{\circ}\mathrm{C}$ the overpotential was so high during charge that the CC phase was completely omitted and only the CV phase was present during the charge. During the charging process an anomaly was detectable in the charge voltage during the CC phase as well as in the CV phase of the cells that omitted the CC phase. This effect was not further discussed since it was not the main topic in Stiefs thesis and will be analyzed in more detail later in chapter 3.2. Stief then opened all cells under protective argon atmosphere and took LSM images of the anodes of all cells, visible in figure 3.3.

It is visible in the LSM images that compared to the new cell in the bottom left all cells show changes of the surface morphology. The surfaces get covered with a mossy layer on top of the graphite particles. It can be seen that a

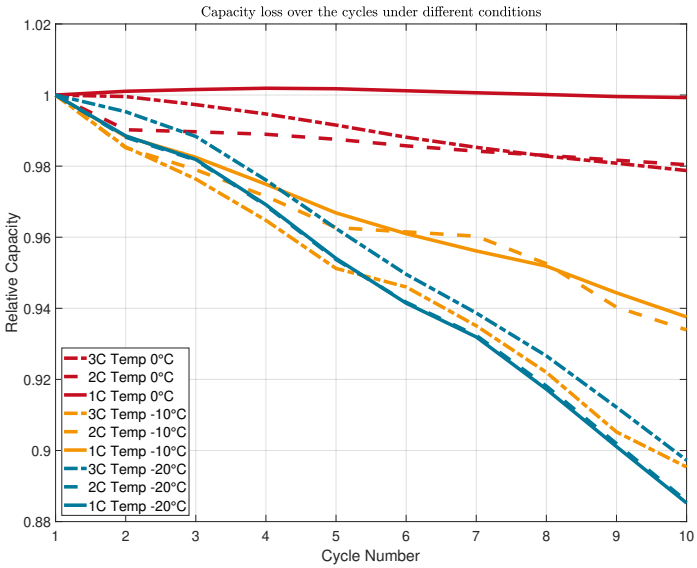

Figure 3.2: Capacity loss of the cells tested under different conditions over 10 cycles

higher capacity loss correlates with more surface coverage. But even the cell cycled at 1C and 0 °C shows a slight coverage compared to the pristine cell which indicates that even though no plating could be detected in the form of stripping or increased capacity degradation the surface analysis revealed a weak coverage similar to the other cells.

Based on the LSM analysis a FIB located in another institute was used to create a more detailed view of these surface coverage found by Stief in the thesis of Wink. For the optical analysis in the thesis of Wink LG Chem 18650HB2 NMC cells have been cycled under normal and plating conditions at −10 °C. One cell was left in its new state, one cell was cycled for 29 cycles at room temperature, three cells have been cycled under plating conditions at −10 °C for 1, 29 and 58 cycles respectively. The cells have then been opened

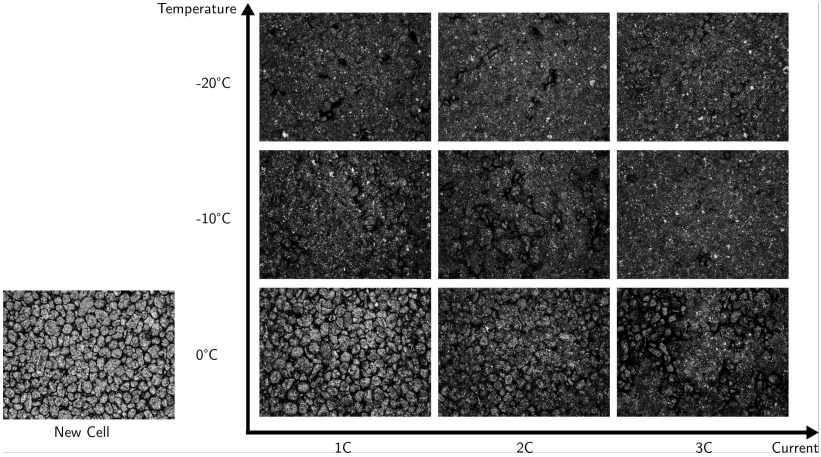

Figure 3.3: The anode surfaces of the cells cycled under different conditions from 1C to 3C at 0 to −20 °C

under protective argon atmosphere in a glovebox and observed using the LSM and FIB. The first test was to analyze the effect of atmospheric exposure on the samples to see whether transport under protective atmosphere to the FIB device is necessary. Figure 3.5 shows the effects of oxygen and moisture exposure on the samples. It is visible in part A that there is no noticeable effect on the microstructure for a new cell. In B on the other hand drastic changed of the structure are visible, even though the cell only had one cycle under plating conditions. Part C shows a much lower effect than B although the number plating cycles is much higher. That leads to the assumption that after a small amount of cycling the chemical composition of the SEI is different compared to further cycled cells. A possible explanation could be that after one cycle there is still a considerable amount of lithium available for plating and thus there is more reversible plated or passivated lithium in its metallic form in the SEI that is highly reactive. Over time this lithium reacts with parts of the SEI and forms less chemically active compounds and together with the fact that in later cycles the irreversible capacity loss, and thus the inventory of available lithium in the cell, is much lower, the amount

of reactive metallic lithium causing degradation at air atmosphere is greatly reduced.

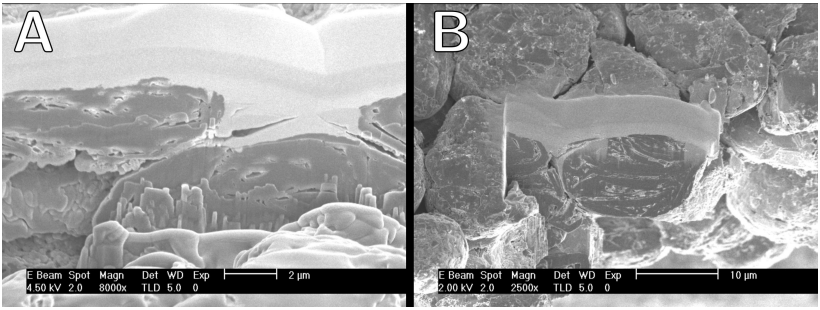

Figure 3.4: FIB cross section of A: new cell and B: cell after 29 cycles under normal conditions

Figure 3.4 shows a FIB cross section of the anode of a completely new cell on the left (A) and a cell after 29 cycles under normal conditions (B). Prior to the cross section a thin film of platinum was sputtered on the surface of the anode to improve the FIB cut, visible in the light stripe in the top part of all cross sections. The graphite particles are clearly visible in both images and there is no surface film on the particles detectable. The average SEI should have a thickness of 40 to 80 nm (see chapter 2.2.1) for a new cell, which both of the samples are. So it would be almost invisible at the magnification of the images. There is also no noticeable change between the new cell and the cycled cell, which is to be expected after only 29 cycles.

Figure 3.6 shows the cross sections for one cycle of plating (A), 29 cycles of plating (B) and 58 cycles of plating (C). Even after only one cycle of plating there is a mossy structure visible in the crevasses between the graphite particles. Over the course of additional cycling under plating condition this mossy layer grows out and covers the complete particles. The border between the graphite particle and the surface layer is not clearly visible everywhere, since the lower part of the layer shows a darker color on the images. This means that the lower part of the layer seems to have a different composition. After 29 cycles the layer has a thickness of 7 µm at its thickest part, more

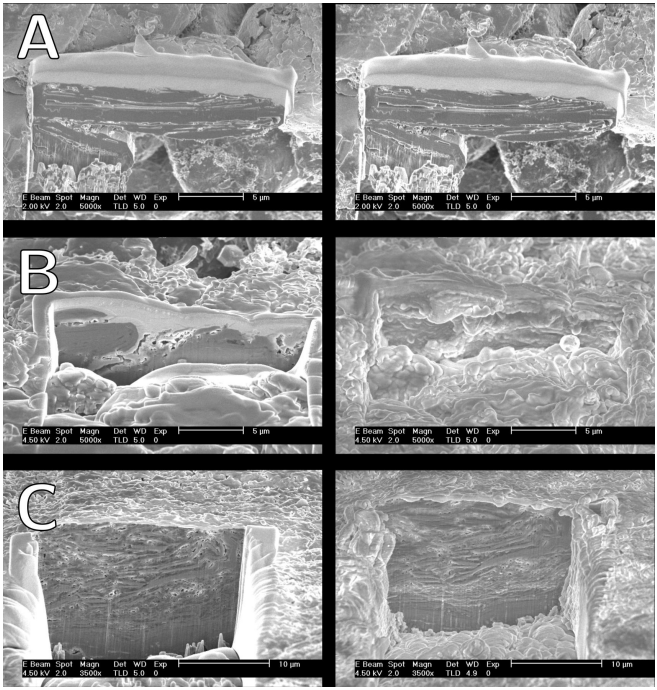

Figure 3.5: 96 hours of air exposure of the FIB cross section for A: new cell, B: 1 cycle of plating at −10 °C and C: 58 cycles of plating at −10 °C (before exposure on the left, after exposure on the right)

than 100 times the thickness of the average SEI of a non-plated cell. After 58 cycles it is visible that the layer has become even thicker, with a thickness of 10 µm at its thickest part. The darker lower part of the layer is even more pronounced. The top of the layer in both image B and C stills shows the mossy structure also visible in image A.

Wink also performed basic image analysis on the FIB images seen in figure 3.6 to separate areas that could be metallic lithium depositions. He used the difference in brightness of the areas that look more solid and sharp compared to the surrounding depositions in the thickened SEI to estimate the volume

of those depositions. The brightness of pixel of a FIB image corresponds to the conductivity of the material present, meaning that brighter areas have a higher conductivity. This would be expected by deposited lithium layer that they should have higher conductivity than the surrounding SEI decomposition compounds and thus have a higher brightness in the FIB image. A comparison of the obtain volume estimation to the theoretical volume of the lithium inventory lost during the plating cycles showed that they are in the same order of magnitude. This is a fist indicator that these layers could be the lithium depositions.

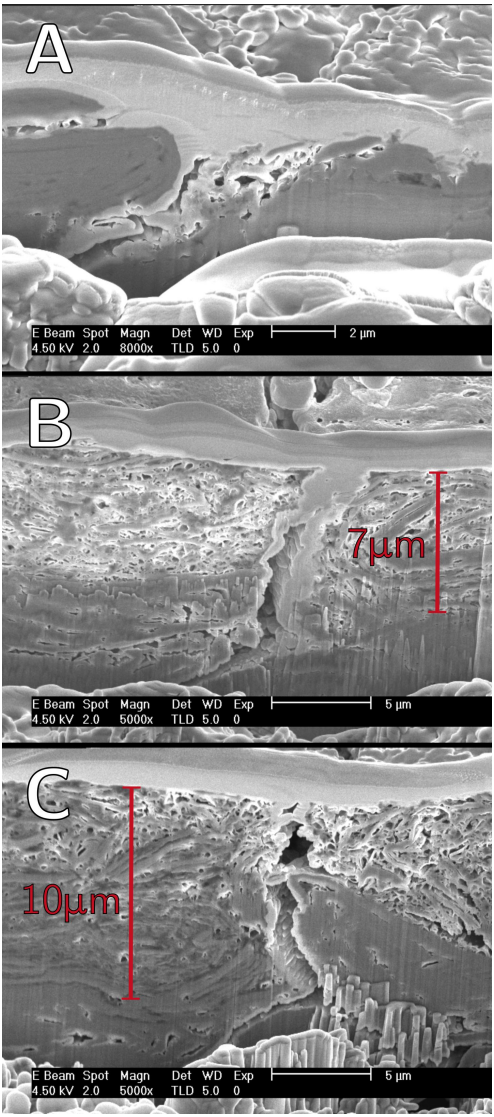

Figure 3.6: FIB cross section of A: 1 cycle of plating, B: cell after 29 cycles of plating and C: cell after 58 cycles of plating

Comparison of Plating in Cells of Different Manufacturers

To then seen whether the effects of plating are different in the cells of different manufacturers Jonack [208] analyzed 6 cells of different manufacturers regarding their susceptibility to plating. She used 2 types of 18650 cells made by Sony, Samsung and LG with one cell of each producer being an NCA cell and one being an NMC cell. As discussed in chapter 2.2.1 the SEI layer is less stable in cells with manganese in the cathode active material. This should also lead to expected higher susceptibility to plating in cells with an NMC cathode compared to an NCA cathode. Table 3.1 shows the six different cells used in her work.

Producer	**Cathode**	**Battery Type**	C_n
Samsung	NMC	ICR18650-22P	2.15 A h
Samsung	NCA	INR18650-25R	2.55 A h
LG	NMC	LGDAHA11865	1.3 A h
LG	NCA	INR18650MF1	2.15 A h
Sony	NMC	US18650VTC3	1.6 A h
Sony	NCA	US18650NC1	2.9 A h

Table 3.1: Cells used in the work of Jonack [208]

All cells have been analyzed using the LSM and electrically characterized in their new state and after 10 cycles of plating at $-20\,^{\circ}\mathrm{C}$. For each experiment 4 cells have been cycled and their average capacity loss was determined. Figure 3.7 shows the irreversible plating induced capacity loss of the cells after the 10 cycles at $-20\,^{\circ}\mathrm{C}$.

The most noticeable result is the consistent difference in capacity loss between the NMC and NCA cells, probably caused by the presence of manganese, as already discussed above. All NMC cells show a significantly higher capacity loss than their NCA counterpart from the same manufacturer. The anodes of the cells have then also been optically analyzed using an LSM under protective atmosphere. Figures 3.8 to 3.9 show the LSM images taken from the anode samples. The left pictures always show the new cell, the right picture the aged cell. The top row corresponding to the NMC and the bottom row to the NCA cells of each producer.

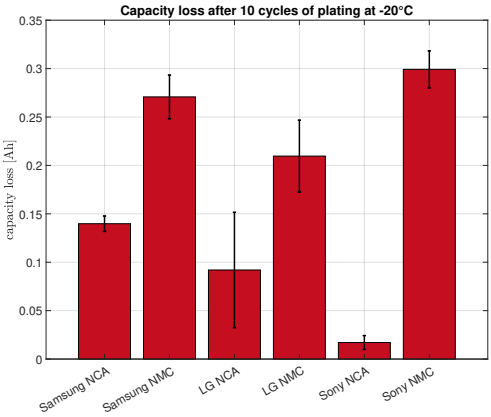

Figure 3.7: Comparison of the capacity loss of the cells used in Jonacks work

Is is visible in all three images that 10 cycles of plating cause a visible change in the surface structure of the anode. A mossy deposition is covering the anode surface in all samples. But while the surface of the NMC cells seems to be almost fully covered with the deposition there are still graphite particles visible in the images of the NCA samples, especially in the image of the Sony NCA sample, that also showed the lowest capacity loss of all tested cells. Thus there seems to be a correlation between the depositions and the capacity loss caused by plating. In the work of Jonack no further significant correlations could be found between any measured cell parameter, whether electrical or optical, and the irreversible capacity loss. For this reason the cells will be used for further experiments in the XPS and optical section in this thesis in the sections 3.3 and 3.4 to identify other possible differences in the cells that could be important for their plating susceptibility.

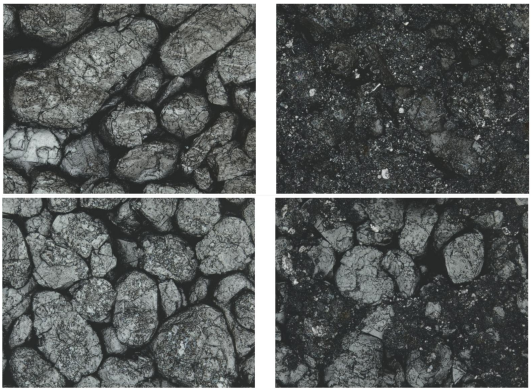

Figure 3.8: Comparison of the anode surface of the new (left) and plated (right) Sony cells. (top: NMC, bottom: NCA)

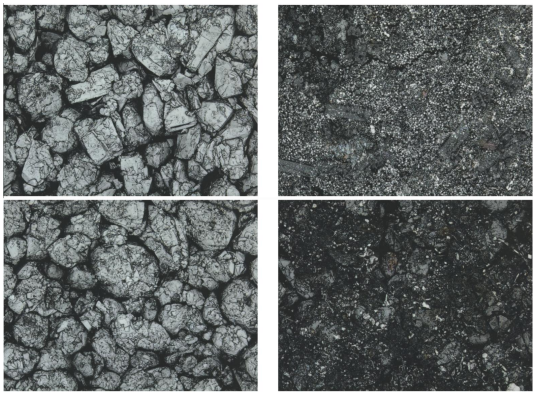

Figure 3.9: Comparison of the anode surface of the new (left) and plated (right) Samsung cells. (top: NMC, bottom: NCA)

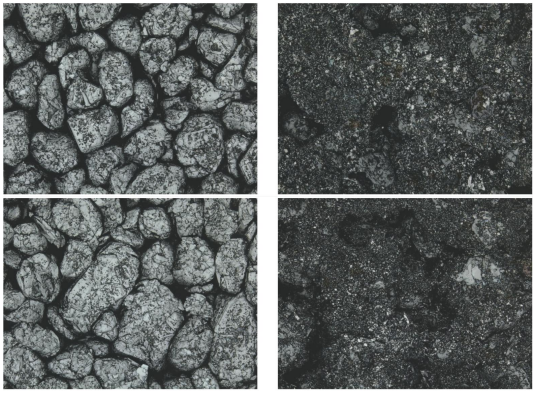

Figure 3.10: Comparison of the anode surface of the new (left) and plated (right) LG cells. (top: NMC, bottom: NCA)

3.2 Charge Anomalies

During the charging process under plating conditions anomalies are visible in the voltage profile during the CC phase as well as in the current profile during the CV phase, as already explained in chapter 2.6.1 and detected in the work of Stief presented in chapter 3.1. These anomalies could potentially not only be used to obtain a deeper understanding of the plating process, but could also help detect plating operando, since the detection only requires a voltage measurement and knowledge of the cell's expected behaviour under non plating conditions.

3.2.1 Overview

The effect in the CV phase only occurs if the CC phase is very short, i.e. at very low temperatures or very high charge currents if the cell is still at a rather low SOC when the charge end voltage is already reached. Figure 3.11 shows two examples of these anomalies obtained from the cell tests of Stief. The left plot shows the CC phase of a cell charged at 0 °C at a current of 2C, the right plot shows the CV phase of a cell of the same type when the CC phase was completely skipped and the charging process solely utilized the CV phase. Both cells show detectable voltage plateaus on discharge, confirming that plating occurred in both cells during charging, as seen in Figure 3.12. The voltage plateau is clearly visible in the discharge voltage curve on the left for the cell charged at −20 °C. For the cell charged at 0 °C the plateau is less visible, since the plating was not as strong compared to −20 °C. There is however an easily visible minimum in the dV/dt curve on the right that denotes the end of the stripping plateau. The ends of the stripping plateaus are marked with the dashed lines for both cells.

In figure 3.11 it is clearly visible that the voltage profile at the beginning of the charge has a change in gradient and is briefly showing a negative voltage gradient. This effect occurs and subsides during the first 20 seconds of the CC phase. This leads to the assumption that it is connected to the lithium metal crystallization process, as discussed in 2.6.1. On the left, the CV phase of a cell charged at −20 °C is visible. The cell was also charged with

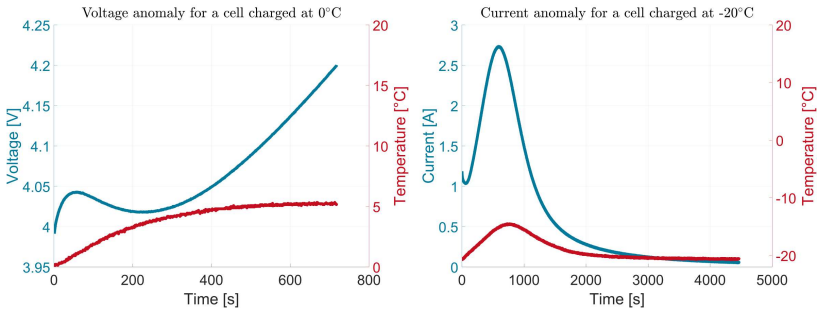

Figure 3.11: Voltage profile (left) during CC phase and current profile (right) during CV phase of two cells under different plating conditions (first cycle)

a current rate of 2C which caused a voltage drop high enough to completely omit the CC phase. The high internal resistance caused by the low cell temperature created an over-potential that caused the cell voltage to rise to the end of charge voltage of 4.2 V within the first measurement point. In this case the expected exponentially dropping current during the CV phase shows a bell shape overlayed that subsides only after almost 2000 seconds. The effects for the voltage and current curves should be equivalent since the voltage and current of the cell are connected via ohms law by the internal cell resistance. Both effects are the result of a decease in internal cell resistance, which is comparable to the findings of Koleti et al. [152], who found the impedance of the spectrum to drastically change when plating occurs. They used a single frequency measurement at the point right before the start of the diffusion branch to measure the real-time change of the resistance during the charge process and state that they can detect the onset of plating by the deviation of the resistance from its regular trend. The effects visible in figure 3.11 should also be caused by the same effect. An interesting difference between the results in [152] however is that they detect plating starting at high SOC at around 80 to 90 % while the change of the resistance visible here occurs at the start of the charging process at a very low SOC. Since both effects could also be caused by an increase in cell temperature that lowers the internal resistance the temperatures at the cell surface have also

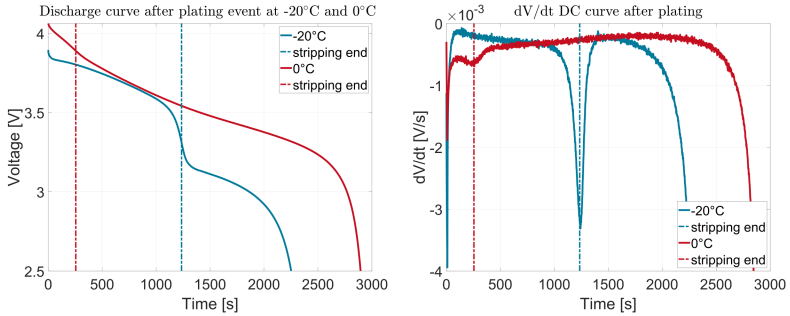

Figure 3.12: Discharge voltage (left) and dV/dt (right) curve for the same measurements as in Figure 3.11 both showing stripping

been recorded during the measurements and are depicted in red. A look at the temperature profiles of both measurements shows a rise in temperature that is to be expected due to ohmic losses. For the CC phase voltage profile on the left the temperature profile is completely de-coupled from the change in voltage and thus is very unlikely to have influenced the voltage anomaly. On the right side the temperature profile is coupled with the current profile during the CV phase but the change in temperature is lagging slightly behind the bell shape and is thus most likely a consequence of the increased current during the bell shape and not the reason for the bell shape to form in the first place. It has to be kept in mind though, that the temperature measured on the surface of the cell is not fully in phase with the cell core temperature which could undermine the previous assumption. Figure 3.13 shows the temperature change of the three cells cycled at $-20\,^{\circ}\mathrm{C}$.

As visible in the plot the total change in temperature is not very high, the change is only from $-20\,^{\circ}\mathrm{C}$ to about $-15\,^{\circ}\mathrm{C}$ and would likely not cause a drop in the total internal resistance by more than a factor of 3.5 necessary to cause the visible current increase during the bell phase. The factor of 3.5 can be calculated by estimating the current during a normal exponential drop CV phase at the time of the peak of the bell and divide is by the bell peak current. To prove this theory the spectra of a cell of the same type have been measured at $-15\,^{\circ}\mathrm{C}$ and $-20\,^{\circ}\mathrm{C}$. Figure 3.14 shows the

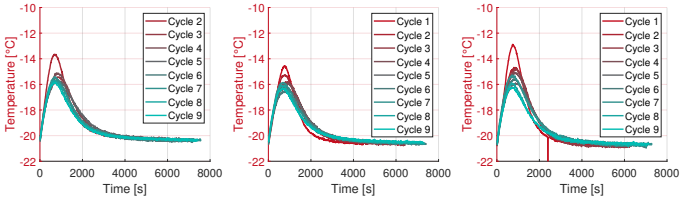

Figure 3.13: Temperature change during the CV phase of the cell cycled at −20 °C

corresponding spectra on the left and the ratio of the real part of the two different measurements on the right.

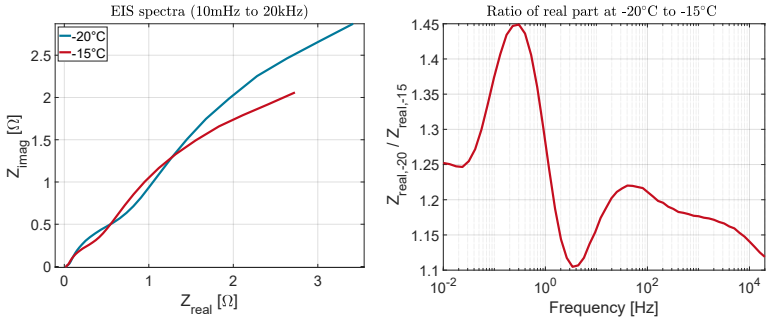

Figure 3.14: Spectra (left) at -15 and −20 °C and ration of the real part of the two spectra over all frequencies (right)

It is visible that the highest change in resistance over the 5 °C of difference during the charge can only increase the current by a factor of 1.45. The peak of the bell shape is occurring after about 600 seconds, which corresponds to a frequency of 17 mHz where the factor has an even lower value of around 1.25. This means that while the change in temperature is influencing the peak shape, the main decrease in resistance can not be caused by the temperature change but must rather be linked to the plating process.

Another aspect that strongly links the effect to plating is that the anomaly diminishes over the cycles. Figure 3.15 and 3.16 show 10 cycles of cells under plating conditions at 0 °C and −20 °C at 2C respectively. For the cell cycled

at 0 °C is it clearly visible that the voltage anomaly is diminishing over the 10 cycles. For the −20 °C cell in figure 3.16 the same can be seen for the bell in the CV phase. Here it is also noticeable that the stripping plateau gets smaller over the cycles as well. In figure 3.15 at 0 °C the stripping plateau is very weak and thus it is hard to determine whether the stripping is also decreasing over the cycles but the stripping plateau for the first cycle is visible higher than in the following cycles.

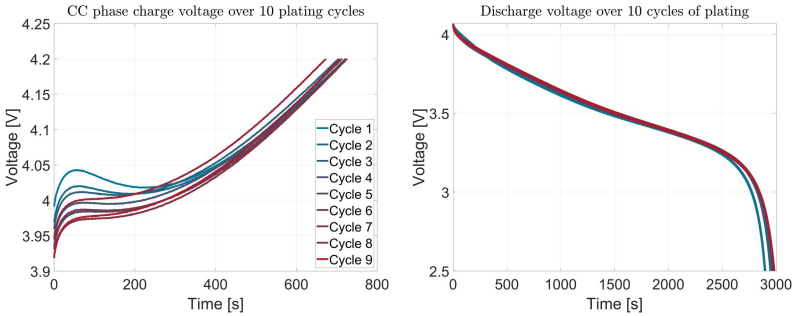

Figure 3.15: Change of the voltage curve during the CC phase (left) and the discharge curve (right) over 10 cycles under plating conditions (at 2C and 0 °C)

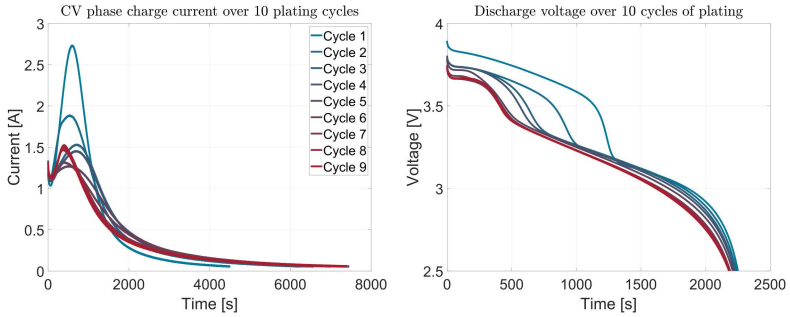

Figure 3.16: Change of the voltage curve during the CC phase (left) and the discharge curve (right) over 10 cycles under plating conditions (at 2C and −20 °C)

Figure 3.17 shows EIS spectra of the cells cycled at 0 °C and −20 °C over the 10 cycles. The spectra were recorded after the cell was characterized at room temperature. It is visible that for both cells the overall resistance is decreasing, which correlates with the diminishing anomalies. For the −20 °C measurements however the change in resistance is very small and could not solely cause the significant change in the bell shape. This leads to the assumption that there must be a temporary change in resistance during the plating occurrence whose magnitude is decreasing if there is already plating induced capacity loss present. To detect a temporary change in resistance EIS spectra have been measured every 6 minutes for 12 hours after the cell was charged for one time under plating conditions at −20 °C.

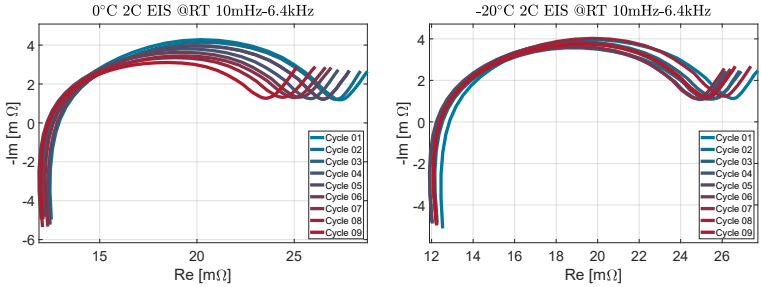

Figure 3.17: EIS spectra of the two cell cycled at 0 °C) (left) and −20 °C) (right) over the 10 cycles. The spectra have been recorded after characterization at room temperature

The resulting spectra are shown in figure 3.18. Right after the charge was finished the impedance (in blue) was much smaller than the the final impedance after 12 hours, which is accordance with the observations of a decrease of resistance in the voltage and current measurements. This measurement is of course superimposed by a small change in cell temperature due to the ohmic losses heating up the cell in the course of the charge that is also influencing the spectra but a cell of this size (type 18650) is equalizing in temperature within less than 2 hours, so only the first measurements should be affected by the temperature change. The internal resistance is not changing during the whole time and thus seems to be unaffected by the plating. It

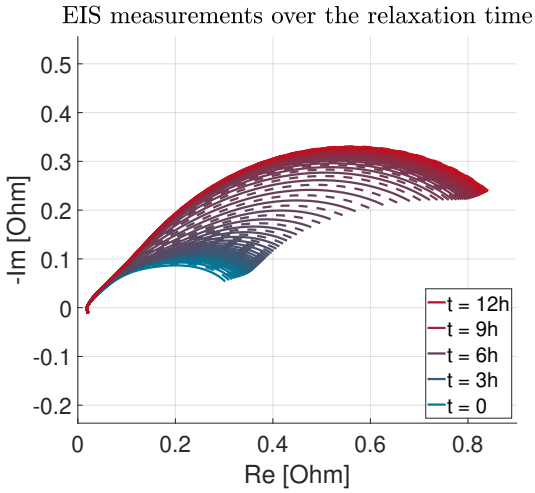

Figure 3.18: 120 EIS spectra measured every 6 minutes for 12 hours directly after charging under plating conditions at −20 °C. (Frequency from 0.1 to 20 kHz)

can be assumed that the change in impedance visible in the spectra is caused by the reversible plating depositions on the surface that are diffusing into the anode over time. The change in impedance could stem from the fact that it is electrochemically favourable for lithium to deposit on existing metallic lithium compared to intercalation into the anode. This should affect to fist semi-circle of the spectrum since that circle depicts the anode double-layer behaviour. The small dent at the beginning of the relaxation is probably caused by the change in temperature of the cell. After that impedance is increasing relatively constantly until a saturation is reached at the end of measurements, which is similar to a diffusion behaviour. This change in impedance is also in good accordance with the findings of Koleti et al. [152].

Further evidence that the anomaly is linked to plating can be found in the correlation of the charge created by the added bell shape and the reversible plating detected during the discharge in the stripping plateau. Figure 3.19 shows the correlation of the charge under the bell shape of the CV phase and the stripping charge during the following discharge.

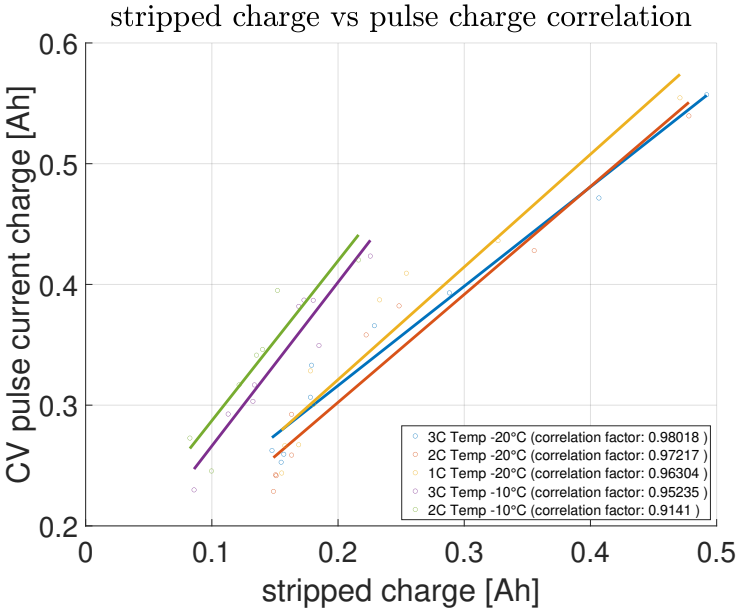

Figure 3.19: Correlation of the charge supplied during the bell anomaly and the corresponding stripping charge detected in the stripping discharge plateau for all cells omitting the CC phase

As discussed in chapter 2.7 during plating a portion of the lithium ions is still intercalating into the anode, while another part is forming the metallic lithium film on the surface. It is assumed that the underlying regular exponential dropping current profile depicts the normal intercalation process, while the superimposed bell shape shows the plating part. To obtain the shape of the current during a regular CV phase a curve composed of two superimposed exponentially dropping functions has been fitted into the measured profile.

$$i_{exp}(t) = i_0 \cdot (e^{-\frac{t}{\tau_1}} + e^{-\frac{t}{\tau_2}})$$

The fit result was then subtracted from the total measured current curve to obtain just the bell shape. The current profile of the extracted bell shape was then integrated to obtain the current supplied during this time. For the discharge profile the length of the stripping plateau was determined by using the deviation of the voltage curve and then the discharge current accordingly integrated to obtain the reversible amount of plated charge. It has to be kept in mind that there is a small error to the amount of charge, since there is also a small amount of de-intercalation and diffusion of the plating lithium in the anode that superimpose the stripping process. So the stripped amount is always slightly underestimated. The results show a very good correlation of more than 0.9 for all cells tested. This means that a measurement using no CC phase can be used to extract only the portion of the plating current from the total charge current. For the measurements that had a CC phase there is no way to extract the plating current since there is no easily obtainable voltage curve that could be used to isolate just the plating anomaly in the voltage curve. And it can be assumed that for these measurements most or all of the plating has been deposited during the CC phase, since none of the measurements show the bell shape anomaly in the following CV phase.

In this thesis the effect of the current anomaly occuring in the CV phase will be analyzed in detail. The voltage anomaly present in the CC phase will be investigated in future works.

3.2.2 Current Anomaly

Under normal operating conditions it should not occur that the CC phase is omitted completely, and if this case should occur this could already be seen as an indicator that there is likely going to be plating during the following charge by itself since the over-potentials in the cell are extremely high. These kinds of over-potentials can only be caused by very low temperatures or very high charging currents, both conditions susceptible to plating. Because of this the bell shape can most likely not help in identifying and preventing plating in a real world application. It is nonetheless helpful in getting a better understanding of the plating process since it can be utilized to estimate the portions of the charge current that go into plating and intercalation. This

could e.g. be used to characterize cells regarding their plating susceptibility in just one cycle. Additionally compared to just analyzing the stripping plateau during discharge the analysis of the pulse characteristics should give a more accurate estimation of the total amount of plating since it should contain the irreversible as well as the reversible plating fractions. It is also not affected by the intercalation of the plated lithium into the anode over time that reduces the amount of detectable lithium when the discharge plateau is utilized for the analysis.

Bell fitting

To better understand the bell effect and its change over the cycles, the obtained cycling measurement data is fitted in this chapter and the resulting parameters are analyzed over the cycles.

Kober et al. [209] also examined the CV phase bell anomaly. They identified logistic growth as possible explanation. This kind of growth process can be implemented using the JMAK model [210, 211, 212]. This model describes isothermal phase transformations and crystallization processes of metals that can be applied to the deposition of lithium on the anode surface. The formula gives the amount of charge deposited on the surface by

$$q\left(t\right) = q_m X\left(t\right) = q_m \left(1 - e^{-\frac{kt^n}{n}}\right).$$

The derivative of the formula then gives the current flowing into the deposition process.

$$i\left(t\right) = \frac{dQ\left(t\right)}{dt} = q_m \frac{dX(t)}{dt} = q_m k t^{n-1} \cdot \ e^{-kt^n/n}$$

The constant k is the rate constant including the nucleation growth rate, the form factor and the rate of the crystal growth. The parameter n denotes the Avrami exponent giving information about the underlying transformation mechanisms. For constant growth and nucleation rates, n only depends on the dimensions of the growth. A value of 2 denotes one dimensional,

e.g. cylindrical growth that could describe dendrites, while a value of three describes a surface coverage expected from mossy plating on a real anode surface [213]. For the deposition of lithium on the anode surface, a dimensionality of 2 to 3 is to be expected [214], since the growth can be either covering the surface in a two dimensional plane or form one dimensional dendrites.

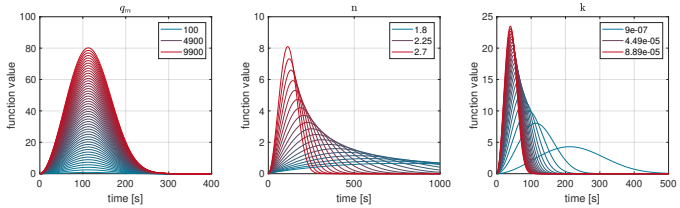

Figure 3.20: Effect of the three parameters q_m, n and k on the shape of the JMAK function

Figure 3.20 shows influence of the three parameters on the JMAK function. The blue curves show a low value and the most red curve ends with the highest value. The plating amount q_m visible in the leftmost plot is simply increasing the total amount of charge and thus the area under the function without changing the shape of the overall function. The Avrami exponent n in the middle plot is shifting the curve to the left and makes it more narrow for higher values. Higher values for n describe growth in more dimensions, which allows more material to deposit in a shorter amount of time thus narrowing the curve. The last parameter k in the right plot shows a similar behaviour with the difference that the effect on the shape of curve seems to be smaller than for n. Since k describes the growth rate a similar explanation as for n can be applied. A fast growth rate will create more deposition in a smaller amount of time.

It has to be kept in mind though that the JMAK equation can only be seen as an approximation since it is based on assumptions that can not be verified for the experiment present or are not very close to real observations in general [215]. These assumptions are:

1. Homogeneous and randomly distributed nucleation
2. Constant growth rate
3. Omnidirectionally equal growth

While the assumption of the nuclei distribution is likely to be true on a macroscopic surface the size of a battery electrode the constant growth rate is limited by the lithium ion diffusion as well as the already present surface coverage in a real cell. It can be assumed however that the growth rate is constant at the beginning of the deposition since the available amount of lithium ions is still sufficient and enough surface area is available for the growth. The equal growth in all directions will be limited by the surface structure but it is not clear how large the influence of this is on the validity of the model function.

To fit the whole curve the JMAK function needs to be superimposed with the underlying intercalation current that can be described with a number of over-layed exponential functions, as described in the chapter before.

$$i_{exp}(t) = i_0 \cdot (e^{-\frac{t}{\tau_1}} + e^{-\frac{t}{\tau_2}} ...)$$

For the measurements in this thesis three exponential functions gave good fitting results and since the functions have no physical meaning and are only utilized to best model the shape of the curve, the exact number of used functions is not of importance for the final results. The exponential part can be roughly pre-fitted using a weighting function only weighting the parts of the current measurement not containing the bell shape overlay to estimate good stating parameters for the exponential functions. The current contribution of the JMAK function is

$$i_{JMAK}\,(t) = q_m k t^{n-1} \cdot \; e^{-\frac{kt^n}{n}}.$$

Where q_m denotes the maximum amount of charge deposited on the surface. The total fitting function can then be written as

$$i_{total}\,(t) = \; i_{exp}\,(t) + i_{JMAK}\,(t)\,.$$

The fitting was performed using a genetic fitting algorithm in MATLAB. However, only using one JMAK function did not yield satisfactory fitting results. The left part of Figure 3.21 shows the fit for the -20°C measurement at 3C with only one JMAK function.

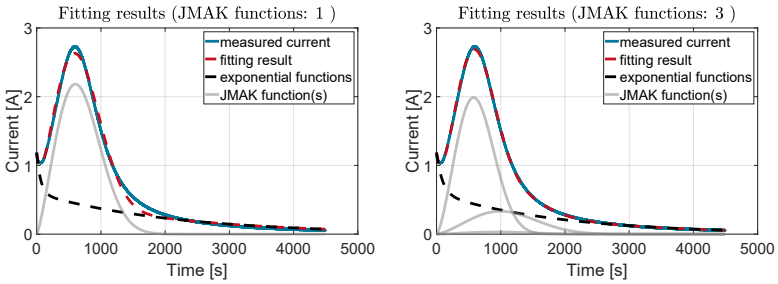

Figure 3.21: Fit with exponential drop and one JMAK functions (left) compared to three JMAK functions (right)

It is visible that the fit has errors at the peak of the bell and in fitting the current decrease when the bell is declining. Fanfoni et al. [216] noticed that for an electrochemical deposition in an electrochemical cell the JMAK equation can only hold true for the initial stage of deposition since new nuclei can be formed on the surface of the already deposited surface layer. For this reason an approach with multiple overlayed JMAK functions is tested. The right part of Figure 3.21 shows the fitting with three JMAK functions overlaying. It can be seen that using multiple JMAK functions in the fit leads to drastically improved fitting results. The exponential functions have only been adjusted slightly by the second fit showing a good consistency of the two fits. The additional JMAK functions needed to improve the fit have a lower amplitude and the maximum is shifted to a later point in time. A theory for this behavior could be that the plating process happens in layers. A large bulk of lithium is forming at the beginning over a wide area of the surface of the anode, represented by the first, larger JMAK function. On top

of this a second layer of lithium forms with a small onset, represented by the second, later and lower JMAK function. The lithium ions use the already existing metal lithium as crystal nuclei. Following this theory, the process would continue with more JMAK functions, forming new layers on top of the last one with smaller and smaller JMAK pulses. To test if this behavior proves to be true the fitting has been repeated using a variable number of JMAK functions. Since this also drastically increases the number of parameters to be fitted, it was tested how many superimposed JMAK functions can lead to good results with minimal computation time. One to eight overlayed JMAK functions have been tested. It was assumed that a higher number of JMAK functions would produce such small bell shapes that they can be neglected. An evolutionary algorithm was used since no individual starting parameters are needed, instead the algorithm takes upper and lower boundaries to create the starting population. To improve the fitting the boundaries of the following, smaller JMAK functions are calculated from the boundaries of the preceding functions. Figure 3.22 shows the evolution of the fitting error when using an increasing number of JMAK functions including the confidence band.

The error first drops until around a number of 4 and then stays almost constant. The error increases slightly again for a number greater 4 with a slightly higher standard deviation, since the fitting becomes increasingly unstable for higher numbers due to the increasing number of parameters that have to be fitted (With 8 JMAK functions, the number of parameters is 35). The fitting error thus shows the expected behavior. From the fitting error results, a number of four JMAK functions is chosen as the optimal amount, since beginning with four there is not much of a benefit regarding the resulting error while the computation time is drastically increasing and the standard deviation is lowest for a JMAK number of 4.

During the fitting process two problems with the fitting and the usage of an evolutionary algorithm in particular become apparent. Figure 3.23 shows the fitting results over all 9 cycles for the cell at $-20\,^{\circ}\mathrm{C}$ that showed no CC phase. The first problem can be seen in the order of the JMAK functions for each cycle. Comparing e.g. the third and forth cycle in the fitting example in figure 3.23 the order of the JMAK functions is changing randomly.

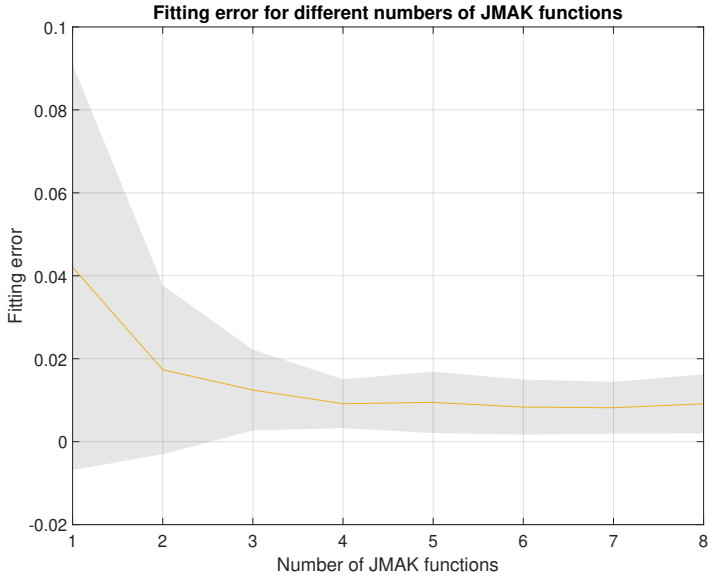

Figure 3.22: Evolution of the fitting error for increasing number of JMAK functions

Function 3 in dark red was the JMAK with the highest amplitude in cycle 3, but in cycle 4 the highest amplitude is now function 1 in light blue. This problem is not important as long as only the overall shape of the fitting result is of interest, but since the parameters of the individual JMAK functions and their evolution over the cycles have to be evaluated, the order of the functions is important for a meaningful analysis. To reduce the impact of this problem and to improve the fitting results first a method was implemented into the evolutionary algorithm to adjust the fitting boundaries depending on the fitting result of the preceding cycle. This increases the likelihood that the functions are logically extended into the next cycle. This reduced the fitting error by a factor of up to 3 for some of the measurements and somewhat alleviated the problem but to achieve good fit results the boundaries still had to be kept as large as $\pm$ 50% of the fitting result of the previous cycle.

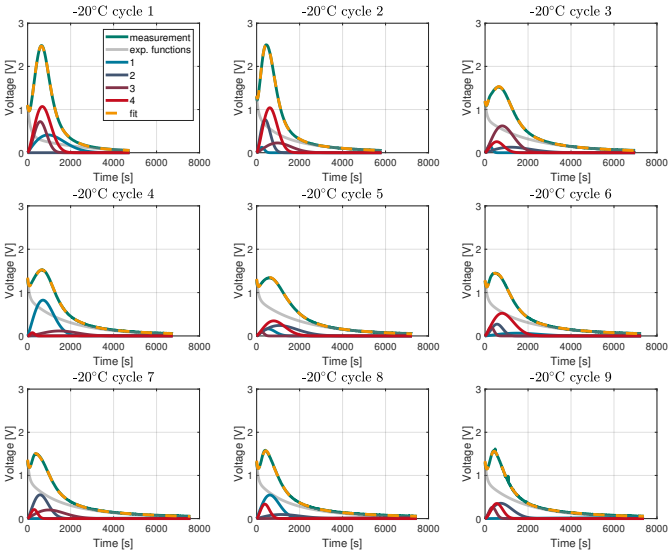

Figure 3.23: Fit results example for all cycles of the cell with no CC phase at $-20\,^{\circ}\mathrm{C}$ and no fitting adjustments

This is why there is still some discontinuity between the order of the fitted JMAK functions between the cycles.

Figure 3.24 shows the fitting results over all 9 cycles for the same cell as figure 3.23 with the boundary updates. It is visible e.g. in cycle 1 and 2 of figure 3.24 that the bell function with the highest amplitude is still changing position. To allow for a consistent analysis of the fitting results the JMAK functions would need to be sorted in logical order. This could have been done by hand, but this way of sorting would most likely lead to strongly biased results. For this reason to reduce human error and biases a method was developed to sort the JMAK functions based of their mathematical likeliness. As a metric of likeliness the location of the peaks as well as their maximum peak height is taken. It is important to take the position as well as the location of the peaks to compare their likeliness since e.g. looking at

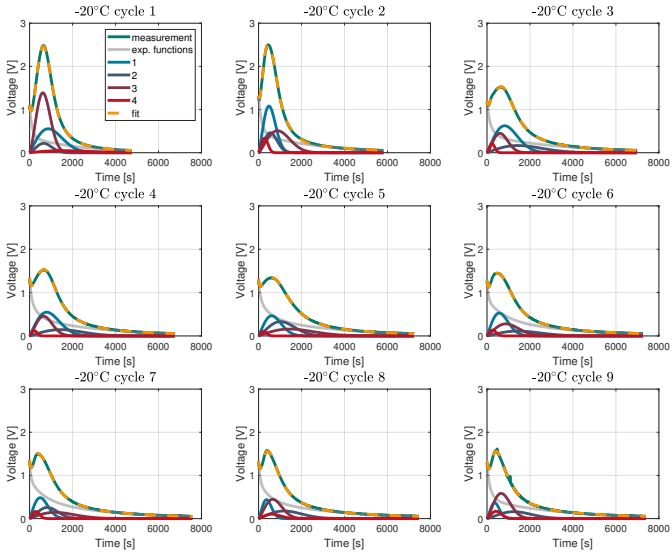

Figure 3.24: Fit results example 1 with boundary adjustments for all cycles of the cell with no CC phase at $-20\,^{\circ}\mathrm{C}$

figure 3.25 and the evolution of the peaks between the first and the second cycle it is visible that all peaks except of the red peak have high likeliness to a corresponding peak. The red peak however is very wide and flat in the first cycle, with its center point been the rightmost of all four peaks but the only possible partner for the red peak in the second cycle, considering the high likeliness of the other three peaks towards their partners, is a very narrow peak that has the leftmost position of all peaks. In this case just considering the peak location would have lead to a sub-optimal result since the the red peak from the first cycle would have been paired with the rightmost peak of the second cycle in consequence causing all other peaks to be paired with much worse partners. For this reason using both location and height is important of the optimal peak allocation. These two parameters are calculated and normalized for each peak. Together with the same parameters of the

previous peak they then form two confidence matrices for position as well as peak height. These two matrices are then combined by taking the weighted average of the two values. Using the weighting function the confidence priority can be shifted towards either the peak position or the peak height. Based on the resulting matrix each peak is then assigned to a peak of the previous cycle by simply calculating which permutation of peaks has the highest total confidence.

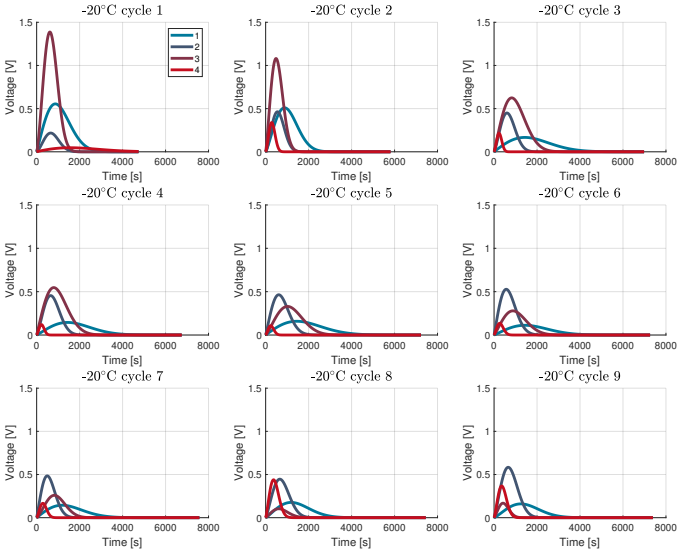

Figure 3.25: Fit results for example 1 with peak sorting for all cycles of the cell with no CC phase at $-20\,^{\circ}\mathrm{C}$

Figure 3.25 shows the sorted peaks for the same measurement as example 1 in figure 3.24. The peaks show a more logical order than the original order visible in figure 3.24 with the red peak always being the furthermost left peak, except from the first to second cycle, where the allocation is not clear and the light blue only starting to be consistent from cycle 3 to the last cycle. The algorithm only shows unexpected results when the peak allocation would

also not be clear from a manual inspection e.g. visible in cycle 4 and 5 where the order of the peaks with the highest value change position. A closer look however reveals that peak 2 in dark blue is almost identical to its counterpart in the next cycle. This is one example where the algorithm is superior to a manual sorting of the peaks.

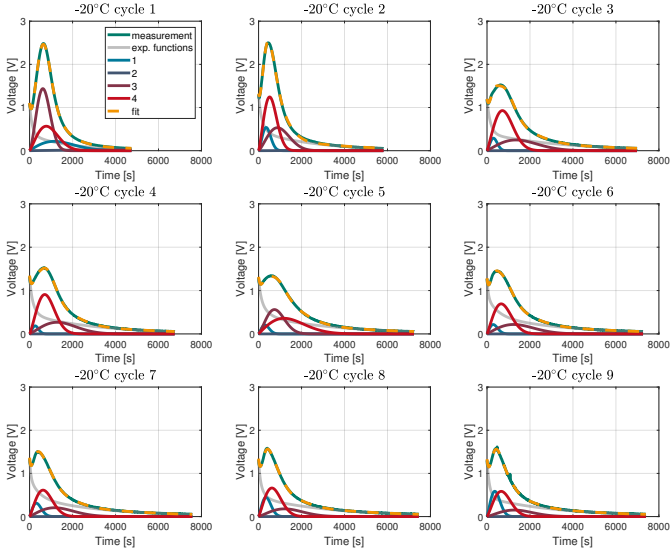

Figure 3.26: Fit results example 2 with boundary adjustments for all cycles of the cell with no CC phase at $-20\,^{\circ}\mathrm{C}$

Figure 3.26 shows the same fit performed a second time on the same measurement data that was already shown in figure 3.24. The fit result is very good in both cases (mean root-mean-square error (RMSE) of 0.0039 for example 1 and 0.0057 for example 2) but it was possible for the fitting algorithm to achieve a good fit with different underlying functions. This is a problem mainly caused by the use of an evolutionary fitting algorithm since for this kind of fitting the fitting parameters are limited less than for other fitting algorithms even using the boundary updates as described before and also

by the fact that the fitting of the first cycle has to have a even larger fitting window. Due to the large number of fitting parameters however and the difference of the measured function shapes the creation of stable starting parameters for other fitting algorithms is impractical. It can be seen that for an increasing cycle number the fitting results in figure 3.24 and 3.26 become more similar. This is caused by the fact that the algorithm uses the fitting results of the previous cycles to update the boundary parameters as discussed above, which puts a very high weight on the first fit and then only allows the algorithm to progressively deviate from the initial fit result. To obtain robust data for the analysis of the behaviour over the cycles a Monte Carlo simulation is performed and the fitting repeated multiple times to calculate the statically most likely correct fitting result. To obtain the most likely fitting result from the repeated fittings the fitting errors are clustered using a simple k-means clustering and the center of the largest cluster is chosen as the most plausible result. The final fit result will then be the fit result whose error is closest to the center of this cluster.

Fitting Results

After fitting the bell curve with 4 JMAK functions for 178 times (this number was the final amount of fits due to available machine time) the most plausible result was chosen and the function order was adjusted as discussed in the previous section. As discussed before 4 JMAK functions have been chosen since for this number of JMAK functions the fitting error was on average the lowest. Figure 3.27 shows the evolution of the 3 parameters of the 4 JMAK functions over the cycles under plating conditions for the 6 cells that showed bell anomalies in the CV phase. Each row represents one JMAK function with the three parameters q_m, n and k from left to right plotted over the cycles. The cell cycled at $-10\,^{\circ}\mathrm{C}$ with a current of 2C had two errors during cycling which could have possibly been caused by a dendrite short circuit. The first of the two cells cycled at $-10\,^{\circ}\mathrm{C}$ at 3C also had one error occurring during cycling. For these two cells the missing data points have been interpolated. This has to be kept in mind during the interpretation since this cells technically didn't have same number of cycles as the other

cells and additional effects caused by the errors could also have an influence of the behaviour of the cells during subsequent cycles after the erroneous cycle. For the cell at 2C the erroneous cycles were cycle 4 and 6, for the cell at 3C the 8th cycle wasn't performed as intended.

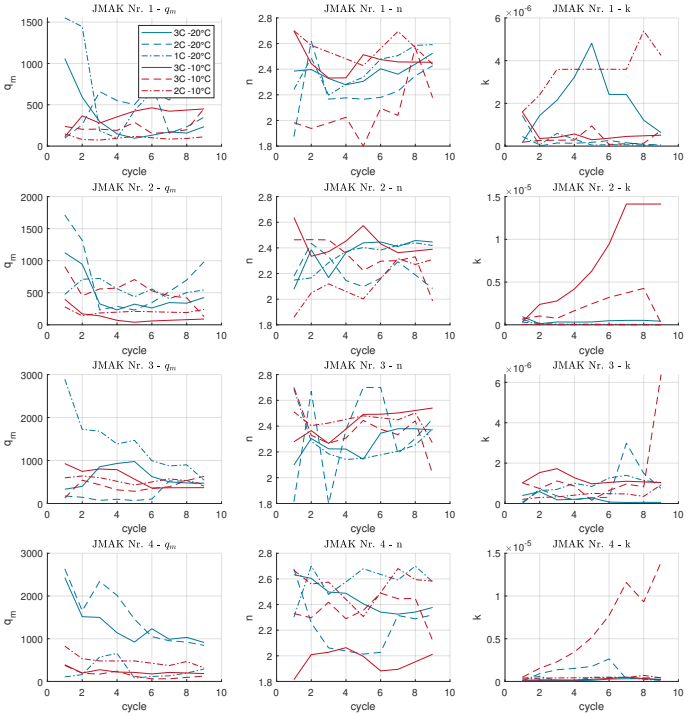

Figure 3.27: Parameter evolution for 4 JMAK functions over the cycles under plating conditions for all 6 test cells that showed the bell CV phase effect

The red lines in figure 3.27 are showing all cells cycled at $-10\,°C$, the blue lines are used for cells cycled at $-20\,°C$. It is visible that the parameters are all very unstable. This means that even though 4 JMAK functions showed

the lowest fitting error, the fitting parameters had too many degrees of freedom and fitting results can not be interpreted in a meaningful way. Only in the parameter q_m a trend is visible in that the curves at $-20\,^{\circ}\mathrm{C}$ show a higher total charge plated and the total amount of charge plated on average decreases for both temperature over the cycles for all JMAK functions. This is to be expected and this parameter could have also been obtained with just fitting the exponential functions and then integrating the remaining current curve without the exponential part. For 4 JMAK functions neither n nor k show any trends.

For this reason the fitting was repeated using a smaller amount of JMAK functions. This will increase the fitting error by disregarding new nuclei forming on top of the already existing depositions as discussed in the previous section. But it should lead to more stable fitting results and thus allow for a meaningful analysis of the fitting parameters over the cycles.

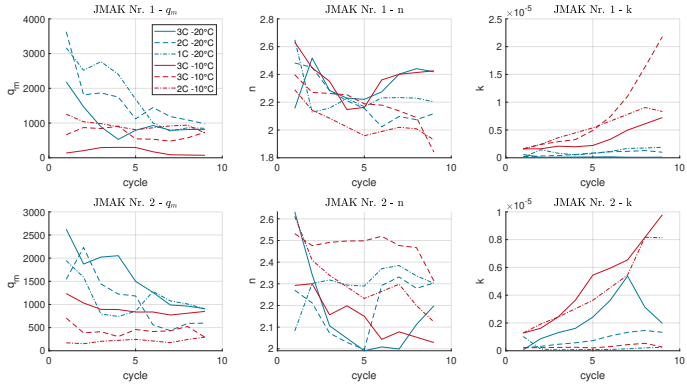

Figure 3.28: Parameter evolution for 2 JMAK functions over the cycles under plating conditions for all 6 test cells that showed the bell CV phase effect

For the fit with two JMAK functions only 10 repeated fits have been performed since the fitting should be much more stable with a significantly reduced amount of parameters to fit. For the parameters shown in figure 3.28 there are already clear trends visible. The total plated charge q_m is

separated in the −20 °C measurements that show a decline over the cycles and a higher value in general and the measurements at −10 °C which have a lower value and stay constant over the cycles. it also seems like the values at −20 °C are approaching the value of the plated charge at −10 °C. This means that the plating mechanism must be somehow different at lower temperatures but this difference is fading over the cycles. It could also be that the amount of plating is decreasing in both cases but the effect is not as pronounced at −10 °C and not visible after only 9 cycles. The Avrami exponent n in the middle plots is still unstable even for only 2 JMAK functions but even though there is not clear distinction between the two test temperatures a general trend of decreasing value over the cycles can be seen for the first JMAK function. This would indicate, that the dimensionality of the growth is shifting from a planar 2D deposition to a more dendritic 1D cylinder shaped deposition over the cycles [213]. If this is true, then this would mean that for this cell the chance of safety hazards caused by dendrite growth would increase with the number of plating cycles. The last parameter k also shows a distinction between the two temperatures but in contrast to q_m here the lower temperature stay rather constant and the higher temperatures at −10 °C are increasing over the plating cycles. The parameter k is mainly influenced by the growth rate so this would indicate that with progressing cycles the deposition becomes faster. This could theoretically be caused by already existing deposition so that the possible deposition surface is larger at the start and no new nucleation is necessary. This however would be true for both temperatures and does not explain the difference between the measurements at −10 °C and −20 °C. It is also noticeable that the parameters of the second JMAK function are more unstable than the parameters of the first one and no additional meaning can be gained from the analysis of the set of parameters of the second JMAK function. For this reason the fitting has been repeated with only one JMAK function to see whether the parameters behave differently.

Figure 3.29 shows the parameter evolution with only one JMAK function over the plating cycles. For 1 JMAK function the fitting was very stable and showed the same result in the majority of the monte carlo fit results meaning that in this case most likely a clear global minimum could be detected. Here

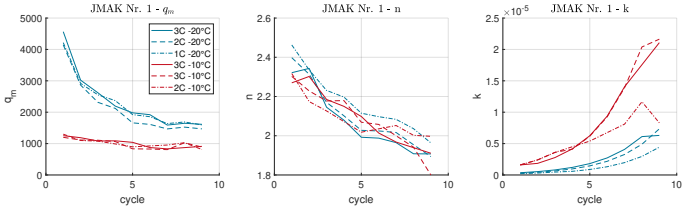

Figure 3.29: Parameter evolution for 1 JMAK function over the cycles under plating conditions for all 6 test cells that showed the bell CV phase effect

the same trends can be seen that have already been discussed above for the fitting case with 2 JMAK functions but the distinctions between the two test temperatures is much clearer for q_m and k and the decrease of the Avrami exponent is also much better visible than in the plots for 2 JMAK functions. It can also be seen that there seems to be no difference for different temperatures regarding the dimensionality of the growth since the parameter n is very similar for all cases. It is also better visible that k is also increasing at $-20\,°C$ which is be expected since both temperatures should lead to a higher amount of existing depositions that can increase the deposition speed as discussed before.

Since none of the measurements at $-20\,°C$ showed any CC phase the current of the measurement is irrelevant and all three can be seen as plating under the same conditions so the results can also be averaged. The same is true for the three measurements at $-10\,°C$. Figure 3.30 shows the averaged parameter curves for the two temperatures as well as the standard deviation for each curve.

It is visible that the trends stay the same as discussed above and that the standard deviation is low enough to distinctively separate the curves for the parameters q_m and k. The large increase in the standard deviation for parameter k in the later cycles is most likely caused by the erroneous measurements in two of the three measurements that have been averaged.

It is also notable that even though for all samples the amount of measured plating obtained from analyzing the current curves is reduced over the cy-

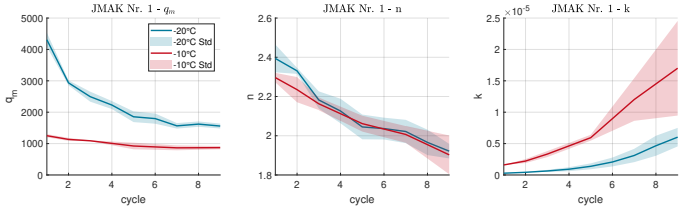

Figure 3.30: Parameter evolution for 1 JMAK function averaged for the different temperatures

cles, the capacity loss is almost constant at the same time, as visible in figure 3.2. If q_m is really depicting the total amount of plating, i.e. reversible and irreversible plating combined, that would mean that the irreversible plating is not directly linked to the amount of reversible plating since the cells at $-20\,^{\circ}\mathrm{C}$ show declining amounts of reversible plating but the irreversible capacity loss stays the same over all cycles. Figure 3.31 shows the comparison of the measured stripping charge added to the irreversible capacity loss detected in the characterization after the plating cycle with the parameter q_m (converted into Ampere hours).

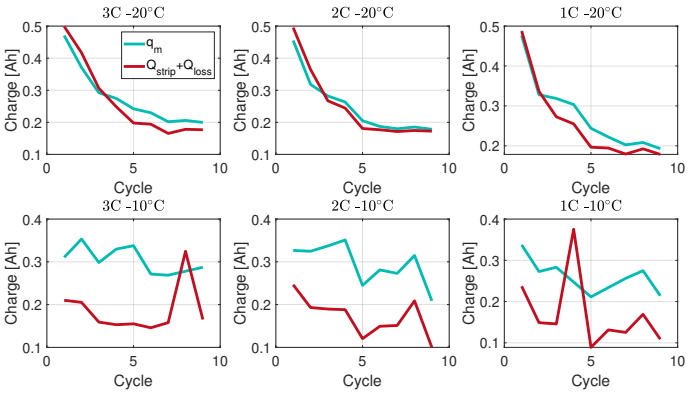

Figure 3.31: Comparison between the fitting parameter q_m and the total plating charge measured

It is visible that for the measurements at −20 °C there is very good agreement between the fitted parameter and the measured plating charge. For −10 °C however the real measured charge is significantly lower than the fitted parameter. This is probably caused by the fact that the diffusion speed at −10 °C is much higher than at −20 °C and thus the charge measured in stripping phase during the discharge is underestimating the real amount of irreversible plating since a significant portion of the lithium is already diffused into the anode during the preceding charge. The shapes of the curves follow quite well, except for two outliers for the −10 °C measurements that show up after the erroneous measurements. This indicates that q_m could be a good measure for the real amount of deposited plating and that it should be closer to the real value than the stripping charge.

3.2.3 Summary of the Current Anomaly Results

In summary the analysis of the current phase anomaly during plating has shown that:

- It could be shown that the effect is not only caused by a temperature change in cell during charging
- The effect can be fitted well using the JMAK function suggesting that the observable effect is a metallic deposition process and is linked to lithium plating
- The fitting parameter n (the dimensionality of the deposition) is changing over the plating cycles which could mean a morphological change in the lithium deposition from mossy to dendritic form, potentially increasing the safety risk
- The fitting parameter q_m could be used for better estimate of the true amount of plating compared to the discharge voltage curve stripping method since it is measured during the charging process and reduces the time frame where deposited lithium can re-intercalate into the anode.

- The obtained parameters could be used to characterize a battery cell regarding its plating susceptibility for battery life prediction.

Future experiments are necessary on cells of different types and manufacturers to investigate whether the effect it generally applicable. To prove that the dimensionalty parameter is connected to the plating deposition morphology further experiments involving more detailed post mortem analysis or in site techniques are necessary.

3.3 XPS Measurements

In this chapter the results of the XPS measurements performed in this thesis are shown and analyzed. The original goal of these experiments was to identify and locate metallic lithium inside of the SEI layer. This was done to answer the questions whether there is any dead lithium in metallic form present in the SEI after plating or if the lithium reacts with XPS compounds to form new compounds and thus degrades over time and if it is present, where in the SEI this lithium can predominantly be found. XPS was chosen as a method to do this since it is one of the few non-destructive measurements methods that is capable of detecting metallic lithium and at the same time also differentiating between elemental lithium and lithium bound within the various SEI compounds. As discussed before in chapter 3.32 the penetration depth of XPS is very low so that the method can only measure the composition of the top layer of the SEI. To gather information about the whole structure of the SEI layer thus a depth profiling experiment was performed using argon etching to get spectra at different depths into the SEI. It became however clear during the first measurements that the application of the XPS measurement onto the surface of the sample produced a visible change to the material that could not be explained in the beginning. It was also notable that the effect only seemed to appear on samples where a higher content of lithium was to be expected, namely the samples that have been plated and the fully charged anode sample, as explained later in this chapter. Since the effect was however apparently located outside of the measurement area it was initially ignored and the depth profiles have been recorded regardless. It became later clear that even though the effect was visibly not present in the measurement area which is only a few square millimeters large, the effect did influence the measurement results significantly. In the following analysis of the measurements results it became apparent that the results did not fit the expectations and where very difficult to logically analyze. For this reason a series of follow up experiments were conducted to identify the cause of this surface change. The results of these experiments showed that the effect was caused by not insulating the samples during the measurements and utilizing a charge compensation mechanism in the XPS device, which are both normal

procedures during XPS measurements. Unfortunately it was not possible to repeat the depth profiling measurements after identifying the problem since the measurement time of the XPS device was limited, it was however possible to utilize the effect and analyze the already measured depth profiling spectra in a meaningful way. The results showed that the effect could be used intentionally in future experiments as a different approach for lithium detection that does not require the destructive method of argon sputtering for depth profiling.

The order in which the experiments are presented in this chapter is not the chronological order in which they have been performed but rather an order that hopefully helps the reader to better understand the measurement results.

3.3.1 Experimental Setup

For the XPS measurements the same cells of different manufacturers presented in chapter 3.1 (table 3.1) as well as the cell-type used in the FIB measurements in chapter 3.1 have been used. Additionally one sample was taken from pristine anode material that was not used inside a cell (sample A). This sample was used to get a reference of the graphite surface without any electrolyte or SEI but can not be directly compared to the commercial cells used for the rest of the experiments since it was composed of a laboratory created anode material and is thus only used as a reference for the C1s peak and not further used in the interpretation of the results. For all cells except for the pristine material, one measurement was done with a fresh cell that only experienced a characterization cycle and a plated cell that was plated at $-20\,^{\circ}\mathrm{C}$. The cells taken from chapter 3.1 have been used in the experiments there [208] where they experienced 10 cycles of plating and afterwards had approximately 6 months of resting time at about 30% SOC before they were characterized again, they were fully discharged after the characterization, then opened and prepared for the XPS measurements, so all residue of reversible plating effects should have diffused into the anode.

To further investigate the influence of the measurement method the samples of the Sony VTC3 also have been electrically insulated, which will be further discussed in chapter 3.3.2.

For these measurements the cells used are new cells of the type LG ICR-18650HB2 NMC, since these were also used in the work of Wink [207] and the FIB measurements shown in chapter 3.1 have been performed on these cells. This cell type will be further abbreviated as LG-FIB. For this cell type two additional cells have been prepared under different conditions. One of the cells was only cycled once to bring it into the desired state, this is technically a new cell. This cell was opened at 100% SOC. The second cell was cycled for only one full cycle at $-20\,^{\circ}\mathrm{C}$ to produce lithium plating in the cell and then opened. In comparison to the plated cells taken from chapter 3.1, this cell had a much shorter resting time of less than a day before it was opened. The fully charged cell was used to investigate the presence of intercalated lithium on the XPS measurement since even in a fully discharged cell there will still be some amount of intercalated lithium in the anode. For the freshly plated cell this is even more important since reversible plating could still intercalate into the anode graphite even if the cell is dismantled and increase the amount of intercalated lithium. Figure 3.32 shows an overview of the all samples used in the XPS measurements. For the LG-FIB also an etching experiment was performed on the new, freshly plated and fully charge cells to be able to compare the resulting depth profile with the FIB cross sections of the SEI, which will be discussed further in chapter 3.3.4. The pristine graphite was also etched as a reference. All cells will further be referenced using their the abbreviations of figure 3.32 with SAM standing for the cells of the manufacturer Samsung and SO for Sony.

All cells were opened inside a MBRAUN Unilab glove box under argon protective atmosphere with $< 10\,\mathrm{ppm}$ of moisture and oxygen concentration. All samples from the opened batteries have been taken from the outermost area of the jellyroll. The samples were then transferred to the XPS device inside a gas tight transport box. The XPS device has an attached mini glove box that was used to transfer the samples from the transport box to the XPS test chamber. Within the mini glove box the samples have been exposed to roughly 100 ppm of oxygen atmosphere for a few minutes before

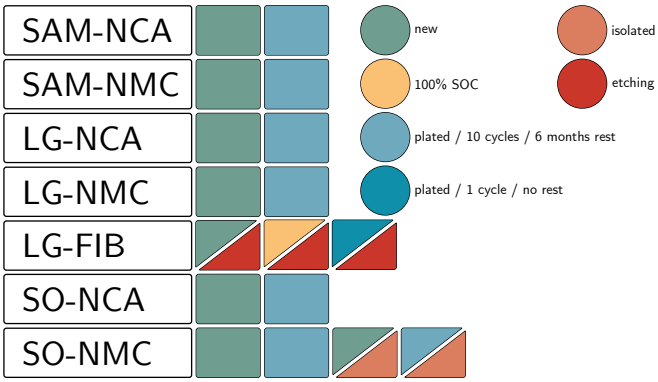

Figure 3.32: Overview over all XPS experiments using the different cell type from table 3.1

entering the high vacuum. It was unfortunately not possible to also measure the moisture content in the mini glove box during the transfer. Oswald et al. [175] performed an experiment to determine the influence of environmental conditions on the samples with a one minute exposure time and found that the lithium content on the surface of lithiated graphite drastically increased. They assume that this was caused by diffusion of lithium to the surface of the graphite and subsequent reactions forming Li_2CO_3. Since transfer conditions prior to the XPS experiments in this study have not been ideal, the effect could also occur to some extend leading to an overestimation of lithium content on the surface of the sample. But since the SEI layer is to be expected much thicker (as shown in chapter 3.1) due to the plating effect on the plated samples this could mitigate the effect for these samples. And it is not clear if the effect can only occur for lithium intercalated into the anode, as seen in their samples, or also for dead lithium within the SEI.

For the XPS measurements a Kratos Axis Supra device located at the Fraunhofer IZM in Berlin was used. It has a base pressure of 2×10^{-9} torr. The photo-electron source is a monochromatic Al Kα X-ray source ($h\nu = 1486.7\,\text{eV}$).

In the measurement process for all samples a complete wide spectrum was recorded, followed by higher resolution detail spectra of the elements of interest that can be found within the SEI layer and anode bulk material. These elements are **fluorine** (F1s), found in in the conductive salt $LiPF_6$ and the most common binder within the anode: PVDF, **oxygen** (O1s), found in most of the organic compounds in the electrolyte, **carbon** (C1s), also present in the organic components and main part of the anode active material, **phosphorus** (P2p), part of the conductive salt as well and **lithium** (L1s), as the electrochemical active ion and part of the conductive salt.

This measurement routine was repeated for several etching steps of different length to obtain a depth profile of the material composition in the SEI for the LG-FIB cells, as mentioned before. The exact parameters for the etching experiment will be discussed in chapter 3.3.4.

General Spectrum Analysis Principles

The first step in the analysis of the measured spectra is the identification of the peaks and their corresponding compounds. The largest problem with the allocation of the peaks are shifts in the spectra. These shifts can be caused by charging of the sample due to the surface charging effect that was already explained in chapter 2.6.2. This is especially difficult for LIB related materials since they can have a varying conductivity with conductive materials in some locations and non conductive materials in other locations when creating a depth profile during the measurement. These shifts due to surface charging always affect the complete spectrum and can be mitigated by using a reference element that is definitely present in the sample. During the measurements the charge neutralization system of the device was always on since the conductivity of the samples is assumed to be very low due to the surface coverage of the SEI. Bear et al. [157] mention that for Kratos Axis systems the charge neutralization often shifts the measured peaks to a lower binding energy. A negative charge on the surface is accelerating the photoelectrons more than the energy they gained from the X-ray exposure while a positive charge on the surface would cause the opposite and slow down the electrons. The electrons are then registered with an erroneous kinetic

energy at the analyzer. Before the data is displayed and analyzed the kinetic energy is transferred into the binding energy. This is done by subtracting the kinetic energy from the X-ray energy (in this case 1486.7 eV). That means that a high kinetic energy corresponds to low binding energy since a larger part of the X-ray energy was transferred into kinetic energy. Looking at the spectra a negative shift in binding energy means that the kinetic energy of the photo-electrons was larger than it should have been which means that the electrons have been accelerated by a negative charge on the surface. Analog a positive shift means a lower kinetic energy caused by a deceleration of the photo-electrons due to positive charge on the surface.

For the present sample the carbon or AC peak at 284.3 eV [170] is chosen as reference since it should be present in all samples and the spectra were shifted accordingly so that the AC peak is also at position of the highest peak in C1s detail spectrum. As mentioned in chapter 2.6.2 the C1s peak is not the ideal reference peak for several reasons but since the samples used in this experiment show very different spectra, the C1s peak was the only peak that could be easily identified in all of the measurements. The value for the AC peak varies slightly in literature between 284.3 eV and 285 eV [162, 169, 170, 171, 172] and this specific value was chosen by finding the best fit with the other peaks in the sample. After the shift of the whole spectrum the individual peaks need to be identified. To do this literature values for the expected compounds are taken. These values however also have a great deviation. Wood et al. [176] analyzed the literature values for the most common LIB compounds and found that while the absolute values for the peaks can be very different, the distances between the individual peaks of each compound, e.g. the distance between the BE for Li1s and O1s in Li_2O, are very similar for all different sources. They conclude that it is better to use the ΔBE as the main indicator for the peak positions. For the compounds present in their study that were of interest for this thesis, namely Li_2O, Li_2CO_3 and LiOH these ΔBE values haven been taken. For the other important compounds not present in their study a similar approach was taken. For these compounds multiple literature values have been compared and their ΔBE values calculated. Then an average for these values was taken and the resulting ΔBE was used in the peak identification. Table 3.2

and 3.3 exemplary show the literature values and the resulting average for LiF and $LiPF_6$ respectively.

	Li1s	**F1s**	**Δ BE**	Source
	56	685	629	[169]
	56.5	685.5	629	[165]
	55.5	686.5	631	[171]
Average:	56	685.66	629.66	

Table 3.2: XPS peaks for LiF

	Li1s	**P2p**	**F1s**	**Δ BE Li/P**	**Δ BE P/F**	Source
	58.2	138.2	687.9	549.7	80	[217]
	57	138	688	550	81	[171]
	58.4	137.8	688.8	551	79.4	[218]
Average:	57.7	137.9	688.4	550.23	80.13	

Table 3.3: XPS peaks for $LiPF_6$

The elemental composition of the SEI is approximately 90% C, 4–6% F, 3–4% O and 1% P [29] as well as small amounts of Li in different compounds. All the possible compounds of the SEI layer found in the literature have been added into the analysis in order to identify as many peaks in the measurement as possible:

- **$LiPF_6$:** The conductive salt found in most commercially available LIBs. May be found on the surface of the anode as a residue of the electrolyte or embedded into the SEI.
- **PVDF:** The binder found in most commercially available LIB anodes. Should not be strongly visible in the XPS signal as long as the SEI on the surface is intact.
- **Adventitous carbon:** Carbon based surface contamination normally visible on all samples, overlaps with the signal for the anode graphite active material underneath the SEI.

	binding energies					
Compound	**Li1s**	**P2p**	**C1s**	**O1s**	**F1s**	**Sources**
$LiPF_6$	57.7	138.2			688.3	[171, 217, 218, 219]
PVDF			286.5/290.9		687	[175]
AC (Carbon)			284.5			[220]
LiF	55.8				685.5	[165, 169, 171, 175]
						[173, 218, 219, 221]
Li_2CO_3	55.4		290.1	531.9		[165, 171, 222, 223, 224]
						[173, 175, 184, 219, 221]
Li_2O	54.1			529.1		[165, 171, 175, 221, 225]
CO			286.3	534.4		[169, 180, 219, 226]
CO_3			289.8	531.9		[169, 219, 227]
$ROCO_2Li$			286	532		[171, 173, 224]
Li_xPF_y	57.1	136.5			687.3	[171, 218, 224]
$LiPF_6$ dec.		134.3				[226]
LiOH	54.6			531.6		[165, 171, 221]
Li_xC	54.6		283.1			[175, 220, 228]
$Li_xPO_yF_z$	55.5	134.8			687.1	[180, 218]

Table 3.4: XPS peaks derived from literature values

- **LiF:** Main salt reduction product in electrolytes with fluorinated salts, like $LiPF_6$, can be caused by water contamination induced HF formation [29].
- **Li_2CO_3:** Reaction product of semicarbonates with HF, water or CO_2 [29].
- **Li_2O:** Degradation product of Li_2CO_3 [29]. Can also be product of metallic lithium with atmopheric contamination.
- **$ROCO_2Li$:** Can be found in the outer layer of the SEI. Electrolyte decomposition product in presence of PC [29], but also EC and DMC [184]. Contains the same amount of one-oxygen C links as three-oxygen C links [223].
- **CO:** C in one oxygen environment.
- **CO_3:** C in three oxygen environment. (can relate to Li_2CO_3)
- **Li_xPF_y and $Li_xPO_yF_z$:** Salt decomposition products [171] in the presence of transition metals [218].

- **$LiPF_6$ dec.:** Other salt decomposition products.
- **LiOH:** Caused by water contamination in the cell [29]. Andersson et al. [173] observed a thick layer of LiOH close to the graphite SEI surface after sputtering and they assume that this layer was created by the sputtering and is not normally found in this quantities in the SEI.
- **Li_xC:** Fully or partially lithiated graphite. Should be visible underneath the SEI in the fully charged sample and in small amounts in all cells, since the cells can not be fully discharged under normal operation.

Typical uncertainties for the XPS peak positions are around $+/-0.2\,\text{eV}$. Also since there always is a small inherent measurement error in the peak positions and it is unknown whether the literature values contained some level of shift it is possible to still shift the values by a small amount ($<1\,\text{eV}$) to fit them into the right position for this measurement. But this shift has to be consistent over all measurements since it is a shift correction of the original measurement of the literature source. Another thing to keep in mind is the shift of SEI components in the presence of metallic lithium or lithiated graphite [172, 174, 175]. This has to be considered in the fully charged sample and the plated sample. In this case certain peaks could show a shift that is independent of other peaks, since the shift is depending on the conductivity of the compound.

For this analysis all the peak locations have been determined by using the first measurement of the fully discharged new SO-NMC cell, since in this sample the lithium content should be the lowest (apart from the pristine sample that was only used for AC calibration) and thus any lithium induced individual shifts should be neglect-able. The shape of the peaks can also contain valuable information about the represented compounds and elements. Metallic samples often show asymmetric peaks due to coupling of the photoelectrons with the conduction electrons in the metal [185]. Peaks at higher BE are usually wider and insulators also have wider peaks than conductors [185].

Before any spectra can be analyzed properly the background has to be removed. This background occurs since not all electrons excited by the X-ray

will reach the detector unhindered, some of the electrons will in-elastically scatter and lose energy before reaching the detector and thus register as electrons with lower kinetic energy (shown as higher binding energy). The background removal of the spectra was performed using a simple iterative Shirley method [229]. The alternative Tougaard's background yields better results for quantitative analysis but requires a wider measurement range around the detail scans of peaks of about 30 eV [177] that was not measured in the experiments present. The Shirley background is also easier to implement and is sufficient for the basic analysis performed on the data in this thesis. The start and endpoints for the Shirley method have been selected by hand for all spectra.

In the following chapter the recorded XPS spectra will be qualitatively analyzed using the compound lines shown in table 3.4. The lines for Li_2CO_3 and $Li_xPO_yF_z$ as well as LiOH and LiF have been merged at the average value since they are so close together that the compounds can not be separately identified within the precision of the XPS device. All spectra have been shifted to the AC peak, if possible, to compensate for surface charging during the measurement. In some cases the AC peak was not the highest peak in the C1s detail spectrum. In this case the other compound present in all samples, LiF was used to shift the spectra. The amount of shift for each spectrum is also recorded and can be found in the description of each plot. All detail spectra have had their background removed using the Shirley method, as discussed before.

3.3.2 Influence on the Samples

As discussed in section 2.6.2 the etching process is a destructive process that can change the chemical composition of the surface. But not only the etching can influence the sample, the energy of the X-ray beam itself can also affect the compounds present, as well as the charging of the surface, called electron damage [157]. Figure 3.33 shows the condition of the four samples of the LG-FIB cell before the measurement, after the first spectrum was recorded and after the first and last etching step.

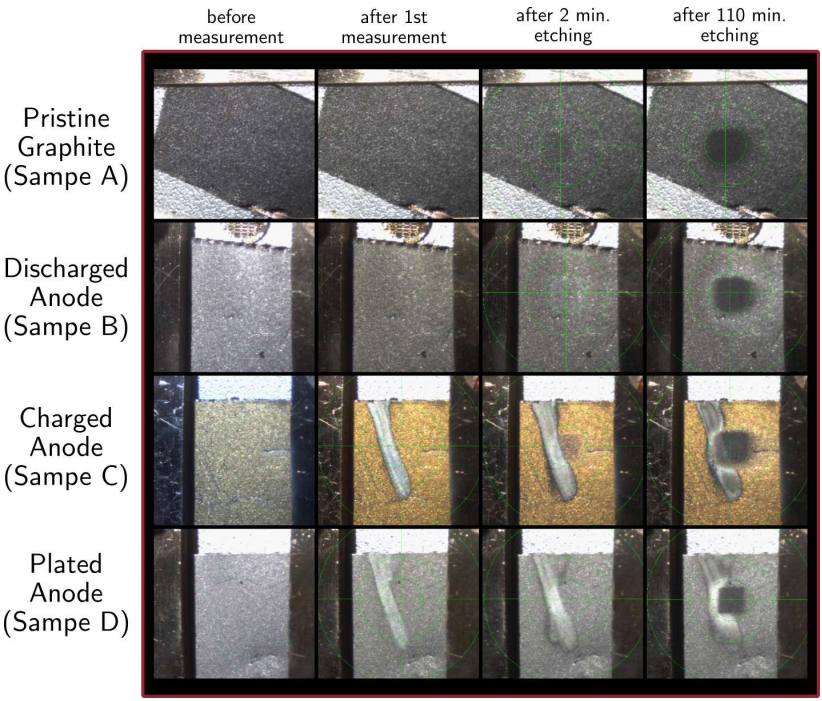

Figure 3.33: Overview of the changes in the sample during the XPS measurement and the etching process

All the samples show a blackening in the etching area that gets darker with increasing etching time. Some change of the surface in the etching area is to be expected since the etching is a very destructive process. More interesting is the diagonal stripe-shaped change of the surface in sample C and D that makes the surface become a metallic silverish color. These are both the samples with a high or higher expected lithium content and possible metallic lithium. This effect is not visible in the pristine and the discharged anode so it is likely that it is connected to the lithium content in the sample. Since the plated anode is also discharged before the cell was opened this is a clear indicator that the SEI of the plated sample must have a different composition from the discharged sample without plating. Interestingly this

discoloration always seems to appear in the same angle and is not located at the actual measurement area. The measurement area is in the center of the etching area, but smaller than the etching area, so this effect seems to be mostly outside if the measurement area. The effect is also not connected to the etching since it appears after the first measurement before the etching process is started. To further investigate this effect and its potential influence on the measurement results additional tests have been conducted.

Striping Experiments

The first experiment to investigate the surface stripes that appear on the samples that contain larger amounts of lithium (i.e. the fully charged and 1 cycle plated LG-FIB samples that have been measured beforehand) was to see whether the effect was caused by the X-rays or by other factors. To do this additional fully charged and plated samples have been prepared and subjected to different combinations of measurement-modes in the XPS device. The device has three main parts that work together during the measurement, the X-Ray beam that is causing the sample to emit the photo electrons, the analyser, which is collecting and separating these electrons by energy and the charge neutralizer (CN) that can be optionally enabled to prevent surface charges from building up that may shift the measured peaks. In all previous tests all three parts were on during the measurement, since CN should be used when the surface of the sample is non conductive, which is the case for the SEI covered anode surface. Figure 3.34 shows all possible combinations of the three parts applied on the plated surface of the SO-NMC anode. Figure 3.35 shows the same experiment on the fully charged anode.

The only combination that creates the stripe on the surface in the experiment is the combination of all three parts. Due to the limitation of the device however it is not possible to activate the analyser without activating the X-Ray, but as it is visible in both figures in part (D) both X-Ray and analyser together don't create any surface change without CN. As a conclusion it is most likely that the combination that can not directly be tested, namely analyser and CN, is what is creating the surface changes. It is also visible by looking at both figures 3.34 and 3.35 that the effect is very similar

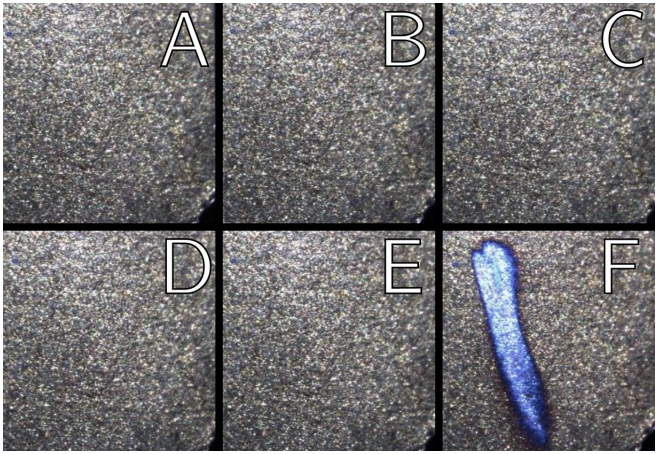

Figure 3.34: Stripe experiment on plated anode with different measurement modes: (A) as received (B) 10 min X-Ray (C) 10 min CN (D) 10 min X-Ray and CN (E) X-Ray and analyser (F) X-Ray, analyser and CN

for the plated and fully charged samples. The stripe seems to be forming at a constant angle to the sample. Figure 3.36 shows the evolution of the stripe on the plated sample over time.

For this experiment all three parts were turned on and the device was doing a regular wide spectrum measurement. It is visible that after around 120 seconds (D) the stripe is fully formed. The effect starts in the top left and propagates following a large circle shape to the lower middle which makes it seem like it is caused by an impact on the sample at a very shallow angle coming from the top left.

Since the effect is connected to the lithium content on the surface of the sample it is most likely caused by electron induced lithium plating, an effect where an electron beam can be used to cause lithium ions from deeper within the sample to be transported to the surface and deposit there as metallic lithium [176, 230]. This effect alone however can not explain the shape of the stripe. The inherent design of the CN system inside of an XPS device should ensure that the coverage of the electrons on the surface is as homogeneous

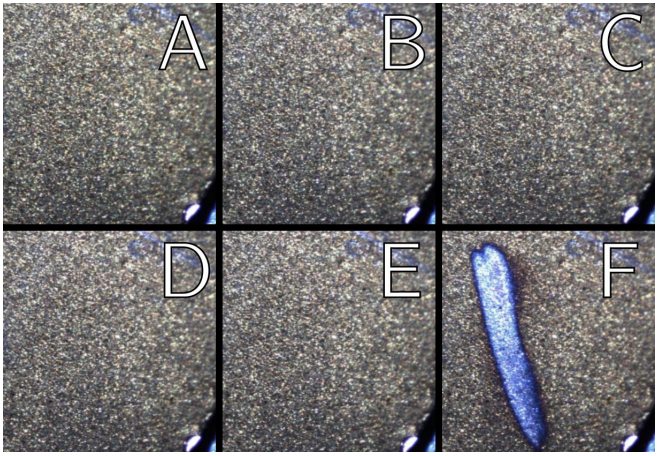

Figure 3.35: Stripe experiment on fully charged anode with different measurement modes: (A) as received (B) 10 min X-Ray (C) 10 min CN (D) 10 min X-Ray and CN (E) X-Ray and analyser (F) X-Ray, analyser and CN

as possible to avoid local charging of the surface. Figure 3.37 shows the schematic of the CN and measurement unit in the Kratos AXIS XPS device that was used in this thesis.

Since the Kratos device does not utilize highly focused X-rays a simple charge compensation system is sufficient. This system consists of a filament that can be heated to emit electrons using the thermoionic effect mounted above the sample and a charge balance plate that is used to give those free electrons some kinetic energy [157]. The magnetic lens underneath the sample that is part of the analyser can then be used to focus these electrons on the analyzed point on the sample. This works since electrons in a magnetic field are subject to a magnetic force perpendicular to their initial movement vector that makes them follow a spiral pathway towards the sample. This motion also causes the electrons to hit the sample from all possible directions avoiding charging due to topological shadowing [157]. This spiral movement may be an explanation why the stripe appears following a curved path on the surface. It is however not clear why the center of the circle that the

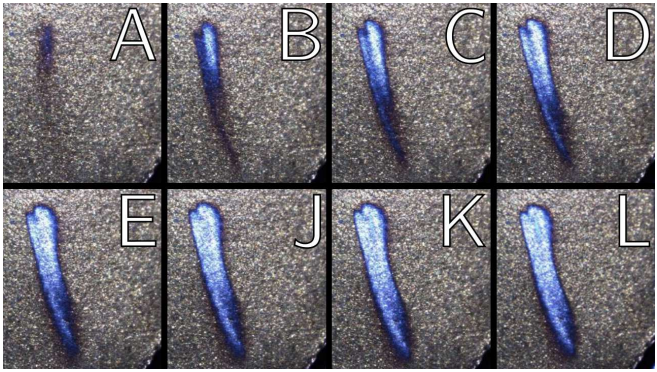

Figure 3.36: Stripe evolution on the plated anode over time with (A) after 30 s and followed by 30 s steps until (L) after 240 s in full measurement mode with all three parts on

stripe effect would close is far outside of the area of sample since according to the data from Baer et al. [157] the spiral helix should focus the electrons on the center of the sample where measurement takes place. And it is also not possible to explain the strong localization of the effect since all electrons hitting the surface should have similar energies obtained from the acceleration caused by the charge balance plate. Some electrons could have more energy due the thermoionic generation energy distribution but these electrons would also be randomly distributed onto the surface and not clustering in one location. It looks like not all electrons hitting the surface can cause this effect, which means that the effect could on the one hand being coupled to the energy of the electrons. These electrons hitting the affected region would have gained more energy than the electrons hitting the other regions for some reason. On the other hand the effect could also be linked to a non-uniform distribution of the electrons hitting the surface and the affected locations are hit by more electrons than the rest of surface and are subsequently charged up, causing this reaction. The second theory is more likely since there is no obvious way for the electrons to gain more energy and then for only those electrons having more energy to hit one specific spot.

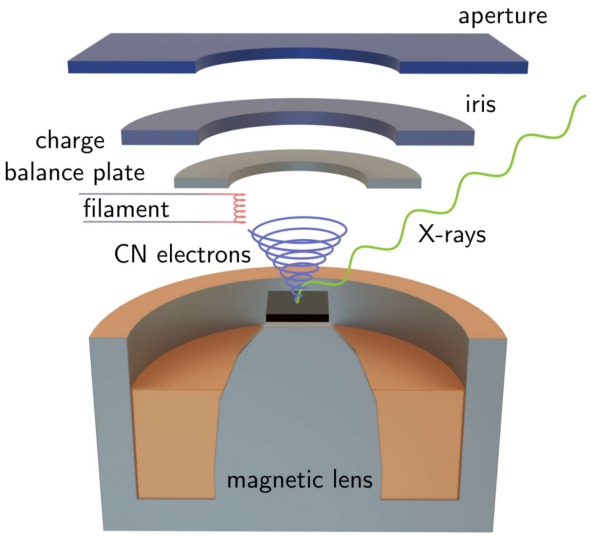

Figure 3.37: Schematic of the Kratos AXIS XPS spectrometer charge neutralization (adapted from [157])

This assumed localized surface charging could also not disperse easily since the SEI covered surface has a very low conductivity.

To further investigate the effect in the next experiment multiple stripes were created on the surface of both samples and then the spectra were measured before and after the striping as well as after a 2 day pause to see the change of the stripes over time. Figure 3.38 shows the optical change on the plated sample (top) and fully charged sample (bottom).

The change in hue in the images after striping for both samples (B and E) is due to the camera automatically changing its white balance and not an effect of the experiment. Due to this automatic white balance adjustment it is hard to identify any changes in the color of the sample. It is however easily visible in B and E that there are two distinct areas for each stripe. In the center of each stripe a lighter, less saturated area is visible, while the

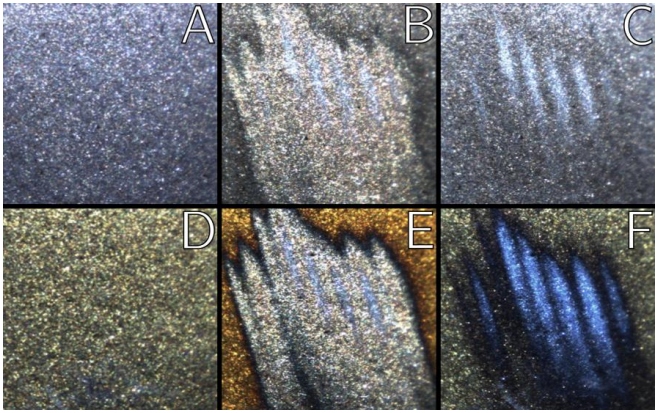

Figure 3.38: Creation of multiple stripes on the plated sample (top) and fully charged sample (bottom). (A) and (D) initial condition, (B) and (E) after the stripe creation, (C) and (F) after two days

area around this core seems to have a sightly more warm hue. There is also a dark coloration at the edges of the stripes. In C and F it can be seen that the effect somewhat diminishes over time, which could be the metallic lithium reacting with gas traces inside of the vacuum chamber or with some parts of the SEI.

If the effect is in fact electron induced plating, it should not occur on fully discharged samples that have not been plated, and the effect should also not occur if the sample is insulated and thus has a floating potential. To test this hypothesis one sample was taken from discharged, non-cycled cells of each type and one was taken from a plated cell of each type. These cell have been obained and cycled about 6 months prior to opening and have been stored at 30% SOC as described in the beginning of this chapter. This means that the plated cells are not freshly plated like the example visible in figure 3.34 but had ample time for any reversible lithium plating to diffuse into the anode.

So the only additional lithium in plated cells compared to the non-plated cells should be irreversible metallic lithium depositions that completely lost contact and the additional lithium embedded in the different components of the thicker SEI layer.

To capture the striping process the sample was recorded on video during the experiments. During the recording of a spectrum the device repeats the same measurement two times and then averages the result. Interestingly it was also visible in the video that the two consecutive measurements of the same sample showed deviations in some of the detail spectra likely showing the effect of the striping on the measurement results. These spectral results will be discussed later in section 3.3.3. Figure 3.39 shows the changes in the non-plated (fresh) samples before (top) and after one full XPS measurement with CN on. Figure 3.40 shows the same measurement on the 6 plated samples.

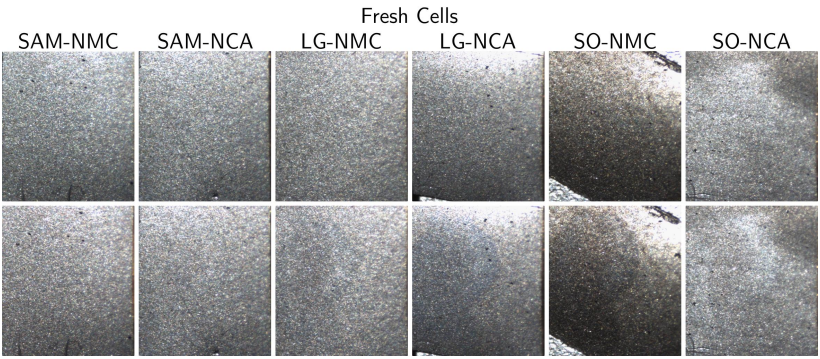

Figure 3.39: Optical change of all 6 fresh tested cells after a full measurement with CN on (before: top / after: bottom)

In figure 3.39 it is visible that this does not only occur in plated or fully charged cells but can also be faintly visible in fresh discharged samples. Not all samples show the effect, but some changes are visible in the LG-NMC, LG-NCA and SO-NMC samples. It is also noticeable that the shape of the effect is much wider and more spot-like compared to the previous experiments. The spot however is still on the left side of each sample and propagates

into a similar direction as before. It is visible by also looking at the plated samples (that all show the effect at different levels) that the shape of the spot is consistent over all samples and thus seems to be rather dependent on the setting during the measurement than any properties of the sample. It could be that the difference in distance of the samples to the filament has an influence on the shape.

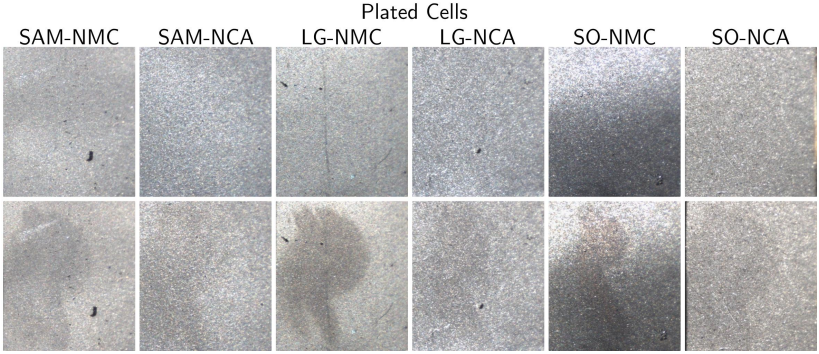

Figure 3.40: Optical change of all 6 plated tested cells after a full measurement with CN on (before: top / after: bottom)

All plated samples in figure 3.40 show the effect at varying intensities but much weaker than with the freshly plated samples used in the previous experiments. In the case of the LG-NCA cell it is not clear if the fresh sample or the plated sample show a more distinct effect. An explanation for the behaviour could be that in the freshly plated samples lithium metal is still present in the area of the SEI in metallic form or low energy bindings and can be pulled to the surface with the electron inducted plating. In the samples that have been rested for 6 months on the other side all lithium has either diffused into the anode or formed more stable compounds within the SEI over time. It is not clear why the effect is also visible in the fresh samples in figure 3.39 but it could be that different additives or components of the electrolyte facilitate different compounds within the SEI that may be more susceptible to the effect than in the other cells.

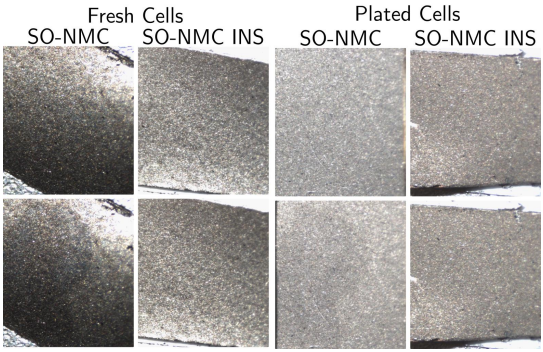

Figure 3.41: Comparison of the surface changes of a full measurement with CN on insulated samples of the fresh and plated SO-NMC sample (INS denotes the insulated samples) (before: top / after: bottom)

Figure 3.41 shows the comparison of insulated vs. non-insulated samples of the SO-NMC cell. The insulated samples have been attached on the surface of the sample holder using double sided tape and the are thus electrically insulated. This creates a floating potential within the anode and thus should inhibit the electron induced plating effect in the samples. For both insulated samples no change in the surface can be observed. This is another indicator that the effect observed is the electron induced plating effect since it requires the sample to be grounded for the effect to occur. The spectra of all the samples are investigate in the next section.

3.3.3 Influence of Sample Washing and First Spectral Analysis

Washing the samples taken from the battery with an appropriate solvent is often done prior to sensitive experiments [14, 54, 86, 124, 156, 162, 231, 232]. This is done to remove any battery electrolyte residue or electrolyte salt rests from the surface of the samples [233]. The solvents used for washing are often the same or similar to the solvents used in the electrolyte (e.g. DMC). Mussa et al. however specifically mentions that washing can dissolve parts of the SEI and does not recommend washing the samples after removing them

from the battery. In this case washing can falsify the measurement results since the layer is not in the original sample state anymore. Somerville et al. [231] did a study on the effects of washing on the surface film of graphite electrodes. They report that some authors could detect a higher sensitivity to atmosphere after the washing, which could be explained by the removal of a passivating surface film (this effect was also observed in [232]). The paper itself focused on the ratio of VC in the electrolyte, an additive commonly used in LIBs to improve the formation of a stable SEI. They postulate that the washing removes the salt and the low boiling point solvents present in the surface layer (in this case EC). Samples with different VC ratios from 0 to 6 vol.% have been prepared by them and analyzed using XPS, SEM, attenuated total reflectance (ATR) and fourier transform infra-red spectroscopy (FTIR). They found two different films dependent on the VC concentration with the two films showing a different SEM image as well as different behaviour in the material composition. The low VC concentration film in contrary to the higher concentration film is also very sensitive to the washing process and for this film not only the salt deposits are removed but also LiF and Li_xPF_y which can only be found in the deeper layers of the SEI. Their results show clearly that whether washing it useful or not strongly depends on the composition of the electrolyte. Andersson et al. [173] report a removal of LiF from the surface by washing in DMC, although LiF is not solvable in DMC and conclude that the LiF depositions are rather loose crystals on the surface than integrated into the SEI.

Additionally there is very little information in literature in what way the washing process is performed. Bach et al. [14] soaked their samples for a total time of 1.5 h changing the solvent bath in between, while other authors don't give any specifics.

For the experiment in this work commercials cells have been used, so it is not possible to obtain any data about the composition of the electrolyte since battery producers generally do not make their internal electrolyte recipes public to the competition. For this reason it could not be determined beforehand whether washing the electrodes before testing is beneficial or harmful. So in the first test run measurements of one washed and one none-washed sample from each battery anode where analyzed and the results have been

compared. The samples have been washed in two DMC baths for about 30 seconds each and then dried for one hour in the glovebox at less than 5 ppm moisture and oxygen content before they were mounted to the sample holder and transferred to the XPS device. The short washing time was chosen to see whether a short wash was already influencing the measurement results.

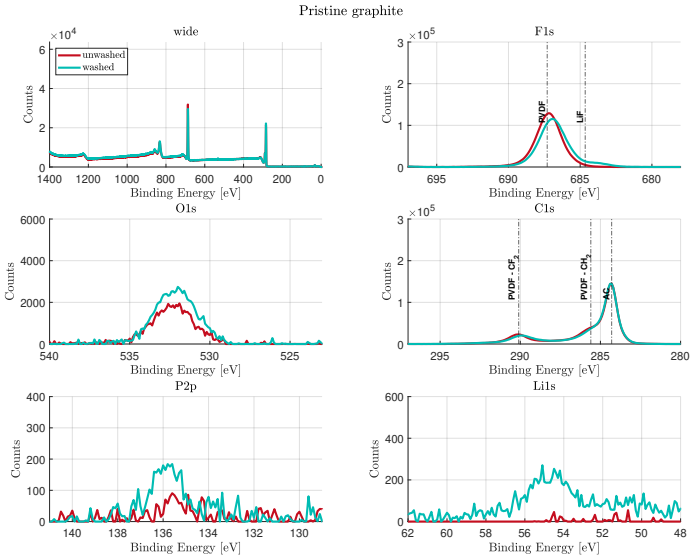

Figure 3.42: XPS spectra of a pristine graphite anode (Sample A) with no SEI. Comparison between the washed and unwashed sample (Shift: 0.0 eV)

Figure 3.42 shows the measurement result for the pristine graphite anode (sample A) that was not inside of a cell prior to the measurement and thus not in contact with any electrolyte prior to the washing. No shift of the spectrum was necessary since the reference peak at 284.3 eV for AC was already at the expected location. This was to be expected, since the graphite should have a good conductivity that prevents the surface from charging up and causes a spectral shift. It is visible that the washing is this case is adding material

to the surface. The signals for P2p and Li1s become stronger after washing, but they are both still very weak. The signal for F1s gets a small shoulder and the O1s is also increasing. The occurrence of P and Li seems to be the effect of cross pollution between the samples since they have been washed within the same electrolyte bath and likely the salt from the other samples ($LiPF_6$ and/or LiF) was deposited on the surface. Cross contamination in the glovebox in general can also not be ruled out as a source of these signals, since the other cells have also been opened in the glovebox before. The increase in oxygen can not be explained by the salt and may be caused by a reaction of the graphite surface with the electrolyte. The expected carbon peak is clearly visible at around 284.3 eV with another carbon peak at 290 eV. The usually used AC peak is at the same position as the graphite peak of the anode active material. Since there should be no SEI on the surface of the sample the second carbon peak is most likely caused by the PVDF binder in the anode since that is located at around 290 eV with another peak at 286 eV which would also explain the shoulder of the carbon peak [161]. The large peak of the fluorine can also be attributed to the binder [163], while the small shoulder at slightly lower energies is probably caused by the above mentioned contamination, also creating small amounts of LiF on the surface, with an F1s peak at around 685 eV. The F1s peak of the $LiPF_6$ is not visible, which may be due to the overlapping stronger PVDF peak that is only 1 to 2 eV higher. It is visible that all peaks are in good accordance with the literature values. The only position slightly off is the P2p peak, which is most likely a measurement error due to the very low signal strength. The test on pristine graphite was performed to analyze the effect of washing on a surface without SEI and the results show that there seems to be at least some interaction of the washing reagent with the graphite surface and that cross-contamination can happen easily even with the very low amounts of original battery electrolyte that stay in the washing solution.

In figure 3.43 the spectra for a fully discharged anode (sample B) are visible. Contrary to sample A the material is taken from a commercial cell and thus has a fully formed SEI. The energy scale was in this case shifted by 1.5 eV to calibrate it to the the AC peak at 284.3 eV. Compared to the graphite of sample A the surface should have a very low conductivity so

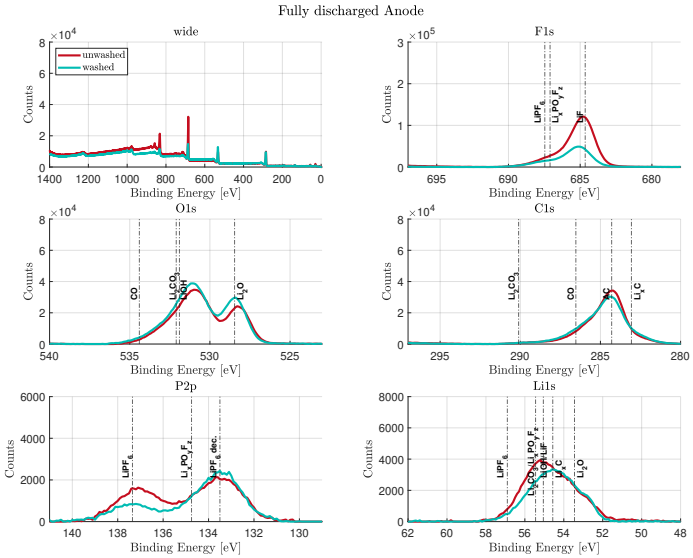

Figure 3.43: XPS spectra of a fully discharged graphite anode with no plating (Sample B). Comparison between the washed and unwashed sample (Shift: 1.5 eV)

a shift in the spectrum was to be expected. The surface charges up positively because electrons are removed in the form photoelectrons and this slows down further emitted photoelectrons reducing their kinetic energy. A reduction in kinetic energy means a shift to higher BE since the device then assumes that more energy of the X-ray was spent to remove the electron from its binding, leaving less energy to be turned into kinetic energy. The compounds of the SEI should be visible in the spectra and these compounds could potentially damaged or altered by the washing process. The active material and binder visible in sample A should not show up in the spectrum of sample B, since even the SEI of a fresh cell should be much thicker than the penetration depth of the XPS X-ray beam. The cell went through one full cycle before disassembly. In the full spectrum it is already visible that the

changes caused by the washing are lager than for sample A. In the spectrum a mixture mainly consisting of $ROCO_2Li$, Li_2O, LiF and Li_2CO_3 is expected on the surface according to the literature possibly with LiOH contamination due to moisture exposure during the transport, and $LiPF_6$ expected to show up in the spectrum before washing. It looks like most of the surface is covered with the salt remains before washing and mainly consists of LiOH and Li_2O otherwise. The shoulder of the carbon peak is assigned to carbon in a one oxygen environment that is often found as part of the AC surface contamination since no part of the PVDF should be visible on the surface of the SEI. The P1s peaks are assigned to the $LiPF_6$ salt residuals as well as phosphorous $LiPF_6$ decomposition products. The strong peak for LiOH most likely stems from surface contamination due to moisture exposure during the transfer from the glovebox to the measurement device. It is surprising that the peaks don't shown any $ROCO_2Li$ on the surface of the SEI, since in literature the top layer of the SEI is theorized to mainly consist of anorganic compounds as discussed in chapter 2.2.1. It could be that the high amount of Li_2O also stems from contamination with atmosphere similar to the LiOH contamination. After washing, the amount of $LiPF_6$ on the surface is reduced, as expected, but at the same time also the amount of LiF seems to be reduced drastically. This is rather unexpected, since LiF should have a very low solubility in the washing reagent [234]. This could mean that the washing process is removing a part of the SEI additionally to removal of the residual salt on the surface or that the LiF is present on the surface as more lose crystals, as discussed before, that do not get dissolved in the washing solution but are simply washed away.

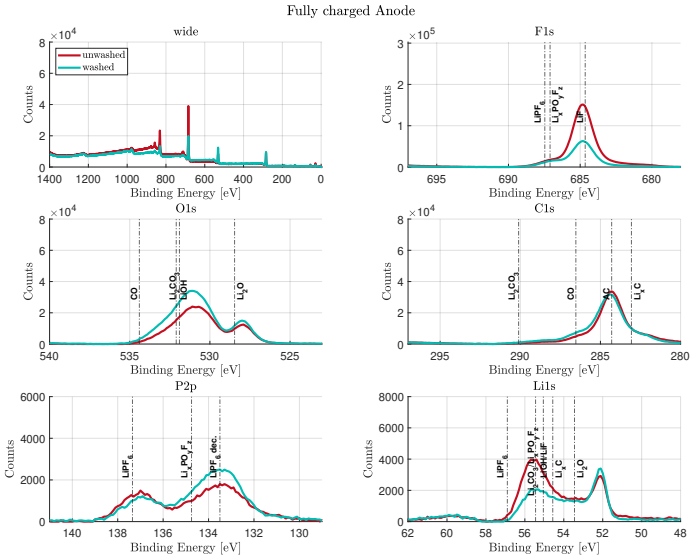

Figure 3.44: XPS spectra of a fully charged graphite anode with no plating (Sample C). Comparison between the washed and unwashed sample (Shift: −2.9 eV)

The first thing noticeable in figure 3.44 for the fully charged anode (sample C) is a change in the lithium signal compared to sample B, the shapes of the other signals are very similar to the discharged anode in figure 3.43. To compensate for BE shifting however the whole spectrum had to be shifted by −2.9 eV to fit the AC reference peak. In light of the electron induced plating effect discussed in chapter 3.3.2 the change of the shift from a positive value in the discharged sample to the charged sample can only be caused by the newly formed lithium plating on the surface. A possible explanation could be that the electrons emitted by the charge compensation device can now easily accumulate at the location of the measurement spot since the surface is covered in a conductive layer of metallic lithium allowing the electrons to flow freely. The underlying material may still be positively charged from the

beginning of the measurement before the surface layer was formed and so the electrons from a double layer on surface, charging the surface negatively, causing the negative shift in the spectrum since the leaving photoelectrons are accelerated further towards the detection unit. For sample B and C the SEI should have a similar thickness and composition, so the conductivity of the SEI should not be significantly different. The penetration depth of the XPS methods is very shallow, with only a few atomic layers and thus should not be influenced much by a charged or discharged anode underneath the SEI since only the top surface of the SEI should be measured. But as discussed in chapter 2.6.2 Oswald et al. [172] found that the SEI compound peak positions can be shifted when the underlying graphite is lithiated and they found a dependency of that shift on the level of lithiation. The discharged anode also showed a thinner SEI with a high Li(O)F content. The fully lithiated anode on the other hand showed a thicker SEI. Their greatest shift however was at around 3 eV while for the samples present in this work the shift between no lithiation and the fully lithiated samples is almost 5 eV. Except for the large shift that cannot be fully explained and the lithium signal the rest of the peaks show a similar behaviour to sample B, with the amount of $LiPF_6$ getting slighly reduced by washing while the amount of LiF is getting reduced much more drastically. The surface is again covered in LiOH and Li_2O. In this sample the LiO_2 could not only be caused by atmospheric exposure but also could be a reaction product of the freshly formed lithium film on the surface since this reaction can happen even in high vacuum due to the extremely high reactivity of metallic lithium with even trace amounts of oxygen [235]. The lithium signal on the other hand shows a very different shape compared to the discharged anode of sample B. The peaks for the LiOH and possible $LiPF_6$ decomposition products stay the same, but a completely new peak appears at around 52 eV. Together with the flat peak at around 60 eV this could be an indicator for metallic lithium, since metallic lithium can mostly be found at 52 eV to 53 eV [165, 176] with plasmon losses between 60 eV and 66 eV. The fact that the plasmon losses are not visible in the discharged sample supports this assumption. This result also strongly supports the theory of the electron induced plating since if this is in fact metallic lithium, this would mean that metallic lithium is

present in the top surface of the fully charged anode even if there was no prior detectable plating event.

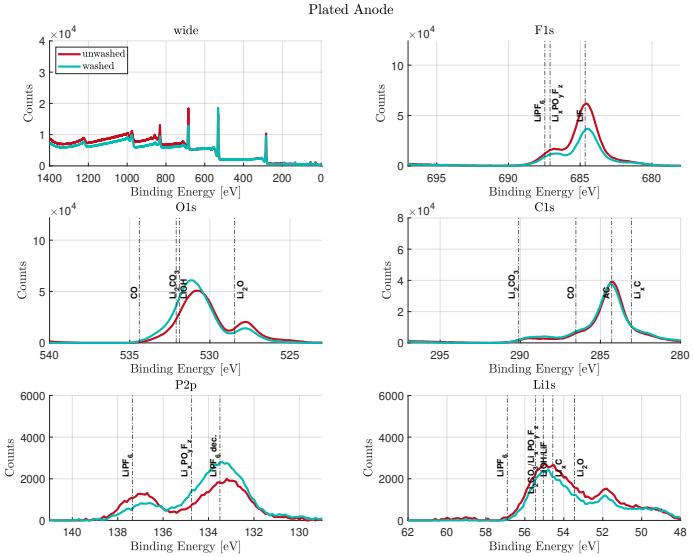

Figure 3.45: XPS spectra of the anode after 1 cycle of plating (Sample D). Comparison between the washed and unwashed sample (Shift: −2.9 eV)

The last sample with a plated anode (sample D) visible in 3.45 was also shifted by the same value as sample C (−2.9 eV) to the reference AC peak. Here the peaks again show a similar behaviour to sample B and C, except for the Li1s peaks. The presumed lithium metal is here also visible at around 52 eV, but the peak as well as the plasmon loss signal are lower than the signal of the fully charged anode. This points to the fact that the electron induced plating is capable of pulling the lithium out of the LiC_6 of the anode and not only dead lithium in the SEI or lithium from other SEI compounds. The question remains however whether the lithium that can be detected on the surface of the plated anode is also pulled from the anode or from dead

lithium caused by plating since it can be assumed that after discharging of the plated anode some reversible plating remained that could have caused the anode to not the be fully discharged by diffusing into the anode over time. Even though the cell was opened one day after the plating cycle and cell was kept at $-20\,^{\circ}\mathrm{C}$ in the temperature chamber until directly prior to the opening the diffusion of reversible plating into the anode can happen even if the cell is already dismantled and does not require the full electrochemical system of an intact cell. But since it was fully discharged the amount of remaining reversible lithium should be very low. Additionally there is also the diffusion inside of the bulk of the graphite anode material that would cause the reversible lithium diffused into the discharged anode to disperse inside the anode and only be present at the surface level with a very low lithium concentration. In conclusion it can not be proven which the source of the surface lithium caused by the electron induced plating truly is, and it likely is a combination of both but the discussion before points at a bigger part being dead lithium from the SEI rather than reversible plating that remained after discharging.

The results for the comparison of the washed versus the unwashed samples shows that while the washing seems to reduce the amount of $LiPF_6$ on the surface it also seems to change the SEI by removing a considerable amount of the LiF that should be part of the SEI and not a surface contamination. It is not really clear why the washing solvent removes a large amount of LiF since its solubility should be very low. It was also shown that cross contamination between the samples is to be expected unless the cleaning solutions are renewed for each sample. These points and the fact that the washing is not really improving the other signals in a significant way lead to the choice to not wash any further samples for the rest of the XPS experiments since the benefits are not really visible and a negative effect on the SEI is very likely.

Spectra Analysis of the Stripe Effect

In this part the spectra of the samples of the striping experiment are analyzed. Both cells are of the type LG FIB and are also the cells used for

the tests in chapter 3.3.3 and that will be analyzed utilizing argon depth profiling in chapter 3.3.4. For the full cell as well as the plated cell a stripe on the surface was created using the combination of options discussed before with activated charge compensation and magnetic lens. For each sample one spectrum was recorded before with no stripe on the sample while the magnetic lens was turned off, so that no stripe was created on the sample. Then the stripe was created by turning the magnetic lens on together with the CN. Then another measurement was done on the location of the stripe with the same settings as the first measurement. Finally the last measurement was performed 2 days later with the sample remaining under high vacuum for the whole time to see how the surface is changing over time. All measurements have much lower electron counts than the spectra recorded in the previous chapter. This is due to the magnetic lens being turned off. The magnetic lens is used to focus the electrons into the analyser. If the magnetic lens is turned off, only a fraction of the photo-electrons reaches the analyser, reducing the signal strength of the resulting spectrum.

Figure 3.46 shows the three measurements for the sample of the fully charged anode. In the original condition (light blue) it can be seen that the surface manly consists of LiF, either LiOH or Li_2CO_3 as well as some $LiPF_6$ together with its decomposition products. The AC peak is clearly the highest peak in the C1s spectrum. A small amount of LiO_2 can also be seen in the O1s detail spectrum. In the Li1s detail spectrum almost no peak at 52 eV is visible, as well as no plasmon loss hinting at lithium on the surface. The visible LiO_2 could be due to normal amounts of LiO_2 in the SEI. Compared to that the second follow up measurement on the location of the stripe (grey) shows a very different spectrum. All previously found surface compounds are reduced, except for LiO_2 and a newly formed lithium peak at around 52 eV that could be metallic lithium. This is to be expected for electron induced lithium plating since the newly formed metallic lithium layer is covering the surface and thus reducing the signal strength of all other surface compounds except for LiO_2 that immediately starts forming on the surface of the lithium metal freshly deposited on the surface of the sample. In the check-up measurement after 2 days (red) that was also performed on the location of the stripe more of the compounds found in the first measure-

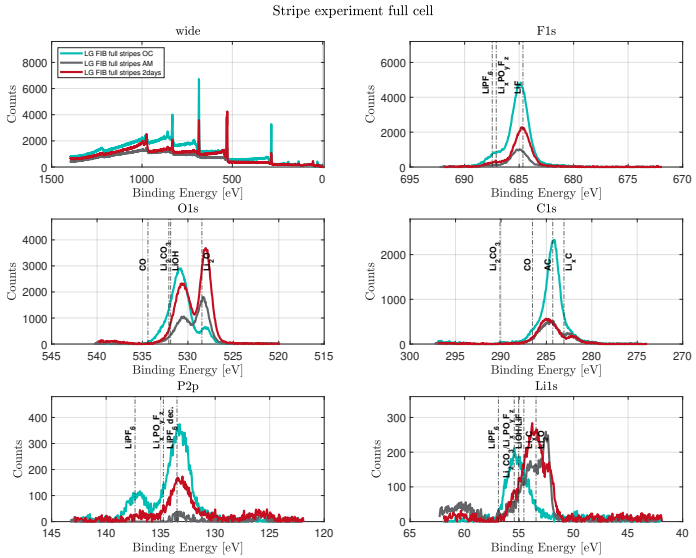

Figure 3.46: XPS spectra of the full anode: original condition (OC), after measurement (AM) and after 2 days under high vacuum. (Shifts: OC −3.0 eV, AM −2.7 eV, 2 days −3.1 eV)

ment can be detected again. The signals for LiF, LiOH or Li_2CO_3 as well as $LiPF_6$ and its decomposition products are stronger again, only the AC peak does stay at the same level. There is also further strong increase in the amount of LiO_2 which is to be expected due to the continuous reaction of trace oxygen with the surface lithium metal.

In the lithium spectrum the 52 eV lithium peak as well as the plasmon peak are diminished compared to the second measurement but still higher than in the measurement of the original condition. This also makes sense since the lithium is transformed into LiO_2 and thus the amount of measurable lithium metal on the surface must decrease. The peak corresponding to LiO_2 in the lithium spectrum is also higher than in the second measurement.

The fact that the level of AC are not increasing anymore leads to the conclusion that the increase of the LiF and $LiPF_6$ decomposition products visible in the last measurement are not the same that were visible in the first spectrum but rather newly formed products on top or within the metallic lithium layer due to salt rests on the surface that may react with the metallic lithium and any trace gases in the vacuum chamber.

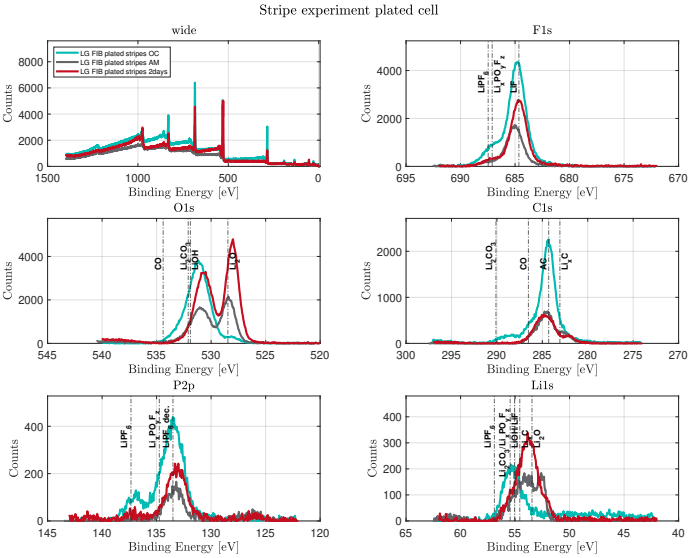

Figure 3.47: XPS spectra of the plate anode: original condition (OC), after measurement (AM) and after 2 days under high vacuum. (Shifts: OC −2.9 eV, AM −2.5 eV, 2 days −3.0 eV)

For the plated sample in figure 3.47 the result looks very similar to the full cell. The only noticeable differences are a higher peak for $LiPF_6$ decomposition products in the P2p peak in the follow up measurement on the stripe and a smaller peak for the surface lithium created by the electron induced plating. This difference in the $LiPF_6$ decomposition peak hints at a different composition of the SEI on the plated cell compared to the full cell

that experienced no plating. A smaller lithium peak is to be expected since the lithium content close to the surface of the cell should be lower than in the full cell. Other than these two differences the trends of the spectra look identical.

In conclusion all results strongly point at the electron induced plating effect as the result of the creation of the stripes. It not clear however, as discussed before, why the effect only locally appears on the surface when the electron source of the charge compensation should be designed in a way to disperse the electrons on the surface of the sample in a homogeneous matter.

Since the electron induced plating effect is linked to the samples not being insulated during the experiments [230] to further proof that the changes in the surface are in fact caused by lithium on the surface, a plated and a non-plated sample of the SO-NMC cell have been attached to the sample holder using double sided tape to insulate them during the measurement. The optical results of this experiment have already been shown before in Figure 3.41 and no optical change was visible in the insulated samples. Here the spectra are analyzed as well to see if the spectra do not show any change compared to their not insulated counterparts either. Figure 3.48 shows the comparison between the insulated (red) and non-insulated sample of a fresh anode. Figure 3.49 shows the same comparison for the plated samples.

It is visible in figure 3.48 and 3.49 that there are significant differences between the insulated and the non-insulated samples. Both spectra show very similar behaviour to the spectra discussed before in the striping experiment. The non-insulated samples that are influenced by the electron induced plating effect show weaker signals for all spectra except in the area of 52 eV in the Li1s detail spectra and the LiO_2 peak in the O1s spectra again most likely caused by the coverage of the surface with lithium metal blocking the X-ray beams from reaching the original SEI compounds underneath. This result was expected for the plated sample but it is unexpected that the spectra also show such a strong difference for the new sample that has a lower lithium content. Since this sample was fully discharged before cell opening that must either mean that even in a fully discharged cell lithium remains in the anode that can be affected by the electron induced plating effect or that there are compounds inside the SEI apart from the irreversible depositions

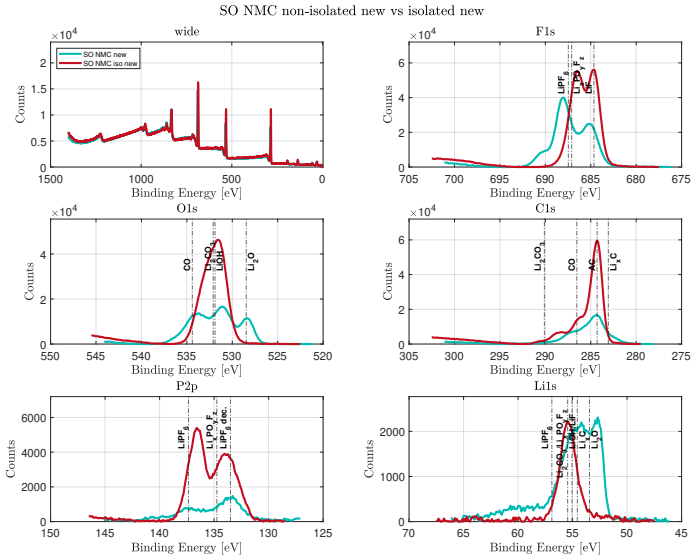

Figure 3.48: XPS spectra of the new anode: not insulated vs. insulated (Shifts: not insulated 1.1 eV, insulated 2.5 eV)

of electrochemically dead lithium metal left by lithium plating that can be affected the effect even though the lithium is part of a compound in the SEI.

It also has to be kept in mind that the sample of the new cell was subjected to calendar ageing at room temperature for one year before the cell was opened. This could meant that the samples used for the previous stripe experiments had a thinner SEI and also have a different composition of the SEI.

Unfortunately the influence of the striping effect on the measurement results was only understood later into the measurements and in the following analysis of the depth profiling as well as the spectra of the cells if different manufacturers all samples have been grounded and thus subjected to this effect, which was changing the measurements results. Due to limited access to the XPS device the measurements could not be repeated so the implica-

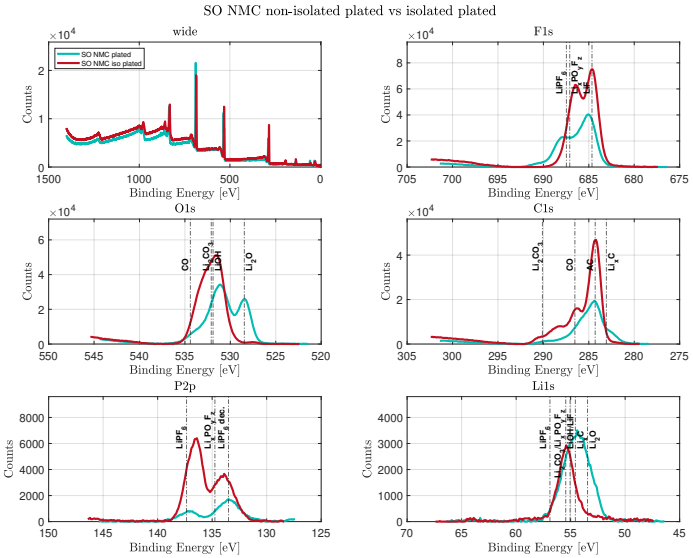

Figure 3.49: XPS spectra of the plated anode: not insulated vs. insulated (Shifts: not insulated 1.4 eV, insulated 2.4 eV)

tions of the effect will be kept in mind during the analysis and all results will be treated accordingly. With the knowledge of the effect occurring during the measurement the results can still be analyzed in meaningful way and the amount of lithium that was deposited on the surface during the measurement can be seen in the lithium peak as well as the LiO_2 peak and can be a very helpful indicator of how much available lithium is close to the surface area of the samples. The electron induced plating could be used in the future in a controlled way to pull the lithium that is bound in less strongly from the SEI to surface without the need for depth profiling. For this it is important however to understand which forms of lithium can be pulled to the surface.

3.3.4 XPS Depth Profiling

In this chapter the resulting spectra for the etching experiments are analyzed. The samples used for the etching experiment are the same samples as used for the comparison of washed vs. unwashed samples in chapter 3.3.3, namely a pristine sample and one fully discharged, one fully charged and one plated samples of the LG-FIB cell. The etching was done on the unwashed samples as discussed in chapter 3.3.3. Goal of the depth profiling was to remove the SEI layer in steps to estimate a distribution of lithium within the thickness of the SEI. The procedure was done for all samples except of the plated sample in three steps with Ar^+ ion sputtering with an Energy of 20 keV on an area of 1.4 mm times 1.4 mm. The etching time was increased with each etching step, with the first step being 2 min, the second step 18 min and the final step 90 min for a total etching time of 110 min. The highest time was chosen to the point when the graphite peak of C_6 stopped to change, meaning that the SEI was fully removed and only the bulk anode material is measured. For the plated sample additional etching steps have been added since the surface composition after 110 min was not indicating that the SEI was fully removed since the carbon peak did not reach the height of the other samples. Additional 90 min steps have been added until the graphite peak was not changing significantly anymore. For this sample the total etching time reached 560 min. On all samples it has to be assumed that electron induced plating took place during the measurement, as discussed in the chapter before, which transported a part of the lithium in the SEI and in the surface regions of the anode material towards the surface of the SEI since the samples have not been electrically insulated during the measurement. This means that from these measurements it will not be possible to precisely identify the location of the lithium in within the SEI but knowing that the effect occurred the amount of lithium and the difference in the surface composition can still lead to meaningful results.

The real achieved etching depth could not be measured since the change on measurement point was too shallow for the LSM to detect so it can only be estimated. The SEI of the fully charged and discharged samples should be in the low nanometer range up to 120 nm as discussed in chapter 2.2.1. The cell

that was subjected to one cycle of plating should have a slightly thicker SEI that could be up to 1 µm, estimated from the FIB measurements done on a cell of the same type shown e.g. in figure 3.6. This thickness is still much lower than the surface roughness caused by the anode graphite particles that have a size in the 5 to 25 µm range. An estimation of the etching depth from the energy of the beam is difficult because the SEI contains a variety of different compounds that are removed at different speeds and whose locations in the SEI are not clear. In the literature Oswald et al. [172] estimated their sputtering depth by using SiO_2 based sputtering rates and sputtered with 0.7 and 3.5 nm min^{-1}. Using the mean of these value of about 2 nm after 110 min a depth of about 220 nm was reached for the non plated samples, which is in good agreement of the estimated SEI thickness of about 120 nm and should have finished etching through the whole SEI. For the plated sample after 560 min a depth of 1120 nm would have been reached, which also is in agreement with the estimated plating SEI thickness.

It also has to be kept in mind that the argon etching process is not destruction free and that the composition of the SEI measured may differ from the actual composition since the beam could alter the chemical composition of the SEI compounds. Shiraishi et al. [166] e.g. showed that prolonged sputtering with Argon lead to an significant increase in LiO_2 content.

Spectral Analysis

In this part the measured spectra for the etching process in all four samples will be analyzed. The first Figure 3.50 shows the spectra for the pristine sample that was not inside of a battery and thus has no SEI layer on the surface of the anode.

For this sample it is expected that the etching is not changing the surface much since it should only remove some surface contamination from handling the samples inside the glovebox in the close proximity of the other samples take enout of the battery. Looking at the spectra it is visible that there is no P2p or Li1s signal whatsoever and that the O1s is very weak and not changing much during the etching process. This is to be expected since the sample should only contain C_6 and some binders and possibly additives

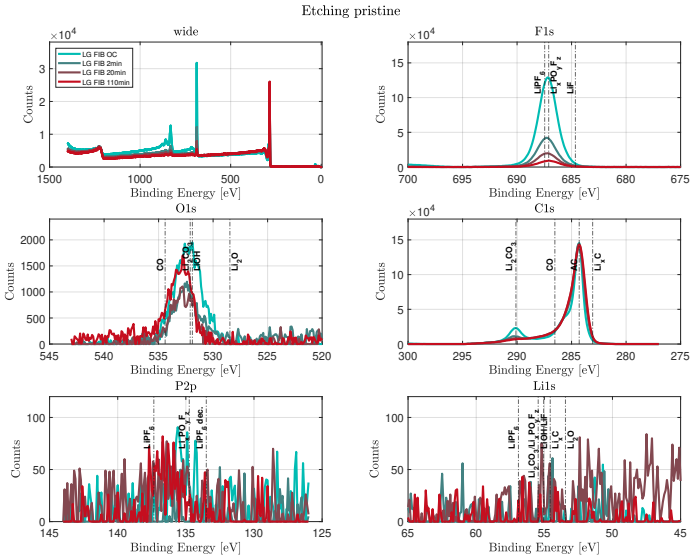

Figure 3.50: XPS spectra of the pristine anode (Shifts: No shifts were necessary since the sample had no insulting SEI on the surface)

that are not known. The main peak in the C1s signal is also not changing except for the small peak at 290 eV that can either be part of the PVDF binder (compare figure 3.42) or Li_2CO_3. In the case of the pristine sample it is most likely the PVDF binder. The same is visible for the big peak in the F1s detail spectrum. This could be some $LiPF_6$ contamination, but is most likely the fluorine peak of the PVDF binder. Even though the binder should be present in the whole bulk of the anode material, it makes sense that the binder is removed almost completely in the measured etching area since the binder is mostly present between the particles and because of its organic nature more easily etched away by the high energy argon beam than the C_6. This effect is also increased by the topology of the surface where completely removing the whole carbon particle is almost impossible within the estimated etching depth since the particles are much thicker as discussed

above and thus only the binder is removed from the surface as well as the area in between the particles while a big part of the actual anode particles is still present even after the full etching time.

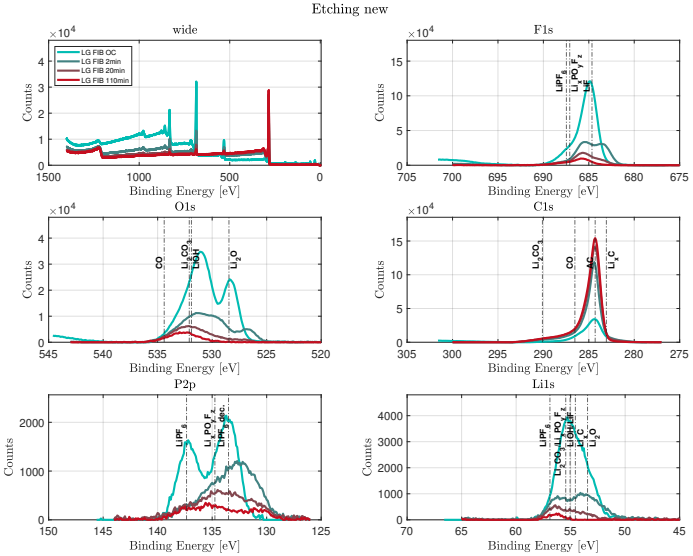

Figure 3.51: XPS spectra of the discharged anode (Shifts: original condition 1.6 eV, 2 min etching 0 eV, 20 min etching 0 eV, 110 min etching 0 eV)

In figure 3.51 the results for the discharged cell with no prior plating cycles are displayed. It is visible in the C1s spectrum that the AC or C_6 peak shows almost no change between the 20 min and 110 min etching step which means that most of the SEI layer was removed after 20 min of etching. This means that the thickness of the SEI on this sample should be in the range of 42 to 210 nm, using the estimated depth values discussed above.This value in thickness for the SEI is reasonable compared to the literature values. The intensity of the C_6 peak also drastically increased over the etching step, revealing more of the anode graphite underneath the SEI. All other elements

show a strong decline during the etching steps. There is no detectable lithium peak at 52 eV as well as no plasmon feature connected to metallic lithium. This is to be expected since there should be a very low amount of available lithium in the anode after a full discharge. $LiPF_6$ seems to be removed by the etching process first and its F1s as well as the P2P peak are almost fully disappearing after the first etching step. This is also logical since the $LiPF_6$ on the surface should mainly be salt rests from the remaining electrolyte on the surface that should make up the top layer. Looking at the shifts necessary to move the AC or C_6 peak at its appropriate position also reveals that the surface became much more conductive after only the first etching step, meaning that a substantial portion of the SEI was already removed after only 2 min of etching.

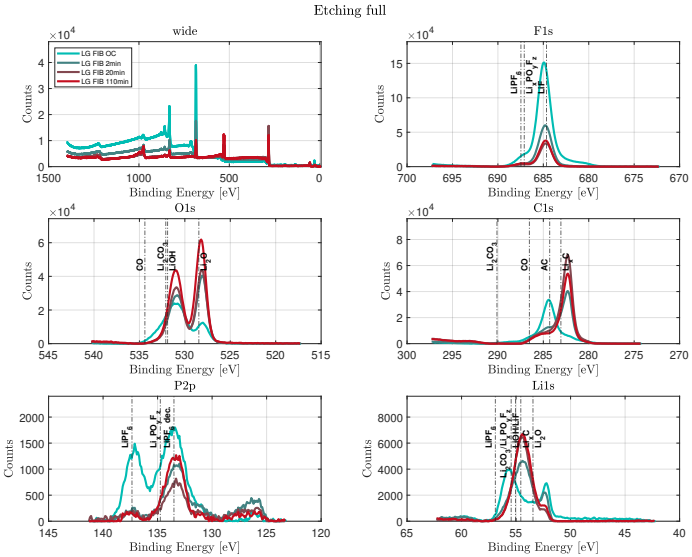

Figure 3.52: XPS spectra of the fully charged anode (Shifts: original condition −2.8 eV, 2 min etching −2.7 eV, 20 min etching −2.7 eV, 110 min etching −2.7 eV)

Figure 3.52 shows the result for the fully charged anode sample. In this sample electron induced plating is to be expected due to the high lithium content. The first shift was done towards the AC peak but in the deeper etching steps the AC peak is not the highest peak in the C1s spectrum anymore. Underneath the SEI lithiated carbon (LiC_6) is expected to show up. For this reason the shift in these measurements was performed towards LiF in the F1s spectrum at 684.54 eV instead of the AC peak, being the second easiest identifiable compound of the SEI. Compared to the discharged spectra in figure 3.51 a new peak appears in the C1s spectrum that is close to where LiC_6 is expected. The literature value from LiC_6 was not shifted in the initial analysis in chapter 3.3.1 since it was not visible in the first measurements so the location here is plausible. And while in the discharged sample all SEI compounds show lower signals after the etching steps, here the signals for LiO_2 as well as LiOH or Li_2CO_3 are increasing. The increase of LiO_2 is liked to the lithium pulled to the surface by the electron induced plating visible in the peak in the the Li1s spectrum at 52 eV and the corresponding plasmon feature. The reason for the increase in either LiOH or Li_2CO_3 on the other hand can not be directly linked to the electron induced lithium plating. It is possible that the lithium also reacted with trace amounts of humidity on the surface and in the vacuum chamber the same way it is reacting with trace amount of oxygen and forming LiOH. Additionally there is a peak in the P2p spectrum that has not been identified in any of the other measurements at around 127 eV that increases first and then diminishes again over the etching steps. The increase of the peak at around 54 eV in the Li1s spectrum can be attributed to the lithium peak of the LiC_6 that is revealed underneath the SEI. The diminishing intensity of the metallic lithium peak caused by the electron induced plating can be explained by the fact that the electron induced plating requires a non conductive layer on the surface of the sample so that a double layer can form that creates the electrical field that drives the lithium transport to the surface. Removal of the SEI layer also removes that insulating layer and thus stops the transport of lithium to the surface, hence the reduction of the lithium peak.

Since the SEI layer of a fully charged cell compared to a discharged cell should not differ in its chemical composition, the lithium pulled to the surface by the double layer must be lithium from the anode material itself.

It is rather unexpected that the shift is not changing much during the etching process. In the discharged sample it could be seen that the shift was becoming 0 eV after the first etching step since the SEI layer was removed and the underlying sample has good conductivity, preventing charge buildup on the surface. For the fully charged sample the shift stayed at the same value even though the spectra suggest that a substantial part of the SEI was removed from surface exposing the charge anode material that should also show good conductivity. It could be that the LiO_2 that is formed from the lithium metal pulled to the surface due to the electron induced plating effect is forming a thin non-conductive layer on the surface that is thin enough for the X-rays to make the underlying anode material visible in the spectrum but still insulating and as such causing the surface to charge. This is supported by the fact that even after the last etching step there are large amounts of LiO_2 detected on the surface, even more than in the original condition of the sample before the etching process was started.

It is furthermore notable that the shift for the fully charge sample is negative, while the shift for the discharged sample was positive. A positive shift is expected during a normal measurement unless the charge compensation is overcompensating since the photo-electric process ejects photo-electrons from the surface material leaving the surface positively charged and thus creating a positive shift. In the case of the fully charged sample however the shift is negative meaning that the surface is negatively charged. To cause the electron induced plating effect the surface needs to be charged negatively but the lithium ions recombining with the electrons on the surface to become metallic lithium should reduce the negative charge on the surface. And for the surface to become negatively charged in the first place the CN must be overcompensating to begin with. Then the question remains why the negative surface charging is no occurring in the discharged sample as well since the same mode of CN is used for both measurements.

Figure 3.53 shows the spectra for the plated sample. Here electron induced plating is also expected. As discussed before for this sample more etching

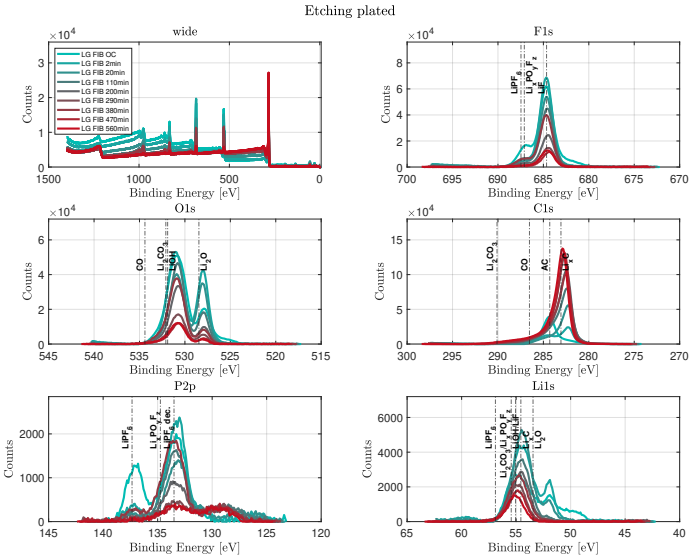

Figure 3.53: XPS spectra of the plated anode (Shifts: original condition −2.8 eV, for the etching steps from start to finish: −2.8 eV / −2.7 eV / −2.6 eV / −2.5 eV / −2.3 eV / −1.9 eV / −2.3 eV / −1.8 eV / −1.6 eV)

steps have been necessary to get to a point where the spectra show almost no more change between the etching steps. This is to be expected since the SEI should be thicker in the plated cell compared to the other samples, as shown in the FIB cross section in chapter 3.1. It is also notable that when trying to determine the shift of the spectra, it became apparent that similar to the fully charged sample in the C1s spectrum the AC peak was not the highest peak anymore after the first etching step and that in this sample also the LiF peak was used for the shifting of all measurements except the first one. Shifting towards LiF leads to reasonable spectra and also reasonable shift values that are comparable to the fully charged sample. The spectra for F1s, O1s and P2p follow mainly the same trend the spectra of the full

cell where following. Over the etching steps the species of the SEI layer dimish in the spectra, namely LiF, various $LiPF_6$ decomposition compounds, Li_2CO_3 and LiOH. Interestingly LiO_2 also diminishes, which is different to the spectra of the full cell, even though in the Li1s spectrum the peak for metallic lithium as well as a small corresponding plasmon feature are visible in the first four etching steps. Looking closely at the LiO_2 peak it is however visible that during the first etching step the peak is actually increasing but then starting to decrease in the following etching steps. This is also different to the fully charged spectra where the highest value was measured in the last etching step. It looks like the lithium available to be pulled to the surface is exhausted after the first four etching cycles, which would make sense since the amount of lithium available in the cell should only be the dead lithium in the SEI caused by irreversible plating as well as potential reversible plating that was not stripped during the discharge step before the cell opening and diffused back into the anode over time after the cell was opened. It is however unlikely that the residual reversible plating is having a huge impact on the amount of lithium available at the surface of the anode since the diffusion process should cause the lithium to be homogeneously distributed in the bulk anode material leaving only a small fraction of the already small amount of the non-stripped reversible lithium available close to the surface. This is however contrary to the peaks visible in the C1s spectrum. Since the cell is fully discharged underneath the SEI C_6 is expected but the spectrum show a strong signal for a charged anode material LiC_6 similar to the fully charged anode. It seems though that in the plated anode no more lithium is pulled to the surface after the initial four etching steps. It could be that in the fully charged cell a similar behaviour could have occurred with additional etching steps but unfortunately no more etching steps have been performed for this sample. The measured LiC_6 peak could mean that traces of reversible lithium in the anode are accumulated at the surface or that the dead lithium pulled out of the SEI layer is capable of diffusion back into the anode again, cause the surface anode material to become LiC_6. This should however over time disperse into bulk of anode and reduce the LiC_6 signal measured on the surface.

Comparing the spectra of the plated sample to the fully discharged sample from figure 3.51 it is clearly visible that not only the thickness of the SEI is changing when a cell is subjected to plating but that the spectra also show a difference in the composition if the SEI.

Looking at the change of the shift value over the etching steps it is visible that on average the shift becomes significantly smaller. This could be because in contrary to the fully charged sample the insulating LiO_2 layer on the surface is removed in the excess etching steps and larger fraction of the surface becomes more conductive be revealing more LiC_6.

It should be noted that all results presented here should be viewed very critically since shifts of individual compounds are possible in the presence of metallic lithium and even lithium intercalated in the anode material as discussed in chapter 3.3.1, causing distortion of the spectra, especially for insulating compounds. The etching process itself can also alter the structure of especially the organic compounds within the SEI leading to spectra that may not really represent to original state of the SEI layer.

3.3.5 XPS on Cells of Different Manufacturers

In this chapter the six cells of different manufacturers used by Jonack in her thesis [208] as described in chapter 3.1 are analyzed further using XPS to see whether the XPS results can be generalized for different cells. For the three manufacturers Samsung, Sony and LG one fresh cell that was only cycled for characterization and one plated cell have been opened, see table 3.1. For the Sony NMC cell SO-NMC additionally isolated samples have been measured, as discussed in chapter 3.3.2.

Comparison of all Cells

Figure 3.54 shows a comparison of the fresh samples of all six cells that not experienced plating. All cells have experience more than one year of calendar ageing at room temperature before disassembly at around 30% SOC. All samples have been shifted to allign their highest C1s peak with AC location. None of these samples have been insulated during the measurement, so electron induced lithium plating is possible.

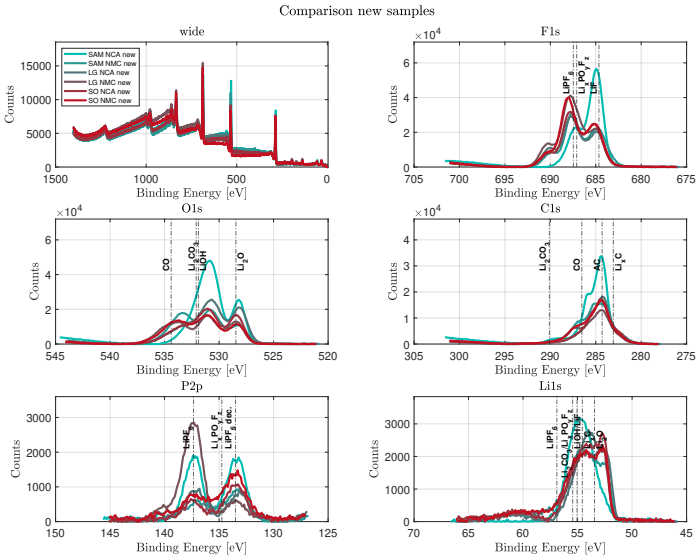

Figure 3.54: XPS spectra of all fresh samples (Shifts: SAM NCA 1.6 eV / SAM NMC 0.8 eV / LG NCA 0.9 eV / LG NMC 1.1 eV / SO NCA 1.1 eV / SO NMC 1.1 eV)

It is visible in the spectra that most cells show a similar shape. The most notable exception is the SAM-NCA cell that shows a distinctively different shape in all spectra. The cell has a much higher LiF content in the to SEI layer in the F1s spectrum as well as higher LiOH or Li_2CO_3 peaks in the O1s spectrum. The shape of the cells Li1s shape is also distinctly different from all other cells. All other cells show signs of lithium probably caused by electron induced plating on the surface. They all show a visible peak at around 52 eV and the corresponding plasmon losses. Interestingly the SAM-NCA cell still has the highest LiO_2 peak in the O1s spectrum normally also associated with this effect. It is not really clear why the non-plated cells also show electron induced plating even though they are fully discharged. It is possible that due the calendar ageing parts of the SEI contain lithium that

is bound in a form so that it can be accessed by this effect or that residual lithium that was not completely removed from the anode during discharge is pull out of the bulk anode, even though this is rather unlikely as discussed in the previous chapter.

Another notable difference in the spectra is the very high $LiPF_6$ peak for the LG-NMC cell in the P2p spectrum that could mean that this cell has an excess amount of $LiPF_6$ salt or some property in the electrolyte that makes the salt stick better to surface when the electrolyte is evaporation, since these samples have not been washed before analysis, as discussed in chapter 3.3.3.

The shifts of all cells are similar, with the SAM-NCA having the largest shift. This may be since if the surface composition of the SEI is differing from the other cells, the conductivity of the layer or the surface topology may also be different. The difference could also be caused by lithium pulled to the surface in the other cells, changing the surface structure compared to a normal SEI surface.

For the plated samples visible in figure 3.55 the most deviant cell is the SO NCA cell. For all the other cells not signs of metallic lithium are visible on the surface. There is no peak at 52 eV and also no plasmon loss peak in the Li1s spectrum. For the SO NCA cell there is a peak in the metallic lithium area but the peak is very broad and stretched and looks more like an artifact, especially since the cell also shows no corresponding plasmon losses. The LG-NMC also shows strong deviations in all other spectra that always extend beyond the other spectra in the the lower BE range. A particularly strong peak can be seen in the C1s spectrum where the peak for lithiated graphite should be. But this peak is also very deformed. It could hint at the fact that the cell was not fully discharged but then the plasmon losses in the Li1s spectrum should be visible. Apart from that some of the cells show a higher LiC_6 content on the surface in the F1s spectrum and slight differences in the LiO_2 and Li_2CO_3 and LiOH contents in the O1s spectrum. In their shift values all cells are very similar, all in the range of 1 eV comparable to the results for the new cells with on exception. The SO NCA cell shows a completely different shift of -1.9 eV which could be another indicator that there was some form of measurement error or mistake in the sample preparation since the non plated version if the SO NCA cell showed a shift similar

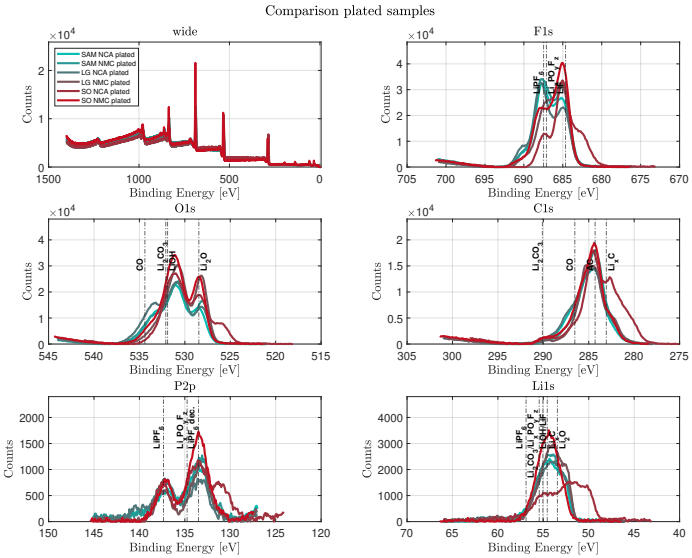

Figure 3.55: XPS spectra of all plated samples (Shifts: SAM NCA 1.0 eV / SAM NMC 1.1 eV / LG NCA 1.0 eV / LG NMC 1.0 eV / SO NCA −1.9 eV / SO NMC 1.4 eV)

to the other cells. The difference between the new and plated spectra will be discussed in more detail for each cell individually below.

Looking back at the capacity loss the cells experienced depicted in figure 3.7 the two cells with the highest plating loses, the Sony NMC and Samsung NMC both don't show any significant differences in their spectra to the other cells that could be linked to the increased capacity loss. The Sony NCA cell on the other hand is the cell with the lowest capacity loss and it shows a significantly different spectrum to the other cells in the plated spectrum. There is however no plausible explanation why the change in spectrum could mean a lower capacity loss during plating. If the spectra for this cell are really valid, it could be argued that for this cell a significant portion of the plated lithium diffused into the anode during the resting period and almost

no irreversible plating remained. But this should not be visible anymore in the spectra since the cells have all been charged and discharged at room temperature before disassembly to equalize their SOC.

Single Cell Spectra: Samsung

Figure 3.56 shows the comparison of the new and the plated spectrum of the SAM NCA cell. In the plated spectrum of the Li1s cell the possible lithium peak as well as a faint plasmon loss peak can be seen, while the spectrum of the new cell does not show this behaviour. This means that in the Li1s spectrum of the plated sample the expected behaviour for electron induced plated is visible. The spectra of the new cell also show higher peaks for almost all SEI contents in the F1s, O1s and P2p spectra, which is also to expected when the metallic lithium surface is covering the SEI. Unexpectedly however the spectrum of the new cell shows a higher LiO_2 peak than the plated one, contradicting the results of the Li1s spectrum.

The spectra for the SAM NMC cell, visible in figure 3.57 shows very similar shapes in all elemental spectra in the new as well as the plated measurements. The new cell shows slightly more C−O compounds while the plated cell has a higher LiF content. Non of the samples shows any surface lithium metal. This leads to the conclusion that the irreversible lithium plated during the plating cycles must be incorporated in the SEI layer in a form that is not accessible for the electron induced lithium plating.

The SAM NMC cell showed higher irreversible lithium losses than the NCA cell but regardless of the higher losses, the lithium in the NCA cells seems to be more accessible to the electron inducted lithium plating than in the NMC cell, even though the SEI layer of the NMC cell should have a higher lithium content in total. This leads to the conclusion that a higher total amount of irreversible plating does not necessarily lead to XPS with a higher amount of electron induced plating.

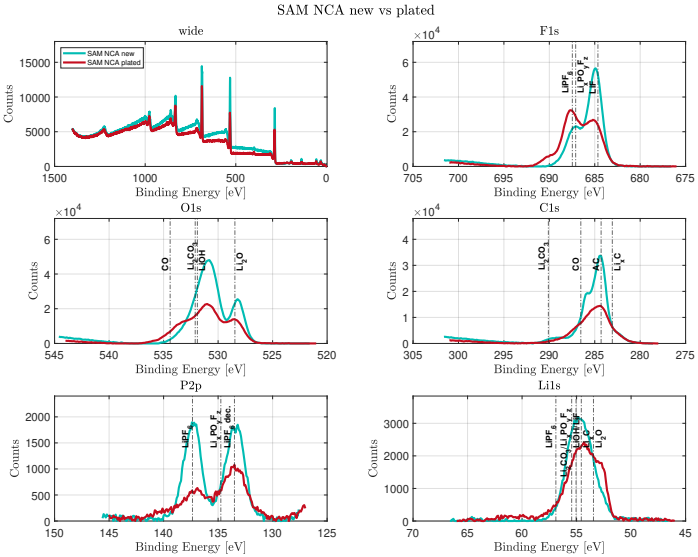

Figure 3.56: XPS spectra of the SAM NCA cell new vs. plated - Shifts: new 1.6 eV / plated: 1.0 eV

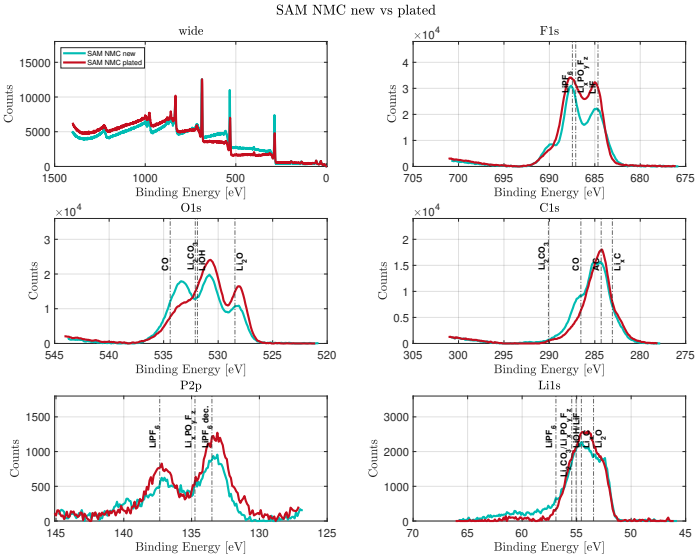

Figure 3.57: XPS spectra of the SAM NMC cell new vs. plated - Shifts: new 0.8 eV / plated: 1.1 eV

Single Cell Spectra: LG

Figure 3.58 shows the comparison of the new and the plated spectrum of the LG NCA cell. Here the spectrum of the new cell shows indicators of accessible lithium in the Li1s spectrum. Both the higher peak at 52 eV as well as a small plasmon peak are visible together with the increased LiO_2 peak in the O1s spectrum. The plated cell shows higher C−O content but other than that the spectra of the new and the plated cells are very similar. And the peak for the C−O is very smeared and overlayed by the AC peak, so it is not clear if there is any C−O present. In this case it might be possible that the lithium visible in the new cell is not lithium that remained from any plating event but lithium that was pulled out of the anode of the cell due to the cell not being fully discharged. The irreversible plating capacity loss of the LG NCA cell also was the second lowest of all cells analyzed so it could be possible that the difference visible in the Li1s spectrum is just an artifact caused by differently successfully discharges, leaving the new cell at a slightly higher SOC than the plated cell and thus leaving enough lithium in the anode to enable the electron induced plating effect. This would mean that to identify any lithium utilizing this effect it is important to fully discharge the anodes of all samples fully to avoid lithium from the anodes. In this experiment all cells have just been discharge with a 1C CC discharge. In future experiments it may be necessary to perform a full cc-cv discharge to remove any residual lithium from the anode.

In the LG NMC cell, visible in figure 3.59 both the plated and the non plated cell show a similar spectrum in the Li1s region. For both samples a peak in the metallic lithium as well as the plasmon loss are visible. The largest difference is the much higher concentration of $LiPF_6$ visible in the F1s and P2p spectra for the new sample. The new sample also shows a higher C−O content, similar to the SAM NMC cell. It is unexpected to see such a difference in the $LiPF_6$ peak since both samples have been treated the same way and the $LiPF_6$ content in the electrolyte should not have changed in the plated sample compared to the new sample. The same is true for the electrolyte composition that could cause more $LiPF_6$ to stick to the surface.

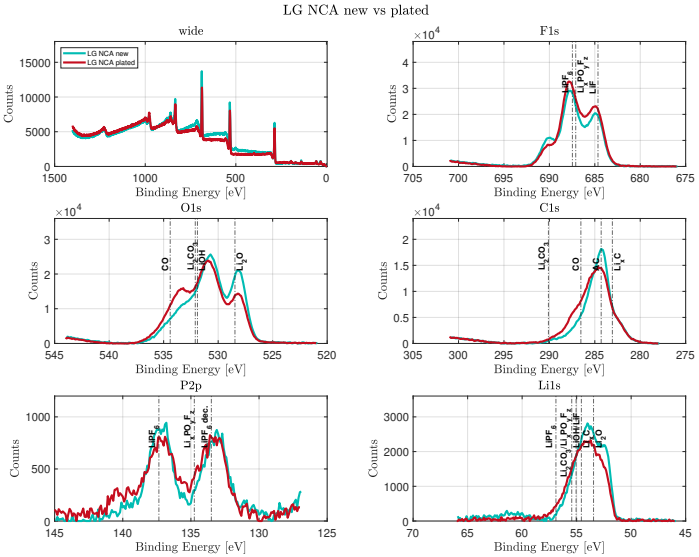

Figure 3.58: XPS spectra of the LG NCA cell new vs. plated - Shifts: new 0.9 eV / plated: 1.0 eV

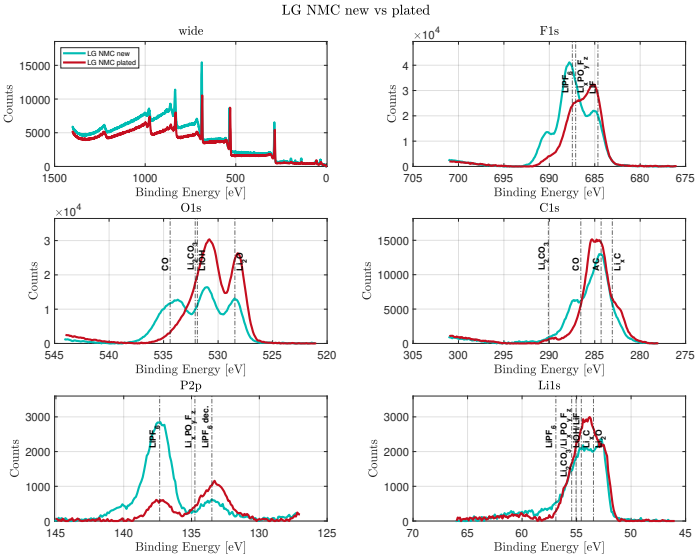

Figure 3.59: XPS spectra of the LG NMC cell new vs. plated - Shifts: new 1.1 eV / plated: 1.0 eV

Single Cell Spectra: Sony

For the NMC samples of the Sony cells not only plated and new samples have been compared but also additional measurement have been performed with isolated samples to see whether the electron induced plating also has other effects on the spectra aside of the metallic lithium peak, the plasmon peak and in the increase in LiO_2 on the surface due to lithium oxidation.

Figure 3.60 shows the spectra for the Sony NCA cell. The spectra of the plated sample of this cell deviated strongly from the other cells, as discussed above and it was not in this sample which peak should be used of the shifting. Utilized the position of the highest peak in the C1s spectrum lead to acceptable results for the LiF peak as well, that is normally used in case it is nor clear which peak is the highest C1s peak for the AC shift. This shift however left shoulders in all spectra towards the lower binding energies.

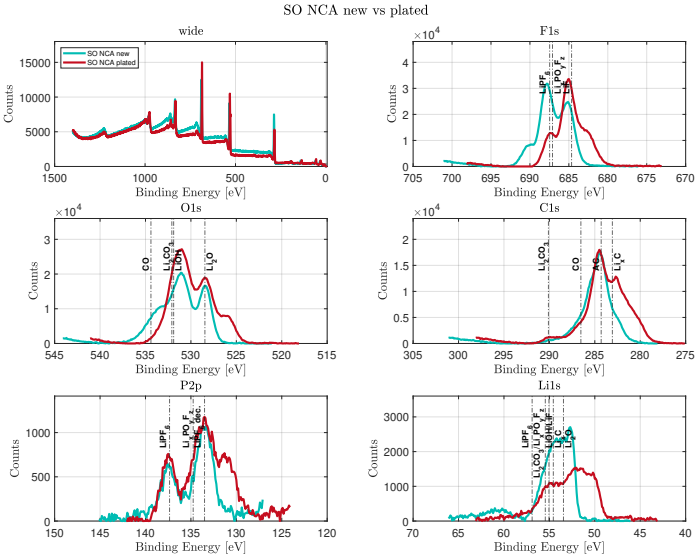

Figure 3.60: XPS spectra of the SO NCA cell new vs. plated - Shifts: new 1.1 eV / plated: −1.9 eV

Figure 3.61 shows a version with a different shift, where the spectrum is shifted to the other peak in the C1s spectrum. Here the shoulder on the right side of the spectra is more reasonable but the peaks in the O1s and P2p spectra show very different results from the spectra of the new sample. It can be assumed, that for the plated sample some kind of measurement error occurred since the spectra can not be shifted in a way that would allow any meaningful analysis of the spectra. All the shoulders on the right ends of the spectra in figure 3.60 can not be identified with any of the elements and compounds that should be present in the SEI except for the small peak in the shoulder of the C1s spectrum that could be LiC_6, as already discussed before, but this peak should not be visible on the surface of the SEI and also in a fully discharged cell. The SO NCA cell also was the cell with the lowest capacity loss of all tested cells and thus should show the smallest difference between the new and the plated sample. Looking at all this evidence it can be concluded that the spectra of the plated SO NCA sample are somehow erroneous and should be considered in the interpretation of the results.

For the spectra of the new cell the lithium metal peak as well as the plasmon losses can be seen in the L1s spectrum, strengthening the conclusion drawn in the discussion of the spectra of the LG NCA cell that the cells probable not were sufficiently discharged with a simple CC discharge.

For the last sample, the Sony NMC cell the spectra are shown in figure 3.62. Here again the new sample shows evidence for metallic surface lithium in the Li1s spectrum in the form of the lithium peak and the plasmon peak. It also shows higher $LiPF_6$ content in the F1s spectrum, but not in the P2p spectrum, which is unexpected. It also shows higher C−O content, which was now already identified in three more of the new samples compared to the plated samples and could may be an identifier for a plating event. In this case an SEI that was subjected to a plating event has a lower content of C−O compounds because these compounds are somehow changed by the reactions happening the SEI during the plating event. But since it was only found in three of the six samples further measurements must performed to proof that these effects are linked. It can however be seen that no cell shows the opposite behaviour so far.

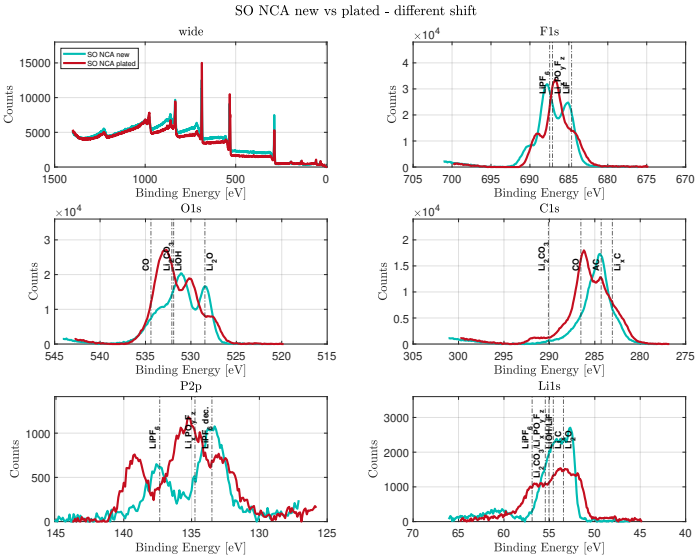

Figure 3.61: XPS spectra of the SO NCA cell new vs. plated (different shift) - Shifts: new 1.1 eV / plated: −0.2 eV

Except for the high $LiPF_6$ peak all peaks of the new sample have a lower intensity compared to the plated sample, which could again be explained by the electron induced lithium surface layer covering the other compounds of the SEI.

Figure 3.63 shows the comparison between the insulated (solid lines) and the non-insulated samples (dashed lines) of the SO NMC cell. The first thing to notice is that the shift for insulated cells needs to be higher, this was expected since an insulated sample means that the surface should be charged more positively by the extraction of the photo-electrons during measurement. The cells also show a more similar shift between the new and plated sample when the samples are insulated.

The first thing noticeable is that the spectra for both isolated samples are looking very similar. It can be assumed that for the insulated sample no

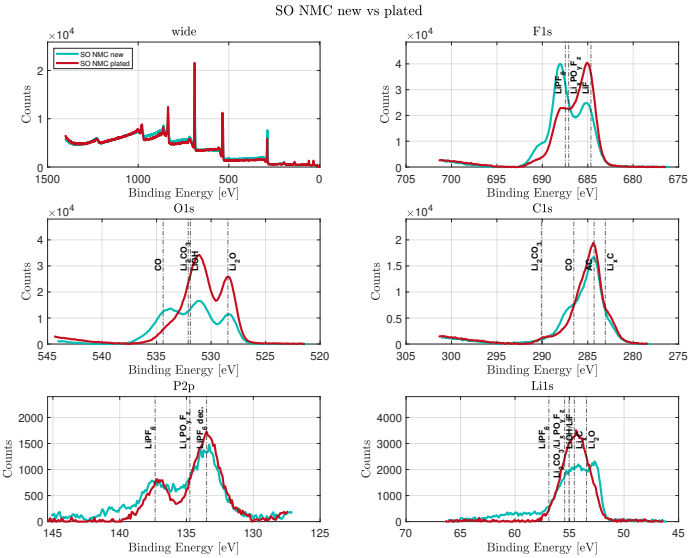

Figure 3.62: XPS spectra of the SO NMC cell new vs. plated - Shifts: new 1.1 eV / plated: 1.4 eV

electron induced plating occurs meaning that the measurement is a more true representation of the surface of the SEI layer. Looking at the penetration depth of XPS with normally less than 10 nm even for a thin SEI layer only the very top surface can be examined for the insulated samples. This shows that the SEI on the surface is very similar for the plated and non-plated samples. The shape of all peaks are almost identical and the only difference is the height of peaks, with the plated sample generally showing higher peaks for all compounds except the AC peak.

Comparing the insulated with the not-insulated samples the first difference is that the insulated samples show higher peaks for all compounds except LiO_2 in the O1s spectrum and the lithium metal peak in the Li1s spectrum. This is in good agreement with the expectations since the surface is not getting covered with the electron induced lithium plating so that the actual SEI

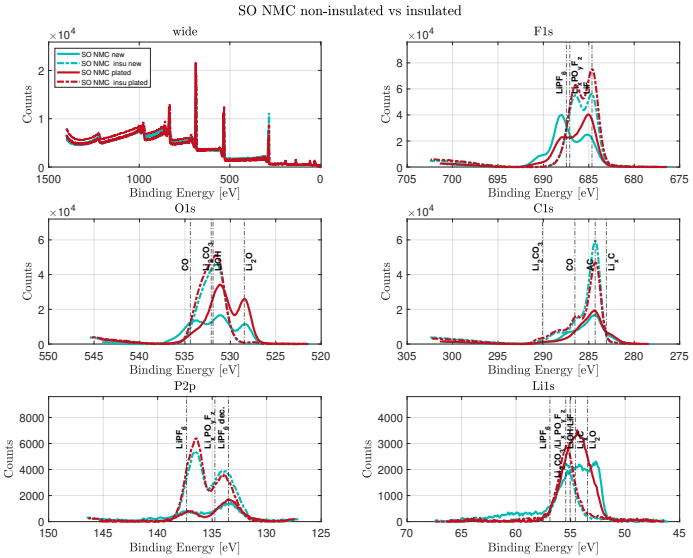

Figure 3.63: XPS spectra of the SO NMC cell insulated vs. non-insulated - Shifts: new 1.1 eV - new insulated 2.5 eV / plated: 1.4 eV - plated insulated 2.4 eV

compounds can me measured with a higher signal strength. It is remarkable however that the difference between the two insulated spectra is almost non-existent while the two non-insulated samples show very strong differences in almost all compounds. And even in the plated samples where no electron induced plating could be easily identified since there was no lithium metal peak nor any plasmon losses visible, there is a strong difference between the insulated and the non-insulated sample. That means that even if the effect is not visible in the spectrum reactions are still occurring during the measurement that are significantly changing the composition of the surface SEI. This also shows that these reactions seem to be different between the plated and the non-plated sample, since the resulting measured SEI composition is different. This means that apart from the lithium available to the electron

induced plating reaction some difference between a regularly formed SEI and an SEI subjected to plating must exist. And even though in the six samples that have been analyzed in this section no clear common feature could be identified that allows to distinguish between a plated and a non plated cell it was shown by the measurements that a significant difference must exist somewhere in the composition of the SEI between plated and non-plated cells.

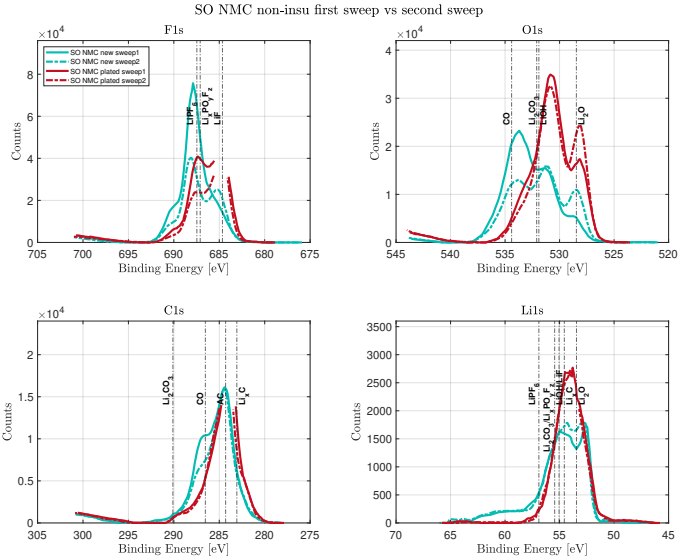

Figure 3.64: XPS spectra of the non-insulted SO NMC cell first sweep vs. second sweep - Shifts: new sweep 1 0.9 eV - new sweep 2 1.2 eV / plated sweep 1 0.8 eV - plated sweep 2 1.1 eV

To possibly give more insight into the reactions occurring during the measurements of the non-insulated samples the measurement was screen-recorded to see the change of the spectra during the measurement. The Kratos device always measures two consecutive sweeps and averages the results during the measurement. It was unfortunately not possible to directly extract the data

of the individual sweeps so the screen was recorded during the measurement and then the data points were extracted from the video afterwards. Some of the data points could not be extracted since parts of the measurement interface where covering this part of the live view of the measurement, these parts have been cut out of the plots. Figure 3.64 show the resulting spectra. Since the P2p spectrum did not show any changes only the other four detail spectra are displayed here. The dashed lines show the second sweep, while the solid lines show the first sweep. The first thing to keep in mind before interpreting these spectra is that the second sweep is already the average of the first and second sweep and it is not possible to extract the pure data of the second sweep. It should also be noted that the first sweep is not the original condition either, since during the measurement of the first sweep the reactions in the SEI have already been taken place. The general trends of the curves can however still be analyzed from the data.

For the new sample the lithium peak shows a slight increase from the first to the second sweep, the same is true for the LiO_2 peak, which is to be expected. There is also a decrease in the C−O peak in both the C1s and O1s spectra and the $LiPF_6$, possibly hinting at the fact that these two species could take part in the reaction. The decrease could also stemming from a surface coverage as discussed in the sections before but since the AC peak stays constant it is unlikely that this is the cause. There is also a slight increase in LiF.

For the plated sample that shows no sign of electron induced plating there is still an increase in LiO_2 and a small decrease in the F1s species. Unfortunately the extend of the LiF peak and the AC peak can not be seen in the spectra since they were covered in the video.

3.3.6 Summary of the XPS Results

In summary the XPS results utilizing etching as well as the electron induced plating effect have shown that:

- Electron induced lithium plating can be utilized to get information about the lithium content close to the surface of the sample. It is

however not clear if only lithium in metallic form can be accessed by the effect or also lithium in different kinds of compounds.

- There is a difference in the composition of the SEI layer for plated and non plated cells, even after 6 months of resting time.
- It is difficult to find a common identifier for plated samples but a difference in the C−O peak was visible in three of the six samples that could be utilized in the future with further research.
- Samples from batteries of different manufacturers show very different spectra which might make it hard to find common features for plating identification and analysis.
- Lithium could in most cases be found in freshly plated cells using electron induced plating but not non-plated discharged cells.

There are however also remaining questions that need to be answered in further experiments:

- Further samples should be discharged with a full cc-cv discharge to ensure that the anode is completely devoid of lithium so that the measurement of the electron induced surface lithium is not distorted by anode lithium and pure consists of lithium deposited by plating.
- The etching experiment should be repeated in the future with an insulated sample so that the true composition of the SEI can be analyzed in the depth profile.
- Measurements alternating between electron induced plating and normal measurements can be used to see the changes of the SEI without distortion caused by further reactions.
- Samples for freshly plated cells should be compared to samples that have been plated and then rested for a long time with the same cell type.

- Targeted experiments to identify which compounds of lithium are susceptible to the electron induced plating effect are necessary to determine which part of the effect can be attributed to lithium plating or other components of the SEI.

3.4 Particle Analysis

In this chapter the anode micro structure of new cells without plating of the different manufacturers described in chapter 3.1 (see table 3.1) is analyzed in more detail using a Keyence VK LSM. Therefore images of the anode surfaces of cells that did not experience plating events are taken. (The changes in micro structure caused by plating have already been analyzed using the LSM in the work of Stief [206] (see chapter 3.1) for a different type of cell). These images are then processed with a particle analysis algorithm to obtain the average particle size and rough shape as well as the particle size distribution. The samples used are from the same opened cells that were also used for the XPS analysis in chapter 3.3. The goal of this analysis is to compare the easily measurable particle size and distribution parameters to the performance of the cells under plating conditions, e.g. their capacity loss during plating cycles visible in figure 3.7 in chapter 3.1. This way it might be possible to identify certain properties that can facilitate plating and avoid these properties in future design of cells. It can also be utilized as a low cost analysis tool for existing cells to estimate their susceptibility to plating inducted capacity loss and safety hazards.

3.4.1 Sample Overview and LSM Measurements

The LSM used for the imaging in this chapter is located inside a Glovebox under protective argon atmosphere. It has four different magnification levels all corresponding to a physical lens, from now on called 10x, 20x, 50x and 150x, as described by the microscope manufacturer. For the measurements the 20x magnification is used to obtain the images that will be analyzed regarding their particle distribution since these images have a resolution high enough to still be able to distinguish the individual particles while at the same time containing enough particles for a statistically significant observation. Additional images at the highest magnification of 150x have been taken to observe the micro-structure of the particles.

Figure 3.65 shows the 150x magnification images for all six cells. It can be seen that the range of particle sizes is similar in all six cells but there are

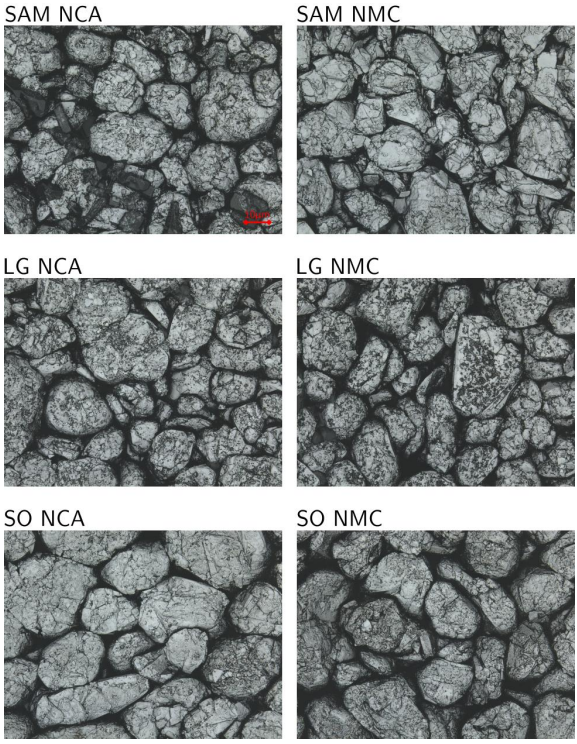

Figure 3.65: LSM Overview of all anode samples at the highest magnification (150x)

small differences in the surface structure of the individual graphite particles between the manufacturers. The Samsung (SAM) cells show more sharp edges and blocky shapes on the surface of the particles. The LG cells on the other hand have a finer surface texture hinting at one or more additives to the anode slurry that deposited on the surface of the graphite particles. This finer surface texture is also visible in the Sony (SO) cell but not as pronounced as in the LG samples.

It was expected that the difference between the NMC and NCA samples should not be visible on the anode surface since the two cell types only

use different cathode materials and the manufacturers would most likely use the same anode material in their productions process. This is true for the LG and SO cells but interestingly the SAM NCA cell shows black smaller particles of rectangular shapes that are not visible in the SAM NMC samples or any of the other samples. It is unclear if these particles are some form of contamination or if they are another additive of unknown function.

To get the images for the particle analysis 10 LSM images have been taken for each sample. Five of these images have been taken from the outer layer of the jelly roll, five images have been taken from the inner layer of the jelly roll to see if there is any difference in the particle distribution along the jelly roll. The images have been taken at random positions around the horizontal center of the jelly roll where there were no visible defects or foreign objects visible that could interfere with the particle detection.

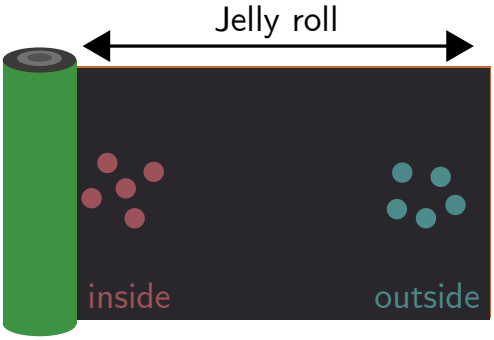

Figure 3.66: Schematic overview of the 10 measurement locations in the jelly roll

Figure 3.67 shows an example image at 20x magnification of the anode of the LG NCA cell. At this magnification the distinction between the particles is visible enough from the particle analysis algorithm to distinguish the individual particles while there are also enough particles visible on each image to allow for a meaningful analysis.

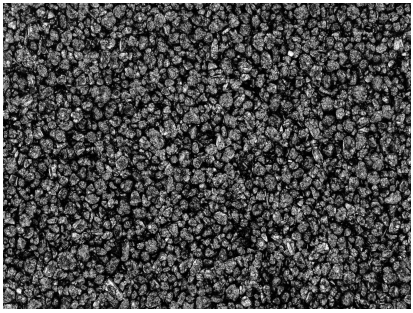

Figure 3.67: Example LSM image of the LG NCA anode (20x)

3.4.2 Particle Detection

For the particle detection a watershed algorithm in Matlab was used. The watershed method uses the height data of the given image to find separations between the particles. The height data is treated like a topographic map to detect ridges and valleys in the image that correspond to the particles and the areas in between the particles. To prepare the images for the watershed operation a series of morphological operations are performed on the images to improve the distinction between the particles.

Figure 3.68 shows the overview of the full particle detection process. After the watershed operation is performed yielding an image with separation lines between the particles at each particle location an ellipse is placed around each particle to get the size of each particle. The resulting size for each particle is the average of the ellipse's long and short diameters.

Even though the parameters for the particle detection have been carefully chosen to yield the best results, some errors in the detection are unavoidable since there is no perfect set of parameters that can handle all situations. The parameters have been chosen so that on average most of the particles are detected correctly. Figure 3.69 shows a zoomed view of the example image from the particle workflow overview in figure 3.68. In this image the two most common errors are marked with circles in the height and watershed image. The red circles denote very small particles that have not been detected and added to area of a neighbouring particle. These errors occur since a minimum

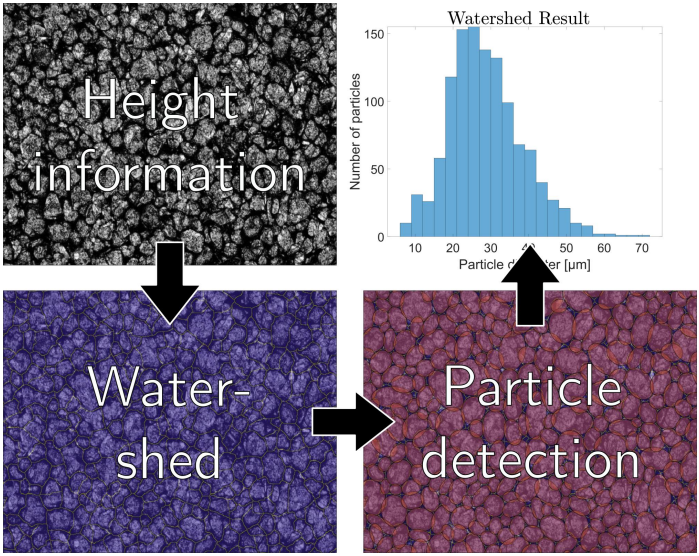

Figure 3.68: Particle detection method workflow overview

size for the detection hast to specified to avoid detection of the particles surface roughness as individual particles. This means that in the resulting size distribution the number of smaller particles will be underestimated and thus the average particle size will be slightly larger than the actual average. But since this error is consistent over all samples the comparison of the samples should not be influenced strongly by this error. The effect could potentially be stronger if one of samples has a very large number of small particles that are below the detection threshold but the images visible in figure 3.65 do not show any of samples having a difference in the very small particles.

The blue circles in figure 3.69 show watershed separation lines going through a solid particle. This can happen when the surface roughness of the particles has a very high contrast leading to a misinterpretation of this area by the watershed algorithm to be a valley between two particles. This problem is linked to the image contrast of the LSM measurements and the parameters have been chosen to minimize this error. Considering the number of particles

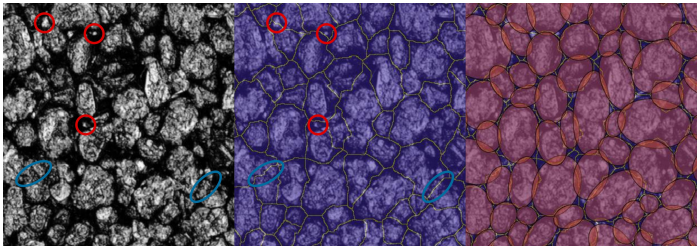

Figure 3.69: Particle detection error example

over all 10 measurements for each sample this error should only marginally influence the results and lead to more particles of average size since bigger particles are more likely to have distinct surface roughness features due to them taking up a larger area of the image and these particles are then falsely detected as two or more particles of smaller size. This error is however also having the same effect on all samples so it should not influence the comparison of the results amongst the samples.

3.4.3 Particle Detection Results

Difference of Inner and Outer Regions

The first step of the analysis of the results is to compare the results for the five measurements at the center of the jelly roll to the results from the outside of the jelly roll. If these results show no significant difference all results can be averaged and thus lead to a better data quality.

Figure 3.70 shows the particle size distributions for the LG NCA cell for each individual LSM measurement. The top five measurements are the measurements at the inside of the jelly roll, the five measurements in the lower part of the figure are the measurements from the outside of the jelly roll. It can be seen that the shape of the distributions in the same area as well as over all measurements is very similar. The average particle size for this cell at the inside of the jelly roll is slightly larger than on the outside, while the standard deviations are also similar.

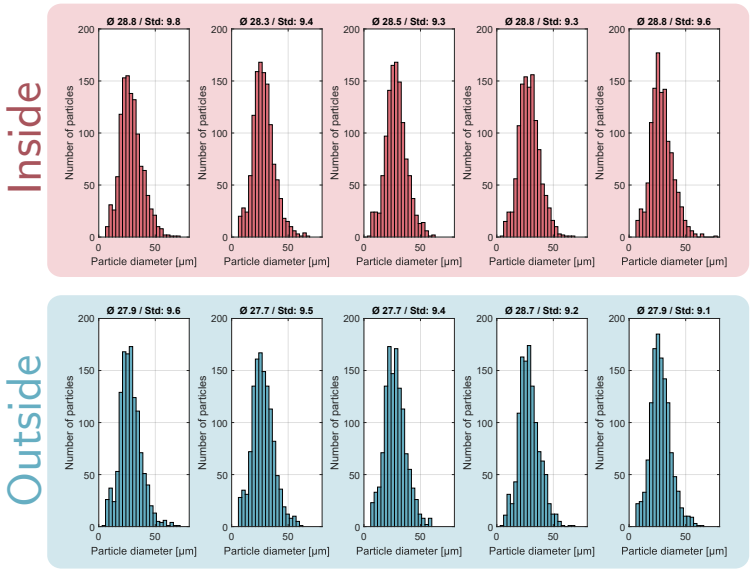

Figure 3.70: Comparison of the particle size distribution at the center of the jelly roll vs. the outer area of the jelly roll for the LG NCA

To analyse whether there is a systematic difference in the mean particle size figure 3.71 shows the mean particle size values and standard deviations for all 10 measurements of each cell. The red dots represent the values of each measurement for the inside of the jelly roll, the blue dots for the outside. It can be seen that there is some grouping of the red and blue dots for the LG NCA cell, with the exception of one outside-area outlier and the SAM NCA and SO NMC cell that show similar behaviour. The SO NCA cell on the other hand shows the opposite behaviour where the particles detected in the inner regions are smaller. For the last two cells (SAM NMC and LG NMC) no discernible grouping can be detected. This seems to be true for the Sony and Samsung cells, the LG cells however show a rather different particle size mean. This difference for the LG cells is also apparent in the

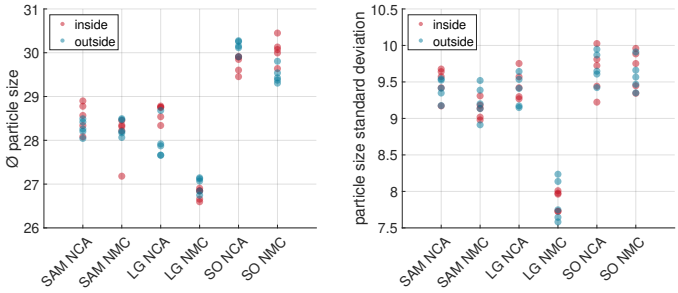

Figure 3.71: Comparison of the mean particle size and standard deviations at the center of the jelly roll vs. the outer area of the jelly roll

standard deviation. One possible explanation for differing particle sizes in the inner and outer regions of the jelly roll could be the difference in pressure, but then the particles in the inner areas for all samples would have to be smaller, which is not the case. It can be assumed the anode materials used in the two cell types by the same manufacturer should be similar in the production process and that the spread is just a coincidence. The difference in the particle sizes for each cell also is smaller than the difference between the different cells and since the spatially resolved plating effect location in the cell cannot be determined by the capacity loss data anyway, for this analysis all 10 measured particle size distributions will be added and then averaged for further analysis.

Parameter Extraction and Correlation

To obtain a mathematical description of the obtained particle size distributions five different parameters have been extracted from each distribution. The first two are the **mean particle size** (Ø) and its standard deviation (σ). The standard deviation of the particle sizes shows the width of the distribution. Furthermore the **total number of detected particles** ($\sum$) has been extracted, describing the density of the particles since all images have the same image area. This parameter has the information about how tightly the graphite particles are packed on the anode surface. Lastly the skewness

(s) and kurtosis (k) have been calculated for each distribution. The **skewness** value describes in which direction the distribution leans, i.e. whether more particles are larger than the average or smaller. In this case a negative skewness means that the distribution leans towards the higher particle size, and a positive skewness that it leans towards the small particles. The **kurtosis** value describes the pointiness of the distribution. A value of three for the kurtosis equals the shape of the normal distribution, values larger than three a more pointy shape, values lower than three a more round shape. This means that the value can be a measure of the occurrence of very small or large particles in a distribution.

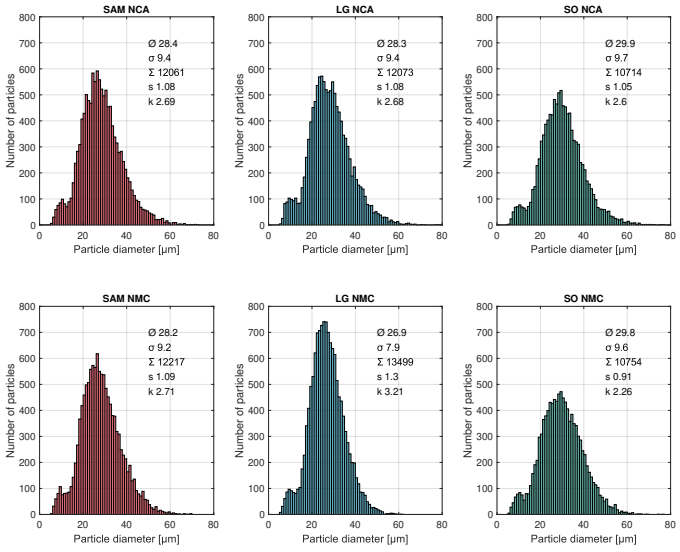

Figure 3.72: Combined particle size distributions for all six cells and the corresponding extracted parameters

Figure 3.72 shows the total particle size distributions for all six cell types measured. As discussed before, the particle distributions for all ten measured images have been added up and all parameters have been calculated based on

the resulting distribution. The axes of the histograms as well as the bin sizes have been normalized to allow for a qualitative comparison of the shapes of the distributions. The top row shows the results for the NCA cells, the lower row for the NMC cells. The colors denote the manufacturers (red for Samsung, blue for LG and green for Sony). It can be seen that there are almost no differences in the NMC and NCA cell distribution shapes for the Sony and Samsung cells as is to be expected for graphite anodes from the same manufacturer. In the LG cell however there is a significant different in the shape of the distributions with the NMC anode material having a higher particle density overall and smaller particles on average. All six cells have a positive skewness meaning that the distributions are all leaning towards the smaller particle sizes.

With the parameters obtained from the particle size distributions the correlation of each parameter to the corresponding plating capacity loss (visible in figure 3.7 in chapter 3.1) was calculated. For the correlation calculation the Pearson correlation was utilized. This yields a correlation coefficient in the range of -1 to 1 where 0 means there is no correlation between the two data sets, 1 being a very strong positive correlation and -1 a very strong negative correlation. Values between -0.3 and 0.3 are considered as negligible correlations.

Figure 3.73 shows the correlation results for the capacity loss of all six cells vs. the extracted parameters. For this measurement all correlation parameters are very low with not parameter having a larger correlation than 0.3 and thus all correlations being negligible. This was to be expected since as discussed in chapter 3.1 there is a very strong difference in the capacity loss of the NMC cells compared to the NCA cells. The NMC cells are all showing a higher plating capacity loss that is most likely caused by the manganese in the cathode crossing over and negatively impacting the SEI reformation after a plating event. For this reason it can be assumed that the impact of the different cathode material is much stronger than the possible impact of the surface structure and for this reason correlation of all samples at the same time is yielding any meaningful results. For this reason the data has been separated into two blocks, one for the three NMC samples and one for the three NCA samples.

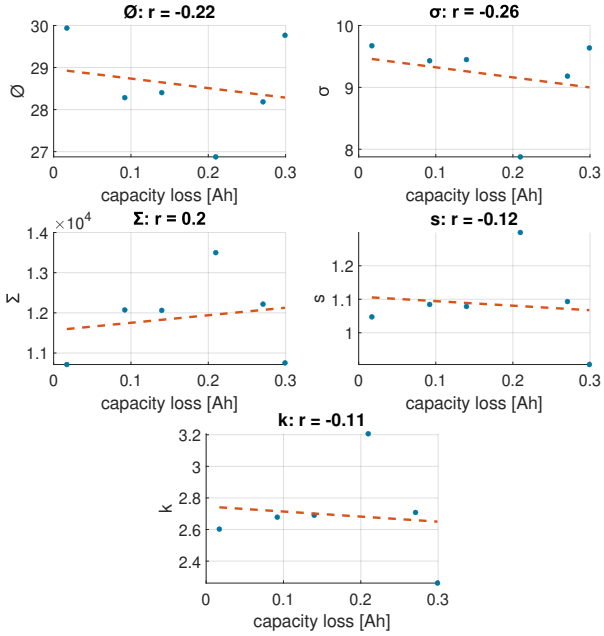

Figure 3.73: Correlation results for all six cells and the extracted parameters

Figure 3.74 shows the same procedure but only for the three cells with NMC cathodes. Here the correlation values show a very different picture, all parameters show a surprisingly high correlation, with the lowest correlation being 0.97 for the mean and particle count values. The mean value and standard deviation show a very strong positive correlation while the particle count, skewness and kurtosis show a very strong negative correlation. It is very unexpected that all 5 parameters show such a high correlation.

For the NCA cells visible in figure 3.75 the results also show strong correlations for all parameters. The overall correlation is a little bit weaker compared to the NMC results with the lowest value being 0.85 for the skewness. What is remarkable however is that all correlations show an opposite

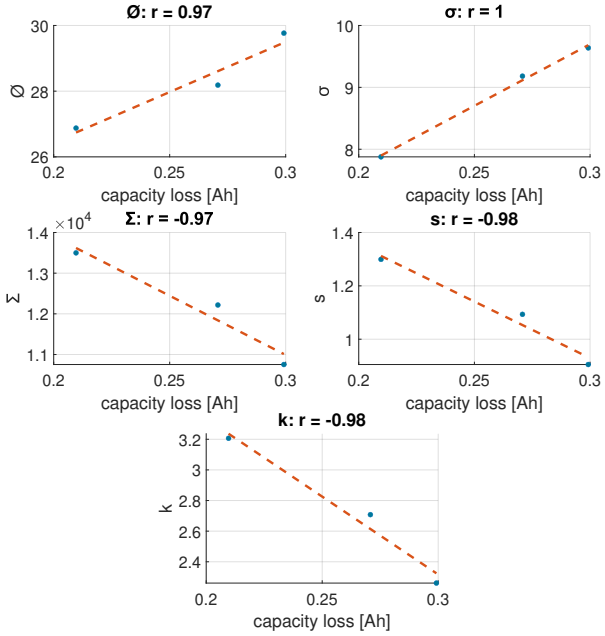

Figure 3.74: Correlation results for the NMC cells and the extracted parameters

relationship to the NMC results. Where the NMC results have a positive correlation, the NCA results show a negative one and vice versa.

The high correlation value for all parameters can be explained by the strong cross correlation between the individual parameters, visible in table 3.5. For this table the results for all six parameters have been correlated to all other parameter results. Especially s and k, as well as the average size and particle count show a correlation of almost one. For the average size and particle count this correlation is negative and was to be expected since with bigger particles on average there will be fewer total particles visible in the observed surface area fraction and vice versa. For the other parameters it is not obvious where this high connection between the extracted parameters

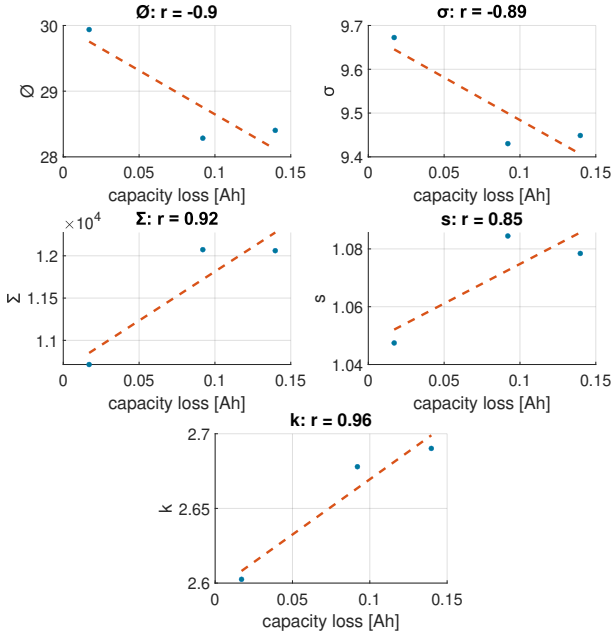

Figure 3.75: Correlation results for the NCA cells and the extracted parameters

stems from. Furthermore the mean and standard deviation are negatively correlated to the other three parameters, explaining the directions in the correlations for both measurements. This however does not explain the swap of the correlation directions between the NMC and NCA cells.

It has to be noted that for all correlations only 3 samples have been used. This is a very low sample size to get a statistically robust results. There are however four battery measurements behind each of the averaged capacity loss values meaning that the total amount is samples is actually 12. This is still a low amount of samples for a correlation analysis [236]. To test the statistical validity of the results a synthetic data set is created from the capacity loss mean values and standard deviations.

	Ø	σ	$\sum$	**s**	**k**
Ø	1	0.8647	−0.9983	−0.8815	−0.8798
σ	0.8647	1	−0.8817	−0.8953	−0.8949
$\sum$	−0.9983	−0.8817	1	0.9034	0.9025
s	−0.8815	−0.8953	0.9034	1	0.9996
k	−0.8798	−0.8949	0.9025	0.9996	1

Table 3.5: Cross correlation of the extracted parameters

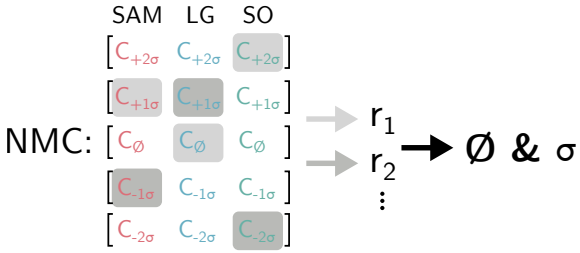

Figure 3.76: Schematic view of the synthetic data generation process for the NMC samples

Figure 3.76 shows a schematic overview of the synthetic data generation process for the NMC samples. For each sample in the NMC and NCA data sets respectively four additional vectors are created with either one or two times the standard deviation σ added to and subtracted from the mean value. From these five resulting vectors all possible permutations are created from the individual elements of all vectors (if the five vectors are denoted A,B,C,D & E that would create $[AAA]$, $[AAB]$, $[ABB]$ and so on until $[EEE]$).

This creates a new data set with 125 entries instead of the 1 original entry containing only the mean values. For each entry in this new data set the correlations is calculated the same way as for the original data creating 125 different r values. These values are then averaged and their standard deviation is calculated.

Figure 3.77 shows the probability density functions for the NMC samples. It is visible that the majority of the results still show a moderate to strong correlation of 0.7 or higher. All parameters still show the same trends of negative or positive correlations as in figure 3.74. The average value is at a

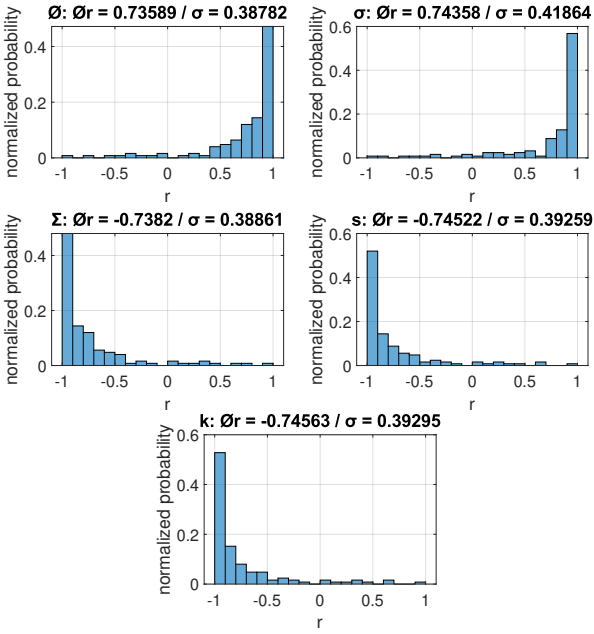

Figure 3.77: Synthetic data correlation results of the NMC samples for all five parameters

moderate correlation of around 0.75 for all parameters. There are however also some values that show a completely different value, even showing the opposite trend. These extreme outliers lead a very high standard deviation for all parameters of around 0.4.

For the NCA samples in figure 3.78 the results are similar, the trends stay opposite of the NMC results. The mean values have a slightly higher spread but are in general also around 0.7. The same is true for the standard deviations but they have a lower value over all at around 0.3.

To estimate the statistical significance of the results of the synthetic data sets for all results the p value is calculated. The p value is the cumulative probability of all results that confirm a null-hypothesis. If the p value is low

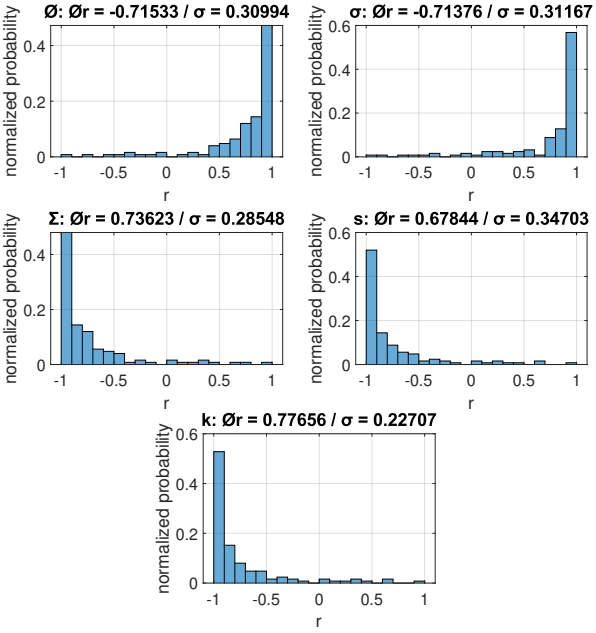

Figure 3.78: Synthetic data correlation results of the NCA samples for all five parameters

enough (normally $p < 0.05$) then the results are statistically significant. As a null-hypothesis here a correlation lower 0.5 is chosen, since all correlation results lower than this are only weak correlations. So p is the probability that for any given parameter the correlation is lower than a strong correlation value of 0.5.

	Ø	σ	$\sum$	**s**	**k**
p - NMC	0.152	0.176	0.152	0.144	0.144
p - NCA	0.240	0.248	0.240	0.3520	0.200

Table 3.6: p values for both sample types and all different parameters

Table 3.6 shows the results for the p-value calculation. It can be seen that none of the values fulfills the $p < 0.05$ criteria. They lowest p value can be found for the skewness and kurtosis of the NMC samples at 0.144. This means that even though the initial correlation values show an almost perfect correlation result, a more thorough statistical analysis revealed that the data is not sufficient for any significant observations.

Even though the p values do not show a high statistical significance it is still valuable to look at the direction of the correlations and why the NMC and NCA cells have opposite directions. Considering the FIB results discussed in chapter 3.1 where it could be seen that the plating starts growing in between the particles, a negative correlation could be expected for the particle size since bigger particles should lead to fewer inter-particle areas and thus reduce the amount of plating. The cell used for the FIB measurements was a NMC cell. The NMC cell samples however show a positive correlation of the average particle size with the capacity loss, contracting the previous assumption. The NCA cells on the other hand show a negative correlation here. The standard deviation σ value describes the spread of the distribution, i.e. a higher σ means that there are more differences in the particle sizes. This could lead to less inter-particle spaces since particles of different sizes can better fill a volume than particles of similar size. Thus here also a negative correlation could be expected and the NMC results show the opposite. It could however also be that not the amount of inter-particle spaces is important but the distance between the particles since a very close distance of the particles could lead to higher electrical field strengths that then in turn lead to higher chance of plating. That would mean that a larger difference in particle sizes can lead to closer packing and thus to smaller inter-particle distances and more plating. The shape parameters skewness and kurtosis are even harder to interpret than the mean size and standard deviation. The skewness shows positive values for all samples, meaning that the amount of smaller particles is higher than the amount of larger particles. The skewness correlation shows a negative direction for the NMC cell meaning that a higher portion of smaller particles leads to higher capacity loss. This would be in line with the theory of the distance between the particles having a larger impact on the plating performance. The kurtosis shows the

same negative correlation and shows values smaller 3 for all samples except the LG NMC sample meaning that for all these distributions the shape is wider than the normal distribution. This means that the amounts of particles of similar sizes do not differ very much from the center of the distribution. In context with the inter-particle spaces this could mean that there enough particles of each size to effectively fill the space and reduce the distance between the particles. But since there could be other effects like electrolyte additives that also affect the plating performance of the cells (similar the difference between the NMC and NCA samples) and overshadow the impact of the surface structure analyzed here, the aforementioned effects are only theses that need to be validated in future experiments.

Summary of the Particle Analysis Results

In summary the results of the particle analysis performed on the cells of six different manufacturers has shown that:

- Correlation trends can be found for different parameters. It is very likely that the surface structure has an impact on the plating performance.
- There seems to be a fundamental difference in the surface interaction in the presence of manganese during plating, visible in the difference of the correlation trends between the NMC and NCA cells.
- The amount of data from the six cells was insufficient to create statically significant results.
- The anode materials of all three manufacturer shows similar particle analysis results.

For further experiments it is important to gather more samples of different cell-types and manufacturers to increase the data basis and reach statistical significance. Another approach could be to manufacture laboratory cells with different anode materials that have differing particle parameters. This could lead to very controlled experiments where all other influencing factors could be eliminated. This however has the problem of the reproducibility of

the laboratory cells and either the availability of sufficiently different anode samples or the additional reproducibility issues for the anode material itself if it is also laboratory made.

Chapter 4

Conclusion and Outlook

In this chapter the results of all three experimental sub-chapters are recapitulated and related to each other. Finally a summarized outlook is given.

4.1 Conclusion

In this thesis three different topics regarding the detection and prevention of lithium plating have been investigated. The first big topic investigated the changes in the voltage curves and current profiles of the cells during the plating process. In the second part XPS spectra have been recorded of plated and non-plated anode samples. In the last part the surface topology of the anodes was analysed using particle detection and the resulting parameters were then investigated regarding their correlation with the plating behaviour of the cells.

All three topics required very different experimental approaches and analytical methods but their results combined can help in better understanding the lithium plating process in lithium-ion batteries. This better understanding can then help to design new cells that are more resilient against lithium plating capacity loss or that show a higher protection against safety hazards caused by lithium plating. It can also help in creating charging procedures that reduce the effect of plating and measurements methods that can be implemented into the BMS to detect the onset of plating and protect the cell from capacity loss by adjusting the charging parameters. Another field of applications is the characterization of existing cells regarding their expected plating behaviour in a fast and inexpensive manner.

Cells charging under plating conditions show deviations from the expected voltage and current curves. In chapter 3.2 the detectable charge anomalies in LIBs were discussed and it was shown that these effects are linked to a lithium deposition and not only caused by a temperature change the cell during charging. The effect on the current shape in the CV phase was analyzed in more detail and it was found that fitting the curve with a JMAK function yields parameters that can be used the characterize the cell regarding its plating behaviour. This function can be used to describe the process of metallic deposition on a surface in an electrochemical system. The behaviour of the parameters of this function have then been analyzed over the plating cycles. The fitting parameter n that describes the dimensionality of the deposition could possibly be used to predict the future cell plating behaviour including the safety risks for the cell in case of a plating event since the dimensionality of the plating can be an indicator of the type of growth, i.e. whether the plating is deposited in a mossy structure or growing dendrites. The parameter q_m was shown to be a better measure for the reversible amount of lithium plating than the stripping method since it is measured during the charging process and thus less lithium can diffuse back into the anode leading to a lower lithium estimate from the discharge stripping step than the actual plated amount. It was also observed during the analysis that the overall effect is diminishing with the plating cycles, which shows that the plating effect is dependent on previous plating cycles. Since it is theorized that prolonged cell ageing under normal conditions can also lead to changes in the SEI that are similar to those caused by plating cycles and cause sudden cell death, this effect could be used to study the sudden cell death effect with faster ageing tests.

In chapter 3.3 the anodes of different cells were analyzed utilizing XPS to better understand the changes in chemical composition of the SEI caused by plating and to locate the plating depositions inside of the SEI. The original goal was to identify the presence of dead lithium within the SEI and to located the dead lithium inside of the SEI. During the measurements however an unwanted side effect of the XPS measurement setup caused metallic lithium to migrate to the surface. This created visible surface changes in

samples that had a higher expected lithium content like the fully charged and the plated sample and no change in the fully discharged samples of new cells. This effects was analyzed in more detail and identified as the electron induced plating effect. It was shown that this effect can be used to get information about to total lithium content in the surface area without destructive and time consuming etching needed and could be used to easily identify samples that had previous plating cycles. The effect was significantly weaker on samples that had plating events but were relaxing for multiple months before cell opening than on samples that were opened immediately after the plating cycle. This means that the lithium that can be activated and migrate to the surface is most likely the dead lithium and that this dead lithium is reacting with the SEI over time to form more stable compounds where the lithium can not be activated anymore.

It was shown that even one plating cycle changes the composition of the SEI. There could however no clear indicator be identified to distinguish a plated and a non plated cell in the XPS spectra since the cells from different manufacturers already show differing spectra in their fresh cell state. A common possible identifier for past plating events could be in the form of a change in the C−O peak, but this change was inconsistent over the different cells.

In the final experimental chapter 3.4 the particle parameters of the anode materials of six different new cells have been extracted and compared to the plating losses cells of this type have shown during plating tests. The particles were identified using a watershed algorithm and from the obtained particle distribution the first four moments of the distributions were calculated. These are the mean value of the distribution, the standard deviation, the skewness and the kurtosis. A surprisingly good correlation ($r > 0.9$) was found between the capacity loss and multiple of the parameters if the cells are separated into two groups according to their cathode material (NMC or NCA). This shows that there must be a different process occurring on the cell surface during plating depending on the presence of manganese in the cell. It was however remarkable that the two groups showed the opposite behaviour in the correlation coefficient. Where the NMC cells showed a pos-

itive correlation, the NCA cells showed a negative one and vice versa. Due to the low number of different cell types additional data was synthetically created from the existing data set to test the correlation for a bigger number of samples. With the synthetic samples the correlation became a weaker ($r \approx 0.7$), but was still significant enough to warrant further investigation.

In summary each topic yielded results that can be used as the basis of further more focused research. This thesis was a very wide approach in finding methods that can be used to gain a better understanding of plating and each of the three presented methods adds a different viewing angle to the topic. The electrical measurements during plating are more close to the application and can lead to future methods for cell characterization regarding the plating behaviour. The XPS measurements give insight into the material composting and influences on the plating process on a electrochemical level and can inform cell design decisions like electrolyte composition or anode additives but require very expensive equipment. The LSM measurement on the other hand could be a cheaper and faster way to analyze the influence of the particle structure and surface morphology on the cell plating behaviour without information about the electrochemical processes and lead to a better design of the anode morphology. This way the three methods show three different magnifications of the same process with the XPS measurements giving the closest look at the plating process, the LSM measurements showing the structural influences on a macro level and the electrical measurements the effect on the behaviour of the whole cell.

4.2 Outlook

The research in this thesis has laid the foundations for further experiments to either confirm the theories presented here or expand the results on more different cells or cell geometries. The most important proposed follow-up experiments are:

- Confirming the theoretical prediction of the JMAK fitting parameter regarding the cell safety. E.g. NMR could be used to observe lithium

plating morphology in situ and compare it to the dimensionality parameter. Furthermore safety tests should be performed to observe the effect of the dimensionality of the cell safety.

- The JMAK fitting needs to be repeated with different cells from other manufacturers and other cell chemistries to see whether the method can be applied in general to all cells that can show lithium plating.

- Analysis of the CC phase voltage curve of the charge anomaly during plating. The voltage curve deviation could enable the detection of the lithium plating onset in the application and prevent plating capacity loss without necessity for extra measuring equipment.

- Decoupling the electron induced plating effect from the XPS device to be able to perform visual plating detection on larger anode surfaces. This can be utilized to detect the spacial distribution of lithium plating fast and at a low cost. To achieve this an effect similar to the charged compensation process in the XPS device has to be recreated. This requires some form of free electron source and most likely at least a low level vacuum around the sample.

- Repeating of the XPS depth profile experiments with isolated samples to obtain the lithium distribution within the SEI using fully cc-cv discharged samples to avoid residual lithium in the anode.

- Particle analysis on more different cell samples. Ideally using reproducible laboratory cells where the particle parameters can be adjusted to obtain a more reliable data basis for the correlation analysis.

Bibliography

[1] Ghassan Zubi, Rodolfo Dufo-López, Monica Carvalho, and Guzay Pasaoglu. "The lithium-ion battery: State of the art and future perspectives". In: *Renewable and Sustainable Energy Reviews* 89 (2018), pp. 292–308. ISSN: 13640321. DOI: 10.1016/j.rser.2018.03.002.

[2] Tobias Placke, Richard Kloepsch, Simon Dühnen, and Martin Winter. "Lithium ion, lithium metal, and alternative rechargeable battery technologies: the odyssey for high energy density". In: *Journal of Solid State Electrochemistry* 21.7 (2017), pp. 1939–1964. ISSN: 1432-8488. DOI: 10.1007/s10008-017-3610-7.

[3] Victor Agubra and Jeffrey Fergus. "Lithium Ion Battery Anode Aging Mechanisms". In: *Materials (Basel, Switzerland)* 6.4 (2013), pp. 1310–1325. ISSN: 1996-1944. DOI: 10.3390/ma6041310.

[4] J. Vetter, P. Novák, M. R. Wagner, C. Veit, K.-C. Möller, J. O. Besenhard, M. Winter, M. Wohlfahrt-Mehrens, C. Vogler, and A. Hammouche. "Ageing mechanisms in lithium-ion batteries". In: *Journal of Power Sources* 147.1-2 (2005), pp. 269–281. ISSN: 03787753. DOI: 10.1016/j.jpowsour.2005.01.006.

[5] Cheng Lin, Aihua Tang, Hao Mu, Wenwei Wang, and Chun Wang. "Aging Mechanisms of Electrode Materials in Lithium-Ion Batteries for Electric Vehicles". In: *Journal of Chemistry* 2015 (2015), pp. 1–11. ISSN: 2090-9063. DOI: 10.1155/2015/104673.

[6] Jiang Fan and Steven Tan. "Studies on Charging Lithium-Ion Cells at Low Temperatures". In: *Journal of The Electrochemical Society* 153 (6) (2006), A1081–A1092. ISSN: 0013-4651.

[7] Thomas Waldmann, Björn-Ingo Hogg, and Margret Wohlfahrt-Mehrens. “Li plating as unwanted side reaction in commercial Li-ion cells – A review”. In: *Journal of Power Sources* 384 (2018), pp. 107–124. ISSN: 03787753. DOI: 10.1016/j.jpowsour.2018.02.063.

[8] Nobis, Claudia und Kuhnimhof, and Tobias. *Mobilität in Deutschland – MiD. Ergebnisbericht. BMVI, infas, DLR, IVT, infas 360. Bonn, Berlin.* 2019.

[9] Amin Farjah, Ehsan Bagheri, Ali Reza Seifi, and Teymoor Ghanbari, eds. *Main and Auxiliary Parts of Battery Storage, Aimed to Fast Charging of Electrical Vehicles.* 2018.

[10] Pedro Nunes and M. C. Brito. “Displacing natural gas with electric vehicles for grid stabilization”. In: *Energy* 141 (2017), pp. 87–96. ISSN: 03605442. DOI: 10.1016/j.energy.2017.09.064.

[11] Rakhmad Indra Pramana, ed. *"Continuous improvement of sustainable energy for eco-mobility": Proceedings : ICSEEA 2017, International Conference on Sustainable Energy Engineering and Application : Indonesia Science Expo, 23-26 Oct. 2017, Balai Kartini, Jakarta.* Piscataway, NJ: IEEE, 2017. ISBN: 9781538617663. URL: http://ieeexplore.ieee.org/servlet/opac?punumber=8258578.

[12] Casey Quinn, Daniel Zimmerle, and Thomas H. Bradley. “The effect of communication architecture on the availability, reliability, and economics of plug-in hybrid electric vehicle-to-grid ancillary services”. In: *Journal of Power Sources* 195.5 (2010), pp. 1500–1509. ISSN: 03787753. DOI: 10.1016/j.jpowsour.2009.08.075.

[13] Xiangwu Yan, Zhengyang Duan, and Zheng Lü, eds. *Control Method of Fractional-order PI Controller Applied in Electric Vehicle to Grid Based Micro-grid Stabilization Device.* 2014.

[14] Tobias C. Bach, Simon F. Schuster, Elena Fleder, Jana Müller, Martin J. Brand, Henning Lorrmann, Andreas Jossen, and Gerhard Sextl. “Nonlinear aging of cylindrical lithium-ion cells linked to heterogeneous compression”. In: *Journal of Energy Storage* 5 (2016), pp. 212–223. ISSN: 2352152X. DOI: 10.1016/j.est.2016.01.003.

[15] Dingchang Lin, Yayuan Liu, and Yi Cui. “Reviving the lithium metal anode for high-energy batteries”. In: *Nature nanotechnology* 12.3 (2017), pp. 194–206. DOI: 10.1038/nnano.2017.16.

[16] Xin-Bing Cheng, Rui Zhang, Chen-Zi Zhao, and Qiang Zhang. “Toward Safe Lithium Metal Anode in Rechargeable Batteries: A Review”. In: *Chemical reviews* 117.15 (2017), pp. 10403–10473. DOI: 10.1021/acs.chemrev.7b00115.

[17] Kengo Okita, Ken-ichi Ikeda, Hikaru Sano, Yasutoshi Iriyama, and Hikari Sakaebe. “Stabilizing lithium plating-stripping reaction between a lithium phosphorus oxynitride glass electrolyte and copper thin film by platinum insertion”. In: *Journal of Power Sources* 196.4 (2011), pp. 2135–2142. ISSN: 03787753. DOI: 10.1016/j.jpowsour.2010.10.014.

[18] K. Brandt. “Historical development of secondary lithium batteries”. In: *Solid State Ionics* 69 (1994), pp. 173–183.

[19] Susannah Guthrie. “Tesla just made its giant battery reserve in South Australia even bigger”. In: *CarAdvice* (2020). URL: https://www.caradvice.com.au/843957/tesla-battery-south-australia/ (visited on 04/24/2020).

[20] Da Deng. “Li-ion batteries: basics, progress, and challenges”. In: *Energy Science & Engineering* 3.5 (2015), pp. 385–418. ISSN: 20500505. DOI: 10.1002/ese3.95.

[21] Yuqi Li, Yaxiang Lu, Philipp Adelhelm, Maria-Magdalena Titirici, and Yong-Sheng Hu. “Intercalation chemistry of graphite: alkali metal ions and beyond”. In: *Chemical Society reviews* 48.17 (2019), pp. 4655–4687. DOI: 10.1039/c9cs00162j.

[22] Martin Winter, Jürgen O. Besenhard, Michael E. Spahr, and Petr Novak. “Insertion Electrode Materials for Rechargeable Lithium Batteries”. In: *Advanced materials (Deerfield Beach, Fla.)* 10.10 (1998), pp. 725–763.

[23] M. C. Smart and B. V. Ratnakumar. “Effects of Electrolyte Composition on Lithium Plating in Lithium-Ion Cells”. In: *Journal of The Electrochemical Society* 158.4 (2011), A379. ISSN: 0013-4651. DOI: 10.1149/1.3544439.

[24] Marius Bauer, Mario Wachtler, Hendrik Stöwe, Jon V. Persson, and Michael A. Danzer. “Understanding the dilation and dilation relaxation behavior of graphite-based lithium-ion cells”. In: *Journal of Power Sources* 317 (2016), pp. 93–102. ISSN: 03787753. DOI: 10.1016/j.jpowsour.2016.03.078.

[25] Rui Wang, Lili Feng, Wenrong Yang, Yinyin Zhang, Yanli Zhang, Wei Bai, Bo Liu, Wei Zhang, Yongming Chuan, Ziguang Zheng, and Hongjin Guan. “Effect of Different Binders on the Electrochemical Performance of Metal Oxide Anode for Lithium-Ion Batteries”. In: *Nanoscale research letters* 12.1 (2017), p. 575. ISSN: 1931-7573. DOI: 10.1186/s11671-017-2348-6.

[26] Nidia C. Gallego, Cristian I. Contescu, Harry M. Meyer, Jane Y. Howe, Roberta A. Meisner, E. Andrew Payzant, Michael J. Lance, Sang Y. Yoon, Matthew Denlinger, and David L. Wood. “Advanced surface and microstructural characterization of natural graphite anodes for lithium ion batteries”. In: *Carbon* 72 (2014), pp. 393–401. ISSN: 00086223. DOI: 10.1016/j.carbon.2014.02.031.

[27] Kevin Eberman, Parthasarathy Gomadam, Gaurav Jain, and Erik Scott. “Material and Design Options for Avoiding Lithium Plating during Charging”. In: *ECS Transactions* 25.35 (2009), pp. 47–58. DOI: 10.1149/1.3414003.

[28] Meinert Lewerenz, Georg Fuchs, Lisa Becker, and Dirk Uwe Sauer. “Irreversible calendar aging and quantification of the reversible capacity loss caused by anode overhang”. In: *Journal of Energy Storage* 18 (2018), pp. 149–159. ISSN: 2352152X. DOI: 10.1016/j.est.2018.04.029.

[29] Seong Jin An, Jianlin Li, Claus Daniel, Debasish Mohanty, Shrikant Nagpure, and David L. Wood. “The state of understanding of the lithium-ion-battery graphite solid electrolyte interphase (SEI) and its relationship to formation cycling”. In: *Carbon* 105 (2016), pp. 52–76. ISSN: 00086223. DOI: 10.1016/j.carbon.2016.04.008.

[30] Yu-Xiao Lin, Zhe Liu, Kevin Leung, Long-Qing Chen, Peng Lu, and Yue Qi. “Connecting the irreversible capacity loss in Li-ion batteries with the electronic insulating properties of solid electrolyte interphase (SEI) components”. In: *Journal of Power Sources* 309 (2016), pp. 221–230. ISSN: 03787753.

[31] Amartya Mukhopadhyay and Brian W. Sheldon. “Deformation and stress in electrode materials for Li-ion batteries”. In: *Progress in Materials Science* 63 (2014), pp. 58–116. ISSN: 00796425. DOI: 10.1016/j.pmatsci.2014.02.001.

[32] Aiping Wang, Sanket Kadam, Hong Li, Siqi Shi, and Yue Qi. “Review on modeling of the anode solid electrolyte interphase (SEI) for lithium-ion batteries”. In: *npj Computational Materials* 4.1 (2018), p. 359. ISSN: 2057-3960. DOI: 10.1038/s41524-018-0064-0.

[33] John B. Goodenough and Youngsik Kim. “Challenges for Rechargeable Li Batteries”. In: *Chemistry of Materials* 22.3 (2010), pp. 587–603. ISSN: 0897-4756. DOI: 10.1021/cm901452z.

[34] M. Rosa Palacín. “Understanding ageing in Li-ion batteries: a chemical issue”. In: *Chemical Society reviews* 47.13 (2018), pp. 4924–4933. DOI: 10.1039/c7cs00889a.

[35] M. Shikano, H. Kobayashi, S. Koike, H. Sakaebe, E. Ikenaga, K. Kobayashi, and K. Tatsumi. “Investigation of positive electrodes after cycle testing of high-power Li-ion battery cells II”. In: *Journal of Power Sources* 174.2 (2007), pp. 795–799. ISSN: 03787753. DOI: 10.1016/j.jpowsour.2007.06.138.

[36] Md. Khalilur Rahman and Yoshiyasu Saito. “Investigation of positive electrodes after cycle testing of high-power Li-ion battery cells”. In: *Journal of Power Sources* 174.2 (2007), pp. 889–894. ISSN: 03787753. DOI: 10.1016/j.jpowsour.2007.06.222.

[37] Lukas Seidl, Slađana Martens, Jiwei Ma, Ulrich Stimming, and Oliver Schneider. “In situ scanning tunneling microscopy studies of the SEI formation on graphite electrodes for Li(+)-ion batteries”. In: *Nanoscale* 8.29 (2016), pp. 14004–14014. DOI: 10.1039/c6nr00825a.

[38] Mathias Petzl and Michael A. Danzer. “Nondestructive detection, characterization, and quantification of lithium plating in commercial lithium-ion batteries”. In: *Journal of Power Sources* 254 (2014), pp. 80–87. ISSN: 03787753. DOI: 10.1016/j.jpowsour.2013.12.060.

[39] E. Peled. “The Electrochemical Behavior of Alkali and Alkaline Earth Metals in Nonaqueous Battery Systems - The Solid Electrolyte Interphase Model”. In: *Journal of The Electrochemical Society* (1979), pp. 2047–2051.

[40] Pankaj Arora, Marc Doyle, and Ralph E. White. “Mathematical Modeling of the Lithium Deposition Overcharge Reaction in Lithium-Ion Batteries Using Carbon-Based Negative Electrodes”. In: *Journal of The Electrochemical Society* 10.146 (1999), pp. 3543–3553.

[41] Bharat Balagopal, Cong Sheng Huang, and Mo-Yuen Chow. “Effect of Calendar Ageing on SEI growth and its Impact on Electrical Circuit Model Parameters in Lithium Ion Batteries”. In: *IEEE* 2018 (2018).

[42] Roman Imhof and Petr Novák. “In Situ Investigation of the Electrochemical Reduction of Carbonate Electrolyte Solutions at Graphite Electrodes”. In: *Electrochemical Science and Technology* (1997).

[43] Pankaj Arora. “Capacity Fade Mechanisms and Side Reactions in Lithium-Ion Batteries”. In: *Journal of The Electrochemical Society* 145.10 (1998), p. 3647. ISSN: 0013-4651. DOI: 10.1149/1.1838857.

[44] Rutooj D. Deshpandezand and Dawn M. Bernardia. “Modeling Solid-Electrolyte Interphase (SEI) Fracture: CoupledMechanical/Chemical Degradation of the Lithium Ion Battery”. In: *Journal of The Electrochemical Society* 2017.164 (2017), A461–A474.

[45] Arun Patil, Vaishali Patil, Dong Wook Shin, Ji-Won Choi, Dong-Soo Paik, and Seok-Jin Yoon. “Issue and challenges facing rechargeable thin film lithium batteries”. In: *Materials Research Bulletin* 43.8-9 (2008), pp. 1913–1942. ISSN: 00255408. DOI: 10.1016/j.materresbull.2007.08.031.

[46] David L. Wood, Jianlin Li, and Claus Daniel. “Prospects for reducing the processing cost of lithium ion batteries”. In: *Journal of Power Sources* 275 (2015), pp. 234–242. ISSN: 03787753. DOI: 10.1016/j.jpowsour.2014.11.019.

[47] Shengshui Zhang, Michael S. Ding, Kang Xu, Jan Allen, and T. Richard Jow. “Understanding Solid Electrolyte Interface Film Formation on Graphite Electrodes”. In: *Electrochemical and Solid-State Letters* 12.4 (2001), A206–A208.

[48] Sandeep Bhattacharya, A. Reza Riahi, and Ahmet T. Alpas. “Role of Voltage Scan Rate on Degradation of Graphite Electrodes Electrochemically Cycled vs. Li/Li +”. In: *MRS Proceedings* 1388 (2012). ISSN: 0272-9172. DOI: 10.1557/opl.2012.8.

[49] Doron Aurbach and Hugo Gottlieb. “The electrochemical behavior of selected polar aprotic systems”. In: *Electrochimica Acta* 34 (1998), pp. 141–156. ISSN: 00134686.

[50] S. Flandrois and B. Simon. “Carbon materials for lithium-ion rechargeable batteries”. In: *Carbon* 37 (1999), pp. 165–180. ISSN: 00086223.

[51] Ken Tasaki, Katsuya Kanda, Takao Kobayashi, Shinichiro Nakamura, and Makoto Ue. “Theoretical Studies on the Reductive Decompositions of Solvents and Additives for Lithium-Ion Batteries near Lithium Anodes”. In: *Journal of The Electrochemical Society* 153 (12) (2006), A2192–A2197.

[52] Chikashi Shinagawa, Hiroshi Ushiyama, and Koichi Yamashita. “Multiscale Simulations for Lithium-Ion Batteries: SEI FilmGrowth and Capacity Fading”. In: *Journal of The Electrochemical Society* 2017.164 (2017), A3018–A3024.

[53] Mengyun Nie, Daniel P. Abraham, Daniel M. Seo, Yanjing Chen, Arijit Bose, and Brett L. Lucht. “Role of Solution Structure in Solid Electrolyte Interphase Formation on Graphite with LiPF 6 in Propylene Carbonate”. In: *The Journal of Physical Chemistry C* 117.48 (2013), pp. 25381–25389. ISSN: 1932-7447. DOI: 10.1021/jp409765w.

[54] K. Jalkanen, J. Karppinen, L. Skogström, T. Laurila, M. Nisula, and K. Vuorilehto. “Cycle aging of commercial NMC/graphite pouch cells at different temperatures”. In: *Applied Energy* 154 (2015), pp. 160–172. ISSN: 03062619. DOI: 10.1016/j.apenergy.2015.04.110.

[55] Abdilbari Shifa Mussa, Anti Liivat, Fernanda Marzano, Matilda Klett, Bertrand Philippe, Carl Tengstedt, Göran Lindbergh, Kristina Edström, Rakel Wreland Lindström, and Pontus Svens. “Fast-charging effects on ageing for energy-optimized automotive LiNi1/ 3Mn1/ 3Co1/ 3O2/ graphite prismatic lithium-ion cells”. In: *Journal of Power Sources* 422 (2019), pp. 175–184. ISSN: 03787753. DOI: 10.1016/j.jpowsour.2019.02.095.

[56] T. D. Tran, J. H. Feikert, and R. W. Rekala. “Rate effect on lithium-ion graphite electrode performance”. In: *Journal of applied electrochemistry* 26 (1996), pp. 1161–1167.

[57] E. Peled, D. Golodnitsky, C. Menachem, and D. Bar-Tow. “An Advanced Tool for the Selection of Electrolyte Components for Rechargeable Lithium Batteries”. In: *Journal of The Electrochemical Society* 145 (10) (1998), pp. 3482–3486.

[58] V. Eshkenazia, E. Peled, L. Burstein, and D. Golodnitsky. “XPS analysis of the SEI formed on carbonaceous materials”. In: *Solid State Ionics* 170.1-2 (2004), pp. 83–91. DOI: 10.1016/S0167-2738(03)00107-3.

[59] Chengcheng Fang, Jinxing Li, Minghao Zhang, Yihui Zhang, Fan Yang, Jungwoo Z. Lee, Min-Han Lee, Judith Alvarado, Marshall A. Schroeder, Yangyuchen Yang, Bingyu Lu, Nicholas Williams, Miguel Ceja, Li Yang, Mei Cai, Jing Gu, Kang Xu, Xuefeng Wang, and Ying Shirley Meng. "Quantifying inactive lithium in lithium metal batteries". In: *Nature* 572.7770 (2019), pp. 511–515. DOI: 10.1038/s41586-019-1481-z.

[60] M. Lu, H. Cheng, and Y. Yang. "A comparison of solid electrolyte interphase (SEI) on the artificial graphite anode of the aged and cycled commercial lithium ion cells". In: *Electrochimica Acta* 53.9 (2008), pp. 3539–3546. ISSN: 00134686. DOI: 10.1016/j.electacta.2007.09.062.

[61] Feng Hao, Zhixiao Liu, Perla B. Balbuena, and Partha P. Mukherjee. "Mesoscale Elucidation of Solid Electrolyte Interphase Layer Formation in Li-Ion Battery Anode". In: *The Journal of Physical Chemistry C* 121.47 (2017), pp. 26233–26240. ISSN: 1932-7447. DOI: 10.1021/acs.jpcc.7b09465.

[62] Kevin Leung. "First-Principles Modeling of Mn(II) Migration above and Dissolution from Li x Mn 2 O 4 (001) Surfaces". In: *Chemistry of Materials* 29.6 (2017), pp. 2550–2562. ISSN: 0897-4756. DOI: 10.1021/acs.chemmater.6b04429.

[63] Fernando A. Soto, Asma Marzouk, Fedwa El-Mellouhi, and Perla B. Balbuena. "Understanding Ionic Diffusion through SEI Components for Lithium-Ion and Sodium-Ion Batteries: Insights from First-Principles Calculations". In: *Chemistry of Materials* 30.10 (2018), pp. 3315–3322. ISSN: 0897-4756. DOI: 10.1021/acs.chemmater.8b00635.

[64] Barbara Stiaszny, Jörg C. Ziegler, Elke E. Krauß, Jan P. Schmidt, and Ellen Ivers-Tiffée. "Electrochemical characterization and post-mortem analysis of aged LiMn2O4–Li(Ni0.5Mn0.3Co0.2)O2/graphite lithium ion batteries. Part I: Cycle aging". In: *Journal of Power*

Sources 251 (2014), pp. 439–450. ISSN: 03787753. DOI: 10.1016/j.jpowsour.2013.11.080.

[65] Rujian Fu, Song-Yul Choe, Victor Agubra, and Jeffrey Fergus. "Modeling of degradation effects considering side reactions for a pouch type Li-ion polymer battery with carbon anode". In: *Journal of Power Sources* 261 (2014), pp. 120–135. ISSN: 03787753. DOI: 10.1016/j.jpowsour.2014.03.045.

[66] Georg Bieker, Martin Winter, and Peter Bieker. "Electrochemical in situ investigations of SEI and dendrite formation on the lithium metal anode". In: *Physical chemistry chemical physics : PCCP* 17.14 (2015), pp. 8670–8679. DOI: 10.1039/c4cp05865h.

[67] Shung-Ik Lee, Un-Ho Jung, Yun-Sung Kim, Myung-Hwan Kim, Dong-June Ahn, and Hai-Soo Chun. "A study of electrochemical kinetics of lithium ion in organic electrolytes". In: *Korean J. Chem. Eng* 19(4) (2002), pp. 638–644.

[68] T. L. Kulova, A. M. Skundin, E. A. Nizhnikovskii, and A. V. Fesenko. "Temperature effect on the lithium diffusion rate in graphite". In: *Russian Journal of Electrochemistry* 42.3 (2006), pp. 259–262. ISSN: 1023-1935. DOI: 10.1134/S1023193506030086.

[69] Kristin Persson, Vijay A. Sethuraman, Laurence J. Hardwick, Yoyo Hinuma, Ying Shirley Meng, Anton van der Ven, Venkat Srinivasan, Robert Kostecki, and Gerbrand Ceder. "Lithium Diffusion in Graphitic Carbon". In: *The Journal of Physical Chemistry Letters* 1 (8) (2010), pp. 1176–1180. ISSN: 1948-7185.

[70] N. Legrand, B. Knosp, P. Desprez, F. Lapicque, and S. Raël. "Physical characterization of the charging process of a Li-ion battery and prediction of Li plating by electrochemical modelling". In: *Journal of Power Sources* 245 (2014), pp. 208–216. ISSN: 03787753. DOI: 10.1016/j.jpowsour.2013.06.130.

[71] Izumi Umegaki, Shigehiro Kawauchi, Hiroshi Sawada, Hiroshi Nozaki, Yuki Higuchi, Kazutoshi Miwa, Yasuhito Kondo, Martin Månsson, Mark Telling, Fiona C. Coomer, Stephen P. Cottrell, Tsuyoshi Sasaki,

Tetsuro Kobayashi, and Jun Sugiyama. “Li-ion diffusion in Li intercalated graphite C6Li and C12Li probed by μ+SR”. In: *Physical chemistry chemical physics : PCCP* 19.29 (2017), pp. 19058–19066. DOI: 10.1039/c7cp02047c.

[72] M. T. Johnson, H. I. Starnberg, and H. P. Hughes. “Electronic Structure of Alkalie Metal Overlayers on Graphite”. In: *Surface Science* 178 (1986), pp. 290–299.

[73] Simon Malifarge, Bruno Delobel, and Charles Delacourt. “Experimental and Modeling Analysis of Graphite Electrodes with Various Thicknesses and Porosities for High-Energy-Density Li-Ion Batteries”. In: *Journal of The Electrochemical Society* 165.7 (2018), A1275–A1287. ISSN: 0013-4651. DOI: 10.1149/2.0301807jes.

[74] Ping Yu. “Determination of the Lithium Ion Diffusion Coefficient in Graphite”. In: *Journal of The Electrochemical Society* 146.1 (1999), p. 8. ISSN: 0013-4651. DOI: 10.1149/1.1391556.

[75] M. D. Levi and D. Aurbach. “The mechanism of lithium intercalation in graphite film electrodes in aprotic media. Part 2. Potentiostatic intermittent titration and in situ XRD studies of the solid-state ionic diffusion”. In: *Journal of Electroanalytical Chemistry* 1997.421 (1996), pp. 89–97.

[76] Andrzej P. Nowak, Beata Wicikowska, Konrad Trzciński, and Anna Lisowska-Oleksiak. “Determination of Chemical Diffusion Coefficient of Lithium Ions in Ceramics Derived from Pyrolysed Poly(1,2-dimethyl-silazane) and Starch”. In: *Procedia Engineering* 98 (2014), pp. 8–13. ISSN: 18777058. DOI: 10.1016/j.proeng.2014.12.480.

[77] Fei Yao, Fethullah Güneş, Huy Quang Ta, Seung Mi Lee, Seung Jin Chae, Kyeu Yoon Sheem, Costel Sorin Cojocaru, Si Shen Xie, and Young Hee Lee. “Diffusion mechanism of lithium ion through basal plane of layered graphene”. In: *Journal of the American Chemical Society* 134.20 (2012), pp. 8646–8654. DOI: 10.1021/ja301586m.

[78] Veronika Zinth, Christian von Lüders, Michael Hofmann, Johannes Hattendorff, Irmgard Buchberger, Simon Erhard, Joana Rebelo-Kornmeier, Andreas Jossen, and Ralph Gilles. "Lithium plating in lithium-ion batteries at sub-ambient temperatures investigated by in situ neutron diffraction". In: *Journal of Power Sources* 271 (2014), pp. 152–159. ISSN: 03787753. DOI: 10.1016/j.jpowsour.2014.07.168.

[79] Madeleine Ecker, Nerea Nieto, Stefan Käbitz, Johannes Schmalstieg, Holger Blanke, Alexander Warnecke, and Dirk Uwe Sauer. "Calendar and cycle life study of Li(NiMnCo)O2-based 18650 lithium-ion batteries". In: *Journal of Power Sources* 248 (2014), pp. 839–851. ISSN: 03787753. DOI: 10.1016/j.jpowsour.2013.09.143.

[80] Johannes Schmalstieg, Stefan Käbitz, Madeleine Ecker, and Dirk Uwe Sauer. "A holistic aging model for Li(NiMnCo)O2 based 18650 lithium-ion batteries". In: *Journal of Power Sources* 257 (2014), pp. 325–334. ISSN: 03787753. DOI: 10.1016/j.jpowsour.2014.02.012.

[81] John Wang, Justin Purewal, Ping Liu, Jocelyn Hicks-Garner, Souren Soukazian, Elena Sherman, Adam Sorenson, Luan Vu, Harshad Tataria, and Mark W. Verbrugge. "Degradation of lithium ion batteries employing graphite negatives and nickel–cobalt–manganese oxide + spinel manganese oxide positives: Part 1, aging mechanisms and life estimation". In: *Journal of Power Sources* 269 (2014), pp. 937–948. ISSN: 03787753. DOI: 10.1016/j.jpowsour.2014.07.030.

[82] Anthony Barré, Benjamin Deguilhem, Sébastien Grolleau, Mathias Gérard, Frédéric Suard, and Delphine Riu. "A review on lithium-ion battery ageing mechanisms and estimations for automotive applications". In: *Journal of Power Sources* 241 (2013), pp. 680–689. ISSN: 03787753. DOI: 10.1016/j.jpowsour.2013.05.040.

[83] G. G. Amatucci, J. M. Tarascon, and L. C. Klein. "Cobalt dissolution in LiCoO,-based non-aqueous rechargeable batteries". In: *Solid State Ionics* 83 (1996), pp. 167–173.

[84] Hansan Liu, Jie Li, Zhongru Zhang, Zhengliang Gong, and Yong Yang. "The effects of sintering temperature and time on the structure and electrochemical performance of LiNi 0.8 Co 0.2 O 2 cathode materials derived from sol-gel method". In: *Journal of Solid State Electrochemistry* 7.8 (2003), pp. 456–462. ISSN: 1432-8488. DOI: 10.1007/s10008-002-0342-z.

[85] M. Wohlfahrt-Mehrens, C. Vogler, and J. Garche. "Aging mechanisms of lithium cathode materials". In: *Journal of Power Sources* 127.1-2 (2004), pp. 58–64. ISSN: 03787753. DOI: 10.1016/j.jpowsour.2003.09.034.

[86] Barbara Stiaszny, Jörg C. Ziegler, Elke E. Krauß, Mengjia Zhang, Jan P. Schmidt, and Ellen Ivers-Tiffée. "Electrochemical characterization and post-mortem analysis of aged LiMn2O4–NMC/graphite lithium ion batteries part II: Calendar aging". In: *Journal of Power Sources* 258 (2014), pp. 61–75. ISSN: 03787753. DOI: 10.1016/j.jpowsour.2014.02.019.

[87] Matthieu Dubarry, Cyril Truchot, Bor Yann Liaw, Kevin Gering, Sergiy Sazhin, David Jamison, and Christopher Michelbacher. "Evaluation of commercial lithium-ion cells based on composite positive electrode for plug-in hybrid electric vehicle applications. Part II. Degradation mechanism under 2C cycle aging". In: *Journal of Power Sources* 196.23 (2011), pp. 10336–10343. ISSN: 03787753. DOI: 10.1016/j.jpowsour.2011.08.078.

[88] Simon Hein and Arnulf Latz. "Influence of local lithium metal deposition in 3D microstructures on local and global behavior of Lithium-ion batteries". In: *Electrochimica Acta* 2016 (2016). ISSN: 00134686.

[89] Yvonne Krämer, Claudia Birkenmaier, Julian Feinauer, Andreas Hintennach, Conrad L. Bender, Markus Meiler, Volker Schmidt, Robert E. Dinnebier, and Thomas Schleid. "A new method for quantitative marking of deposited lithium by chemical treatment on graphite anodes in lithium-ion cells". In: *Chemistry (Weinheim an der*

Bergstrasse, Germany) 21.16 (2015), pp. 6062–6065. DOI: 10.1002/chem.201406606.

[90] Rajeswari Chandrasekaran. "Quantification of bottlenecks to fast charging of lithium-ion-insertion cells for electric vehicles". In: *Journal of Power Sources* 271 (2014), pp. 622–632. ISSN: 03787753. DOI: 10.1016/j.jpowsour.2014.07.106.

[91] Claudia Birkenmaier, Bernhard Bitzer, Matthias Harzheim, Andreas Hintennach, and Thomas Schleid. "Lithium Plating on Graphite Negative Electrodes: Innovative Qualitative and Quantitative Investigation Methods". In: *Journal of The Electrochemical Society* 162.14 (2015), A2646–A2650. ISSN: 0013-4651. DOI: 10.1149/2.0451514jes.

[92] L. E. Downie, L. J. Krause, J. C. Burns, L. D. Jensen, V. L. Chevrier, and J. R. Dahn. "In Situ Detection of Lithium Plating on Graphite Electrodes by Electrochemical Calorimetry". In: *Journal of The Electrochemical Society* 160.4 (2013), A588–A594. ISSN: 0013-4651. DOI: 10.1149/2.049304jes.

[93] Maureen Tang, Paul Albertus, and John Newmana. "Two-Dimensional Modeling of Lithium Deposition during Cell Charging". In: *Journal of The Electrochemical Society* 156 (5) (2009), A390–A399.

[94] L. Gireaud, S. Grugeon, S. Laruelle, B. Yrieix, and J.-M. Tarascon. "Lithium metal stripping/plating mechanisms studies: A metallurgical approach". In: *Electrochemistry Communications* 8.10 (2006), pp. 1639–1649. ISSN: 13882481. DOI: 10.1016/j.elecom.2006.07.037.

[95] Georg Fuchs, Lisa Willenberg, Florian Ringbeck, and Dirk Uwe Sauer. "Post-Mortem Analysis of Inhomogeneous Induced Pressure on Commercial Lithium-Ion Pouch Cells and Their Effects". In: *Sustainability* 11.23, 6738 (2019). DOI: 10.3390/su11236738.

[96] John Cannarella and Craig B. Arnold. "The Effects of Defects on Localized Plating in Lithium-Ion Batteries". In: *Journal of The Electrochemical Society* 162.7 (2015), A1365–A1373. ISSN: 0013-4651. DOI: 10.1149/2.1051507jes.

[97] C. Uhlmann, J. Illig, M. Ender, R. Schuster, and E. Ivers-Tiffée. “In situ detection of lithium metal plating on graphite in experimental cells”. In: *Journal of Power Sources* 279 (2015), pp. 428–438. ISSN: 03787753. DOI: 10.1016/j.jpowsour.2015.01.046.

[98] Daniel R. Baker and Mark W. Verbrugge. “Modeling Overcharge at Graphite Electrodes: Plating and Dissolution of Lithium”. In: *Journal of The Electrochemical Society* 2020.167 (2020).

[99] Mark W. Verbrugge and Brian J. Koch. “The effect of large negative potentials and overcharge on the electrochemical performance of lithiated carbon”. In: *Journal of Electroanalytical Chemistry* 436 (1997), pp. 1–7.

[100] Upender Rao Koleti, Cheng Zhang, Truong Quang Dinh, James Marco, Tazdin Amietszajew, and Romeo Malik. “A new concept to improve the lithium plating detection sensitivity in lithium-ion batteries”. In: *International Journal of Smart Grid and Clean Energy* (2019), pp. 505–516. ISSN: 23154462. DOI: 10.12720/sgce.8.5.505-516.

[101] C.-K. Huang, J. S. Sakamoto, J. Wolfenstine, and S. Surampudi. “The Limits of Low-Temperature Performance of Li-Ion Cells”. In: *Journal of The Electrochemical Society* 147 (8) (2000), pp. 2893–2896.

[102] Keith B. Oldham. “Edge Effects in Semiinfinite Diffusion”. In: *Journal of The Electroanalytical Society* 122 (1981), pp. 1–17.

[103] Ningxin Zhang and Huaqiong Tang. “Dissecting anode swelling in commercial lithium-ion batteries”. In: *Journal of Power Sources* 218 (2012), pp. 52–55. ISSN: 03787753. DOI: 10.1016/j.jpowsour.2012.06.071.

[104] Dirk Kehrwald, Paul R. Shearing, Nigel P. Brandon, Puneet K. Sinha, and Stephen J. Harris. “Local Tortuosity Inhomogeneities in a Lithium Battery Composite Electrode”. In: *Journal of The Electrochemical Society* 158.12 (2011), A1393. ISSN: 0013-4651. DOI: 10.1149/2.079112jes.

[105] J. Schmitt, F. Treuer, F. Dietrich, K. Dröder, T.-P. Heins, U. Schröder, U. Westerhoff, and M. Kurrat. *Coupled Mechanical and Electrochemical Characterization Method for Battery Materials*. IEEE, 2014. ISBN: 1479948489.

[106] T. Waldmann, S. Gorse, T. Samtleben, G. Schneider, V. Knoblauch, and M. Wohlfahrt-Mehrens. "A Mechanical Aging Mechanism in Lithium-Ion Batteries". In: *Journal of The Electrochemical Society* 161.10 (2014), A1742–A1747. ISSN: 0013-4651. DOI: 10.1149/2.1001410jes.

[107] Elham Sahraei, Joseph Meier, and Tomasz Wierzbicki. "Characterizing and modeling mechanical properties and onset of short circuit for three types of lithium-ion pouch cells". In: *Journal of Power Sources* 247 (2014), pp. 503–516. ISSN: 03787753. DOI: 10.1016/j.jpowsour.2013.08.056.

[108] Bramy Pilipili Matadi, Sylvie Geniès, Arnaud Delaille, Claude Chabrol, Eric de Vito, Michel Bardet, Jean-Frédéric Martin, Lise Daniel, and Yann Bultel. "Irreversible Capacity Loss of Li-Ion Batteries Cycled at Low Temperature Due to an Untypical Layer Hindering Li Diffusion into Graphite Electrode". In: *Journal of The Electrochemical Society* 164.12 (2017), A2374–A2389. ISSN: 0013-4651. DOI: 10.1149/2.0491712jes.

[109] Neelima Paul, Johannes Wandt, Stefan Seidlmayer, Sebastian Schebesta, Martin J. Mühlbauer, Oleksandr Dolotko, Hubert A. Gasteiger, and Ralph Gilles. "Aging behavior of lithium iron phosphate based 18650-type cells studied by in situ neutron diffraction". In: *Journal of Power Sources* 345 (2017), pp. 85–96. ISSN: 03787753. DOI: 10.1016/j.jpowsour.2017.01.134.

[110] Shuang Liu, L. Xiong, and C. He. "Long cycle life lithium ion battery with lithium nickel cobalt manganese oxide (NCM) cathode". In: *Journal of Power Sources* 261 (2014), pp. 285–291. ISSN: 03787753. DOI: 10.1016/j.jpowsour.2014.03.083.

[111] Thomas Waldmann, Marcel Wilka, Michael Kasper, Meike Fleischhammer, and Margret Wohlfahrt-Mehrens. "Temperature dependent ageing mechanisms in Lithium-ion batteries – A Post-Mortem study". In: *Journal of Power Sources* 262 (2014), pp. 129–135. ISSN: 03787753. DOI: 10.1016/j.jpowsour.2014.03.112.

[112] Indrajeet V. Thorat, David E. Stephenson, Nathan A. Zacharias, Karim Zaghib, John N. Harb, and Dean R. Wheeler. "Quantifying tortuosity in porous Li-ion battery materials". In: *Journal of Power Sources* 188.2 (2009), pp. 592–600. ISSN: 03787753. DOI: 10.1016/j.jpowsour.2008.12.032.

[113] Martin Ebner, Ding-Wen Chung, R. Edwin García, and Vanessa Wood. In: *Advanced Energy Materials* 4.5, 1301278 (2014). ISSN: 16146832. DOI: 10.1002/aenm.201301278.

[114] Sa Li, Mengwen Jiang, Yong Xie, Hui Xu, Junyao Jia, and Ju Li. "Developing High-Performance Lithium Metal Anode in Liquid Electrolytes: Challenges and Progress". In: *Advanced materials (Deerfield Beach, Fla.)* 30.17 (2018), e1706375. DOI: 10.1002/adma.201706375.

[115] Kuan-Hung Chen, Kevin N. Wood, Eric Kazyak, William S. LePage, Andrew L. Davis, Adrian J. Sanchez, and Neil P. Dasgupta. "Dead lithium: mass transport effects on voltage, capacity, and failure of lithium metal anodes". In: *Journal of Materials Chemistry A* 5.23 (2017), pp. 11671–11681. ISSN: 2050-7488. DOI: 10.1039/C7TA00371D.

[116] Jens Steiger, Dominik Kramer, and Reiner Mönig. "Microscopic observations of the formation, growth and shrinkage of lithium moss during electrodeposition and dissolution". In: *Electrochimica Acta* 136 (2014), pp. 529–536. ISSN: 00134686. DOI: 10.1016/j.electacta.2014.05.120.

[117] Jun-ichi Yamaki, Shin-ichi Tobishima, Keiichi Saito, Yasue Nemoto, and Masayasu Arakawa. "A consideration of the morphology of electrochemically deposited lithium in an organic electrolyte". In: *Journal of Power Sources* 74 (1998), pp. 219–227. ISSN: 03787753.

[118] Thomas F. Fuller, Marc Doyle, and John Newman. “Simulation and Optimization of the Dual Lithium Ion Insertion Cell”. In: *Journal of The Electrochemical Society* 141 No. 1 (1994).

[119] Mark W. Verbrugge and Brian J. Koch. “Microelectrode investigation of ultrahigh-rate lithium deposition and stripping”. In: *Journal of Electroanalytical Chemistry* 367 (1994), pp. 123–129.

[120] D. Anseán, M. Dubarry, A. Devie, B. Y. Liaw, V. M. García, J. C. Viera, and M. González. “Operando lithium plating quantification and early detection of a commercial LiFePO4 cell cycled under dynamic driving schedule”. In: *Journal of Power Sources* 356 (2017), pp. 36–46. ISSN: 03787753. DOI: 10.1016/j.jpowsour.2017.04.072.

[121] Fumihiro Sagane, Ryosuke Shimokawa, Hikaru Sano, Hikari Sakaebe, and Yasutoshi Iriyama. “In-situ scanning electron microscopy observations of Li plating and stripping reactions at the lithium phosphorus oxynitride glass electrolyte/Cu interface”. In: *Journal of Power Sources* 225 (2013), pp. 245–250. ISSN: 03787753. DOI: 10.1016/j.jpowsour.2012.10.026.

[122] F. Orsini, Du Pasquier. A., B. Beaudoin, J. M. Tarascon, M. Trentin, N. Langenhuizen, E. de Beer, and P. Notten. “In situ Scanning Electron Microscopy SEM observation of interfaces within plastic lithium batteries”. In: *Journal of Power Sources* 76 (1998), pp. 19–29. ISSN: 03787753.

[123] F. Orsini, A. Du Pasquier, Beaudouin. B., J. M. Tarascon, M. Trentin, N. Langenhuizen, E. de Beer, and P. Notten. “In situ SEM study of the interfaces in plastic lithium cells”. In: *Journal of Power Sources* 81-82 (1999), pp. 918–921. ISSN: 03787753.

[124] Niloofar Ghanbari, Thomas Waldmann, Michael Kasper, Peter Axmann, and Margret Wohlfahrt-Mehrens. “Inhomogeneous Degradation of Graphite Anodes in Li-Ion Cells: A Postmortem Study Using Glow Discharge Optical Emission Spectroscopy (GD-OES)”. In: *The Journal of Physical Chemistry C* 120.39 (2016), pp. 22225–22234. ISSN: 1932-7447. DOI: 10.1021/acs.jpcc.6b07117.

[125] Asghar Aryanfar, Daniel Brooks, Boris V. Merinov, William A. Goddard, Agustín J. Colussi, and Michael R. Hoffmann. "Dynamics of Lithium Dendrite Growth and Inhibition: Pulse Charging Experiments and Monte Carlo Calculations". In: *The journal of physical chemistry letters* 5.10 (2014), pp. 1721–1726. DOI: 10.1021/jz500207a.

[126] Doron Aurbach, Orit Youngman, Yosef Gofer, and Arie Meitav. "The electrochemical behaviour of 1,3-dioxolane—LiClO4 solutions—I. Uncontaminated solutions". In: *Electrochimica Acta* 35.3 (1990), pp. 625–638. ISSN: 00134686.

[127] B. Rieger, S. F. Schuster, S. V. Erhard, P. J. Osswald, A. Rheinfeld, C. Willmann, and A. Jossen. "Multi-directional laser scanning as innovative method to detect local cell damage during fast charging of lithium-ion cells". In: *Journal of Energy Storage* 8 (2016), pp. 1–5. ISSN: 2352152X. DOI: 10.1016/j.est.2016.09.002.

[128] Amaia Iturrondobeitia, Frederic Aguesse, Sylvie Genies, Thomas Waldmann, Michael Kasper, Niloofar Ghanbari, Margret Wohlfahrt-Mehrens, and Emilie Bekaert. "Post-Mortem Analysis of Calendar-Aged 16 Ah NMC/Graphite Pouch Cells for EV Application". In: *The Journal of Physical Chemistry C* 121.40 (2017), pp. 21865–21876. ISSN: 1932-7447. DOI: 10.1021/acs.jpcc.7b05416.

[129] J. C. Burns, D. A. Stevens, and J. R. Dahn. "In-Situ Detection of Lithium Plating Using High Precision Coulometry". In: *Journal of The Electrochemical Society* 2015.162(6) (2015), A959–A964.

[130] Mathias Petzl, Michael Kasper, and Michael A. Danzer. "Lithium plating in a commercial lithium-ion battery – A low-temperature aging study". In: *Journal of Power Sources* 275 (2015), pp. 799–807. ISSN: 03787753. DOI: 10.1016/j.jpowsour.2014.11.065.

[131] Bernhard Bitzer and Andreas Gruhle. "A new method for detecting lithium plating by measuring the cell thickness". In: *Journal of Power Sources* 262 (2014), pp. 297–302. ISSN: 03787753. DOI: 10.1016/j.jpowsour.2014.03.142.

[132] N. Ghanbari, T. Waldmann, M. Kasper, P. Axmann, and M. Wohlfahrt-Mehrens. “Detection of Li Deposition by Glow Discharge Optical Emission Spectroscopy in Post-Mortem Analysis”. In: *ECS Electrochemistry Letters* 4.9 (2015), A100–A102. ISSN: 2162-8726. DOI: 10.1149/2.0041509eel.

[133] Meike Fleischhammer, Thomas Waldmann, Gunther Bisle, Björn-Ingo Hogg, and Margret Wohlfahrt-Mehrens. “Interaction of cyclic ageing at high-rate and low temperatures and safety in lithium-ion batteries”. In: *Journal of Power Sources* 274 (2015), pp. 432–439. ISSN: 03787753. DOI: 10.1016/j.jpowsour.2014.08.135.

[134] Thomas Waldmann, Michael Kasper, and Margret Wohlfahrt-Mehrens. “Optimization of Charging Strategy by Prevention of Lithium Deposition on Anodes in high-energy Lithium-ion Batteries – Electrochemical Experiments”. In: *Electrochimica Acta* 178 (2015), pp. 525–532. ISSN: 00134686. DOI: 10.1016/j.electacta.2015.08.056.

[135] D. A. Stevens, R. Y. Ying, Reza Fathi, J. N. Reimers, J. E. Harlow, and J. R. Dahn. “Using High Precision Coulometry Measurements to Compare the Degradation Mechanisms of NMC/LMO and NMC-Only Automotive Scale Pouch Cells”. In: *Journal of The Electrochemical Society* 161.9 (2014), A1364–A1370. ISSN: 0013-4651. DOI: 10.1149/2.0971409jes.

[136] Meinert Lewerenz, Alexander Warnecke, and Dirk Uwe Sauer. “Introduction of capacity difference analysis (CDA) for analyzing lateral lithium-ion flow to determine the state of covering layer evolution”. In: *Journal of Power Sources* 354 (2017), pp. 157–166. ISSN: 03787753. DOI: 10.1016/j.jpowsour.2017.04.043.

[137] Peter Keil and Andreas Jossen. “Charging protocols for lithium-ion batteries and their impact on cycle life—An experimental study with different 18650 high-power cells”. In: *Journal of Energy Storage* 6 (2016), pp. 125–141. ISSN: 2352152X. DOI: 10.1016/j.est.2016.02.005.

[138] J. C. Burns, Adil Kassam, N. N. Sinha, L. E. Downie, Lucie Solnickova, B. M. Way, and J. R. Dahn. "Predicting and Extending the Lifetime of Li-Ion Batteries". In: *Journal of The Electrochemical Society* 160.9 (2013), A1451–A1456. ISSN: 0013-4651. DOI: 10.1149/2.060309jes.

[139] M. Broussely, Ph. Biensan, F. Bonhomme, Ph. Blanchard, S. Herreyre, K. Nechev, and R. J. Staniewicz. "Main aging mechanisms in Li ion batteries". In: *Journal of Power Sources* 146.1-2 (2005), pp. 90–96. ISSN: 03787753. DOI: 10.1016/j.jpowsour.2005.03.172.

[140] Meinert Lewerenz, Jens Münnix, Johannes Schmalstieg, Stefan Käbitz, Marcus Knips, and Dirk Uwe Sauer. "Systematic aging of commercial LiFePO 4 |Graphite cylindrical cells including a theory explaining rise of capacity during aging". In: *Journal of Power Sources* 345 (2017), pp. 254–263. ISSN: 03787753. DOI: 10.1016/j.jpowsour.2017.01.133.

[141] Stefan Schindler, Marius Bauer, Mathias Petzl, and Michael A. Danzer. "Voltage relaxation and impedance spectroscopy as in-operando methods for the detection of lithium plating on graphitic anodes in commercial lithium-ion cells". In: *Journal of Power Sources* 304 (2016), pp. 170–180. ISSN: 03787753. DOI: 10.1016/j.jpowsour.2015.11.044.

[142] J. Illig, J. P. Schmidt, M. Weiss, A. Weber, and E. Ivers-Tiffée. "Understanding the impedance spectrum of 18650 LiFePO4-cells". In: *Journal of Power Sources* 239 (2013), pp. 670–679. ISSN: 03787753. DOI: 10.1016/j.jpowsour.2012.12.020.

[143] S. S. Zhang, K. Xu, and T. R. Jow. "The low temperature performance of Li-ion batteries". In: *Journal of Power Sources* 115.1 (2003), pp. 137–140. ISSN: 03787753. DOI: 10.1016/S0378-7753(02)00618-3.

[144] Mickael Dolle, Francois Orsini, Antoni S. Gozdz, and Jean-Marie Tarascona. "Development of Reliable Three-Electrode Impedance Measurements in Plastic Li-Ion Batteries". In: *Journal of The Electrochemical Society* 148 (8) (2001), A851–A857.

[145] Andrew N. Jansen, Dennis W. Dees, Daniel P. Abraham, Khalil Amine, and Gary L. Henriksen. “Low-temperature study of lithium-ion cells using a LiySn micro-reference electrode”. In: *Journal of Power Sources* 174.2 (2007), pp. 373–379. ISSN: 03787753. DOI: 10.1016/j.jpowsour.2007.06.235.

[146] Dennis W. Dees, Andrew N. Jansen, and Daniel P. Abraham. “Theoretical examination of reference electrodes for lithium-ion cells”. In: *Journal of Power Sources* 174.2 (2007), pp. 1001–1006. ISSN: 03787753. DOI: 10.1016/j.jpowsour.2007.06.128.

[147] Chunsheng Wang, A. John Appleby, and Frank E. Little. “Low-Temperature Characterization of Lithium-Ion Carbon Anodes via Microperturbation Measurement”. In: *Journal of The Electrochemical Society* 149 (6) (2002), A754–A760.

[148] Evgenij Barsoukov, Jong Hyun Kim, Jong Hun Kim, Chul Oh Yoon, and Hosull Lee. “Kinetics of lithium intercalation into carbon anodes: in situ impedance investigation of thickness and potential dependence”. In: *Solid State Ionics* 116 (1999), pp. 249–261.

[149] G. Hsieh, T. O. Mason, and L. R. Pederson. “Experimental limitations in impedance spectroscopy: Part II - electrode artifacts in three-point measurements on Pt/YSZ”. In: *Solid State Ionics* 91 (1996), pp. 203–212.

[150] G. Hsieh, S. J. Ford, T. O. Mason, and L. R. Pederson. “Experimentall limitations in impedance spectroscopy: Part I - simulation of reference electrode artifacts in three-point measurements”. In: *Solid State Ionics* 91 (1996), pp. 191–201.

[151] Q. Q. Liu, R. Petibon, C. Y. Du, and J. R. Dahn. “Effects of Electrolyte Additives and Solvents on Unwanted Lithium Plating in Lithium-Ion Cells”. In: *Journal of The Electrochemical Society* 164.6 (2017), A1173–A1183. ISSN: 0013-4651. DOI: 10.1149/2.1081706jes.

[152] Upender Rao Koleti, Truong Quang Dinh, and James Marco. “A new on-line method for lithium plating detection in lithium-ion batteries”. In: *Journal of Power Sources* 451 (2020), pp. 1–12. ISSN: 03787753. DOI: 10.1016/j.jpowsour.2020.227798.

[153] Xiao-Guang Yang, Shanhai Ge, Teng Liu, Yongjun Leng, and Chao-Yang Wang. “A look into the voltage plateau signal for detection and quantification of lithium plating in lithium-ion cells”. In: *Journal of Power Sources* 395 (2018), pp. 251–261. ISSN: 03787753. DOI: 10.1016/j.jpowsour.2018.05.073.

[154] Fumihiro Sagane, Ken-ichi Ikeda, Kengo Okita, Hikaru Sano, Hikari Sakaebe, and Yasutoshi Iriyama. “Effects of current densities on the lithium plating morphology at a lithium phosphorus oxynitride glass electrolyte/copper thin film interface”. In: *Journal of Power Sources* 233 (2013), pp. 34–42. ISSN: 03787753. DOI: 10.1016/j.jpowsour.2013.01.051.

[155] Johannes Wandt, Peter Jakes, Josef Granwehr, Rüdiger-A. Eichel, and Hubert A. Gasteiger. “Quantitative and time-resolved detection of lithium plating on graphite anodes in lithium ion batteries”. In: *Materials Today* 21.3 (2018), pp. 231–240. ISSN: 13697021. DOI: 10.1016/j.mattod.2017.11.001.

[156] Doron Aurbach, Idit Weissman, and Alexander Schechter. “X-ray Photoelectron Spectroscopy Studies of Lithium Surfaces Prepared in Several Important Electrolyte Solutions. A Comparison with Previous Studies by Fourier Transform Infrared Spectroscopy”. In: *Langmuir* 12 (1996), pp. 3991–4007.

[157] Donald R. Baer, Kateryna Artyushkova, Hagai Cohen, Christopher D. Easton, Mark Engelhard, Thomas R. Gengenbach, Grzegorz Greczynski, Paul Mack, David J. Morgan, and Adam Roberts. “XPS guide: Charge neutralization and binding energy referencing for insulating samples”. In: *Journal of Vacuum Science & Technology A* 38.3 (2020), p. 031204. ISSN: 0734-2101. DOI: 10.1116/6.0000057.

[158] Teignmouth Science and Technology Centre. “A Beginners Guide to XPS”. 2017.

[159] Rabeb Grissa, Vincent Fernandez, Neal Fairley, Jonathan Hamon, Nicolas Stephant, Julien Rolland, Renaud Bouchet, Margaud Lecuyer, Marc Deschamps, Dominique Guyomard, and Philippe Moreau. “XPS and SEM-EDX Study of Electrolyte Nature Effect on Li Electrode in Lithium Metal Batteries”. In: *ACS Applied Energy Materials* (2018). ISSN: 2574-0962. DOI: 10.1021/acsaem.8b01256.

[160] Bramy Pilipili Matadi, Sylvie Geniès, Arnaud Delaille, Claude Chabrol, Eric de Vito, Michel Bardet, Jean-Frédéric Martin, Lise Daniel, and Yann Bultel. “Irreversible Capacity Loss of Li-Ion Batteries Cycled at Low Temperature Due to an Untypical Layer Hindering Li Diffusion into Graphite Electrode”. In: *Journal of The Electrochemical Society* 164.12 (2017), A2374–A2389. ISSN: 0013-4651. DOI: 10.1149/2.0491712jes.

[161] Arianna Moretti, Diogo Vieira Carvalho, Niloofar Ehteshami, Elie Paillard, Willy Porcher, David Brun-Buisson, Jean-Baptiste Ducros, Iratxe de Meatza, Aitor Eguia-Barrio, Khiem Trad, and Stefano Passerini. “A Post-Mortem Study of Stacked 16 Ah Graphite//LiFePO4 Pouch Cells Cycled at 5 °C”. In: *Batteries* 5.2 (2019), p. 45. DOI: 10.3390/batteries5020045.

[162] S. Oswald, K. Nikolowski, and H. Ehrenberg. “Quasi in situ XPS investigations on intercalation mechanisms in Li-ion battery materials”. In: *Analytical and bioanalytical chemistry* 393.8 (2009), pp. 1871–1877. DOI: 10.1007/s00216-008-2520-z.

[163] S. Naille, R. Dedryvère, H. Martinez, S. Leroy, P.-E. Lippens, J.-C. Jumas, and D. Gonbeau. “XPS study of electrode/electrolyte interfaces of η-Cu6Sn5 electrodes in Li-ion batteries”. In: *Journal of Power Sources* 174.2 (2007), pp. 1086–1090. ISSN: 03787753. DOI: 10.1016/j.jpowsour.2007.06.043.

[164] S. Oswald, D. Mikhailova, F. Scheiba, P. Reichel, A. Fiedler, and H. Ehrenberg. “XPS investigations of electrolyte/electrode interactions for various Li-ion battery materials”. In: *Analytical and bioanalytical chemistry* 400.3 (2011), pp. 691–696. DOI: 10.1007/s00216-010-4646-z.

[165] S. Shiraishi, K. Kanamura, and Z. Takehara. “Effect of surface modification using various acids on electrodeposition of lithium”. In: *journal of applied electrochemistry* 25 (1995), pp. 584–591.

[166] S. Shiraishi, K. Kanamura, and Z-I. Takehara. “Influence of initial surface condition of lithium metal anodes on surface modification with HF”. In: *journal of applied electrochemistry* 29 (1999), pp. 869–881.

[167] Y. Li, M. Bettge, B. Polzin, Y. Zhu, M. Balasubramanian, and D. P. Abraham. “Understanding Long-Term Cycling Performance of Li 1.2 Ni 0.15 Mn 0.55 Co 0.1 O 2 –Graphite Lithium-Ion Cells”. In: *Journal of The Electrochemical Society* 160.5 (2013), A3006–A3019. ISSN: 0013-4651. DOI: 10.1149/2.002305jes.

[168] S. Verdier, L. El Ouatani, R. Dedryvère, F. Bonhomme, P. Biensan, and D. Gonbeaua. “XPS Study on Al2O3- and AlPO4-Coated LiCoO2 Cathode Material for High-Capacity Li Ion Batteries”. In: *Journal of The Electrochemical Society* 2007.154 (2007), A1088–A1099. ISSN: 0013-4651.

[169] S. Leroy, H. Martinez, R. Dedryvère, D. Lemordant, and D. Gonbeau. “Influence of the lithium salt nature over the surface film formation on a graphite electrode in Li-ion batteries: An XPS study”. In: *Applied Surface Science* 253.11 (2007), pp. 4895–4905. ISSN: 01694332. DOI: 10.1016/j.apsusc.2006.10.071.

[170] R.I.R. Blyth, H. Buqa, F. P. Netzer, M. G. Ramsey, J. O. Besenhard, P. Golob, and M. Winter. “XPS studies of graphite electrode materials for lithium ion batteries”. In: *Applied Surface Science* 2000.167 (2000), pp. 99–106. ISSN: 01694332.

[171] M. Herstedt, A. M. Andersson, H. Rensmo, H. Siegbahn, and K. Edström. "Characterisation of the SEI formed on natural graphite in PC-based electrolytes". In: *Electrochimica Acta* 49.27 (2004), pp. 4939–4947. ISSN: 00134686. DOI: 10.1016/j.electacta.2004.06.006.

[172] S. Oswald, M. Hoffmann, and M. Zier. "Peak position differences observed during XPS sputter depth profiling of the SEI on lithiated and delithiated carbon-based anode material for Li-ion batteries". In: *Applied Surface Science* 401 (2017), pp. 408–413. ISSN: 01694332. DOI: 10.1016/j.apsusc.2016.12.223.

[173] A.M Andersson, A. Henningson, H. Siegbahn, U. Jansson, and K. Edström. "Electrochemically lithiated graphite characterised by photoelectron spectroscopy". In: *Journal of Power Sources* 119-121 (2003), pp. 522–527. ISSN: 03787753. DOI: 10.1016/S0378-7753(03)00277-5.

[174] Steffen Oswald, Franziska Thoss, Martin Zier, Martin Hoffmann, Tony Jaumann, Markus Herklotz, Kristian Nikolowski, Frieder Scheiba, Michael Kohl, Lars Giebeler, Daria Mikhailova, and Helmut Ehrenberg. "Binding Energy Referencing for XPS in Alkali Metal-Based Battery Materials Research (II): Application to Complex Composite Electrodes". In: *Batteries* 4.3, 36 (2018). DOI: 10.3390/batteries4030036.

[175] S. Oswald. "Binding energy referencing for XPS in alkali metal-based battery materials research (I): Basic model investigations". In: *Applied Surface Science* 351 (2015), pp. 1–43. ISSN: 01694332. DOI: 10.1016/j.apsusc.2015.05.029.

[176] Kevin N. Wood, K. Xerxes Steirer, Simon E. Hafner, Chunmei Ban, Shriram Santhanagopalan, Se-Hee Lee, and Glenn Teeter. "Operando X-ray photoelectron spectroscopy of solid electrolyte interphase formation and evolution in Li2S-P2S5 solid-state electrolytes". In: *Nature communications* 9.1, 2490 (2018). DOI: 10.1038/s41467-018-04762-z.

[177] Alexander G. Shard. “Practical guides for x-ray photoelectron spectroscopy: Quantitative XPS”. In: *Journal of Vacuum Science & Technology A* 38.4, 041201 (2020). ISSN: 0734-2101. DOI: 10.1116/1.5141395.

[178] R. Dedryvère, L. Gireaud, S. Grugeon, S. Laruelle, J-M Tarascon, and D. Gonbeau. “Characterization of lithium alkyl carbonates by X-ray photoelectron spectroscopy: experimental and theoretical study”. In: *The journal of physical chemistry. B* 109.33 (2005), pp. 15868–15875. ISSN: 1520-6106. DOI: 10.1021/jp051626k.

[179] J. H. Scofield. “Hartree-Slater Subshell Photoionization Cross-Sections at 1254 and 1487 eV”. In: *Journal of Electron Spectroscopy and Related Phenomena* 8 (1976), pp. 129–l 37.

[180] Mengyun Nie, Julien Demeaux, Benjamin T. Young, David R. Heskett, Yanjing Chen, Arijit Bose, Joseph C. Woicik, and Brett L. Luchta. “Effect of Vinylene Carbonate and Fluoroethylene Carbonate onSEI Formation on Graphitic Anodes in Li-Ion Batteries”. In: *Journal of The Electrochemical Society* 2015.162 (2015), A7008–A7014.

[181] Martin Schmid, Hans-Peter Steinrück, and J. Michael Gottfried. “A new asymmetric Pseudo-Voigt function for more efficient fitting of XPS lines”. In: *Surface and Interface Analysis* 46.8 (2014), pp. 505–511. ISSN: 0142-2421. DOI: 10.1002/sia.5521.

[182] D. Briggs and J. T. Grant. *Surface analysis by Auger and x-ray photoelectron spectroscopy*. Chichester, UK: IMPublications, 2003. ISBN: 1-901019-04-7.

[183] Julia Maibach, Fredrik Lindgren, Henrik Eriksson, Kristina Edström, and Maria Hahlin. “Electric Potential Gradient at the Buried Interface between Lithium-Ion Battery Electrodes and the SEI Observed Using Photoelectron Spectroscopy”. In: *The journal of physical chemistry letters* 7.10 (2016), pp. 1775–1780. DOI: 10.1021/acs.jpclett.6b00391.

[184] Killian R. Tallman and Bingjie Zhang. “Anode Overpotential Control via Interfacial Modification: Inhibition of Lithium Plating on Graphite Anodes: Supporting Information”. In: *ACS Applied Energy Materials* 11 (2019), pp. 46864–46874. ISSN: 2574-0962.

[185] John F. Moulder, William F. Stickle, Peter E. Sobol, and Kenneth D. Bomben. *Handbook of X-ray Photoelectron Spectrocopy: A Reference Book of Standard Spectra for Identification and Interpretation of XPS Data*. 1992.

[186] Jie Shu. “Electrochemical behavior and stability of Li4Ti5O12 in a broad voltage window”. In: *Journal of Solid State Electrochemistry* 13.10 (2009), pp. 1535–1539. ISSN: 1432-8488. DOI: 10.1007/s10008-008-0723-z.

[187] F. Grimsmann, T. Gerbert, F. Brauchle, A. Gruhle, J. Parisi, and M. Knipper. “Determining the maximum charging currents of lithium-ion cells for small charge quantities”. In: *Journal of Power Sources* 365 (2017), pp. 12–16. ISSN: 03787753. DOI: 10.1016/j.jpowsour.2017.08.044.

[188] W. Lu and J. Prakash. “In Situ Measurements of Heat Generation in a Li/Mesocarbon Microbead Half-Cell”. In: *Journal of The Electrochemical Society* 150 (3) (2003), A262–A266.

[189] Norio Takami. “Structural and Kinetic Characterization of Lithium Intercalation into Carbon Anodes for Secondary Lithium Batteries”. In: *Journal of The Electrochemical Society* 142.2, 371 (1995). ISSN: 0013-4651. DOI: 10.1149/1.2044017.

[190] Christian von Lüders, Veronika Zinth, Simon V. Erhard, Patrick J. Osswald, Michael Hofmann, Ralph Gilles, and Andreas Jossen. “Lithium plating in lithium-ion batteries investigated by voltage relaxation and in situ neutron diffraction”. In: *Journal of Power Sources* 342 (2017), pp. 17–23. ISSN: 03787753. DOI: 10.1016/j.jpowsour.2016.12.032.

[191] Rangeet Bhattacharyya, Baris Key, Hailong Chen, Adam S. Best, Anthony F. Hollenkamp, and Clare P. Grey. “In situ NMR observation of the formation of metallic lithium microstructures in lithium batteries”. In: *Nature materials* 9.6 (2010), pp. 504–510. ISSN: 1476-1122. DOI: 10.1038/nmat2764.

[192] Hee Jung Chang, Nicole M. Trease, Andrew J. Ilott, Dongli Zeng, Lin-Shu Du, Alexej Jerschow, and Clare P. Grey. “Investigating Li Microstructure Formation on Li Anodes for Lithium Batteries by in Situ 6 Li/ 7 Li NMR and SEM”. In: *The Journal of Physical Chemistry C* 119.29 (2015), pp. 16443–16451. ISSN: 1932-7447. DOI: 10.1021/acs.jpcc.5b03396.

[193] Lin Zhuang, Juntao Lu, Xinping Ai, and Hanxi Yang. “In-situ ESR study on electrochemical lithium intercalation into petroleum coke”. In: *Journal of Electroanalytical Chemistry* 397 (1995), pp. 315–319.

[194] Johannes Wandt, Cyril Marino, Hubert A. Gasteiger, Peter Jakes, Rüdiger-A. Eichel, and Josef Granwehr. “Operando electron paramagnetic resonance spectroscopy – formation of mossy lithium on lithium anodes during charge–discharge cycling”. In: *Energy & Environmental Science* 8.4 (2015), pp. 1358–1367. ISSN: 1754-5692. DOI: 10.1039/C4EE02730B.

[195] Thomas Waldmann, Björn-Ingo Hogg, Michael Kasper, Sébastien Grolleau, César Gutiérrez Couceiro, Khiem Trad, Bramy Pilipili Matadi, and Margret Wohlfahrt-Mehrens. “Interplay of Operational Parameters on Lithium Deposition in Lithium-Ion Cells: Systematic Measurements with Reconstructed 3-Electrode Pouch Full Cells”. In: *Journal of The Electrochemical Society* 163.7 (2016), A1232–A1238. ISSN: 0013-4651. DOI: 10.1149/2.0591607jes.

[196] H.-p. Lin, D. Chua, M. Salomon, H-C. Shiao, M. Hendrickson, E. Plichta, and S. Slaneb. “Low-Temperature Behavior of Li-Ion Cells”. In: *Electrochemical and Solid-State Letters* 4 (6) (2001), A71–A73.

[197] John Newman and William Tiedemann. “Potential and Current Distribution in Electrochemical Cells”. In: *Journal of The Electrochemical Society* 140 (7) (1993), pp. 1961–1968.

[198] E. McTurk, C. R. Birkl, M. R. Roberts, D. A. Howey, and P. G. Bruce. “Minimally Invasive Insertion of Reference Electrodes into Commercial Lithium-Ion Pouch Cells”. In: *ECS Electrochemistry Letters* 4.12 (2015), A145–A147. ISSN: 2162-8726. DOI: 10.1149/2.0081512eel.

[199] A. Blyr, G. Amatucci, D. Guyomard, Y. Chabre, and J-M. Tarascon. “Self-Discharge of LiMn2O4/C Li-Ion Cells in Their Discharged State”. In: *Journal of The Electrochemical Society* 145 (1) (1998), pp. 194–209.

[200] G. Hsieh, T. O. Mason, E. J. Garboczi, and L. R. Pederson. “Experimental limitations in impedance spectroscopy: Part III. Effect of reference electrode geometry/position”. In: *Solid State Ionics* 96 (1997), pp. 153–172.

[201] Qunwei Wu, Wenquan Lu, and Jai Prakash. “Characterization of a commercial size cylindrical Li-ion cell with a reference electrode”. In: *Journal of Power Sources* 88 (2000), pp. 237–242. ISSN: 03787753.

[202] D. Aurbach, B. Markovsky, I. Weissman, E. Levi, and Y. Ein-Eli. “On the correlation between surface chemistry and performance of graphite negative electrodes for Li ion batteries”. In: *Electrochimica Acta* 45 (1999), pp. 67–86. ISSN: 00134686.

[203] Jiqiang Wang, I. D. Raistrick, and R. A. Huggins. “Behavior of Some Binary Lithium Alloys as Negative Electrodes in Organic Solvent-Based Electrolytes”. In: *Journal of The Electrochemical Society* (1986), pp. 457–461.

[204] Daniel P. Abraham, Steven D. Poppen, Andrew N. Jansen, Jun Liu, and Dennis W. Dees. “Application of a lithium–tin reference electrode to determine electrode contributions to impedance rise in high-power lithium-ion cells”. In: *Electrochimica Acta* 49.26 (2004), pp. 4763–4775. ISSN: 00134686. DOI: 10.1016/j.electacta.2004.05.040.

[205] G. Nagasubramanian. “Two- and three-electrode impedance studies on 18650 Li-ion cells”. In: *Journal of Power Sources* 87 (2000), pp. 226–229. ISSN: 03787753.

[206] Christian Stief. “Ortsaufgelöste Untersuchung von Plating an Lithium-Ionen Batterien mit optischen Methoden”. MA thesis. TU Berlin, 2017.

[207] André Wink. “Untersuchung der Oberfläche von geplateten Lithium-Batterien mit Hilfe eines Focused-Ion-Beam”. MA thesis. TU Berlin, 2018.

[208] Feodora Jonack. “Einfluss von Zellinhomogenitäten auf Lithium-Plating an Lithium-Ionen-Zellen: Master Thesis”. MA thesis. TU Berlin, 2020.

[209] Delf Kober, Inna Kübler, Julia Kowal, and Aleksander Gurlo. *Post mortem investigations and Li plating model of aged lithium ion batteries at low temperature*. KWB 2016 Poster. 2016.

[210] Melvin Avrami. “Kinetics of Phase Change. I General Theory”. In: *The Journal of Chemical Physics* 7.12 (1939), pp. 1103–1112. ISSN: 0021-9606. DOI: 10.1063/1.1750380.

[211] Melvin Avrami. “Kinetics of Phase Change. II Transformation–Time Relations for Random Distribution of Nuclei”. In: *The Journal of Chemical Physics* 8.2 (1940), pp. 212–224. ISSN: 0021-9606. DOI: 10.1063/1.1750631.

[212] Melvin Avrami. “Granulation, Phase Change, and Microstructure Kinetics of Phase Change. III”. In: *The Journal of Chemical Physics* 9.2 (1941), pp. 177–184. ISSN: 0021-9606. DOI: 10.1063/1.1750872.

[213] Ling Zhang. *Lecture 15: Kinetics of Phase Growth: single-component or composition-invariant transformation*. Ed. by University of Utah - Department of Materials Science and Engineering. 2004. URL: https://my.eng.utah.edu/~lzang/images/lecture-15.pdf (visited on 06/02/2021).

[214] E. Bosco and S. K. Rangarajan. “Electrochemical Phase Formation (ECPF) and Marcrogrowth: Part I: Hemispherical Models”. In: *Journal of Electroanalytical Chemistry* 134 (1982), pp. 213–224.

[215] Helmut Föll. *Iron, Steel and Swords*. URL: https://www.tf.uni-kiel.de/matwis/amat/iss/kap_8/illustr/s8_4_3b.html#!Mehl (visited on 06/02/2021).

[216] M. Fanfoni and M. Tomellini. “The Johnson-Mehl- Avrami-Kohnogorov model: A brief review”. In: *IL NUOVO CIMENTO* 20D (1998), pp. 7–8.

[217] R. Dedryvère, S. Leroy, H. Martinez, F. Blanchard, D. Lemordant, and D. Gonbeau. “XPS valence characterization of lithium salts as a tool to study electrode/electrolyte interfaces of Li-ion batteries”. In: *The journal of physical chemistry. B* 110.26 (2006), pp. 12986–12992. ISSN: 1520-6106. DOI: 10.1021/jp061624f.

[218] Elisa Musella, Angelo Mullaliu, Thomas Ruf, Paula Huth, Domenica Tonelli, Giuliana Aquilanti, Reinhard Denecke, and Marco Giorgetti. “Detailing the Self-Discharge of a Cathode Based on a Prussian Blue Analogue”. In: *Energies* 13.15 (2020), p. 4027. DOI: 10.3390/en13154027.

[219] C. Marino, A. Darwiche, N. Dupré, H. A. Wilhelm, B. Lestriez, H. Martinez, R. Dedryvère, W. Zhang, F. Ghamouss, D. Lemordant, and L. Monconduit. “Study of the Electrode/Electrolyte Interface on Cycling of a Conversion Type Electrode Material in Li Batteries”. In: *The Journal of Physical Chemistry C* 117.38 (2013), pp. 19302–19313. ISSN: 1932-7447. DOI: 10.1021/jp402973h.

[220] G. K. Wertheim, P.M.Th.M. van Attekum, and S. Basu. “Electronic Structure of Lithium Graphite”. In: *Solid State Communications* 33 (1980), pp. 1127–1130.

[221] Kiyoshi Kanamura, Soshi Shiraishi, Hideharu Takezawa, and Zen-ichiro Takehara. “XPS Analysis of the Surface of a Carbon Electrode Intercalated by Lithium Ions”. In: *Chemistry of Materials* 9 (1997), pp. 1797–1804. ISSN: 0897-4756.

[222] Salvatore Contarini and J. Wayne Rabalais. “ION BOMBARDMENT-INDUCED DECOMPOSITION OF Li AND Ba SULFATES AND CARBONATES STUDIED BY X-RAY PHOTOELECTRON SPECTROSCOPY”. In: *Journal of Electron Spectroscopy and Related Phenomena* 35 (1985), pp. 191–201.

[223] S. Leroy, F. Blanchard, R. Dedryvère, H. Martinez, B. Carré, D. Lemordant, and D. Gonbeau. “Surface film formation on a graphite electrode in Li-ion batteries: AFM and XPS study”. In: *Surface and Interface Analysis* 37.10 (2005), pp. 773–781. ISSN: 0142-2421. DOI: 10.1002/sia.2072.

[224] K. Edström, T. Gustafsson, and J. O. Thomas. “The cathode–electrolyte interface in the Li-ion battery”. In: *Electrochimica Acta* 50.2-3 (2004), pp. 397–403. ISSN: 00134686. DOI: 10.1016/j.electacta.2004.03.049.

[225] Satoru Tanaka, Masaki Tanigucho, and Hisashi Tanigawa. “XPS and UPS studies on electronic structure of Li2O”. In: *Journal of Nuclear Materials* 283-287 (2000), pp. 1405–1408.

[226] In-Jun Park, Tae-Heum Nam, and Jung-Gu Kim. “Diphenyloctyl phosphate as a solid electrolyte interphase forming additive for Li-ion batteries”. In: *Journal of Power Sources* 244 (2013), pp. 122–128. ISSN: 03787753. DOI: 10.1016/j.jpowsour.2013.03.031.

[227] Damin Lee, Qi Xun Xia, Je Moon Yun, and Kwang Ho Kim. “High-performance cobalt carbonate hydroxide nano-dot/NiCo(CO 3)(OH) 2 electrode for asymmetric supercapacitors”. In: *Applied Surface Science* 433 (2018), pp. 16–26. ISSN: 01694332. DOI: 10.1016/j.apsusc.2017.10.066.

[228] K. Ciosek Högström, S. Malmgren, M. Hahlin, H. Rensmo, F. Thébault, P. Johansson, and K. Edström. “The Influence of PMS-Additive on the Electrode/Electrolyte Interfaces in LiFePO 4 /Graphite Li-Ion Batteries”. In: *The Journal of Physical Chemistry C* 117.45 (2013), pp. 23476–23486. ISSN: 1932-7447. DOI: 10.1021/jp4045385.

[229] D. A. Shirley. “High-Resolution X-Ray Photoemission Spectrum of the Valence Bands of Gold”. In: *Physical Review B* 5.12 (1972), pp. 4709–4714.

[230] Svenja-K. Otto, Yannik Moryson, Thorben Krauskopf, Klaus Peppler, Joachim Sann, Jürgen Janek, and Anja Henss. “In-Depth Characterization of Lithium-Metal Surfaces with XPS and ToF-SIMS: Toward Better Understanding of the Passivation Layer”. In: *Chemistry of Materials* 33.3 (2021), pp. 859–867. ISSN: 0897-4756. DOI: 10.1021/acs.chemmater.0c03518.

[231] L. Somerville, J. Bareño, P. Jennings, A. McGordon, C. Lyness, and I. Bloom. “The Effect of Pre-Analysis Washing on the Surface Film of Graphite Electrodes”. In: *Electrochimica Acta* 206 (2016), pp. 70–76. ISSN: 00134686. DOI: 10.1016/j.electacta.2016.04.133.

[232] Sara Malmgren, Katarzyna Ciosek, Rebecka Lindblad, Stefan Plogmaker, Julius Kühn, Håkan Rensmo, Kristina Edström, and Maria Hahlin. “Consequences of air exposure on the lithiated graphite SEI”. In: *Electrochimica Acta* 105 (2013), pp. 83–91. ISSN: 00134686. DOI: 10.1016/j.electacta.2013.04.118.

[233] Li Yang, Boris Ravdel, and Brett L. Luchta. “Electrolyte Reactions with the Surface of High Voltage LiNi0.5Mn1.5O4 Cathodes for Lithium-Ion Batteries”. In: *Electrochemical and Solid-State Letters* 2010.13 (2010), A95–A97.

[234] Arthur v Cresce, Selena M. Russell, David R. Baker, Karen J. Gaskell, and Kang Xu. “In situ and quantitative characterization of solid electrolyte interphases”. In: *Nano letters* 14.3 (2014), pp. 1405–1412. DOI: 10.1021/nl404471v.

[235] Kevin N. Wood and Glenn Teeter. “XPS on Li-Battery-Related Compounds: Analysis of Inorganic SEI Phases and a Methodology for Charge Correction”. In: *ACS Applied Energy Materials* 1.9 (2018), pp. 4493–4504. ISSN: 2574-0962. DOI: 10.1021/acsaem.8b00406.

[236] F.N David. *Tables of the Ordinates and Probability Integral of the Distribution of the Correlation Coefficient in Small Samples*. 2009. ISBN: 9780521124126.

Schriftenreihe **Elektrische Energietechnik an der TU Berlin**
Hrsg.: Prof. Dr. Sibylle Dieckerhoff, Prof. Dr. Julia Kowal, Prof. Dr. Ronald Plath, Prof. Dr. Uwe Schäfer

ISSN 2367-3761 (print)
ISSN 2367-377X (online)

1: Dinca, Christian: Motor design for maximum material exploitation and magnetization procedure with in-line quality check for mass production. - 2017. - XV, 168 S.
ISBN **978-3-7983-2883-9** (print) EUR **13,00**
ISBN **978-3-7983-2884-6** (online)
DOI 10.14279/depositonce-5630

2: Gkountaras, Aris: Modeling techniques and control strategies for inverter dominated microgrids. - 2017. - 169 S.
ISBN **978-3-7983-2872-3** (print) EUR **12,00**
ISBN **978-3-7983-2873-0** (online)
DOI 10.14279/depositonce-5520

3: Wolz, Christoph: Ein schnelles und genaues Simulationsmodell für permanentmagneterregte Kommutatormotoren kleiner Leistung mit Zahnspulen unter Berücksichtigung nichtlinearer Eigenschaften. - 2017. - XXI, 178 S.
ISBN **978-3-7983-2934-8** (print) EUR **14,00**
ISBN **978-3-7983-2935-5** (online)
DOI 10.14279/depositonce-5911

4: Zerbe, Johannes: Innovative Wickeltechnologien für Statorspulen zur Erhöhung des Füllfaktors und Reduzierung der Beanspruchungen im Wickelprozess. - 2019. - 227 S.
ISBN **978-3-7983-3045-0** (print) EUR **13,50**
ISBN **978-3-7983-3046-7** (online)
DOI 10.14279/depositonce-7533

5: Schneider, Simon Michael: Test bench design for power measurement of inverter-operated machines in the medium voltage range. - 2018. - xii, 128 S.
ISBN **978-3-7983-3024-5** (print) EUR **11,00**
ISBN **978-3-7983-3025-2** (online)
DOI 10.14279/depositonce-7222

6: Winkler, Tammo: Untersuchungen an weich schaltenden DC/DC Konvertern zur Versorgung von Hochleistungs-Diodenlasern. - 2019. - vi, 133 S.
ISBN **978-3-7983-3078-8** (print) EUR **12,00**
ISBN **978-3-7983-3079-5** (online)
DOI 10.14279/depositonce-8324

7: Sarmadi, Mohammed-Ali: Entwurf und Konstruktion einer vertikal laufenden Windturbine nach dem Widerstandsprinzip unter Nutzung der aerodynamischen Eigenschaften eines Flügelprofils. - 2018. - XX, 122 S.
ISBN **978-3-7983-3043-6** (print) EUR **11,00**
ISBN **978-3-7983-3044-3** (online)
DOI 10.14279/depositonce-7659

8: Eial Awwad, Abdullah: On the perspectives of SiC MOSFETs in high-frequency and high-power isolated DC/DC converters. - 2020. - xvii, 158 S.
ISBN **978-3-7983-3096-2** (print) EUR **13,00**
ISBN **978-3-7983-3097-9** (online)
DOI 10.14279/depositonce-8556

9: Dong, Rong: Design and comparison of two brushless DC drives for an electric propulsion system of solar-power unmanned aerial vehicles. - 2020. - x, 115 S.
ISBN **978-3-7983-3126-6** (print) EUR **11,00**
ISBN **978-3-7983-3127-3** (online)
DOI 10.14279/depositonce-9331

10: Böh, Magnus: Effizienzuntersuchung einer weich- und hartschaltenden Konverterstruktur mit Siliziumkarbid-Halbleitern als DC/DC-Wandler für Hybrid- und Elektrofahrzeuge. - 2020. - viii, 203 S.
ISBN **978-3-7983-3133-4** (print) EUR **14,00**
ISBN **978-3-7983-3134-1** (online)
DOI 10.14279/depositonce-9540

11: Böcker, Jan: Analyse und Optimierung von AlGaN/GaN-HEMTs in der leistungselektronischen Anwendung. - 2020. - viii, 203 S.
ISBN **978-3-7983-3141-0**(print) EUR **15,00**
ISBN **978-3-7983-3142-6** (online)
DOI 10.14279/depositonce-9678

12: Just, Hendrik: Modeling and control of power converters in weak and unbalanced electric grids. - 2021. - XXIII, 208 S.
ISBN **978-3-7983-3207-2** (print) EUR **14,00**
ISBN **978-3-7983-3208-9** (online)
DOI 10.14279/depositonce-11674

13: Korth Pereira Ferraz, Pablo: Auswirkungen der hochfrequent alternierenden Ströme leistungselektronischer Schaltungen auf das Betriebs- und Alterungsverhalten von Lithium-Ionen-Batterien. - 2022. - XV, 203 S.
ISBN **978-3-7983-3241-6** (print) EUR **14,00**
ISBN **978-3-7983-3242-3** (online)
DOI 10.14279/depositonce-12657

Universitätsverlag der TU Berlin

Detection and characterization of lithium plating

Lithium plating is one of the most severe ageing mechanisms in lithium-ion batteries. It is becoming more and more important with the increasing presence of electric vehicles that need to be charged under more extreme environmental conditions. This thesis aims at a better understanding of the lithium plating process on three different levels. On the cell level the behaviour of the whole cell is examined under plating conditions and a method is derived to predict the future plating aging of a cell based on the current profile of the cells during plating.
In the second part the chemical composition of the surface electrolyte interphase of plated and non-plated cells is investigated using X-ray-photoelectron spectroscopy to detect differences in the chemical and morphological composition. In the last part the particle structure of cells of different manufacturers is investigated to understand the impact of the particle parameters on plating. The results of these experiments are used to inform decisions in cell design to minimize plating and gain a better understanding of lithium plating.

ISBN 978-3-7983-3278-2 (print)
ISBN 978-3-7983-3279-9 (online)

ISBN 978-3-7983-3278-2

https://verlag.tu-berlin.de